Title
Substitutional Heteroatom Doping and Topological Band Engineering in Graphene Nanoribbons

Author
Piskun, Ilya

Publication Date
2020

Peer reviewed|Thesis/dissertation

Substitutional Heteroatom Doping and Topological Band Engineering in Graphene Nanoribbons

by

Ilya Piskun

A dissertation submitted in partial satisfaction of the

requirements for the degree of

Doctor of Philosophy

in

Chemistry

in the

Graduate Division

of the

University of California, Berkeley

Committee in charge:

Professor Felix Fischer, Chair
Professor Thomas Maimone
Professor Eli Yablonovitch

Fall 2020

Abstract

Substitutional Heteroatom Doping and Topological
Band Engineering in Graphene Nanoribbons

by

Ilya Piskun

Doctor of Philosophy in Chemistry

University of California, Berkeley

Professor Felix Fischer, Chair

The exponentially increasing demand for smaller, faster, and more energy efficient electronic devices represents a monumental challenge in designing the next generation of post-silicon functional electronic materials. Traditionally, device architectures based on organic/inorganic semiconductors are fabricated using a top-down approach; their performance is inherently limited by the spatial resolution of photolithographic techniques. Fischer group's goal is to understand, control, and to be able to harness the exceptional electronic/magnetic properties emerging from nanoscale graphitic materials by developing novel synthetic strategies toward graphene nanoribbons (GNR) via bottom-up synthesis from atomically defined molecular precursors. The semiconducting properties of GNRs can be modulated by varying their width, edge structure and the identity of atoms in the periodic lattice.

My thesis work will detail the power of organic synthesis in design of molecular precursors en route to GNRs, the nanoribbon formation analysis techniques, and the outlook toward application of GNRs in a low-power, tunneling field-effect transistor device architecture (Chapter 1). A large part of my work has aimed at developing new synthetic strategies to access heteroatom-substituted GNRs. After making advances toward BN-substituted GNR precursors, I have discovered a molecular scaffold which furnishes the first example of a surface-mediated C–N bond formation in the context of a 7-AGNR segment (Chapter 2). I have also prepared a series of molecular precursors that have led to the formation of a new family of nitrogen-substituted zigzag GNRs, which possess intriguing spin-separated states along the edges (Chapter 3). In addition to exploring heteroatom substitution, I investigated all-carbon GNR scaffolds that utilize topological band engineering concepts in order to explore new variables that will allow rational tuning of electronic properties in GNRs. I have prepared multiple precursors to continue the realization of topologically protected interface states in GNRs, which are generated by construction of a superlattice of well-defined ribbon segment heterojunctions (Chapter 4).

Acknowledgements

I want to extend my warmest thanks to everyone that has been supportive of me throughout my journey up to this point.

Special thanks goes to my high school AP Chemistry teacher, Ms. Karina Bletsch - you have inspired me to become seriously interested in a career in Chemistry, and you have showed me how exciting and useful chemistry can be.

As for my time at Florida State University, I want to thank Prof. D. Tyler McQuade for a great course in organic chemistry, after which I have decided to pursue undergraduate research. To Prof. Igor Alabugin, thanks for taking me under your wing and enabling me to study organic chemistry at a highest level. In my upperclass studies, Prof. John Dorsey, Prof. Ken Goldsby, and Dr. David Gormin have done an amazing job of mentorship and setting up a great example of how to think and write about chemistry among other things.

During my Ph.D. studies, I have enjoyed great conversations with Prof. Felix Fischer (my thesis advisor), Prof. Mike Crommie and Prof. Jeff Bokor. Your unadulterated excitement for science really carries on with everything that you do, and I am certain that you will be a great source of inspiration for many generations of great scientists to come. Huge shoutout to the entirety of Fischer group that I've gotten a chance to interact with, and I hope that we have learned a lot about science together, and that we all will stay connected and continue to support each other like we did during the difficult days in the lab.

I also would be remiss not to mention the support I've had from my family - my mother Olga, my father Vladimir, my grandmother Lucy, my wife Ashley, and the rest of my multicontinental extended family who have always taken their time to check in on me and helped me stay grounded in my pursuits. Additionally, I must acknowledge Jose Roque, Alec Christian, and John Philbin for basically becoming a part of the family as we have all navigated our way through grad school.

Contents

List of Figures

List of Tables

List of Schemes

1 Carbon electronics: the rise of sp^2-hybridized materials.

> Carbon is unique as an electronic material. It can be a good metal in the form of graphite, a wide gap semiconductor in the form of diamond or fullerenes, a superconductor when intercalated with appropriate guest species, or a polymer when reacted with hydrogen and other species. Furthermore, carbon-based electronic materials provide examples of materials showing the entire range of dimensionalities from fullerenes, which are zero-dimensional quantum dots, to carbon nanotubes, which are one-dimensional quantum wires, to graphite, a two-dimensional layered anisotropic material, and finally to diamond, a three-dimensional wide gap semiconductor.
>
> *M.S. Dresselhaus and G. Dresselhaus, Annu. Rev. Mater. Sci. 1995. 25: 487-523.*

A quote[1] from M.S. Dresselhaus and G. Dresselhaus succinctly describes the versatility of carbon electronic materials, as well as predicts a great future in discovery and developement of the new technology. This chapter will briefly describe the advances in sp^2-hybridized carbon materials (with a focus on the electronic properties of various allotropes), describe the operation of the tunneling field effect transistor (TFET) device that is slated to serve as a breakthrough toward the new generation of computing, and postulate the merit of graphene nanoribbons as a perfectly suitable material for the TFET operation.

1.1 Tunneling field-effect transistor - toward ultra-low power electronics

Silicon-based functional electronic materials are virtually ubiquitous at this stage of our societal developement. The rise of cell phones and powerful personal computers has allowed the humanity an unprecedent access to information and world wide communication. The architecture and the economic viability of modern day electronics heavily relies on an ever increasing number of transistors in the chips, as succinctly postulated by G. Moore, colloquially known as Moore's Law.[2]

As the device size gets smaller and smaller, the power dissipation becomes a fundamental issue in nanoelectronic circuits. Dennard scaling postulates that the power density in transistors remains constant – this leads to the level-off at the safe clock speed and power consumption of a processor as the leakage currents in the chips dissipate too much power and can damage the circuit if not controlled. Currently, the complementary metal-oxide-semiconductor (CMOS) field-effect transistor (FET) architecture is omnipresent technology utilized for state-of-art microprocessors. MOSFET operating principle is based on thermionic injection of electrons over the energy barrier, which is fundamentally limited by the steepness of the transition slope from the *off* to *on* state in the I/V curve (Figure 1). The common figure of merit, the subthreshold swing S,(T) is dependent on the thermal voltage factor $\frac{kT}{q}$, and is fundamentally limited to ∼60 mV/decade.[3] Extrapolating this to a generic *on*/*off* current ratio of 10^6, one needs a voltage of approximately 0.5 V to switch the MOSFET transistor via the thermionic injection mechanism under ideal conditions.

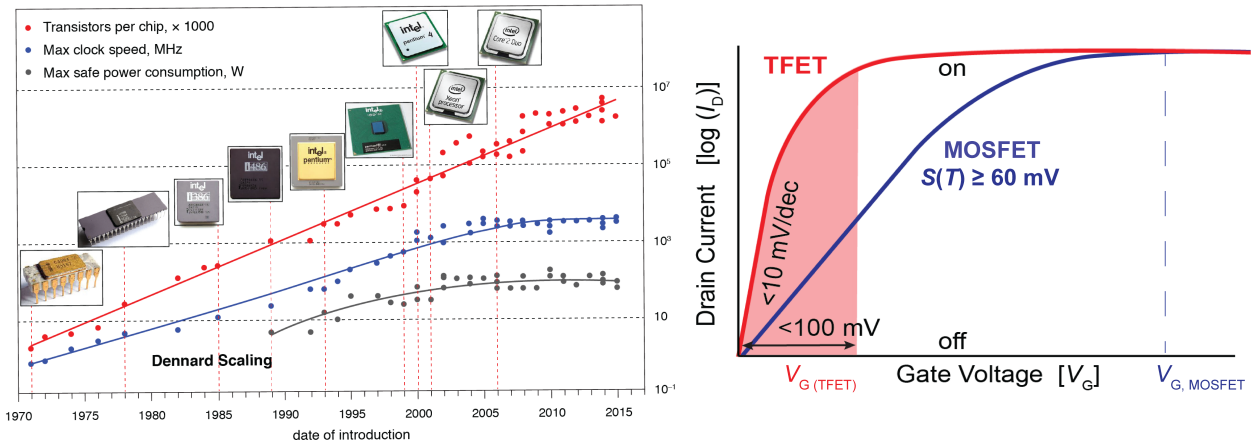

Figure 1: Scaling of the silicon semiconductor devices (1993-2015, reproduced from Intel Press Releases), and comparison of the I_D/V_G curves in MOSFET and TFET devices.

There is a strong push in the academic realm toward a new paradigm in low-power device architecture that can fundamentally change the voltage supply mechanism. A new low-power operating mechanism is also desired in the wearable electronics space, where off-state leakage currents can adversely affect the lifetime of the battery that is required to operate the device. Tunneling field-effect transistors (TFET) represent one potential design that can improve upon thermal injection-type MOSFETs by relying on band-to-band tunneling[4] (BTBT) for charge carrier injection. This removes the dependence on the thermionic charge carrier injection, and has the potential to lower the required gate voltage V_G down to ∼100 mV (Figure 1), which will be an extraordinary improvement in the nanoelectronics.

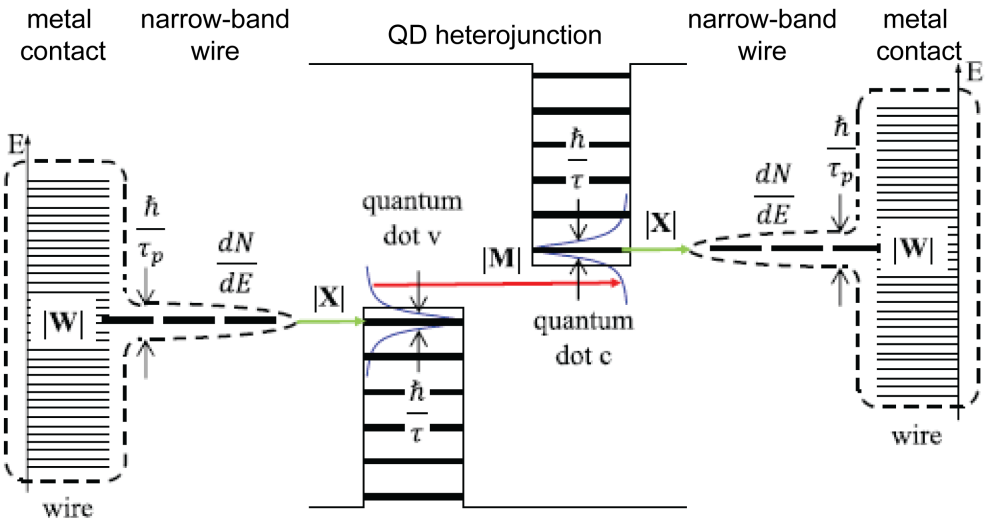

Figure 2: Idealized double quantum dot TFET heterojunction (adapted from reference [5]).

An idealized TFET heterojunction band diagram is proposed in Figure 2, portrayed in an off state. Two metal contacts are connected to narrow-band wires – a material with sharp enery levels and high charge carrier mass (i.e. flat band in the band structure). The narrow-band wires are in-turn connected to a quantum dot heterojunction which performs a function of energy filtering via well-defined energy levels. QD heterojunction energy levels can be aligned/misaligned via application of V_G, so that the device can be turned on/off. QDs are broadly defined in this case as materials with in-gap states that are available for tunneling of the charge carriers.

In order to achieve minimum V_G in a TFET junction, it is imperative that the materials selected for this architecture have (1) sharp, well-defined energy levels to avoid off-state leakage currents, (2) high electrical mobility, and (3) similar lattice constant of segments to avoid Schottky barriers at the heterojunction (i.e. QDs, tunneling barriers, and narrow-band wires should ideally be prepared from the same material). Low-dimensional materials such as derivatives of graphene and transition metal chalcogenides hold the most promise for efficient junctions due to the high current desnity, easily tunable electronic properties, and possibility of clean surfaces and efficient interfaces.[6]

1.2 Carbon electronic materials: from polyacetylene to graphene

The rise of carbon electronic materials has been historically fueled by the inquiry into the conjugated organic polymers. From exotic electronic properties of polyacetylene[7] to discovery of fullerenes,[8] carbon nanotubes[9–11] and ultimately graphene,[12] carbon electronic materials have taken up a rightful share of attention from the community due to the allotropes' highly tunable properties (Scheme 1). A large effort has been documented on developing functional materials based on the sp^2-hybridized carbon materials,[13,14] with one of the goals being that they ultimately perform an essential function in a new generation of electronic devices. One of the standout materials that have been discovered by the fundamental interest in carbon materials is graphene.

Graphene is an atomically thin 2D-material that is composed of a honeycomb lattice of sp^2-bonded carbon atoms (Scheme 1, right). The report by Geim and Novoselov[12] has found that few-layer graphene films are "a two-dimensional semimetal with a tiny overlap between valence and conduction bands, and they exhibit strong ambipolar electric field effect" with excellent electron-

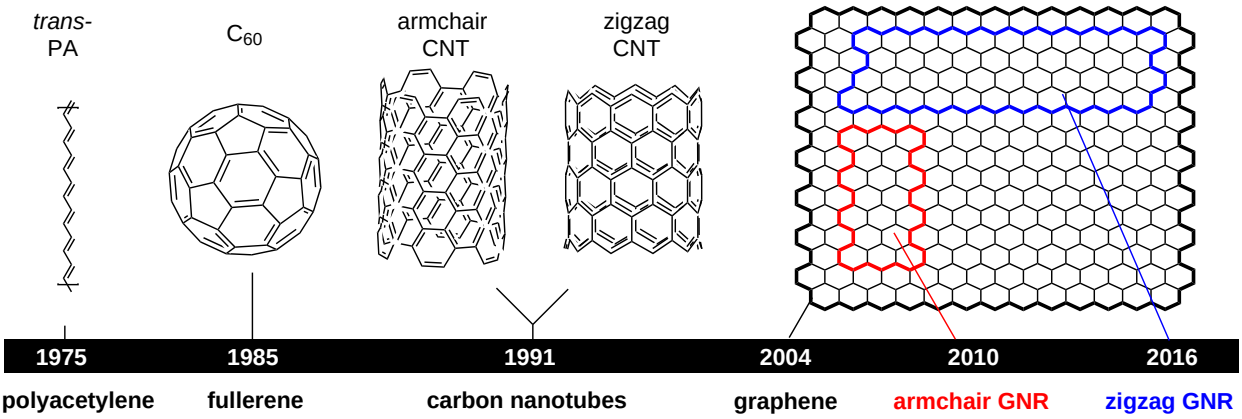

Scheme 1: A timeline of discovery in sp^2-hybridized materials: from polyacetylene to graphene

and hole-mobility at room temperature. This work has kickstarted a tremendous research effort in exploring the electronic properties of few-layer and monolayer graphene.[15–22] Synthetic methods toward graphene preparation now include mechanical exfoliation, top-down lithography, graphene oxide reduction, and oxidative plasma etching.[23] All of these methods yield high-quality flakes of graphene, but the atomic precision of edge structure of the resulting sample is ill-defined, which will have profound effect on the electronic structure as the graphene dimensions are reduced to nanoscale.[24]

For the TFET application, graphene can likely be used for the electrode/metal contact, but the BTBT tunneling architecture requires that QDs and tunneling barrier material utilize well-defined semiconducting materials. In this regard, carbon nanotubes and graphene nanoribbons[25] hold the most promise[19,26,27] as the materials where the quantum confinement effects induce a inherent bandgap.

Carbon nanotubes Carbon nanotubes (CNTs) have been at the forefront of the carbon materials community since 1991,[9] where they have found successful application as a strong, high aspect ratio, thermally conductive material with ballistic transport properties. CNTs are seamless cylinders of sp^2-hybridized carbon with either closed or open ends. The chirality (orientation of the graphene lattice with respect to the tube axis) of the carbon nanotube is correlated to its electronic properties. The synthetic access toward SWCNT (single wall CNT) and MWCNT (multi-wall CNT) production is available via carbon-arc discharge, laser ablation, or chemical vapor deposition.[11]

The progress in the nanoscale electronic applications of CNTs for an application such as TFET has been obstructed by the difficulty in synthesis and purification of the nanotubes of single chirality. While heterogeneity of the CNT mixture is acceptable for lightweight thermally conductive material (e.g. admixing into polymer matrices, thin film deposition)[28] applications, the field-effect transistors based on CNTs suffer due to irreproducibility in semiconducting properties of the nanotubes. Nevertheless, some exploration in single carbon nanotube FET devices is reported with success,[29–32] and the field is continuously growing.[33]

1.3 Graphene nanoribbons

Atomically defined graphene nanoribbons (GNRs) are high-aspect ratio, two-dimensional segments of graphene with intrinsic semiconducting properties. The ability to rationally tune quantum confinement effects at the nanometer scale in GNRs is an intriguing factor that has stimulated recent research in the area. Development of bottom-up methods for preparation of semiconducting GNRs at the nanometer scale (less than 5 nm in width) surpasses the current lithographic resolution limit for a top-down approach to metal-oxide semiconducting wires and is essential for advancement in molecular electronic device architectures.

A trailblazing first-principles DFT study of graphene nanoriibbons by Son *et al*. presents scaling rules of the band gaps of armchair-edge (Figure 3) and zigzag-edge (Figure 24) graphene nanoribbons as a function of their width.[34] Three families of armchair GNRs were found where the difference in the gap can be explained by combining the quantum confinement effect and edge termination effect. The band gap in ZGNRs is determined to be due to staggered sublattice potentials that result from spin-ordered states at the edges. This study made clear that the atomic precision is paramount in strucutres < 5 nm, and has paved the way for exploration of bottom-up synthetic approach toward atomically precise GNRs as opposed to the lithographic techniques[35–38] and carbon nanotube unzipping[10,39,40] approaches which produce GNRs with irregular width and edge structure.

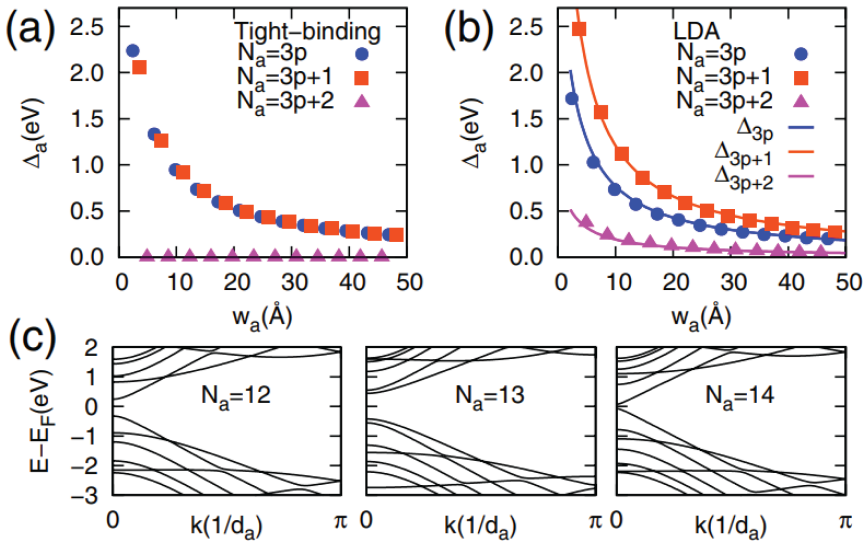

Figure 3: The variation of band gaps in AGNRs as a function of width obtained (a) from TB calculations with $t = 2.70$ eV and (b) from first-principles calculations. (c) First-principles band structures of 12-AGNR, 13-AGNR, and 14-AGNR, respectively. Figure reproduced from reference [34]

1.3.1 Bottom-up atomically precise synthesis of GNRs on metal surfaces

A report by Cai *et al*. first described the bottom-up methodology for 7-carbon atom wide armchair GNR (7-AGNR) synthesis on a Au (111) surface starting from 10,10'-dibromo-9,9'-bisanthracene (DBBA).[41] The sublimation of DBBA onto a Au(111) surface is accomplished via Knudsen cell evaporation under ulta-high vacuum (UHV) conditions ($<10^{-9}$ torr) inside of a scanning tunneling

microscope (STM) setup, and the stepwise anneal of the surface results in polymerization (T = 200 °C) and cyclodehydrogenation/planarization (T = 400 °C) to yield an atomically precise 7-AGNR.

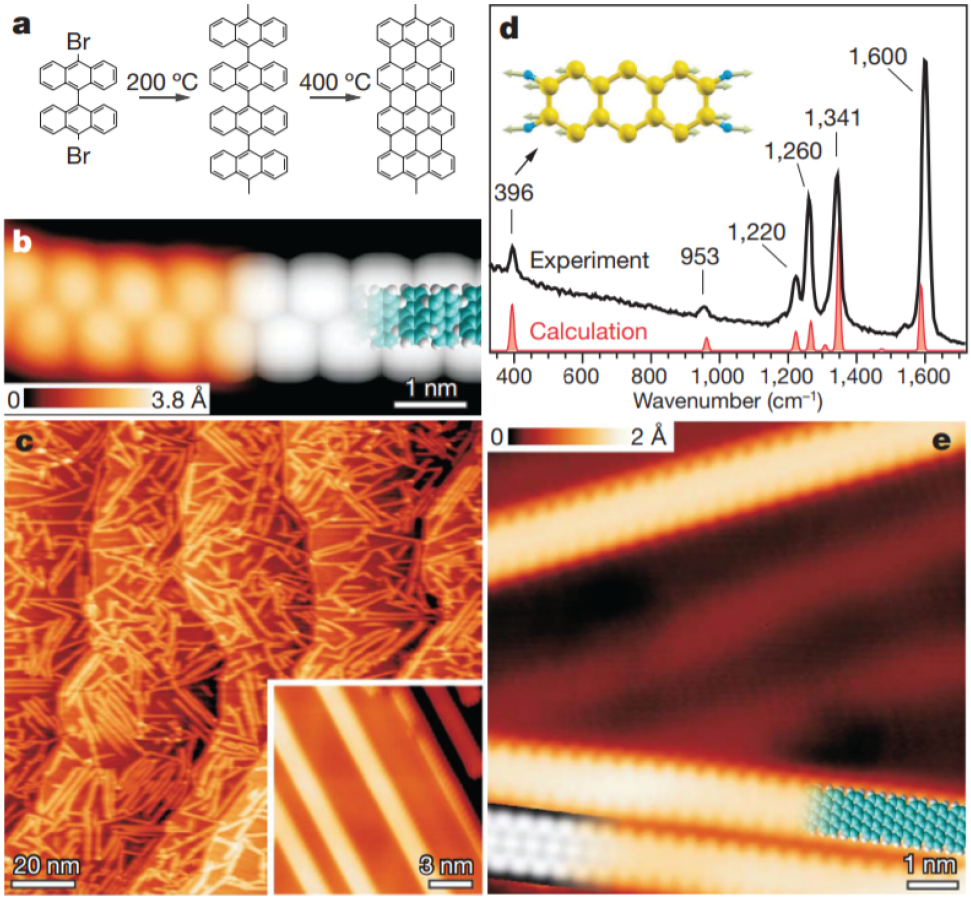

Figure 4: (a) Reaction scheme to transformation of DBBA to 7-AGNRs. (b) STM image taken after surface assisted C–C coupling at 200 °C and DFT-based simulation of the STM image (right) with partially overlaid model of the polymer. (c) Overview STM image after cyclodehydrogenation at 400 °C, showing straight 7-AGNRs. The inset shows a higher-resolution STM image. (d) Raman spectrum (532 nm) of straight 7-AGNRs, overlaid with the theoretical prediction. (e) High-resolution STM image with partially overlaid molecular model of the 7-AGNR. The figure is reproduced from reference [41]

The breakthrough concept of surface-mediated synthesis relies on a pre-defined monomer that can be controllably activated on a surface. In this case, the homolytic cleavage of C–Br bonds leads to a formation of carbon-centered radicals that recombine on the Au(111) surface to form new C–C bonds. Further annealing leads to a cyclodehydrogenation that yields the graphene nanoribbon 7-AGNR, which is only 0.74 nm wide. This precedent opens up a new avenue for creating small molecule precursors with rationally designed structures that can afford a subnanometer-wide nanoribbon on a surface. In the same work, Cao *et al*. report the formation of the chevron-edge GNR (Figure 5), which showcases the potential versatility of the on-surface synthesis. Even though the GNR was synthesized and imaged in UHV conditions, X-ray photoelectron spectroscopy analysis of a sample that was exposed to ambient conditions shows no oxidative degradation over time

(Figure 5d, the lines in the inset correspond to expected oxidative degradation signature).

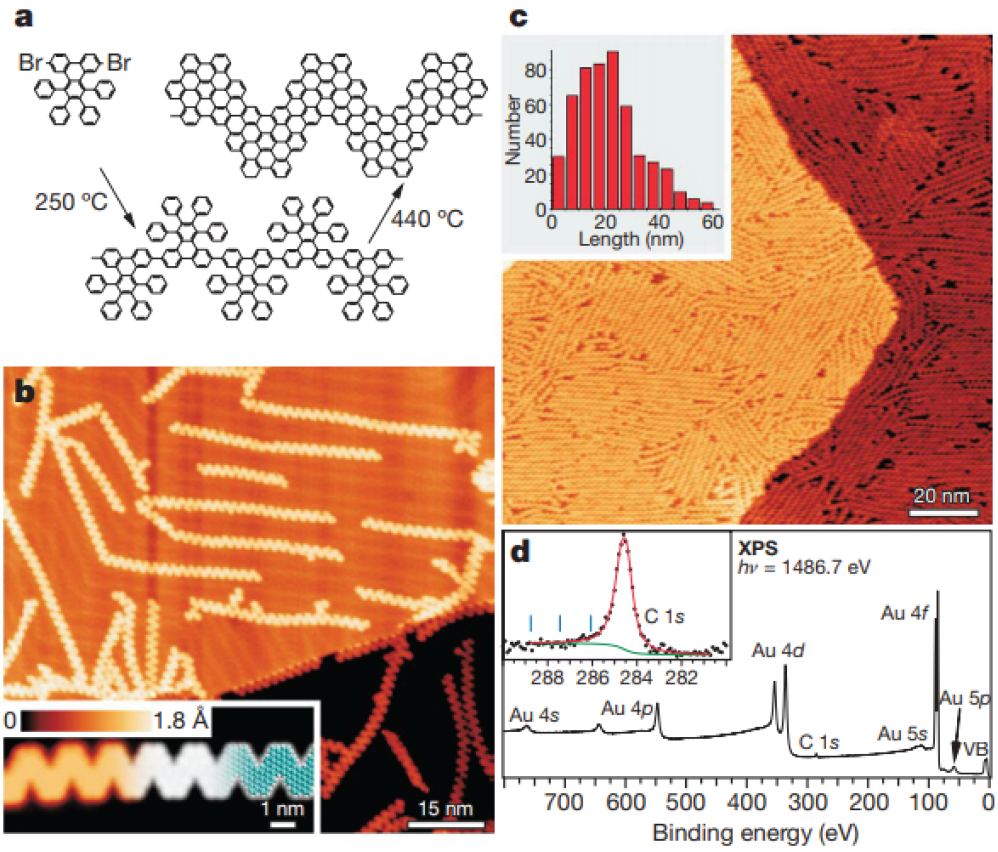

Figure 5: (a) Au(111)-induced transformation of 6,11-dibromo-1,2,3,4-tetraphenyltriphenylene to chevron-type GNRs upon stepwise annealing. (b) Overview STM image of chevron-type GNRs fabricated on a Au(111) surface. The inset shows a high-resolution STM image and a DFT-based simulation of the STM image (greyscale) with partly overlaid molecular model of the ribbon. (c) Monolayer coverage of chevron GNRs on Au(111), STM image and corresponding ribbon length distribution. (d) XPS survey of a monolayer sample of chevron-type GNRs with core levels and valence band (VB) labeled. The figure is reproduced from reference [41].

Aside from the ability to access atomically resolved images, the scanning tunneling microscope can also provide exceptional level of electronic structure characterization of GNRs via scanning tunneling spectroscopy (STS).[42,43] Point spectroscopy and dI/dV mapping are the two main techniques that the field relies on to evaluate the electronic structure, and these results are used for the direct comparison with the theoretical electronic structure calculation. Point spectroscopy is defined by locking the position of the tip over the ribbon (at a defined height and position in the x-y plane relative to the ribbon), and measuring the tunneling current as a function of the tip voltage bias. The peaks in the resulting spectra can be directly inferred as the density of states at that particular energy. The dI/dV mapping can provide the snapshot of the density of states of the overall ribbon at a set voltage. A representative example of STS application is a report from Merino-Diez *et al*., where various constituents of N=3p AGNR family are synthesized via surface-assisted lateral fusion of *para*-polyphenylene, and how STS is applied to ascertain the bandgap of the GNRs of varying width (Figure 6).

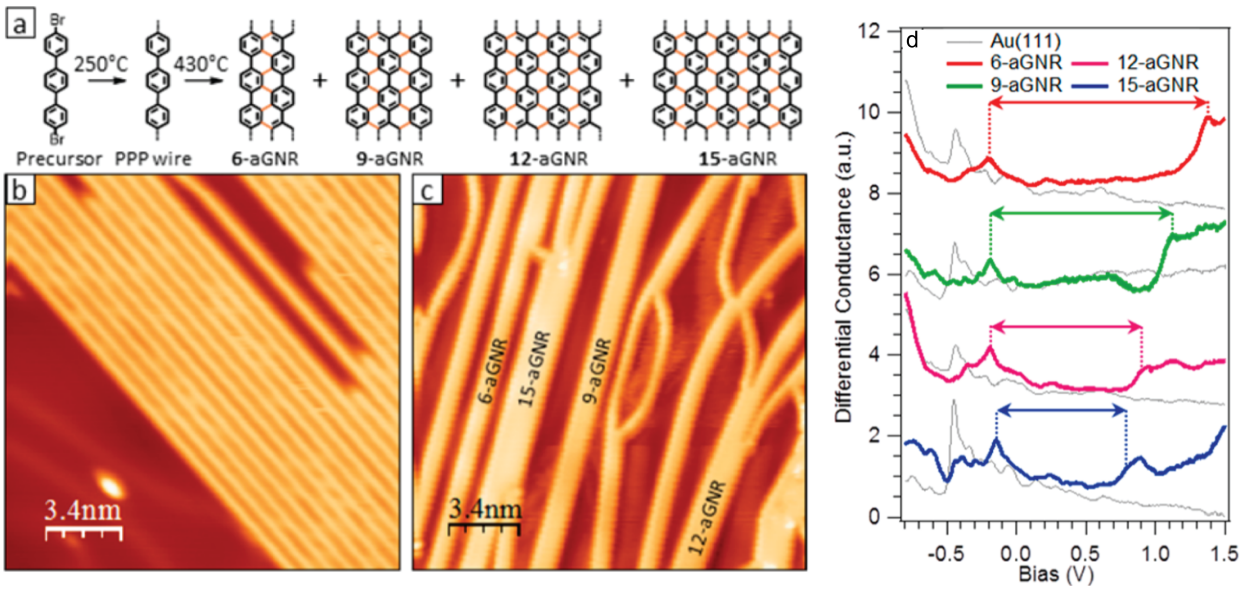

Figure 6: *Para*-polyphenylene synthesis via surface-mediated polymerization, and lateral fusion to achieve 3p family of AGNRs. (a) Synthetic outline. (b) PPP wire as formed after polymerization of the dibromoterphenyl precursor. (c) Surface image after anneal to 450 °C. AGNRs of various widths are observed. (d) Scanning tunneling spectroscopy of sample GNRs. A trend of bandgap decrease is observed, along with Fermi level pinning of the valence band (features @ -0.1 V). Data reproduced from reference [44]

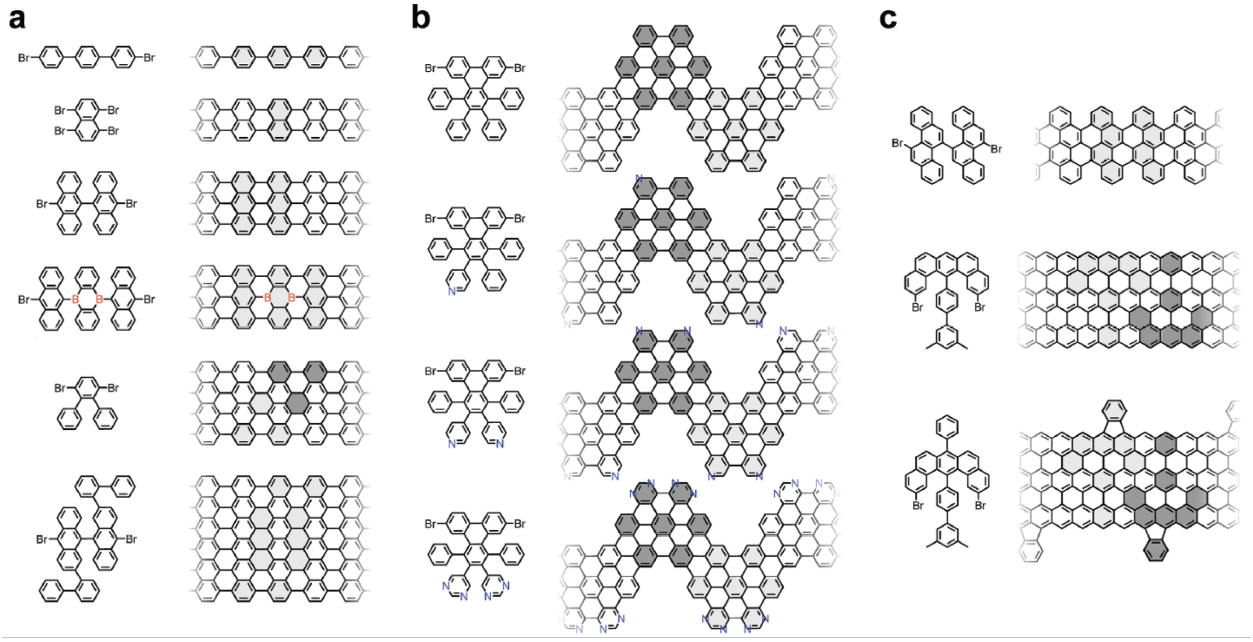

Figure 7: Catalogue of molecular precursors for the on-surface synthesis of atomically precise graphene nanoribbons. (a) armchair GNRs, (b) chevron GNRs, (c) zigzag-like GNRs. The outline of the molecular precursors in the final structure of GNR highlights the versatility of the bottom-up synthetic approach. Figure is reproduced from reference [45].

A singificant research effort has been devoted to the exploration of various monomer scaffolds and various surfaces that can be used for GNR growth and characterization. A medley of various AGNR, chevron, and zigzag GNRs have been discovered as of the end of 2016 and summarized in a review by Talirz *et al*. (Figure 7).[45] 5-AGNRs,[46] 9-AGNRs[47] and 13-AGNRs[48] were prepepared to align the theoretical prediction with experimental results, and a *para*-polyphenylene (dubbed 3-AGNR) was used to explore lateral fusion profile for synthesis of wider ribbons with moderate success. Zigzag-edged nanoribbons (ZGNR) were also explored, which resulted in a synthesis of a cove-zigzag hybrid GNR[49] (this scaffold can also be considered as 5–ZGNR with a regioregular missing carbon atom defect), and a pristine 6-ZGNR as well as the phenylated analog of 6-ZGNR.[50]

As the pristine GNRs were investigated, a theme of bandgap engineering was also investigated in inter-ribbon heterojunctions. A 7/13-AGNR heterojunction, reported by Chen *et al*., demonstrates a first width-modulated GNR, where 7-AGNR and 13-AGNR heterojunction segments have evolved via co-deposition of the two corresponding brominated precursors.[51] The resulting properties of the interribbon states can be related to that of the type I heterojunction behavior, which hold promise for TFET lateral heterojunction architecture.

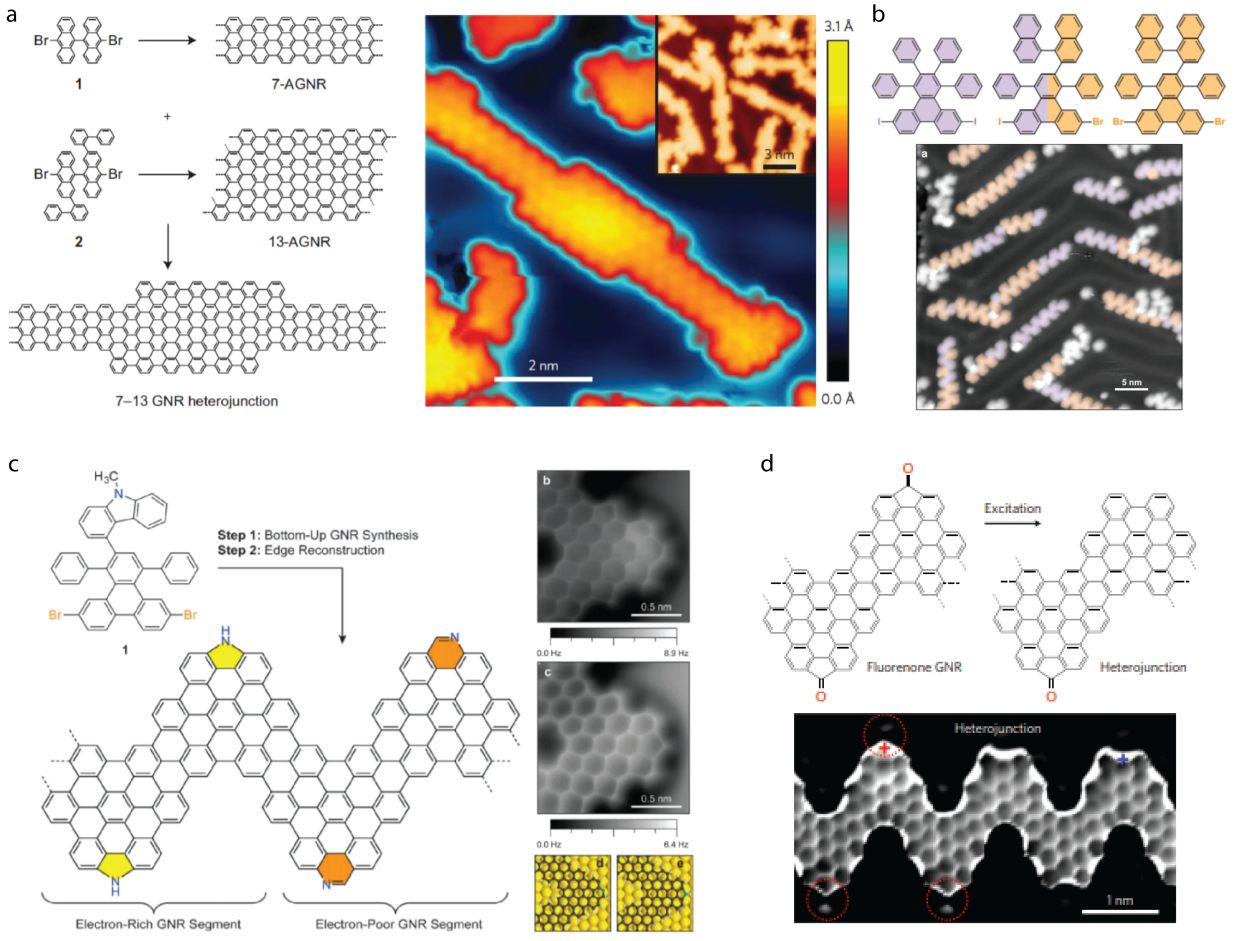

Figure 8: GNR-based heterojunctions. (a) 7/13–AGNR,[51] (b) hierarchical growth of chevron GNR,[52] (c) surface-mediated carbazole-phenanthridine rearrangement,[53] (d) tip-induced CO-extrusion from fluorenone GNR.[54]

Due to randomness of the 7/13 linkages, a point of interest was to establish synthetic methods that allow for better degree of control over the heterojunction architecture. A first idea to precisely control the GNR sequence was the design of molecular precursors that can be merged into block co-polymer GNR precursors based on the aryl-halogen bond dissociation difference (Ar-I vs Ar-Br). This concept was demonstrated by Bronner and Durr *et al*. (Figure 8b) in the chevron GNR scaffold, where segments of chevron GNRs of different width were fused together via sequential activation of C-I and C-Br bonds (Figure 8b).[52] Another approach toward the heterojunction control is based on the monomer edge reconstruction - here, a single monomer is used to form a GNR, and then an external factor such as temperature gradient or STM tip manipulation could be used to enact a precise edge reconstruction pattern. A proof of concept was described in the phenanthridine rearrangement work where both electron-rich and electron poor fragments can be formed upon annealing of the ribbon (Figure 8c). An additional hypothesis that has been tested is the STM tip manipulation of a GNR made from fluorenone-functionalized precursor (Figure 8d), which resulted in an obesrvation of a type II heterojunction behavior.[54]

1.3.2 Surface role in the GNR formation process - Au(111), Ag(111), Cu(111).

While Au(111) tends to be a common surface used for GNR preparation in literature, the reactivity of DBBA has been analyzed on other catalytically active metal surfaces such Ag(111) and Cu(111), and it has become evident that understanding surface-directed reactivity in also an essential part of the bottom-up GNR desgin. With model compound DBBA, Ag(111) produces similar reactivity to that of Au(111) – 7-AGNR is observed – but the mechanism of the polymerization is different. Annealing DBBA on Ag(111) to ∼200 °C leads to the formation of organometallic species that can be observed in STM imaging rather than diradical diffusion and recombination that is observed with Au(111) as a substrate.[55] In contrast, the reactivity of DBBA on Cu(111) changes drastically, and the chiral (3,1) GNR is observed. The coupling selectivity that is introduced by halogen substitution is overruled by the structural and catalytic properties of the substrate, which is proven by formation of the same (3,1) GNR from the non-halogenated DBBA precursor (Scheme 2, bottom).[56] Therefore, the underlying surface in an important factor in GNR synthesis that can not be overlooked.

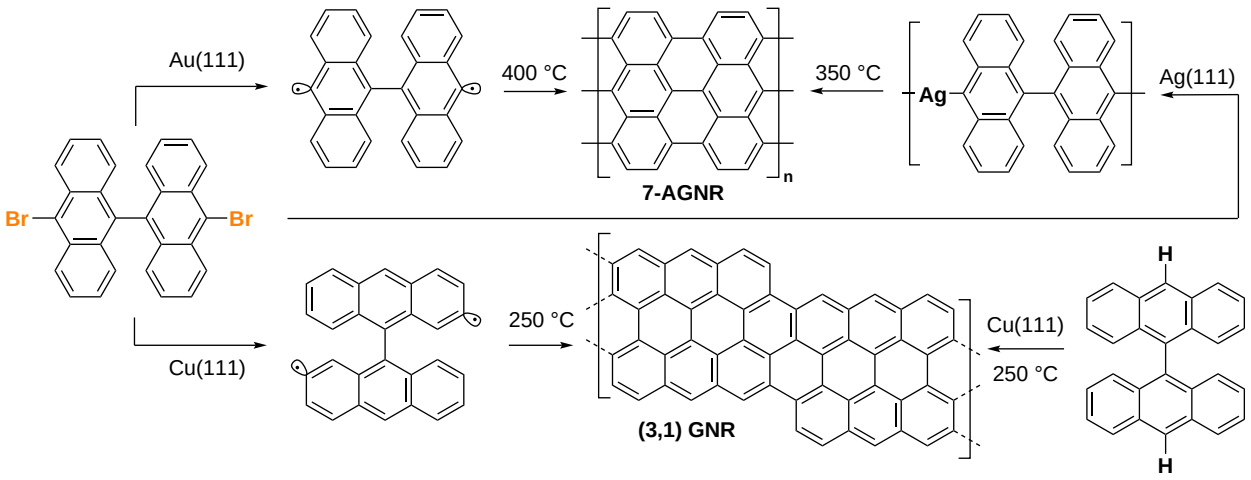

Scheme 2: The surface-induced variation of DBBA reactivity – 7-AGNR vs chiral (3,1) GNR.

1.3.3 Solution-synthesized polyphenylene precursors towards GNR production

The exploration and synthesis of graphene nanoribbons is not limited to the metal surface-induced proceesses. A large effort has been documented in utilizing the rich solution chemistry to prepare poly-phenylene polymers which can then be oxidized into fully planar GNR.[57] An advantage of solution phase synthesis of GNR is in the chemical that we have at our disposal for the precursor polymer synthesis. Given a random arene, one can utilize a variety of polymerization conditions to prepare a well-defined polymer. Step-growth polymerizations based on tranisiton metals (such as Suzuki, Yamamoto polymerization) and Diels-Alder reaction (Scheme 3), as well as chain growth (living alkyne metathesis polymeriation) have been explored in the literature, and have been previously utilized for the GNR synthesis. The last step in reliable synthesis of GNRs in solution is the oxidation/cyclodehydrogenation step. It is commonly achieved by harsh oxidative conditions, such as Scholl reaction ($FeCl_3$) and DDQ/trifluoromethanesulfonic acid.[58]

One representative informed synthesis of a fully characterized solution-grown GNR is the chevron GNR prepared by Sinitskii group.[59,60] In this case, the precursor is exactly the same as the one that was used for Au(111)-induced growth - the tetraphenyldibromotriphenylene **1**.[41] Yamamoto polymerization conditions were used to access the polyphenylene which was previously synthesized in 2009,[61] and the resulting polymer was then carried forward to the GNR via the $FeCl_3$-mediated oxidative cyclization. The method has showcased the robustness of the prep, and was the first method to achieve gram scale quantitites of chevron GNR. This work has been further extrapolated toward the synthesis of wider chevron GNRs.[62] Similarly, Suzuki polymerization was used for synthesis of 9-AGNR by Li *et al*.[63]

Another method pioneered by the Müllen group is the use of the Diels-Alder polymerization[64,65] to access the cove GNR scaffold.[66] A study by Narita *et al*. has designed and prepared a monomer **3**, which consists of a cyclopentadienone core and and alkyne side chain, and these two moeities undergo a formal Diels-Alder cyclization followed by cheleotropic CO extrusion to furnish the polyphenylene polymer **4**. The cyclodehydrogenation is accomplished again by $FeCl_3$ conditions to yield cove GNR **5**. The cyclopentadienone assembly via Knoevenagel condensation has proven versatile enough to incorporate a wide variety of the side chains onto a cyclopentadienone core. This synthetic method has been explored further to widen the ribbon,[67,68] and to attach fluorescent probes to GNRs for super-resolution optical microscopy imaging.[69]

As the interest in the solution synthesized GNRs increased, more sophisticated polymerization methods have been developed toward more controlled GNR growth – Yamamoto, Suzuki, and Diels-Alder polymerizations can be classified as step-growth polymerizations, which normally lead to a wide polydispersity in the resulting polymer. A ring-opening alkyne metathesis polymerization (ROAMP) strategy was used by von Kugelgen *et al*.[70] to convert a strained diyne **9** into a well-defined (Đ= 1.2) biphenylene ethynylene polymers **10**, which were further transformed into a chevron GNR pre-polymers via a Diels-Alder reaction with a solubilized tetraphenylcyclopentadienone (Scheme 4). The $FeCl_3$-induced cyclodehydrogenation yields chevron GNR samples that match the Raman spectra of chevron GNRs prepared via Yamamoto coupling.

After the final cyclodehydrogenation step, the characterization of solution-synthezied GNRs is severly limited in comparison to that of the surface synthesis, as the atomic precision of resulting ribbons can not be unambiguously confirmed as it can be in STM/UHV system. However, Raman,[71] IR[72,73] and solid-state NMR[70] spectroscopy can be used to confirm the essential structural characteristics of the ribbons.

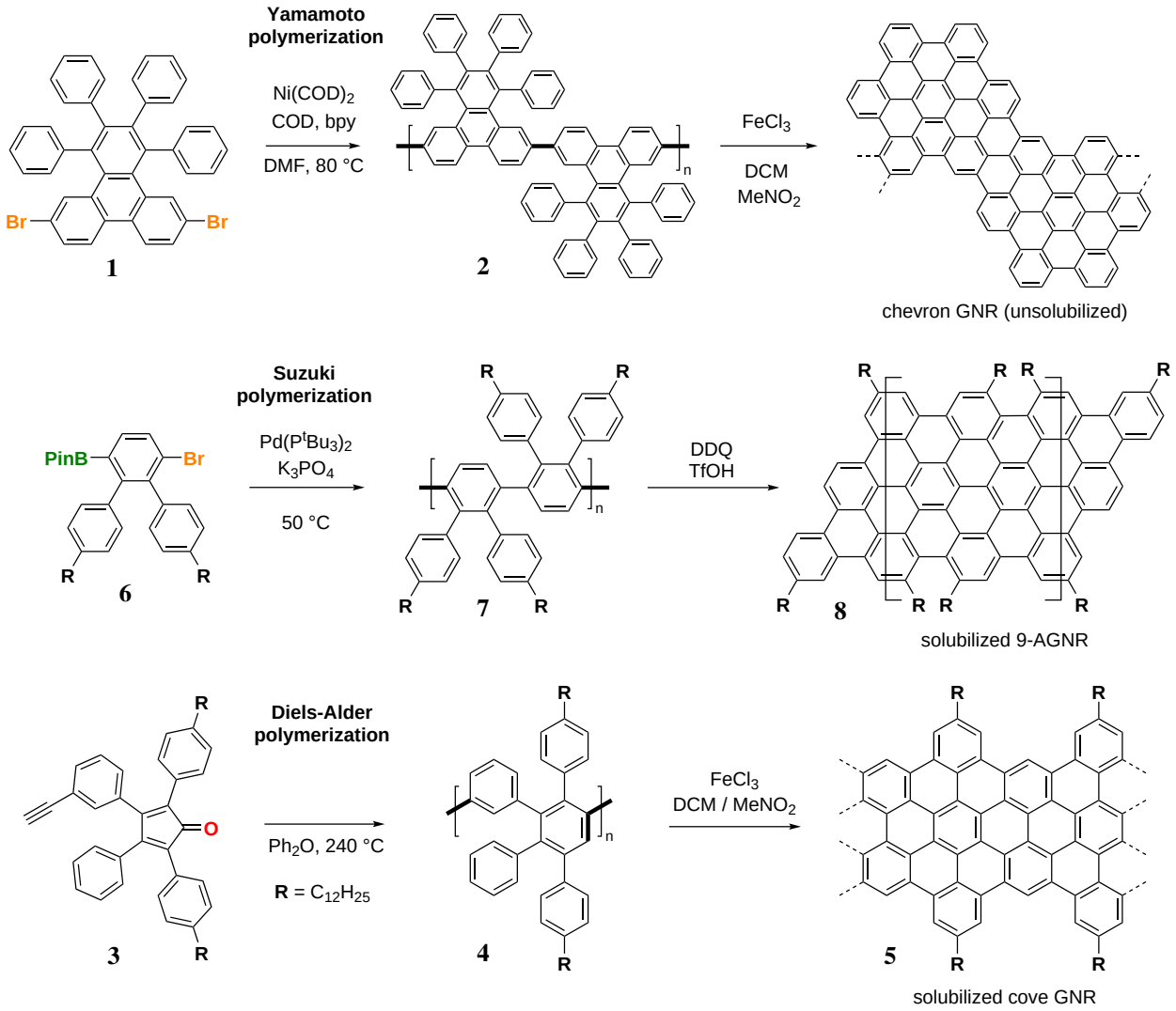

Scheme 3: Step-growth polymerization approaches - Yamamoto, Suzuki, and Diels-Alder polymerization - towards bulk chevron GNRs, 9-AGNRs and cove GNRs.

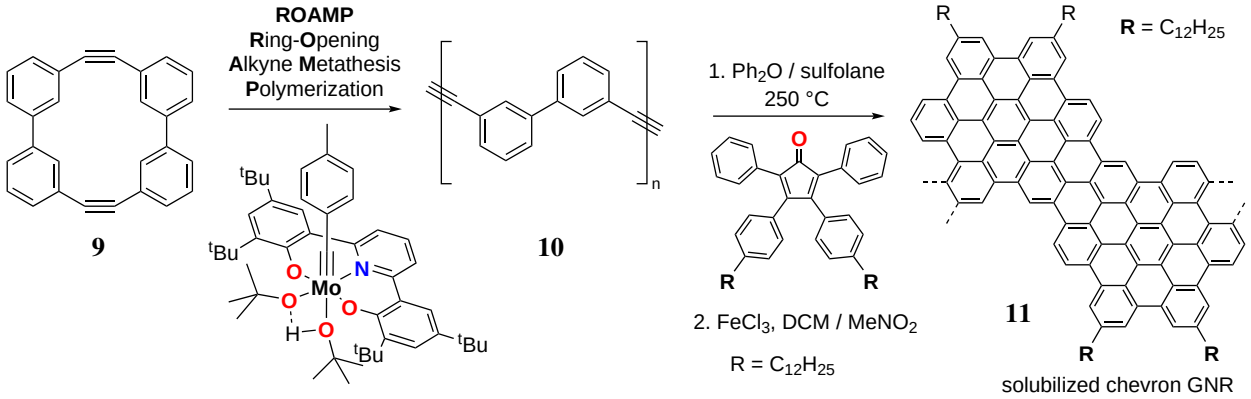

Scheme 4: Ring-opening alkyne metathesis polymerization (ROAMP) toward chevron GNRs.

An experimental realization of GNR-FETs is considered an important milestone towards GNR-TFET architecture, as a lot of work remains to be done in heterojunction control and engineering of the proper device arcitecture. Bennett *et al.*[74] and Llinas *et al.*[75] have shown functional FETs based on 7-AGNR, 9-AGNR, and 13-AGNR that were synthesized on a Au(111) or a Au(788)[76] surface. A key development here is the realization of a wet transfer process that suspends GNRs from Au(111) surface in an aqueous solution via an etch cycle, and then resulting GNRs are pulled onto a SiO_2 substrate. Then, the metal contacts are patterned on top of the GNRs@SiO_2, and device measurements are performed. A summary of such study on 9-AGNR is shown in Figure 9. After aggressive scaling down of the gate dielectric material to 1.5 nm of HfO_2, the 9-AGNRFET can produce promising $I_{ON} > 1$ μM and an *on/off* ratio of 10^5. This transfer technique, along with satisfactory results from the GNRFET, holds great promise for the high-performance TFET devices as long as the suitable GNR heterojunction can be prepared.

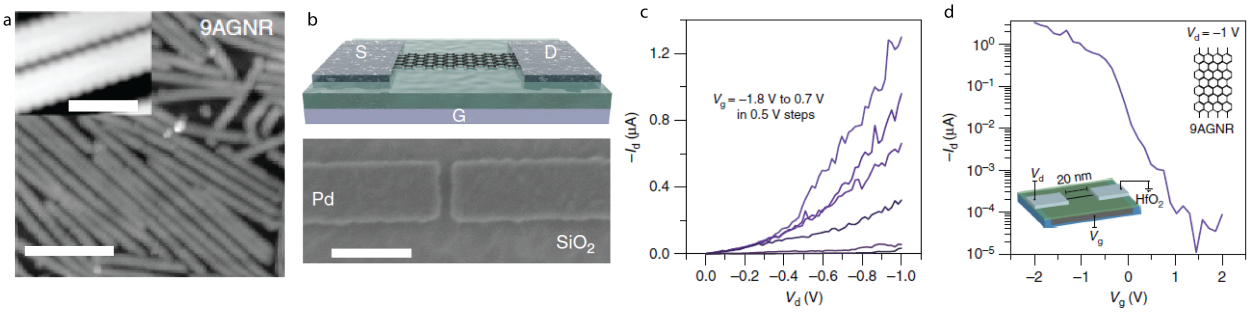

Figure 9: Summary of the 9-AGNRFET fabrication and device measurements. (a) Sample view of 9-AGNR on Au(111) (scale bar = 10 nm, inset scale bar = 1 nm). (b) Schematic of the device along with the SEM image of the contact. (c) I_d–V_d characteristics at various V_g. (d) Demonstration of a $I_{ON} > 1$ μM, and a I_{ON}/I_{OFF} ratio of $\sim 10^5$. Data and images reproduced from reference [75].

Conclusion This chapter serves to show the immense potential of the bottom-up approach in atomically precise synthesis and use of GNRs in the future generation of electronic devices. The material property benchmarks for TFET architecture have been outlined, and the current progress on versatility of the bottom-up synthesis of GNRs for tuning the electronic structure and heterojunction preparation is established. With this in mind, the following work is set to investigate additional bottom-up synthetic methods and bandgap engineering techniques in GNRs while keeping in line with new discoveries in the field.

2 Substitutional heteroatom doping in armchair GNRs

As the scaffold investigation in AGNRs has progressed, the extension of the electronic effect investigation by the virtue of heteroatom substitution of the precursors has become an interesting subject. In this chapter, I will discuss my efforts toward core heteroatom substitution routes toward investigating new electronic effects in 7-AGNR and chevron scaffolds.

My interest in heterocyclic chemistry combined with interest in new GNR synthetic routes and electronic effects led me to exploring the introduction of both boron and nitrogen atom substituents in the core of 7-AGNR. I present a rationale and an approach toward BN substitution in GNRs which is based on syntheses of azaborine heterocycles in an attempt to prepare a 7-AGNR precursor with BN core substitution.

I have also become interested in exploring ways to directly incorporate carbon-heteroatom bond formation reactions in the on-surface repertoir of reactions, rather than relying solely on precedented approach of C–H bond activation for cyclodehydrogenation. This is a paradigm that would open new avenues in GNR synthesis, as not every single carbon-heteroatom bond will have to be pre-installed in the precursor, and we will be able to utilize greater freedom in molecular design. C–N and N–N bond formation hypotheses were investigated in a context of a chevron GNR scaffold with mixed success. In continuation, I have developed a precursor toward nitrogen-substituted 7-AGNR where a robust C-N bond formation reaction that precludes the surface-mediated polymerization is discovered. This knowledge is then applied to a synthesis of a second generation of precursors toward N-7-AGNR that take advantage of this discovery.

Parts of this chapter have been published in: Covalent C–N Bond Formation through a Surface Catalyzed Thermal Cyclodehydrogenation. Piskun, I. Blackwell, R. Jornet-Somoza, J. Zhao, F., Rubio, A., Louie, S. G., Fischer, F. R. *J. Am. Chem. Soc.* **2020**, *142*, *8*, 3696–3700.

2.1 Heteroatom doping in graphene nanoribbons - challenges and effects

GNR modification by heteroatom doping is a logical extension of the bottom-up surface assisted technique, as different chemical functionalities can be introduced into the monomer by virtue of organic synthesis. The research direction in precise introduction of heteroatoms is expected to provide tools to accurately tune electronic and physical properties of the nanoribbons while keeping the lateral width constant. One should expect to introduce new states in the band structure of the nanoribbon akin to conventional n- and p-doping, adjust the Fermi level for band alignment in device heterojunctions, and control the surface-directed reactivity of the precursor.

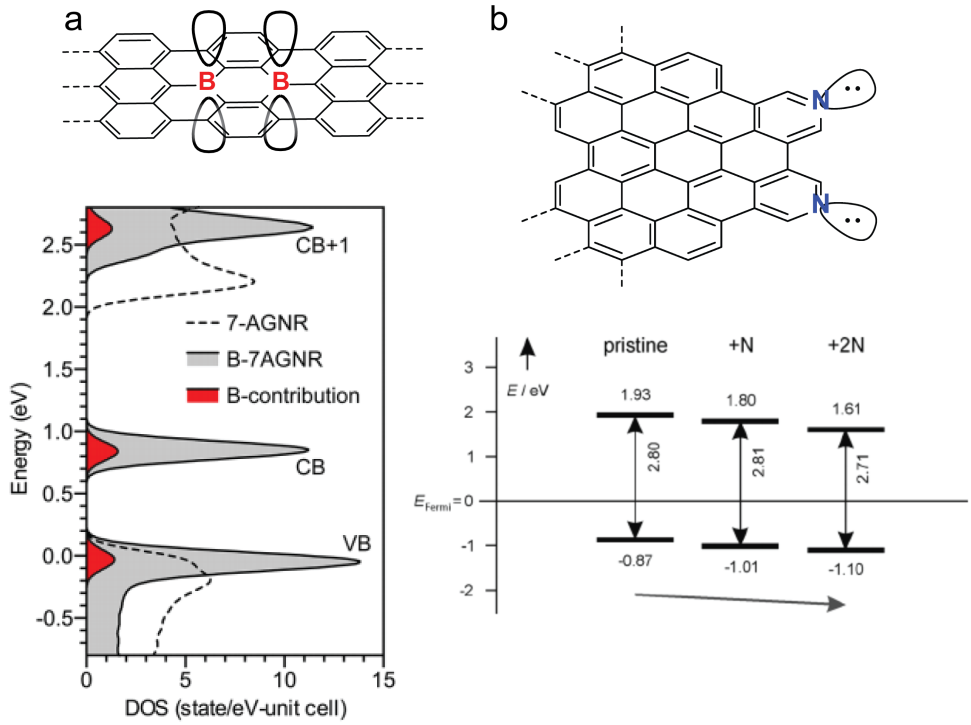

Figure 10: (a) Core substitutional boron doping in 7-AGNR (density of states plot reproduced from reference [77]). (b) Edge nitrogen atom substitution (band diagram reproduced from reference [78]).

Figure 10 presents two types of approaches towards heteroatom doping of a GNR. Nitrogen atom edge-doping in chevron GNRs reported by Bronner *et al*. has led to a rigid bandgap shift to lower energy in the electronic structure of GNR.[77] In this case, the filled sp^2-orbitals on edge-localized nitrogen atoms have no significant overlap with the 2D plane of the ribbon, and therefore do not have a significant contribution in altering the valence and conduction bands of the ribbon (Figure 10b). An electronegative atom effect is observed–as the number of nitrogens is increased, the overall energy gap shifts down in energy in relation to the vacuum energy level. On the other hand, backbone-doping, or core doping, reported by Cloke *et al*., implies that dopant orbitals are forced into full conjugation with the extended π-system and are expected to introduce filled/empty states within the band gap of the GNR. A proof of concept for this strategy was demonstrated by replacing carbon atoms along the core of semiconducting 7-carbon-wide armchair GNRs with boron atoms. The empty p-orbital on boron is in full conjugation with the extended π-system of the GNR

and thus serves as a p-type hole-dopant. Scanning tunneling spectroscopy (STS), in agreement with first principle QM calculations at the GW level, reveals that B-doping in GNRs introduces a deep acceptor state within the band gap (Figure 10a).[78] This exact discovery was also made independently by Kawai *et al*.,[79] and the electronic structure and characterization is in agreement between two studies.

2.2 BN pair substitutional doping in 7-AGNR scaffold

My first project focused on modulating the electronic structure and physical properties of 7-AGNR by simultaneous introduction of two different heteroatoms (i.e. group III and group V elements) along the core of the nanoribbon. As a small molecule analog of the doping pattern, 1,4-azaborine (Scheme 5) is an ideal candidate for this goal. 1,4-azaborine belongs family of heterocyclic rings that are isoelectronic to benzene, being derived through a replacement of two carbon atoms in a benzene ring by a boron atom and a nitrogen atom. Physical properties and chemical reactivity of azaborines are altered from benzene due to B-N dipole moment that azaborines possess (orientation varies with the geometric arrangements of B and N atoms).[80]

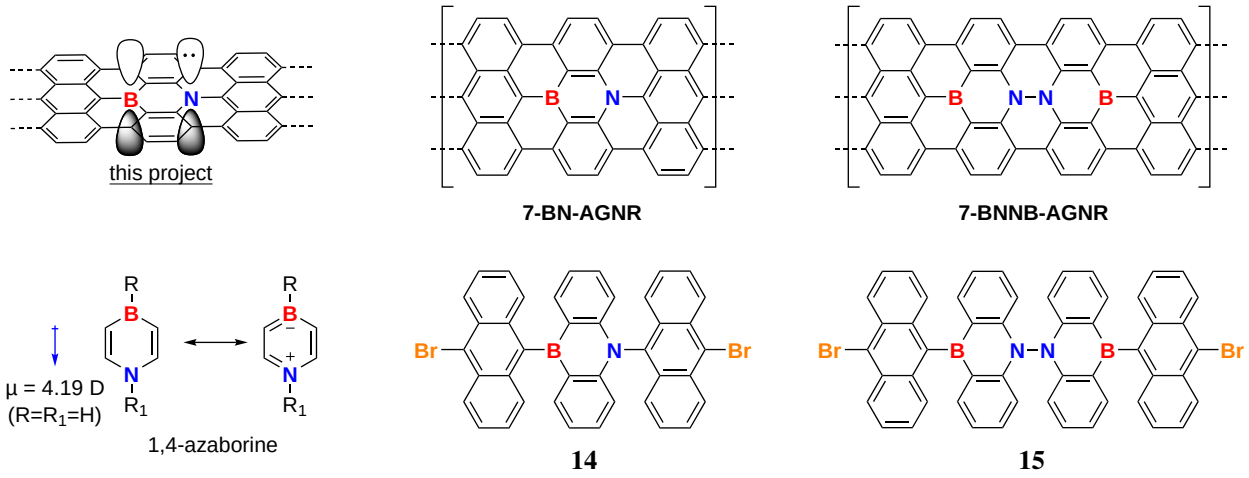

Scheme 5: The proposed two 7-AGNRs with BN substitutional doping.

The initial goal of this project is to develop a synthetic route toward the molecular precursors for 7-BN-AGNR and 7-BNNB-AGNR (Scheme 5) that would be suitable for on-surface synthesis, with a follow-up experimental investigation of heteroatom-induced electronic effects and the midgap state. The synthetic targets **14** and **15** are rationally designed to be isostructural to DBBA, featuring *peri*-linked, anthracene-like units with C–Br bonds in a steric environment similar to that of DBBA. Following the design and the synthesis of molecular precursors, monomers will be deposited and annealed on a Au(111) surface to induce a polymerization. Dehydrogenative ring closures will yield a 7-carbon-wide GNR featuring heteroatoms at predefined positions along the backbone. The atomic structure of the GNR and the precursor polymer will be characterized by scanning tunneling microscopy (STM) and atomic force microscopy (AFM), whereas the electronic structure of the fully cyclized GNR will be elucidated by scanning tunneling spectroscopy (STS).

Introduction of the 1,4-azaborine moiety along the nanoribbon backbone is hypothesized to induce a local electronic perturbation without altering the overall electronic structure of the nanorib-

bon. In comparison with the boron-doped 7-AGNR, this system features both boron and nitrogen p-orbitals in conjugation with the extended GNR π-system. Therefore, the number of the electrons in the π-system will be the same as in the pristine all-carbon 7-AGNR due to the combination of an empty p-orbital on boron and filled p-orbital on nitrogen. These dopants are expected to invoke new midgap states that are inaccessible to pristine 7-AGNR, thus effectively lowering the band gap of the nanoribbon (Figure 11). The electronic effect induced by the heteroatoms should incorporate a strong dipole moment in a regioregular 7-BN-AGNR, whereas 7-BNNB-AGNR will have two antiparallel aligned dipole moments, resulting in a quadrupole moment aligned with the long axis of the GNR – it is intriguing to investigate how these disturbances will affect spectroscopic and transport properties of the nanoribbons.

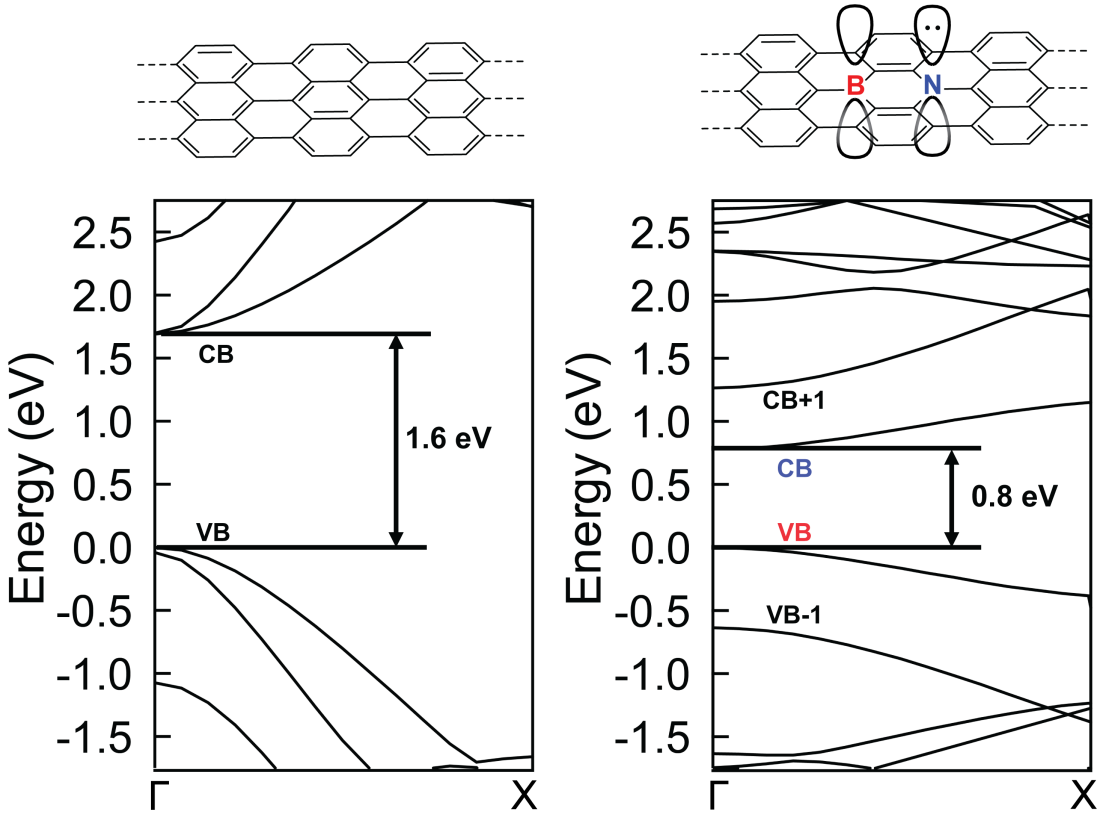

Figure 11: DFT-LDA calculations of 7-AGNR and 7-BN-AGNR.

Two retrosynthetic approaches toward the BN monomer **14** that were explored in the following chapter are summarized in Scheme 6. The assembly of the dianthryl azaborine core is the key challenge, which was approached on two fronts: (1) assembly of the azaborine core and the attempt at the C-N Buchwald-Hartwig type cross-coupling with 9-bromoanthracene, and (2) assembly of the difunctionalized triarylamine that can be further modified to incorporate the boron atom as the key step.

A forward synthetic process to prepare both BN-doped nanoribbon precursors **14** and **15** via the azaborine-first assembly route is outlined in Scheme 7. The azaborine ring assembly is adapted from the route to prepare the 1,4-dibenzoazaborine ring system by Kawashima.[81] Bromination of diphenylamine with NBS affords a tetrabrominated amine **20**, which is then protected with an ethoxy

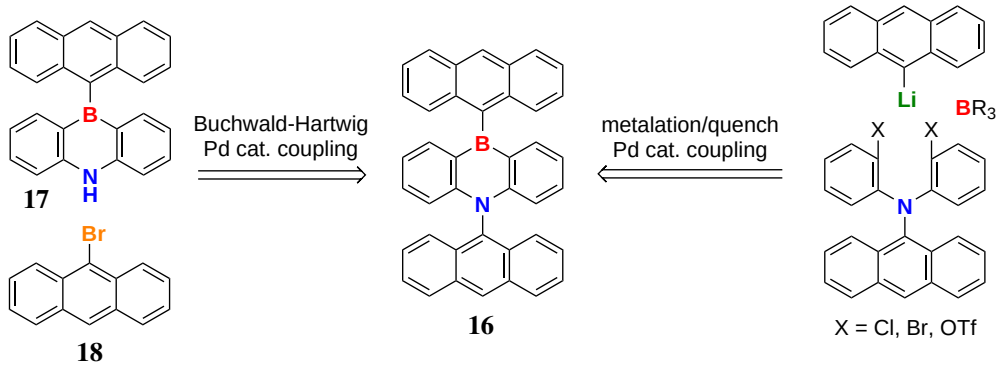

Scheme 6: Retrosynthetic approach toward **16**, the full carbon skeleton toward the BN-7-AGNR precrusor.

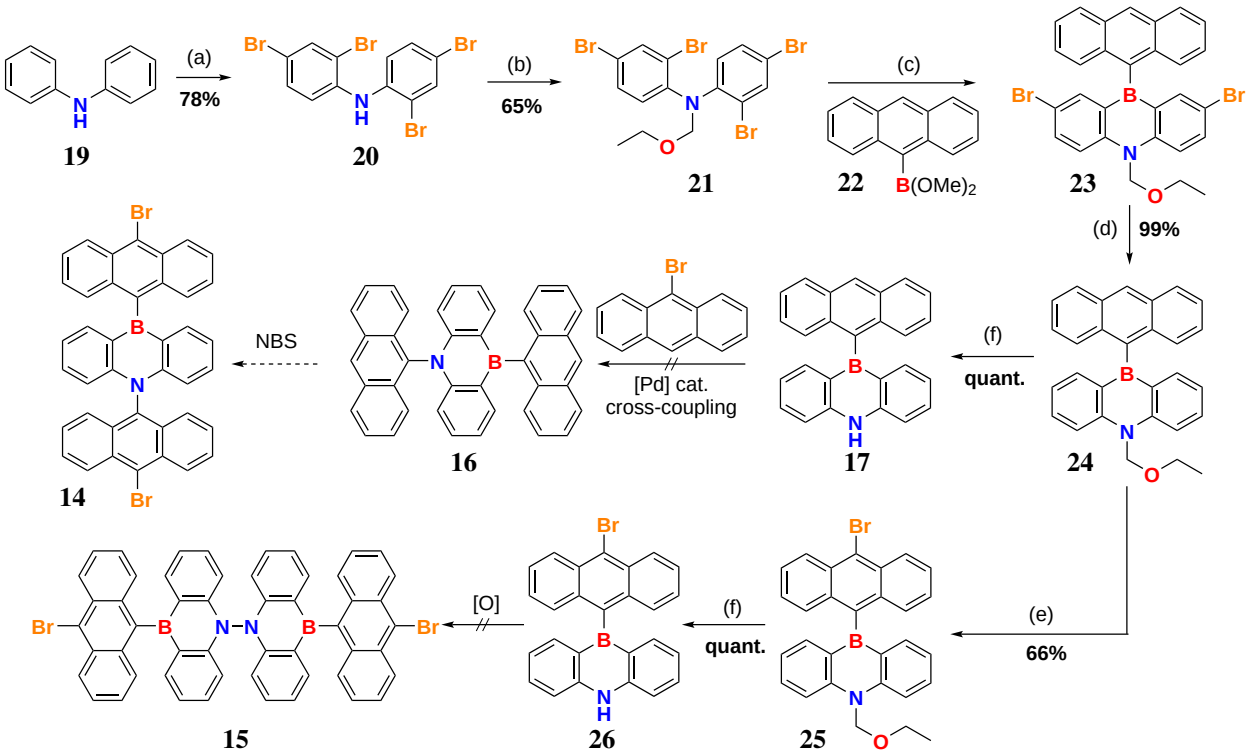

Scheme 7: (a) 4 equiv NBS, acetone, 0 °C, 15 min. (b) 1.2 equiv LDA, THF, –78 °C, 30 min, then 2 equiv chloromethyl ethyl ether. (c) 2.0 equiv BuLi, Et_2O, –78 °C, 45 min, then 1.4 equiv **22**. (d) 2.0 equiv BuLi, Et_2O, –78 °C, 30 min, then 1M HCl quench (e) 1.0 equiv NBS, DCM, 30 min. (f) 12 M HCl, EtOAc, 30 min.

methyl protecting group in order to mask the acidic proton. The ethoxy methyl group then acts as a directing group to guide the subsequent lithium-halogen exchange *ortho*- to the protected nitrogen. Indeed, treatment of **21** with 2 equiv. of BuLi, followed by reaction with 9-anthracentyl boronic methyl ester **22** (prepared in situ from 9-bromoanthracene, BuLi, and $B(OMe)_3$) yields 1,4-dibenzoazaborine **23** in 42% yield. Treatment of **23** with BuLi, followed by dilute acidic hydrolysis affords a nearly quantitative yield of **24**. Removal of the ethoxy methyl protecting group from **24** is achieved via acid hydrolysis with 12M HCl in ethyl acetate to quantitatively afford the 1,4-dibenzohydroazaborine **17**.

With **17** in hand, a Buchwald-Hartwig type cross coupling was envisaged as a feasible route toward **16**, although to date no cross-coupling conditions on the N-terminus of the 1,4-hydroazaborine were present in literature. An exploratory ligand screen (Table 1) was performed on the substrate **17** and 9-bromoanthracene as a coupling partner, and a molecular species of the desired MW = 531.24 was detected in a few cases by mass spectrometry. Further attempts were made to investigate the scope of the base, resulting in metalated amides as a preferred reagent (Table 3).

Table 1: Ligand variation for C–N cross-coupling optimization of 9-bromoanthracene and **17**. All reactions performed on 10 mg scale of **17** with 1.5 equiv of base, (a): packed in ambient atmosphere under N_2 flow, 3 h. (b): packed in N_2 glovebox, 3 h. (c): packed in N_2 glovebox, 18 h.

Entry #	Pd source	Ligand	Base	Solvent, T	Mass spec.
1[a]	$Pd(OAc)_2$	SPhos	LiHMDS	PhMe, 110 °C	n.d
2[a]	$Pd(dba)_2$	SPhos	LiHMDS	PhMe, 110 °C	n.d
3[a]	$Pd(dba)_2$	$P(tBu)_3$	LiHMDS	PhMe, 110 °C	Peak @ 531.24
4[a]	$((allyl)PdCl)_2$	SPhos	Cs_2CO_3	PhMe, 110°C	n.d
5[b]	$Pd(dba)_2$	DIPhos	KHMDS	PhMe, 100 °C	n.d
6[b]	$Pd(dba)_2$	$P(tBu)_3$	KHMDS	PhMe, 100 °C	n.d
7[b]	$Pd(dba)_2$	RuPhos	KHMDS	PhMe, 100 °C	n.d
8[b]	$Pd(dba)_2$	PCy_3	KHMDS	PhMe, 100 °C	Peak @ 531.24
9[c]	$Pd(dba)_2$	PCy_3	KHMDS	PhMe, 100 °C	Peak @ 531.24
10[b]	$Pd(dba)_2$	dppf	KHMDS	PhMe, 100 °C	n.d
11[b]	$Pd(dba)_2$	$P(o\text{-tol})_3$	KHMDS	PhMe, 100 °C	n.d
12[b]	$Pd(dba)_2$	CyJohnPhos	KHMDS	PhMe, 100 °C	n.d
13[b]	$Pd(dba)_2$	$MePPh_2$	KHMDS	PhMe, 100 °C	Peak @ 531.24
14[c]	$Pd(dba)_2$	PCy_3	KHMDS	*o*-xyl:PhMe, 9:1, 130 °C	n.d
15[b]	$Pd(dba)_2$	PMe_3	KHMDS	PhMe, 100 °C	n.d
16[b]	$Pd(dba)_2$	SPhos	KHMDS	PhMe, 100 °C	n.d
17[b]	$((allyl)PdCl)_2$	SPhos	KHMDS	PhMe, 100 °C	n.d

The isolation of the desired molecular weight product proved challenging, as the yield of >5% was not observed with any set of catalytic conditions. Stoichiometric palladium coupling was not successful either, only affording a trace of the product. As this point, it was essential to isolate a pure product sample to confirm the desired reactivity and to assess whther further optimization of this route is warranted. Combination of successful batches has yielded a pure compound with desired molecular weight via preparatory thin layer chromatography. However, the ^1H NMR experiments have confirmed that N-H activation does not happen, but rather the C-H activation on the benzene

ring adjacent to the azaborine ring is observed. If the desired product is formed then all of the protons except those that correspond to the 10-anthracenyl position should integrate to 2 due to the mirror symmetry of the molecule. It is not the case here, as a clear doublet signal that with an integration of 1 is observed at 7.79 ppm, hinting at asymmetric substitution of the dibenzoazaborine core. (Figure 12). With this result in hand, this route exploration was halted and the focus is shifted to the triarylamine assembly. While this reactivity is unexpected, no further effort was expended on this route, as it clearly did not lead to the desired scaffold **16** nor did it proceed in a modest yield.

Table 2: Stoichiometric palladium experiments for C–N cross-coupling optimization (1.0 equiv of **17**, 5 equiv 9-bromoanthracene, 1.0 equiv of Pd source, 1 equiv of ligand, 5 equiv of base)

Entry #	Pd source	Ligand	Base	Solvent, T	Mass spec.
1	$Pd(dba)_2$	PCy_3	KHMDS	PhMe, 100 °C	Peak @ 531.24
2	$Pd(PPh_3)_4$	PCy_3	KHMDS	PhMe, 100 °C	n.d
3	$Pd(OAc)_2$	PCy_3	KHMDS	PhMe, 100 °C	n.d

Table 3: Base variation. Metalated amides (NaHMDS, LDA, LiTMP, Et_2NLi) were the only bases that yielded the desired peak in MALDI. *tert*-butoxide bases were also tested, and led to quantitative SM decomposition (not listed).

Entry #	Pd source	Ligand	Base	Solvent, T	Mass spec.
1	$Pd(dba)_2$	PCy_3	NaHMDS, 2.6 equiv	PhMe, 100°C	n.d
2	$Pd(dba)_2$	PCy_3	KHMDS, 1.5 equiv	PhMe, 100°C	Peak @ 531.24
3	$Pd(dba)_2$	PCy_3	NaHMDS, 10 equiv	PhMe, 100°C	n.d
4	$Pd(dba)_2$	PCy_3	Cs_2CO_3,10 equiv	PhMe, 100°C	n.d
5	$Pd(dba)_2$	PCy_3	KBn, 10 equiv	PhMe, 100°C	n.d
6	$Pd(dba)_2$	PCy_3	NaH, 10 equiv	PhMe, 100°C	n.d
7	$Pd(dba)_2$	PCy_3	Et_2NLi, 10 equiv	PhMe, 100°C	Peak @ 531.24
8	$Pd(dba)_2$	PCy_3	LDA, 10 equiv	PhMe, 100°C	Peak @ 531.24
9	$Pd(dba)_2$	PCy_3	LiTMP, 10 equiv	PhMe, 100°C	Peak @ 531.24
10	$Pd(dba)_2$	PCy_3	$LiNMe_2$, 10 equiv	PhMe, 100°C	n.d

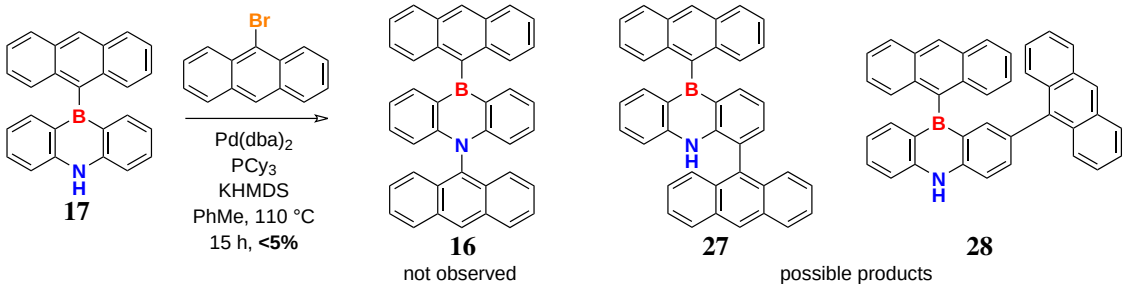

Scheme 8: Predicted regioselectivity of the cross-coupling.

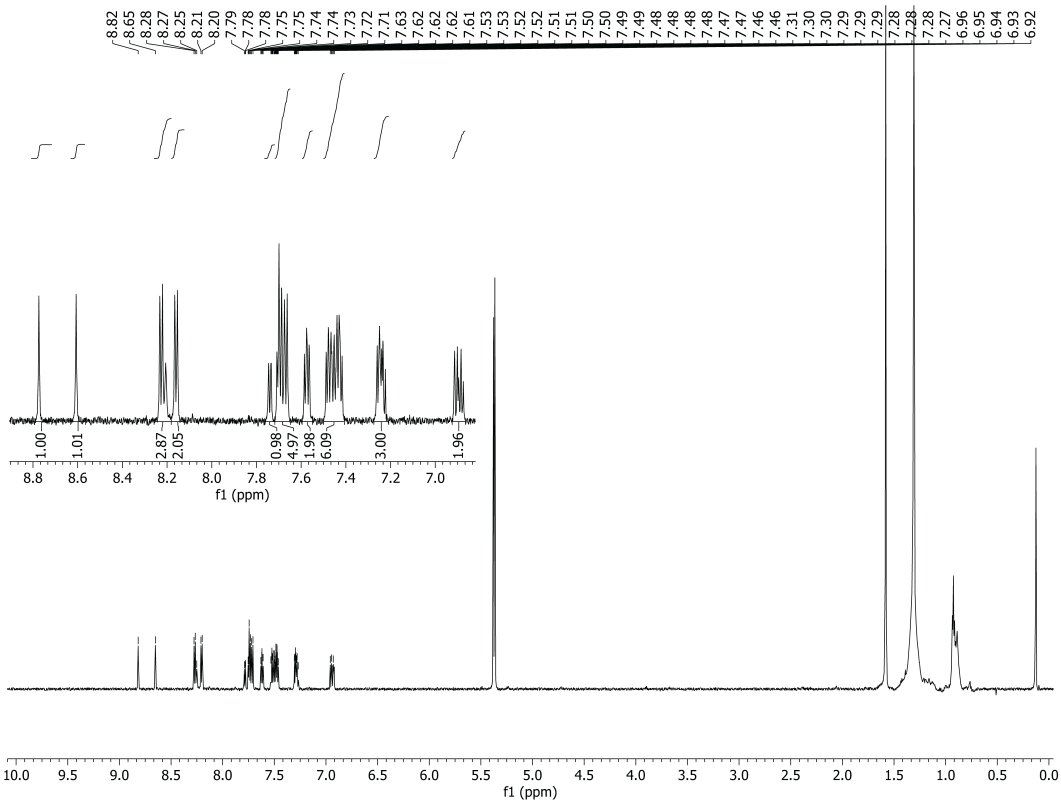

Figure 12: ^{1}H NMR spectrum of the suspected product of N-H activation of **17** (CD_2Cl_2, 700 MHz, 24 °C) which corresponds to peak @ 531.24 in mass spectrometry.

The second general route has explored the assembly of the triarylamine with a boron atom introduction as the key step. A few valuable intermediates toward this strategy are listed in Scheme 9. Here, a focus is made on assembling the diphenylanthracenylamine core first, and then using the *ortho*-functionalization on the phenyl rings to introduce the boron atom.

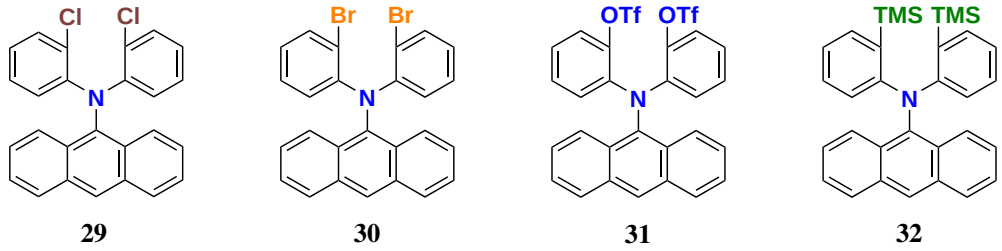

29 **30** **31** **32**

Scheme 9: A list of precursors toward the incorporation of boron toward the BN-7-AGNR precursor.

A dibromotriarylamine **30**, along with the dichlorotriarylamine **29** can serve as metal-halogen exchange sites that can be quenched with a 9-anthracenyl boronic ester similarly to the synthesis in the first approach. Secondly, a ditriflate **31** is proposed to be useful for the palladium-catalyzed introduction of the boronic acid moeity via the aminoborane as the coupling partner. Lastly, a disilylintermediate **32** can potentially be used for the reaction with a BX_3-type boron precursor, as the boron-silicon exchange is extensively reported as a method for various boracycle formation. Incidentally, our lab has used this methodology to prepare the 9,10-dibromo-9,10-dihydro-9,10-diboraanthracene toward the B-7-AGNR.[78]

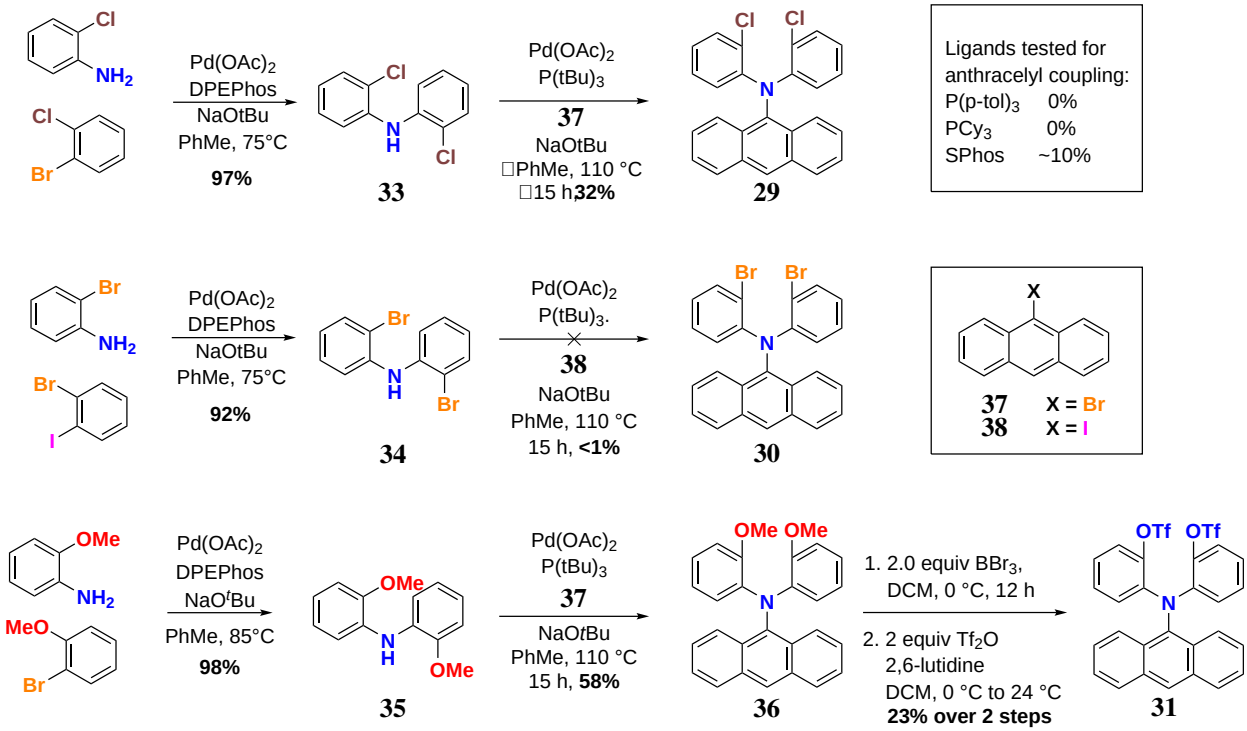

Scheme 10: Synthetic access to the triarylamine precursors toward the BN-7-AGNR precursor.

The successful synthetic approaches toward these precursors is described in Scheme 10. The dichlorotriarylamine **29** is prepared from the Buchwald Hartwig cross-coupling of the aniline **33** and 9-bromoanthracene in a modest 32% yield utilizing the strongly electron donating tri-*tert*-butylphosphine ligand. Similar procedure however does not work with the synthesis of the dibromo analog **30**, as the harsh conditions necessary to activate the 9-haloanthracene position can also affect the bromine substituents that are already installed on the aniline. Aniline **34** exhibits self-reactivity in control experiments that omit the anthracene coupling partner. A trace of **30** is detected by mass spectrometry, but it was never isolated in sufficient amounts ($\sim$1g) to continue with the synthesis. The approach toward ditriflate **31** utilizes the same strategy as above, with two additional steps required to convert the dimethoxy species **36** to the desired ditriflate via the BBr_3 demethylation followed by the trifluoromethanesulfonation with Tf_2O/2,6-lutidine conditions. The trimethylsilyl derivative **32** was not obtained due to the inability to obtain the corresponding disilyl aniline on scale.

Table 4: Activation of dichlorotriarylamine **29** via metal-halogen exchange (Scheme 11). [a] in the Rieke Mg case, anthryl cleavage is observed, which is the major product.

Entry #	Metal source	Solvent	T	**29/39/40**
1	tBuLi	THF	−40 °C	decomp.
2	BuLi	Et_2O	−78 °C	100/0/0
3	BuLi	Et_2O	24 °C	100/0/0
4	*ipr*MgCl · LiCl	THF	0 °C to 24 °C	100/0/0
5	*ipr*MgCl · LiCl	THF	66 °C	86/14/0
6	*ipr*MgCl · LiCl	dioxane	100 °C	100/0/0
7	Rieke Mg	THF	100 °C	0/0/20[a]

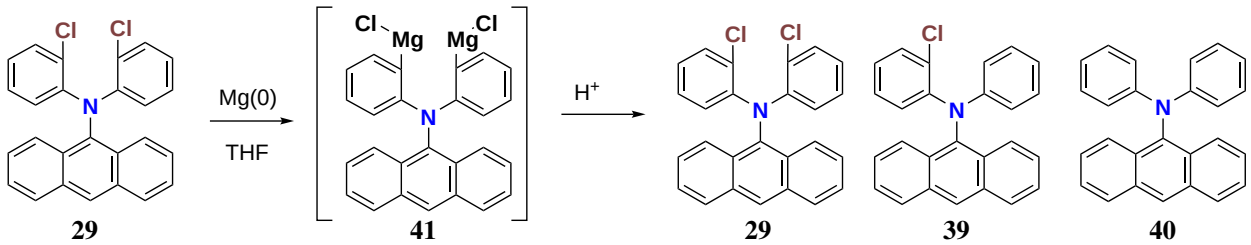

Scheme 11: Optimization of metal-halogen exchange on **29** with an acid quench

The strategy of the dichloro intermediate **29** is based on utilizing metal-halogen exchange (Li, Mg) followed by quenching with a 9-anthracenyl boronic ester source. A summary of these two approaches is outlined in Scheme 12. A few tests are performed to ascertain if any metal-halogen exchange happens in this system, with Rieke magnesium[82] activation being the only set of condition that yields acceptable conversion (Table 4). Unfortunately the combination of the activated species **41** with various boronic esters (the procedure is similar to that of the formation of **23** where the boronic ester must be prepared *in situ*) was not successful (Scheme 12, bottom) - the desired product molecular weight was not observed by mass spectrometry after multiple attempts.

The ditriflate route is based on a recent discovery of the synthesis of cyclic diarylborinic acids by Igarashi *et al*.[83] via Pd-catalyzed cross coupling with diisopropylamine-borane.[84] This cross-

coupling in tandem with 9-anthracenyllithium quench was also not successful in producing the desired product when analyzed by MALDI mass spectrometry (Scheme 12, top).

The lack of control in reaction sequence (carrying multiple reactions forward as crude mixture) in both dichloro and ditriflate cases has prompted me to stop exploration of these routes, and move on to different synthetic targets. I have not been able to observe a desired molecular weight in mass spectrometry after attempting multi-reaction one-pot processes, which was not an encouraging sign to continue using time toward this route.

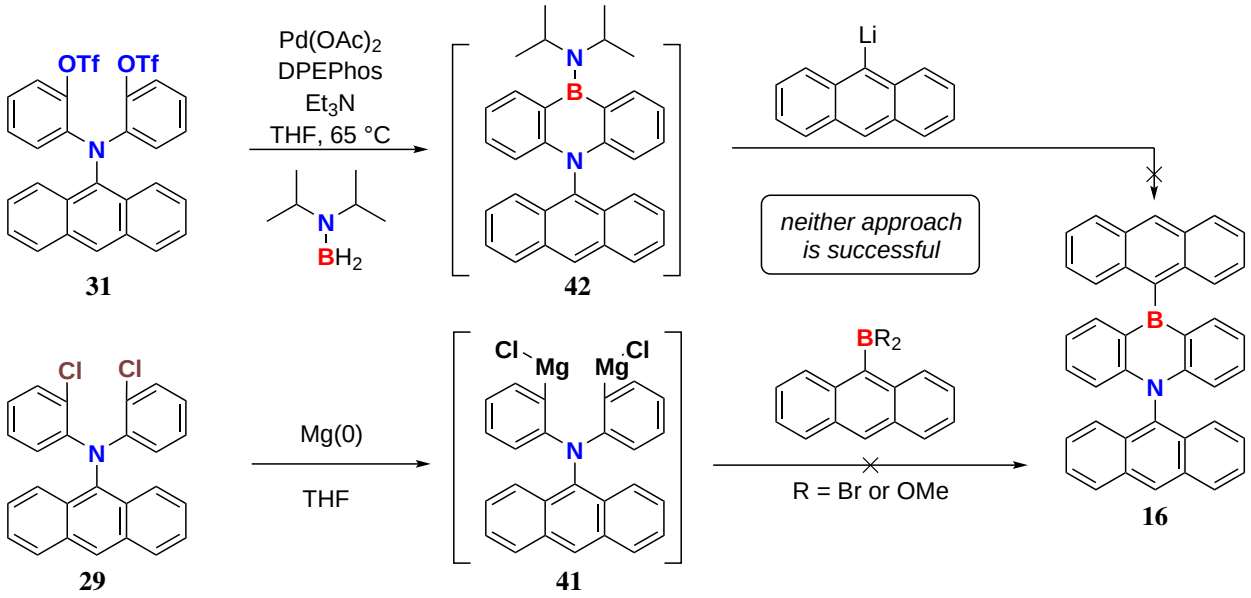

Scheme 12: Two attempted routes toward the BN monomer precursor **16**

In summary, two additional routes toward the **16** were explored, and unfortunately an authentic sample of the desired product could not be obtained from either of the routes in a reasonable time frame. At this junction the BN-pair incorporation project was put on hold, along with exploration of the BNNB monomer **15** and the related structures. With increasing difficulty in installation of heteroatoms in the molecular precursors, I had to reassess my approach toward heteroatom substitution in GNRs. The challenging monomer synthesis toward electronically interesting precursors does not bode well for the future implementation of these precursors in the electrical engineering application. In retrospect, a number of previously unreported azaborines and triarylamines are prepared and fully characterized, which can be useful for future synthetic applications.

An interesting perspective in a regioregular azaborine unit incorporation into GNRs that is immediately from this work is related to end state modulation in GNRs. With the precursor **26** in hand and as the UHV STM technique becomes more available, a hypothetical study can combine growth of the 7-AGNR precursor polymer from DBBA and the endcapping of the polymer with various arene precursors (such as **26** or others) to rationally terminate the GNR. In a pure DBBA growth, the end state of the 7-AGNR has been thoroughly analyzed, and the existense of a reactive Tamm state is found due to the small zigzag fragment at the end of the ribbon.[85] The effect of the end-capping of the Tamm state with a heteroatom-based moeity is predicted to be a worthwhile research effort as the GNR technology finds its niche in the applied materials.

2.3 Investigation of C–N and N–N bond formation in chevron GNR scaffold

Chevron-edge graphene nanoribbon was one of the first types of bottom-up prepared ribbons that was reported in 2010 by Cao *et al*. The synthetic pathways was based on a 6,11-dibromo-1,2,3,4-tetraphenyltriphenylene monomer **1**, which was polymerized and successfully cyclodehydrogenated to yield the chevron GNRs (namesake is due to the shape of the ribbon, which is colloquially accepted by the community).

In recent years, many studies focused on edge modification of the chevron GNRs. Along with previously mentioned study of **43** by Bronner *et al*., a few studies attempted to modulate the width and heteroatom content of the chevron-type ribbon. The synthetic access to this type of monomers relies on a Diels-Alder type reaction of a triphenylenedienone with a substituted tolane, which allows for a simple entry into this GNR scaffold. Our research group has published a magnum opus on edge heteroatom doping of the chevron GNRs, which explores incorporation of oxygen, sulfur, and nitrogen atoms at the periphery of the chevron ribbon via an on-surface synthesis and characterization.[86] This work is closely related to a collaborative effort that reported the mechanistic rearrangement of methylcarbazole unit to phenanthridine along the periphery of a chevron GNR,[53] and a follow-up study of a length-dependent heterojunction evolution in the same ribbon.[87] Additional studies based on thiophene incorporation have been reported as well.[88,89]

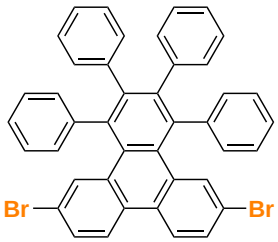

1

C-C bond formation only
No heteroatom substitution
Nature, **2010**, *466*, 470–473

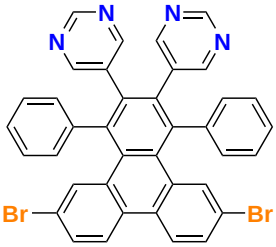

43

C-C bond formation only
Nitrogen **edge** substitution
ACIE, **2013**, *52*, 4422–4425

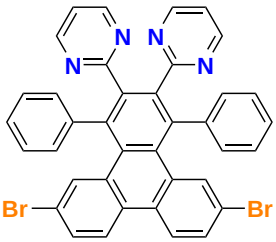

44

C-C, **C-N**, **N-N** bond formation
Nitrogen **core** substitution
this work

Scheme 13: Design of the new 4N chevron GNR monomer, and comparison to previous work

In all aforementioned cases, the carbon-heteroatom bonds were pre-installed in the monomer structure, and the surface synthesis has relied on the omnipresent C–X bond cleavage / radical recombination / cyclodehydrogenation strategy. After continued exploration into heteroatom incorporation along the core, we have found it increasingly difficult to pre-install all of the necessary carbon-heteroatom bonds into the monomer structure, and only utilize C–X/C–H/C–C bond chemistry. A refreshing approach to synthesis of heteroatom-substituted materials, then, is a process which directly forms desired carbon-heteroatom bonds during the polymerization or cyclodehydrogenation step. Therefore, at this stage of my research endeavor I have postulated a hypothesis that has driven my thesis work as it pertains to core nitrogen substitution in GNRs:

Hypothesis Formation of C–N and/or N–N bonds is possible on Au(111) or Ag(111) under thermal conditions, and there will be a sizeable difference between these bond formation onset temperatures and that of the C–C bond formation at the cyclodehydrogenation stage.

The first test for this hypothesis has come along with the idea of a N-core substituted chevron GNR. It is feasible to invert the position of the nitrogen atoms in the monomer scaffold such that the overall chevron shape is preserved, but the nitrogen atoms are now pre-positioned along the core of the GNR rather than the periphery (**43** vs **44**). If the cyclodehydrogenation happens as predicted and the resulting ribbon is planar, this would ensure that the lone pairs on the nitrogen must interact pi-orbitals of the carbon atoms, thus enabling a significant change in the electronic properties of the ribbon.

The monomer design and comparison to previously reported chevron GNR monomers of interest is shown in Scheme 13. Both **1** and **43** grow long, good quality GNRs, as reported in respective publications, so it is hypothesized that the new monomer **44** would be able to at the very least grow polymers. The fidelity of the cyclodehydrogenation step was hard to predict, as we have introduced two possible new modes of reactivity that have never been observed before.

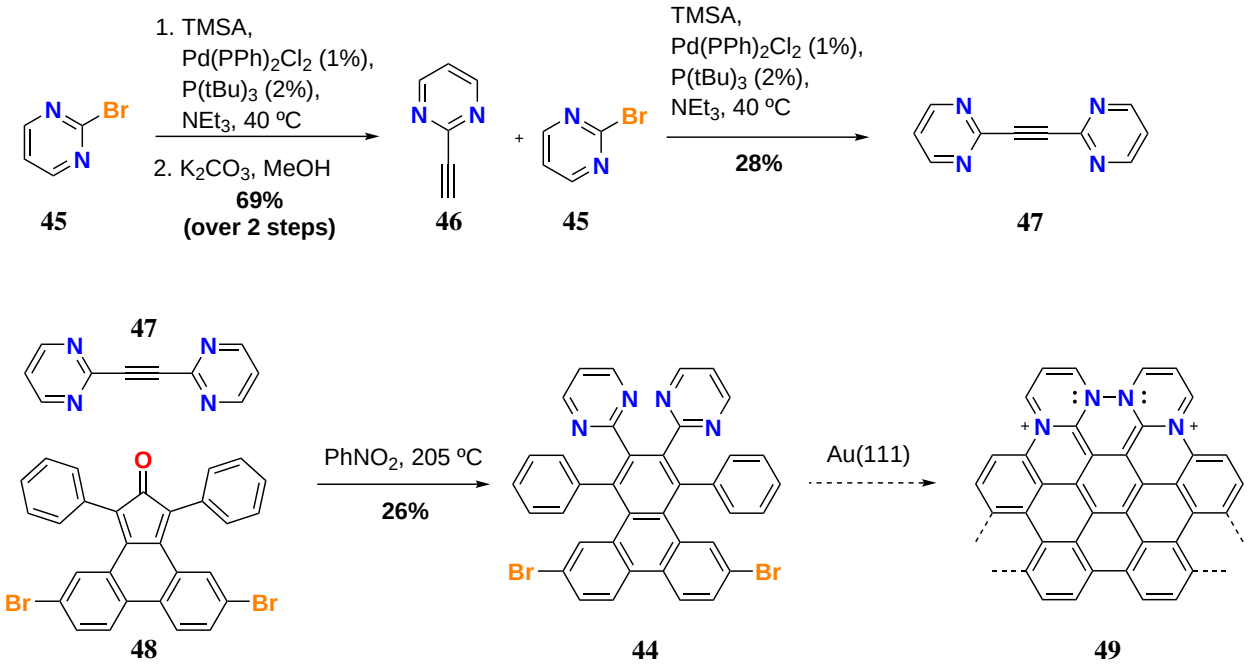

Scheme 14: Synthesis of **44** en route toward 4N-cGNR

The synthesis of **44** is oulined in Scheme 14. The buildup of pyrimidin-2-yl tolane **47** is accomplished via Sonogashira cross-coupling strategy. 2-bromopyridine **45** is coupled with (trimethysilyl)acetylene, then the resulting alkyne is deprotected to yield **46** in 69% yield. A second Sonogashira cross-coupling with **45** resulted in the desired symmetrical tolane **47**. A Diels-Alder reaction followed by cheleotropic extrusion of CO is used to couple **47** with **48**, and **44** is obtained in 26% yield. The synthesis was completed on a first pass, and no additional attempts to increase the yield of the monomer were performed.

With **44** in hand, the surface growth optimization was underway. Precursor **44** was deposited from a Knudsen cell evaporator under UHV onto a Au(111) surface held at 24 °C, which resulted in clean deposition of the precursor (Figure 13a). The surface is annealed to 200 °C, and formation of a polymer is observed (Figure 13b), which is in agreement with the pristine chevron GNR sytnthesis on Au(111).[41] Bright protrusions on the periphery of the polymer indicate that the ribbon

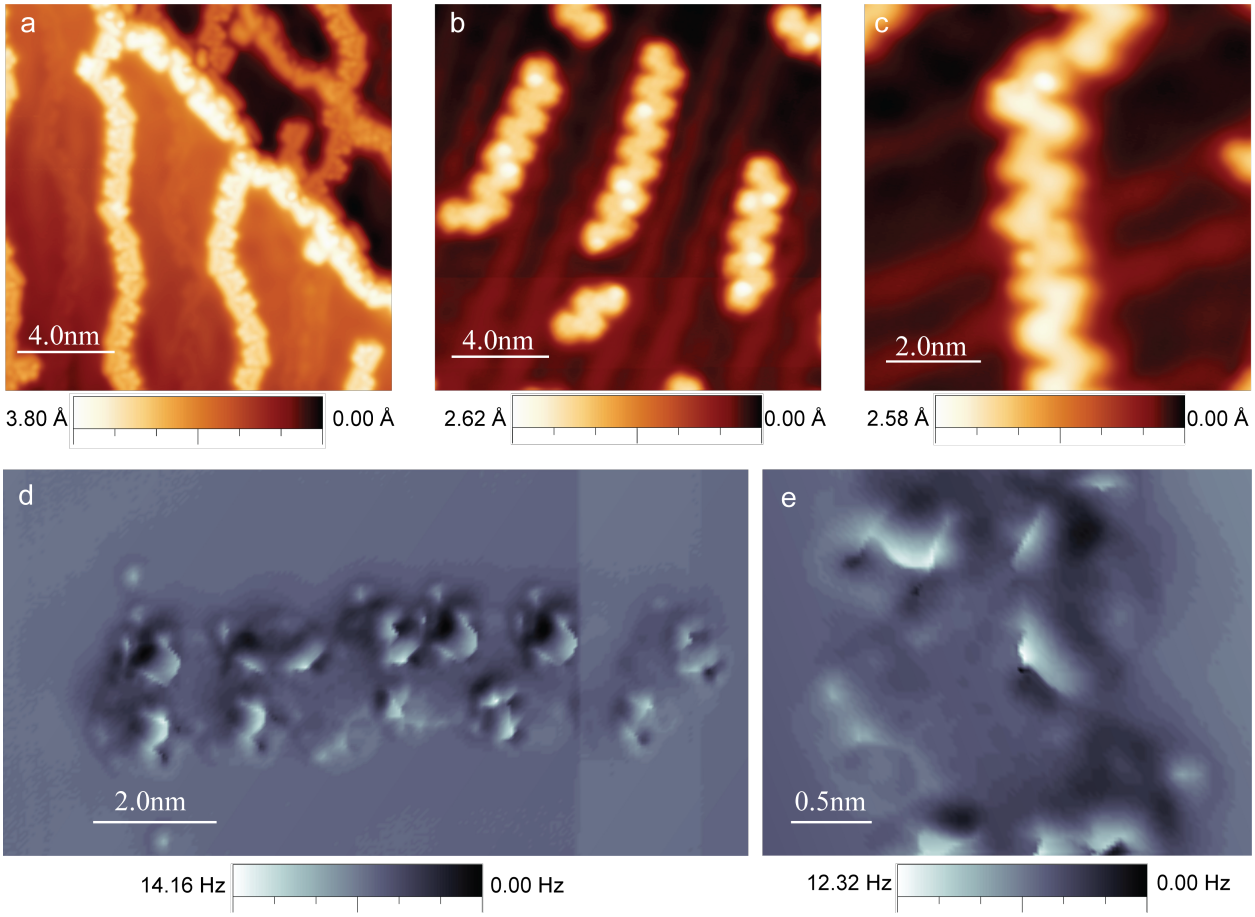

Figure 13: Deposition and annealing of **44** on Au(111) - topographical and bond-resolved images. (a)-(c): Monomer(a)-to-polymer(b)-to-GNR(c) transformation of **44**, in correspondence with Scheme 15. (d), (e) Bond resolved STM images from a sample that was annealed to 400 °C. The protrusions indicate that full planarization of the ribbon does not occur, specifically on the periphery where pyrimidinyl rings are expected to be.

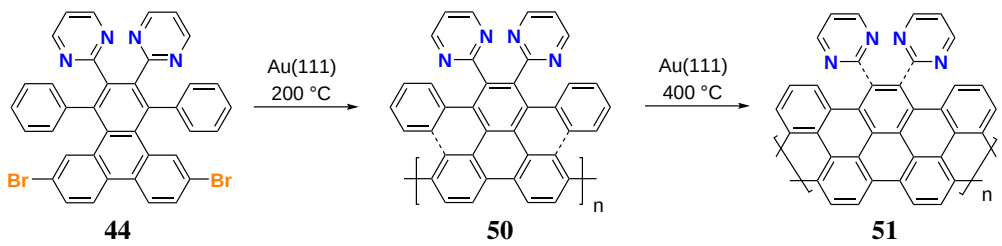

44 **50** **51**

Scheme 15: Deposition and annealing of **44** on Au(111) - proposed structures

is not fully cyclodehyrogenated. Another observation is that the ribbon shape begins to deviate from the linearity - the ribbon in bottom-right corner of Figure 13b appears somewhat kinked. Further annealing to 400 °C has resulted in formation of very irregular structures such as presented in Figure 13c. The bond-resolved STM imaging on the sample that was annealed to 400 °C has confirmed that the cyclodehydrogenation of ribbon does not proceed in a regioregular fashion, and it is very difficult to discern the final structure due to evident non-planarity. Temperature variation (slow 1K/min ramp, or fast 5–10 K/min ramp, both to 400 °C) was not successful in changing the inherent reactivity of the monomer. Scheme 15 summarizes the observed results – it is likely that core C–C bonds have been formed, but it is unclear whether pyrimidine rings have been engaged in cyclodehydrogenation.

In an attempt to reduce the complexity of the ribbon structure, another logical approach toward incorporation of nitrogen atoms along the core of the chevron ribbon could be based on using two nitrogen atoms instead of four. The corresponding pyridyltolane **52** can easily be prepared via the same strategy, and the surface monomer **53** all the same, but a regioselectivity problem arises. Scheme 16 showcases the issue - the monomer preparation is straightforward, but the rotation around the pyridine-triphenylene bond can incur problems with the regioselectivity of the C–N bond formation. Whether it does/does not form the C–N (or even N–N) bonds, the resulting ribbon would not have any lateral symmetry, and it would likely consist of random lateral heterojunctions of various modes of the closed-down structure. This does not go along with the goal of atomic precision during GNR formation, and thus this experiment was not performed, although the value solely proving the C–N bond formation still remained as an unknown quantity.

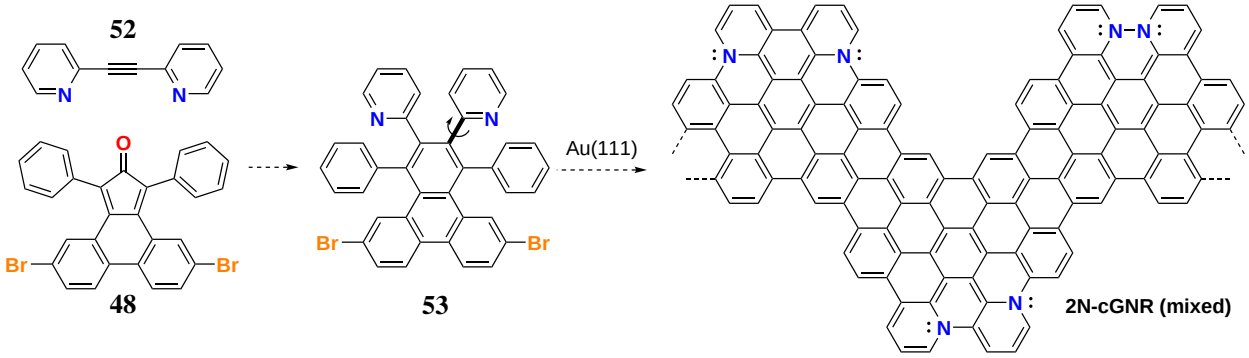

Scheme 16: Hypothetical route toward 2N-cGNR – regioselectivity issue

In summary, the on-surface growth experiments with **44** did not yield a clear result; however, it can not be ruled out that either C–N or N–N bonds can not be made. The project can be thought of as a low-risk–high-reward, as the synthesis was extremely straightforward and two new unprecedented bonding motifs were slated to be investigated.

2.4 Investigation of heteroatom bond formation in 7-AGNR scaffold

In the pursuit of the heteroatom bond formation protocol, and the nitrogen substitution in armchair GNRs in general, 7-AGNR were investigated as a possible familiar scaffold. Our research group was successful with the incorporation of boron atoms along the core of 7-AGNR,[78] but the challenge in creating a similar ribbon with nitrogen atoms substituted into the core of the ribbon re-

mained unconquered. A few possible candidates that would yield high-value GNRs are depicted in Scheme 17. The first logical target toward the nitrogen incorporation in AGNRs is 2N-7-AGNR – it is isostructural to B-7-AGNR, and it would yield the most direct comparison of the electronic structure change. A few graduate students in our group have attempted the synthesis of the corresponding precursor **54**[90,91] and this monomer was isolated in principle (characterized by mass spectrometry). However the purification of **54** was not successful, and even a crude sample of **54** did not exhibit proper thermal stability to endure the Knudsen cell evaporation needed for on-surface synthesis.

Going along the hypothesis of C–N / N–N bond formation, **55** and **56** have been hypothesized as two precursors that can potentially accomplish C–N and N–N bonding, respectively, within the 7-AGNR framework. Precusor **55** would lead to 4N-7-AGNR, which would have 9.5% nitrogen content (4 nitrogen atoms / 42 total atoms in the unit cell) – here a new number of new variables is reduced, and only the C–N bond formation is the unknown variable. Precursor **56** would lead to 28.5% nitrogen content in a ribbon (8 nitrogen atoms / 28 total atoms), and only N–N bond formation will be required for the cyclodehydrogentaion/planarization of the ribbon.

The electronic properties of corresponding nanoribbons have been analyzed by DFT-LDA method by Louie group (UC Berkeley), and these results have been extremely encouraging (Figure 14). The 12N-7-AGNR was predicted to be metallic, meaning that the Fermi energy of the material crossed both VB and CB (VBs are highlighted in red, while CBs are highlighted in blue), which was somewhat unexpected of a GNR. The 4N-7-AGNR's band diagram is also shown, and here the band diagram looks more similar to the all-carbon 7-AGNR. The appearance of the gap is evident, but the Fermi level in the system (E_F = 0) is pushed up into the CB – there are extra electrons in the system, which is rationalized as the lone pair on the core substituted nitrogen atoms participation in π-delocalization in the GNRs.

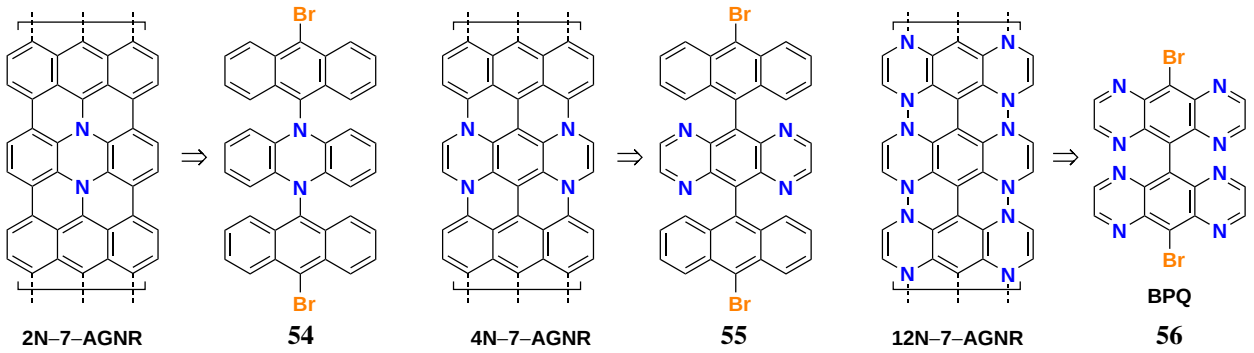

Scheme 17: Substitutional nitrogen doping in 7-AGNR scaffold

2.4.1 Covalent C–N Bond Formation through a Surface Catalyzed Thermal Cyclodehydrogenation

The synthesis of dianthryl pyrazino[2,3-g]quinoxalines toward 4N-7-AGNR is depicted in Scheme 18. Condensation of 2,5-dihydroxy-1,4-benzoquinone **57** with ethylenediamine followed by catalytic dehydrogenation gives pyrazino[2,3-g]quinoxaline **59** in 10% yield over 2 steps. Dibromination of **59** with NBS and subsequent Suzuki-Miyaura cross-coupling with 2-(anthracen-9-yl)-4,4,5,5-tetramethyl-1,3,2-dioxaborolane yields the parent dianthryl pyrazino[2,3-g]quinoxaline **61**. While **55** can be obtained through direct bromination with N-bromosuccinimide in 70% yield, a two-step

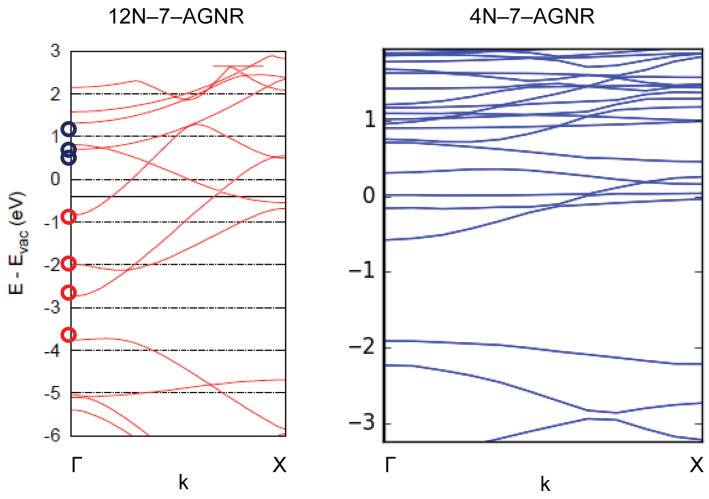

Figure 14: Band structures of 12N-7-AGNR (Fermi energy level is denoted as a solid line) and 4N-7-AGNR (the zero energy is aligned to the Fermi level in the system)

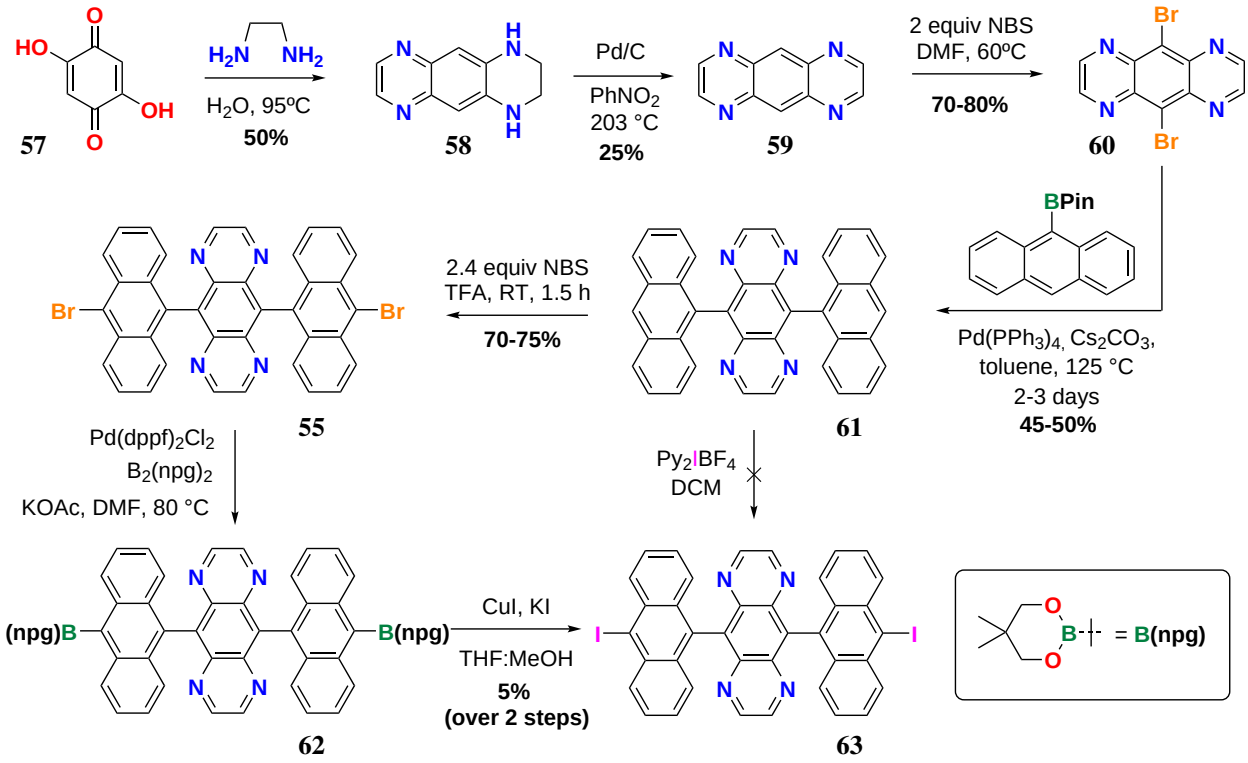

Scheme 18: Synthesis of dianthrylpyrazinoquinoxaline series toward 4N-7-AGNR

sequence of Miyaura borylation followed by treatment of the intermediate mixture of neopentyl(glycol) boronic esters with copper iodide is required to obtain the diiodinated pyrazino[2,3-g]quinoxaline **63** albeit in a lower yield (7% over two steps).

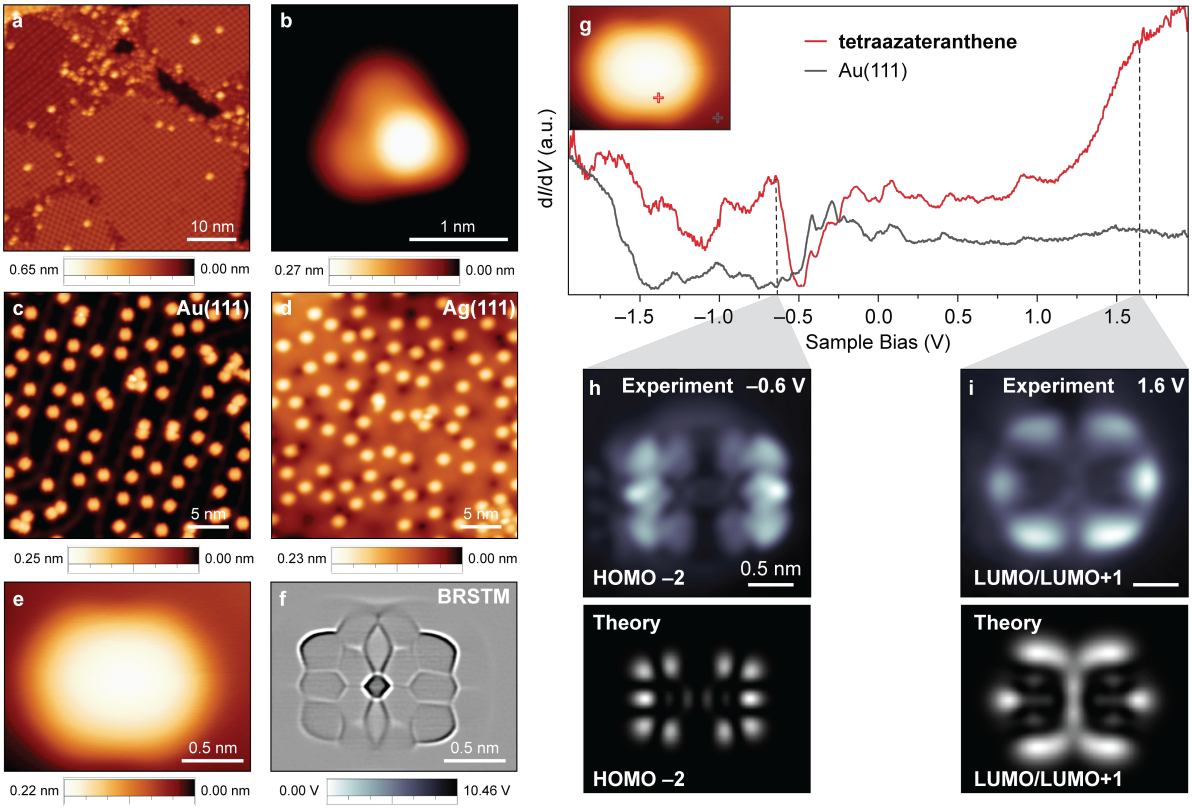

Figure 15: STM topographic image of (a) self-assembled islands and (b) an isolated molecule of **61** on a Au(111) surface. STM topographic image of (c) a Au(111) and (d) a Ag(111) surface after annealing to 100 °C showing the clean transformation of **61** to **64**. (e) STM topographic and (f) BRSTM image of fully cyclized tetraazateranthene **64** on Au(111). (g) STM dI/dV point spectrum of **64** on Au(111). Experimental dI/dV spatial maps and calculated position dependence of the LDOS map of states with energy fixed at (h) V_s = –0.6 V (I_t = 0.60 nA) and (i) V_s = +1.6 V (I_t = 0.75 nA). Calculated lateral spatial distribution of LDOS at fixed energy is evaluated at a height of 4 Å above the plane.

Pyrazino[2,3-g]quinoxalines **61**, **55**, and **63** were deposited from a Knudsen cell evaporator in ultra-high vacuum (UHV) onto Au(111) and Ag(111) surfaces held at 24 °C. Figure 15a shows a representative STM topographic image at 5 K of self-assembled multi-layer islands of **61** on a Au(111) crystal surface. Isolated molecules of **61** adsorb preferentially in a conformation that places the anthracenyl groups at either end of the molecule nearly coplanar to the underlying surface. One side of the central pyrazino[2,3-g]quinoxaline ring protrudes high above the plane of the molecule and appears as a characteristic bright feature in in the topographic image in Figure 15b, which is consistent with the simulated STM image and simulated adsorption geometry (Figure 16). Annealing of molecule decorated surfaces at temperatures as low as 75–100 °C for 15 min induces a thermal cyclodehydrogenation of all *peri*-positions to form tetraazateranthene **64** (Figure 15c,d). STM images on Au(111) or Ag(111) reveal a sub-monolayer coverage of the surface with discrete

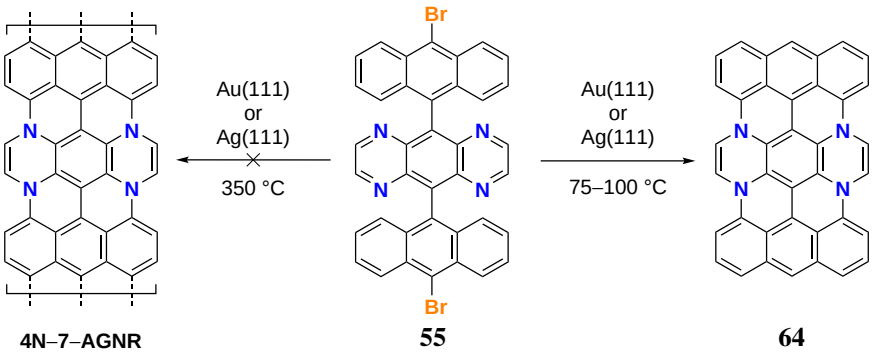

Scheme 19: Summary of the STM investigation of the reactivity of **55** – facile C–N bond formation dominates and precludes the polymerization step, affording exclusively tetraazateranthene **64**.

rectangular structures measuring 0.95 ± 0.05 nm, 1.20 ± 0.15 nm, and 0.19 ± 0.02 nm in width, length and height, respectively (Figure 15e). There is no observable difference in cyclodehydrogenation conditions between Au(111) and Ag(111).

Bond-resolved STM (BRSTM) imaging, where the STM tip is functionalized with a carbon monoxide (CO) molecule to conduct imaging in the Pauli repulsive regime, confirms the tentative structural assignment and shows the fully fused core along with the four covalent C–N bonds of tetraazateranthene **64** (Figure 15f). Large area scans on Au(111) and Ag(111) highlight the remarkable selectivity and the high yield of this transformation (Figure 15c,d). Even in the presence of C–Br and C–I bonds in **55** and **63** cyclodehydrogenation is observed at temperatures below $<$ 100 °C, in addition to facile dehalogenation of the precursor as confirmed by direct observation of formation of atomic bromine (Figure 17b) and iodine (Figure 17c), respectively. In attempt to observe any desired polymerization, an experiment where the high-coverage deposition of **55** was annealed to 250 °C was performed. Only isolated instances of **64** and random lateral fusion species were observed (Figure 17a). Thus we conclude that the planarization precludes the possible radical step-growth polymerization on the surface in the case of **55** and **63** (Scheme 19).

Differential conductance (dI/dV) point spectra collected above the nitrogen atoms along the armchair edge of tetraazateranthene **64** (Figure 15g) reveals two characteristic features associated with an occupied and an unoccupied state at a sample bias of –0.6 V and +1.6 V, respectively. dI/dV maps recorded at the corresponding energies ((Figure 15h,i) show the spatial distribution of the local density of states (LDOS) across the surface of the adsorbed molecule.

In an effort to assign the peaks in the differential conductance spectra to molecular frontier orbitals we performed density functional theory (DFT) calculations with local density approximation (LDA)[92] as well as a GW calculation which incorporates the electron self-energy in a many-electron Green function approach.[93,94] Calculation results are summarized in Figure 19. The peak at –0.6 V closely resembles the projection of the HOMO–2 orbital of tetraazateranthene, while the broader feature at +1.6 V is best represented by a superposition of the LUMO and the LUMO+1 orbitals. While the degeneracy between LUMO and LUMO+1 is not immediately apparent from calculations within the LDA framework alone, quasiparticle calculations using the GW correction confirm that LUMO and LUMO+1 of **65** are separated by $\Delta E < 50$ meV. An analysis of wavefunction symmetry of the frontier orbitals of tetraazaanthene **64** calculated in the gas phase suggests strong hybridization of HOMO and HOMO–1 states with the underlying Au(111) or Ag(111) substrate. The resulting significant broadening prevents an unambiguous assignment of the HOMO and HOMO–1

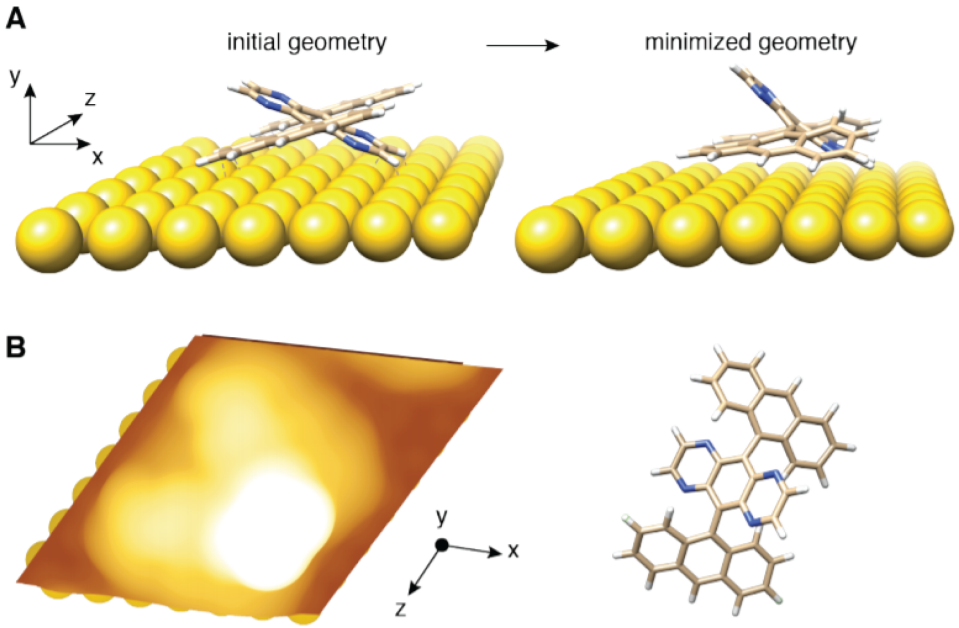

Figure 16: Optimization of adsorption geometry of **61**. (A) Comparison of starting geometry (left) and final geometry (right) for **61**. Starting geometry is placed 3.5 Å from the surface, central torsion angle between anthracene and pyrazino[2,3-g]quinoxaline moieties is 40°, four Au layers are used in calculation. (B) Simulated STM image of **61**, which is directly comarable with the experimental observation in Figure 15b.

feature in the dI/dV spectrum.

Further insight into the mechanism of the surface-assisted cyclodehydrogenation of **61** including the formation of four C–N bonds was obtained from ab initio calculations using the all-electron FHI-aims code.[95] We determined the reaction-energy landscape including all transient intermediates and transition states using density functional theory (DFT) at PBE+VdW+ZORA level for four discrete cyclization sequences. While the calculated rate determining transition states range between $\Delta E^{\ddagger}$ = 0.6–3.5 eV above the starting materials (**61** physisorbed on Au(111)), this discussion focuses only on the most plausible mechanism involving the lowest overall activation barrier (Figure 18).

An initial step involving the concerted formation of two C–N bonds between the physisorbed side of the pyrazino[2,3-g]quinoxaline and the two anthracene units represents the rate determining transition state and is associated with an activation barrier of $\Delta E^{\ddagger}$ = +0.6 eV. The transition state structure **TS1** is characterized by an allylic diradical that undergoes a rapid suprafacial [1,2] hydrogen shift (red H atoms in **TS1**) to give the stabilized benzylic radical intermediate **Int1**. The subsequent transfer of the two hydrogen atoms closest to the substrate (black H atoms in **Int1**) to the Au(111) surface is virtually barrierless ($\Delta E^{\ddagger}$ = +0.3 eV) and leads to the partially cyclodehydrogentated intermediate **Int2** featuring two out of the four C–N bonds in the tetraazateranthene **64**. It is important to point out that we have never observed **Int2** during UHV experiments; the only two unimolecular species that can be observed on the surface are **61** (or **55**, or **63**) after the deposition, and **64** after the anneal (Figure 17b,c). The cyclization of the remaining pyrazino[2,3-g]quinoxaline wing protruding from the surface proceeds through a single transition state, albeit with a higher activation barrier ($\Delta E^{\ddagger}$ = +1.1 eV). The two remaining C–N bonds are formed through an approach of

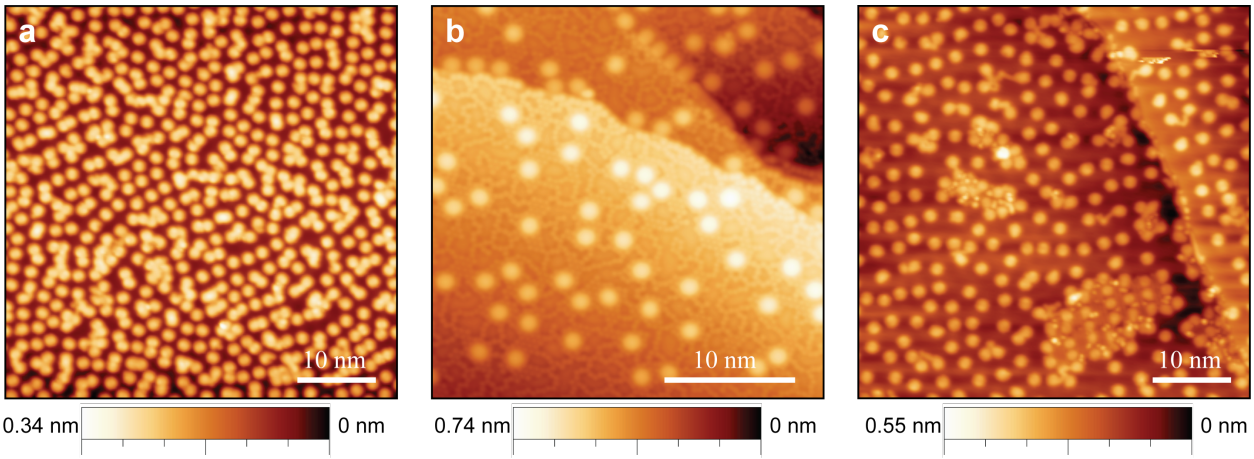

Figure 17: SPM topographic images of results of **55** and **63** surface reactivity on Au(111) and Ag(111). (a) SPM topographic image of a high-coverage deposition of **55** on a Au(111) surface followed by annealing to 250 °C. The predominant molecular species on the surface is the cyclized product **64**. The few fused species observed on the surface can be attributed to random C–H bond dissociation processes that lead the formation of dimers and trimers. No structures that extend via the halogenated positions can be identified on the surface observed. (b) SPM topographic image of a high-coverage deposition of **55** on a Ag(111) surface followed by annealing to 100 °C. The predominant molecular species on the surface is the cyclized product **64**. The closely packed structure below the layer of molecules is atomic bromine adsorbed to the Ag(111) surface. (c) SPM topographic image of a high-coverage deposition of **63** on a Au(111) surface followed by annealing to 100 °C. The predominant molecular species on the surface is the cyclized product **64**. The closely packed spherical structure below the layer of molecules is atomic iodine adsorbed to the Au(111) surface.

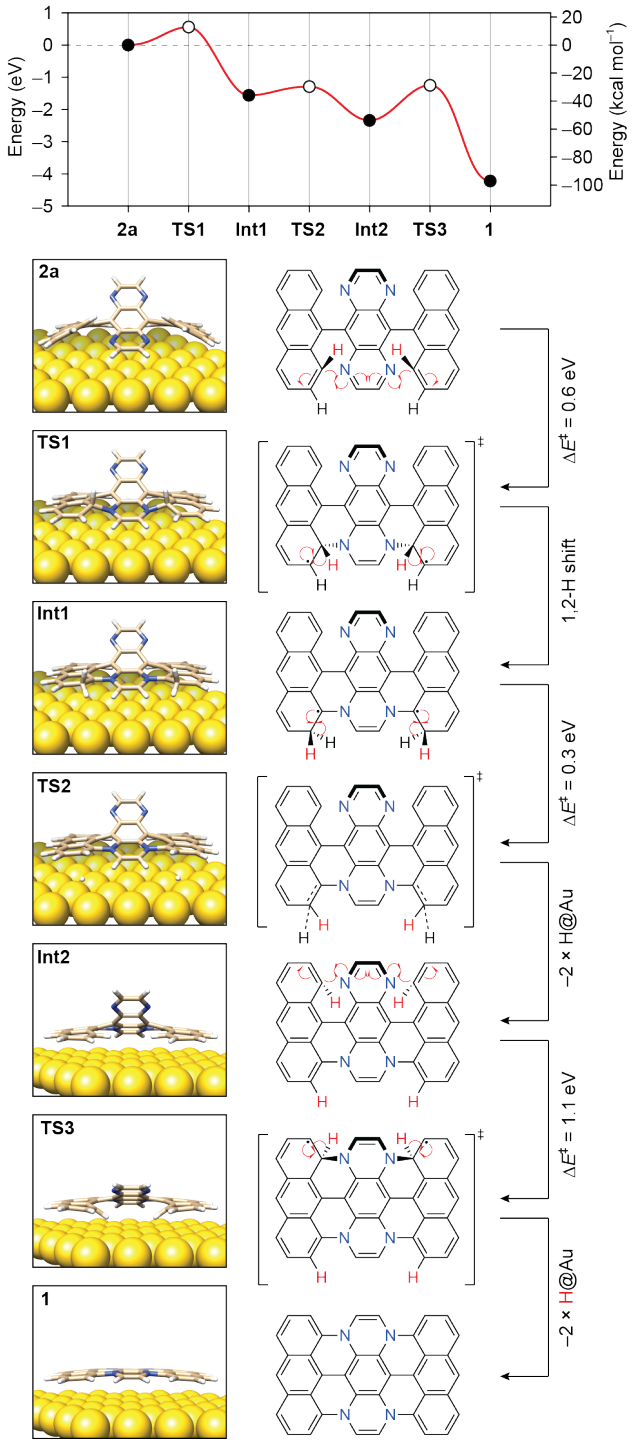

Figure 18: Calculated energy diagram for the stepwise cyclodehydrogenation of **61** to **64**. The graph shows the ab-initio energy landscape for intermediates and transition states along the reaction pathway from **61** to **64**. Calculated activation energies are shown next to the reaction arrows.

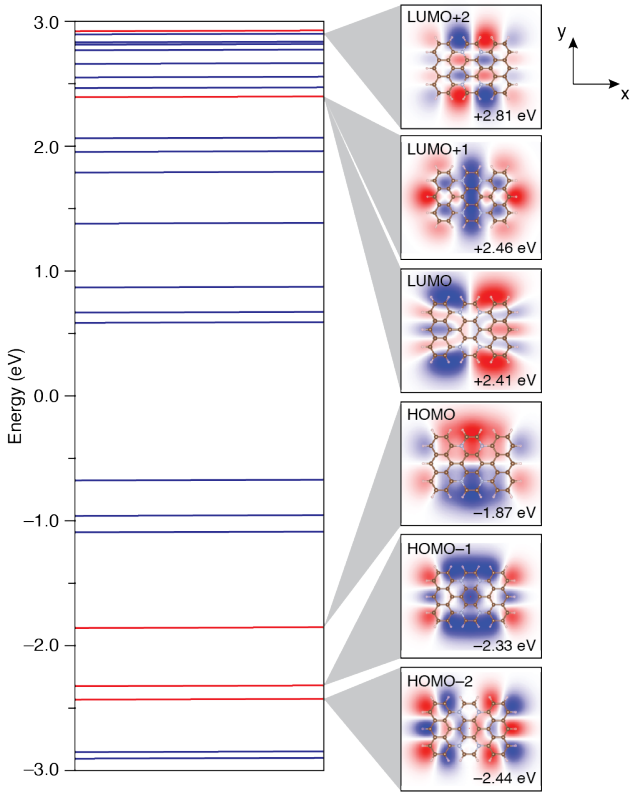

Figure 19: Gas phase DFT (blue) and GW (red) energy levels and the orbital wavefunctions of **64**. Red/blue color in the wavefunction plot show the plus/minus sign of the wavefunction. The values of energy levels marked below the wavefunction plots are the GW energy levels, referred to an arbitrary zero of energy in the middle of the HOMO-LUMO gap.

the pyrazino[2,3-g]quinoxaline wing from above the plane of the anthracenes placing the red hydrogen atoms in the allyl diradical-like transition state **TS3** in a position pointing directly towards the underlying Au(111) surface. Direct transfer of these hydrogen atoms to the surface yields the fully cyclized tetraazateranthene **64**. A question might arise as to whether the cyclodehydrogenation on one side of the molecule is truly concerted, or whether it can proceed stepwise (i.e each C–N bond is formed independent of each other). Figure 20 compares these possibilities side-by-side, with the conclusion that both stepwise and concerted mechanisms are very similar in energy (0.4 eV for stepwise, and 0.6 eV for concerted), and thus it is reasonable to suggest that both mechanisms are possible.

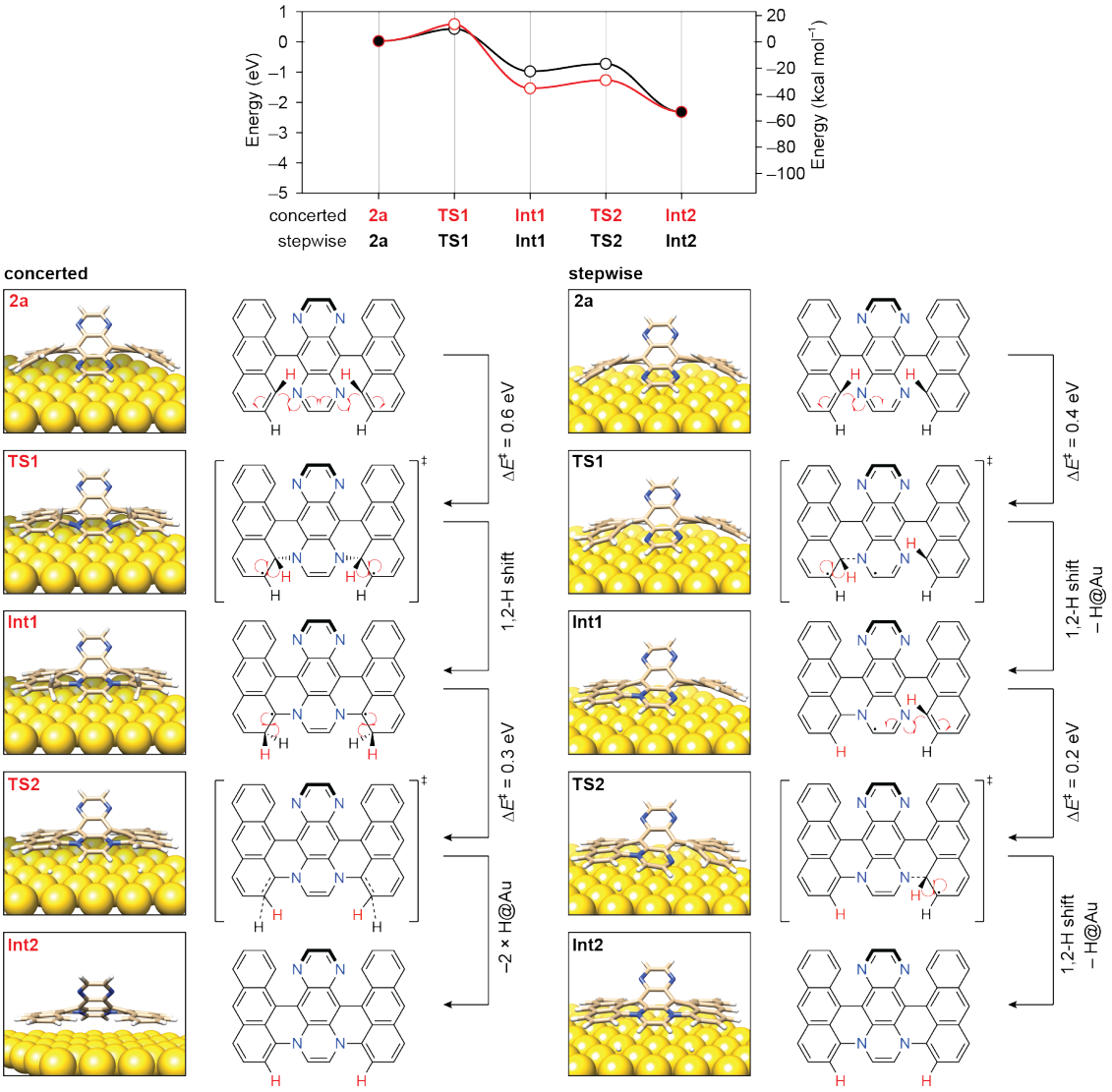

Figure 20: Calculated energy diagram for the concerted (left) and stepwise (right) cyclodehydrogenation step that leads from of **61** to **Int2**. The graph shows the ab-initio energy landscape for intermediates and transition states along the reaction pathway from **61** to **Int1**. Calculated activation energies are shown next to the reaction arrows.

In summary, an unusually mild thermally induced oxidative cyclodehydrogenation of dianthryl pyrazino[2,3-g]quinoxalines to form four covalent C–N bonds in tetraazateranthene on Au(111) and Ag(111) surfaces is discovered and characterized to the fullest extent possible. SPM imaging reveals that molecular precursors **61**–**63** adsorb in a chair-like conformation on metal substrates and undergo a clean conversion to tetraazateranthene **64**. Bond resolved STM and differential conductance spectroscopy unambiguously confirm the structural assignment. Mechanistic analysis based on ab-initio DFT calculations reveals the most likely stepwise mechanism featuring a rate determining barrier of only = 0.6 eV, consistent with the experimentally observed reaction conditions (T = 75–100 °C, 15 min).

The overall conclusion from this study leads to conclusion that scaffold **55** is not applicable for the GNR growth as originally predicted to form a 4N-7-AGNR. However, the discovery of C–N bond formation is immediately impactful, as it provides pertinent knowledge about the temperature range and structural constraints that must be accounted for in this particular system. This knowledge has fueled the design of the next generation monomeric precursors to N-GNRs which are described in the next section.

2.4.2 Nitrogen-doped 7-AGNR access - second generation of precursors

With the discovery of C–N bond formation conditions in the bisanthracenyl-(pyrazinoquinoxaline) scaffold, the challenge remained to vary the monomer architecture in order to achieve a polymer such that we can take advantage of the C–N bond formation for GNR growth.

Based on that knowledge, a few variants of modification to the original system that can potentially allow for polymerization of the monomer unit while making use of facile cyclodehydrogenation are pursued. Firstly, lateral extension (precursor **66**) is hypothesized to induce steric hindrace in adsorption of the monomer onto the metal surface (compared to **61**, Figure 16), which can increase the temperature needed for access to C–N bonds, thus allowing for polymerization to take place at an acceptable rate. A second proposition is the polymerization axis extension (precursor **67**), where two additional anthracenyl units are added to outfit the monomer with polymerization sites that are spatially separated from the future C–N bonds, and these units will enforce proper cruciform conformation needed for the polymerization. If the on-surface polymeriation turns out to be an unsurmountable challenge, the precursor polymer **68** can be made in solution and transferred onto a metal surface with direct contact transfer (DCT) technique, thus leaving cyclodehydrogenation as the only surface-induced step.

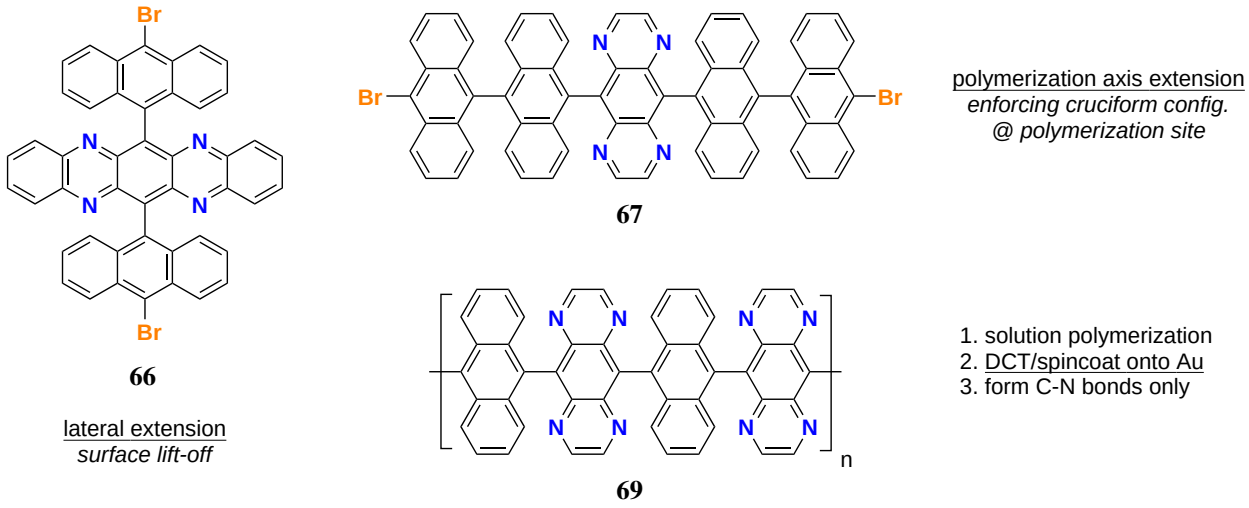

Scheme 20: New approaches to nitrogen core doping in 7-AGNR – incorporating the C–N bond formation reaction into new architectures.

The synthetic route toward the laterally extended monomer is based on the relatively simple access to the tetraazapentacenequinone **70**. The condensation of *o*-phenylenediamine and 2,5-dihydroxy-1,4-benzoquinone in the melt yields the dihydroquinoxalinophenazine **71**, which is oxidized to the tetraazapentacenequinone **70** upon treatment with potassium dichromate and sulfuric acid. A double nucleophilic attack of anthracenyllithium (derived from treatment of 9,10-dibromoanthracene with 2.0 equiv. of BuLi) and consequent sodium hypophosphite reduction under acidic conditions yields the 9-bromoanthracene-flanked dihydroquinoxalinophenazine **72**. This process suffers from poor solubility of **70**, steric hindrance on the anthrcenyllithium reagent, and high complexity of generated mixture, thus the yield of only 1.4% is obtained over 2 steps. 20 mg of **72** was isolated, which is enough to move the material forward to the oxidation step. Treatment with manganese dioxide oxidation affords the desired monomer **66** in 80% yield.

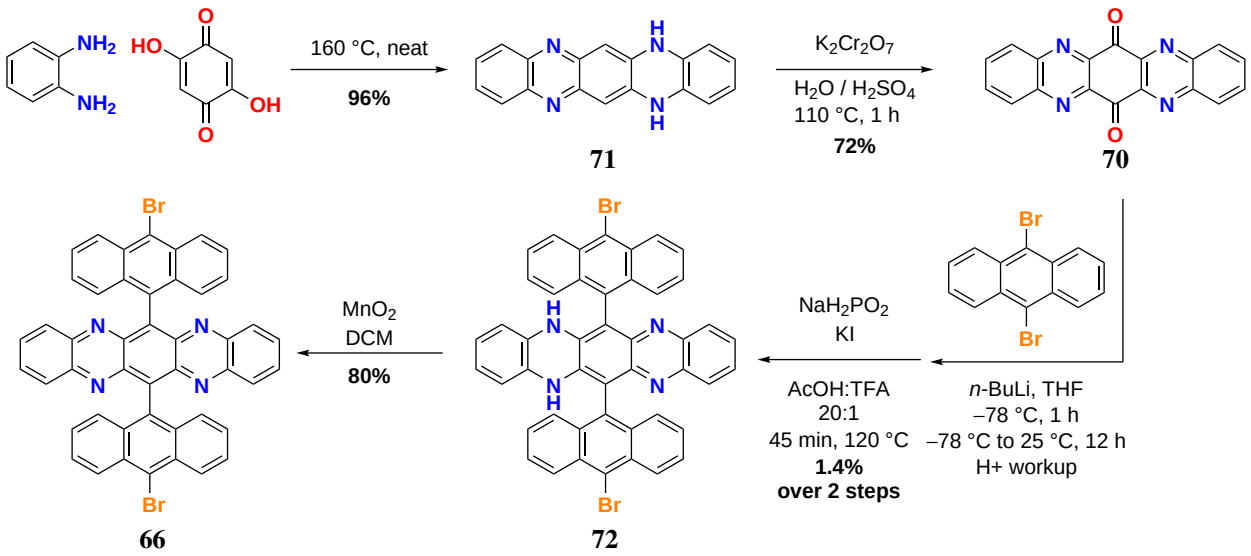

Scheme 21: Synthesis of laterally extended monomer **66** for nitrogen core doped 7-AGNR

It should be noted that both **66** and **72** have merit for the consideration for the on-surface reaction. There is precedent for depositing **71** on Au(111) surface, where it turns out to have planar adsorption,[96] which is encouraging for the scaffold which suffered from the non-planar adsorption of the pyrazinoquinoxaline unit although it might not be a defining factor. The adsorption geometry of non-halogenated variants of both **66** and **72** have been predicted (Figure 21). It appears that the geometry of **66**' is very similar to that of **61**, whereas the geometry of **72**' is strikingly different (one can see a sharp kink in the reduced ring system).

In summary, a synthetic route toward complex dianthyl quinoxalinophenazines **72** and **66** is reported, and both precursors have been isolated in high purity on 10 mg scale. In the case that this modification does not result in graphene nanoribbon formation (as the adsorption geometry prediction is not encouraging), a direct comparison between **72** and **66** can be used for the study of the dependence of redox states on the rate of C–N bond fomation in this scaffold.

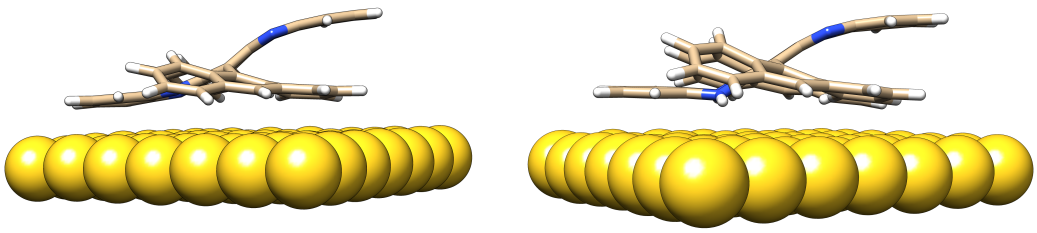

(a) Adsorption geometry of **66**' on Au(111). (b) Adsorption geometry of **72**' on Au(111).

Figure 21: Adsorption geometries of laterally extended precursors toward N-7-AGNR (non-halogenated)

A second approach toward N-7-AGNR is based on the polymerization axis extension of the monomer scaffold, as shown in Scheme 22. Here, the extended (relative to **55**) monomer **67** is proposed to ameliorate the inherent fast C–N bond fomation. The addition of two extra anthracenyl units onto the scaffold should ensure that at the polymerization stage, the activated monomer will be constrained into a cross-shaped structure even after the C–N bonds are formed (intermediate **73**), and that the polymerization is likely proceed as it did with the boron-doped monomer[78] or other precursors of similar scaffold.[97,45]

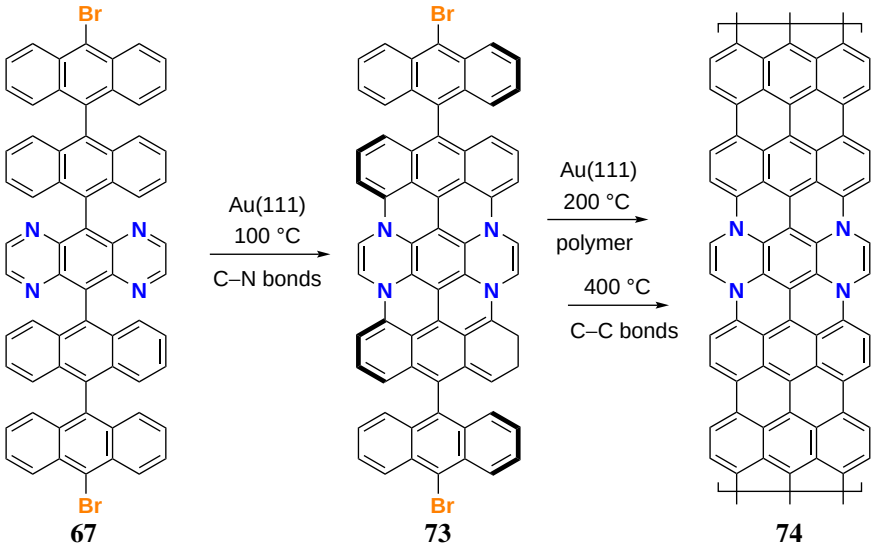

Scheme 22: Proposed on-surface reactivity for polymerization axis extension monomer **67**. Even though C–N bonds will form at a lower temperature, the resulting intermediate **73** will still have appropriate conformation on the periphery that will allow for polymerization and further cyclodehydrogenation to yield GNR **74**.

The synthesis of **67** is outlined in Scheme 23. The approach is based on the access to the original monomer, where the Suzuki cross-coupling in the key step that affords the desired carbon skeleton of the precursor. Dibromobisanthracene **75** is subjected to lithium-halogen exchange / triisopropoxyboralane quench to obtain **76**, the Suzuki cross-coupling partner for coupling with **60**. Desired cross-coupling products are insoluble and not amenable to column chromatography or routine solution-state NMR analysis. **67** can be isolated on 5–10 mg scale by extensive MeOH and hexanes washes and characterized only by mass spectrometry due to its extreme insolubility. The characterization rigor is similar to the original dianthryl pyrazino[2,3g]quinoxaline **61**, which was also extremely insoluble in common solvents.

In summary, the synthesis of the extended monomer **67** is reported, and this precursor is slated to form a 5% nitrogen atom content GNR **74** in spite of the C–N bond formation. If successful, serve as the precursor to a first pristine N-substituted 7-AGNR that will be directly comparable to 7-AGNR and B-7-AGNR in its electronic properties, and it can be used in heterojunction syntheses as a metal contact segments (recall Figure 2, the GNR TFET design) in the future studies.

The last hypothesis toward the N-7-AGNRs relies on the recently reported direct contact transfer (DCT) technique. Lyding group, in collaboration with Sinitskii group, has shown that a solution-sythesized chevron GNR can be transferred onto a Si(100) surface under UHV conditions.[98] The

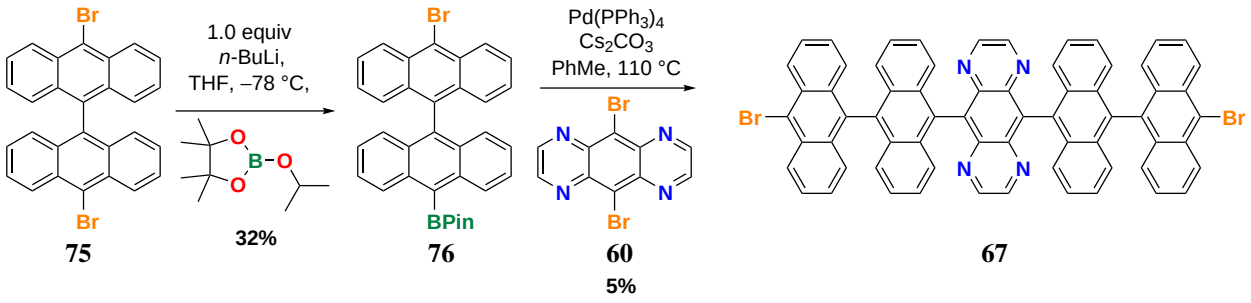

Scheme 23: Synthesis of polymer-axis-extended monomer **67** for nitrogen core doped 7-AGNR.

research effort has allowed to use STM to image the solution-synthesized GNRs on the surface, and to perform STS studies to elucidate the electronic structure of these ribbons and their interaction with the silicon surface.

If a GNR can be successfully transferred to a surface in a UHV, then it is plausible to suggest that a solution-synthesized polymer can also be transferred onto a substrate. This research direction will allow to make use of the rich solution-state controlled polymerization techniqies in combination with the unique surface reactivity, and reduce our reliance on the surface-induced polymerization. A N-7-AGNR precursor polymer is hypothesized as a precursor toward a nitrogen-substituted 7-AGNR (Scheme 24). The synthesis towards this polymer can rely on the Suzuki coupling polymerization, where the 5,10-dibromopyrazino[2,3g]quinoxaline **60** can be polymerized with a diboronic ester **77**. The forward synthesis toward this polymer is shown in Scheme 24. 9,10-diboronic ester **77** is prepared in one step from 9,10-dibromoanthracene, and then **77** is polymerized with **60** using the same conditions as they were for the synthesis of **61**.

The Suzuki cross-coupling conditions ($Pd(PPh_3)_4$, Cs_2CO_3, dry toluene, 110 °C) are used again with moderate success. The MALDI data of the crude mixture is shown in Figure 42, and it is clear that the oligomeric species have been formed. No effort to controllably terminate the polymer chain[99] was made besides a generic aqueous workup, so MALDI spectra contain product peaks from R-Br, R-H and R-BPin types of termination in oligomers.

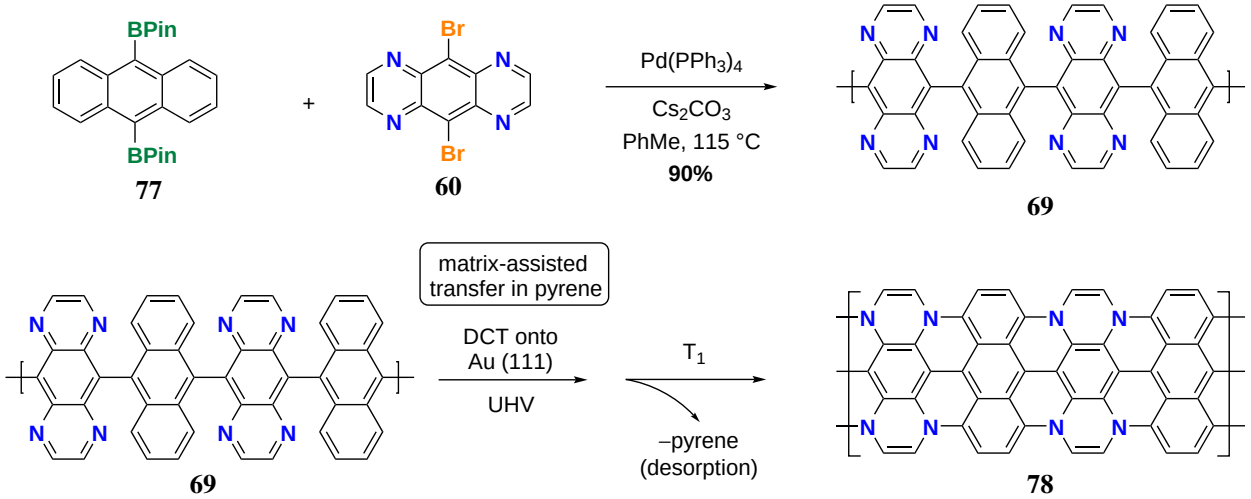

Scheme 24: Synthesis of solution-synthesized polymer **69** for DCT transfer onto Au(111) surface.

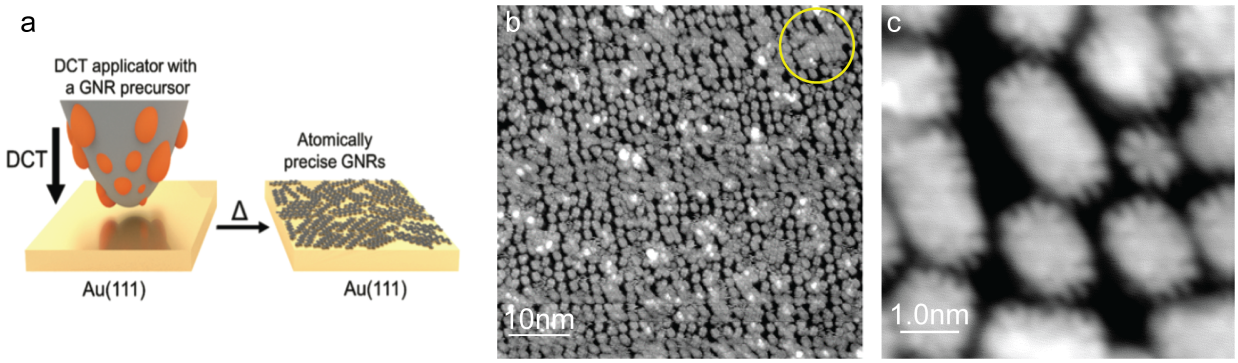

Figure 22: (a) DCT transfer schematic. (b) Preliminary results of deposition of **69** followed by an anneal to 280 °C. Longer segments can be observed (marked by the circle). (c) Zoom-in on a smaller area of the sample from (b). Isolated segments of ∼2 nm of GNR **78** can be found.

The future outlook is the optimization of the polymerization (increasing the polymer length, controlling termination, etc) and of transfer procedure. The current plan of action is to use a matrix-assisted transfer, where the polymer is dissolved in molten pyrene, and then the polymer-pyrene mixture is stamped directly onto Au(111) surface within an STM via the fiberglass applicator. Upon annealing, we expect to see desorption of pyrene and small oligomers while the longer polymers stay behind. These studies are currently in progress, with encouraging preliminary results of a successful transfer of **69** (Figure 22), and observation of oligomer-derived segments of **78**.

If the surface characterization yields good results and long GNR pre-polymers can be transferred via DCT in the STM chamber, then the ultimate goal would be to suspend the polymer onto a Au(111) film, which can then be pumped into a preparatory UHV system. Our lab has the capability to anneal larger-size Au(111) surfaces in the PVD 75 Pro Line stand-alone vapor deposition system. In this setup, the anneal to GNR temperature in UHV conditions can be performed, Raman spectroscopy can be used to assay the quality of the resulting GNRs, and the sample will be ready to go for electrode patterning and device measurements. This method has not seen a lot of use in literature due to its novelty, but we are hopeful that it may provide a necessary connection between the bulk synthesis of solution-synthesized GNR polymer precursors and the device fabrication.

In summary, this section outlines the progress toward core-substituted GNR based on 7-AGNR scaffold. Three types of precursors that constructively utilize the discovered surface-induced C–N bond formation are proposed, and their synthesis is reported. A laterally extended (**72**, **66**) and longtitdinally extended (**67**) precursors have been synthesized and fully characterized, and those await the surface studies as the group instrument schedule permits. A first pass at the synthesis of the solution-synthesized N-7-AGNR precursor polymers is performed, and it is found that the oligomerization proceeds as expected and the polymer quality is suitable for an experiment on the Au(111) surface in UHV. These polymer samples are ready to go for the DCT studies which are expected resume promptly as the COVID-19 public health advisory restrictions are lifted.

2.4.3 12N-7-AGNR preliminary studies

The synthetic route toward **56**, the precursor for 12N-7-AGNR has been pursued as well, and the synthetic route toward the precursor is summarized in Scheme 25. **60** is used again as the building block, and Yamamoto homocoupling conditions were applied. The purification of **56** was extremely arduous, and the compound could only be isolated via preparatory TLC (Figure 23a). Addition of bipyridine as a ligand for the coupling leads to detection of oligomers in MALDI mass spectrum, which makes separation more difficult. Thus, the conditions where 0.5 equiv of $Ni(COD)_2$ are used to limit the oligomerization and attempt to isolate the dimer unit while taking a hit in yield. Only 1.0 mg total of **56** could be isolated as a yellow film by the way of multiple prep TLC plates followed by cold EtOAc rinses to to remove trace **59**, trace of which always was detected in the spot (ii).

The precursor **56** was then deposited onto Au(111) held at 24 °C for initial studies. As seen in Figure 23b and Figure 23c, the molecular features that correspond to a desired monomer can be observed, and it appears similar to that of DBBA which is structurally similar to **56** and is expected to adopt a similar cruciform adsorption geometry. Unfortunately, further annealing to 200 °C only yielded clean surfaces (n=3) and at no time were any polymeric structures observed via STM topographic imaging. At this stage due to difficulty in obtaining large amounts of **56** and lack of conviction in the polymerization, this research direction was not explored further.

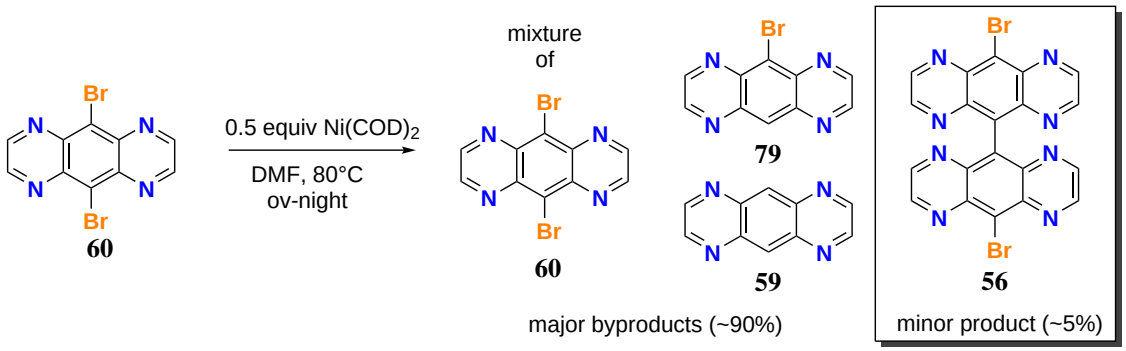

Scheme 25: Synthetic access to **56** via Yamamoto coupling

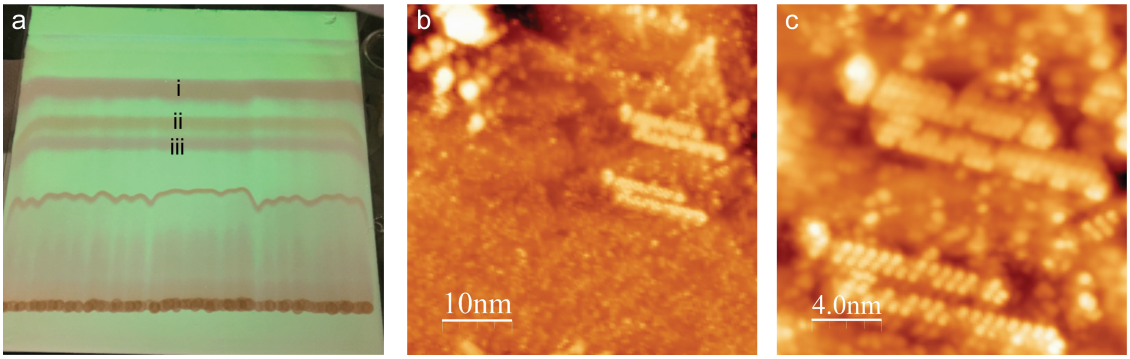

Figure 23: Purification of **56** and surface deposition results. (a) Prep TLC of the Yamamoto coupling reaction (eluent is 100% EtOAc). (i) is **79**, (ii) is desired product **56**, (iii) is **59**. (b) 50x50 nm scan window of deposition of **56** on Au(111). (c) 20x20 nm window zoom-in on (b).

3 Nitrogen edge substitution in zigzag graphene nanoribbons

This chapter focuses on improving synthetic access to the zigzag family of graphene nanoribbons (ZGNRs). These nanoribbons are quite different from previously discussed armchair- and chevron-edge GNRs, as the ZGNR possess intricate spin properties that are associated with the extended ferromagnetically aligned states along the edge of the ribbon.

So far, only one method of preparing pristine ZGNR is reported in the literature (6-ZGNR), and herein I describe our advances toward nitrogen-substituted N-6-ZGNRs, which are contrived in order to investigate the nature of heteroatom doping in ZGNRs. Synthetic routes toward the surface-ready precursors and surface characterization of N-6-ZGNR and 2N-6-ZGNR are disclosed, both of which were accomplished via a variation of a dibenzodihydroacridine synthesis. An initial study toward a solution-synthesized hybrid cove-zigzag GNR (N-czGNR) based on the similar acridine scaffold is also described. Full monomer synthesis, polymerization and cyclodehydrogenation conditions are described, and the nanoribbon's quality is ascertained by Raman and IR spectroscopy. Post-graphitization modification of the N-czGNR via the acridine moiety is successfuly accomplished.

3.1 All-carbon ZGNRs - inspiration, theory, and precedent

The edge structure of a graphene nanoribbon is paramount to the electronic and chemical properties of the material. Zigzag-edge graphene nanoribbons (ZGNRs) are a distinct class of GNRs that are predicted to have unique spin-polarized edge electronic states. The edge states of the ZGNRs are predicted to couple ferromagnetically along the edge, and antiferromagnetically between the edges.[100] These properties can be utilized in spintronic applications, where spins of the extended system can be manipulated in order to perform logic operations.[101] These electronic states in graphene and other low-dimensional materials have been receiving a considerable amount of attention.[16]

The width-dependent bandgap engineering in ZGNRs was postulated by Son *et al*.[34] The calculated band structure and the contour map of 12-ZGNR (12 zigzag rows, different nomenclature than in AGNRs) exemplify the unique electronic structure of the ZGNRs (Figure 24). The two edge-localized states are indeed ferromagnetically coupled along the edge, and antiferromagnetically coupled across the ribbon. The bandgaps of ZGNR are smaller compared to that of an AGNR of the similar width (Figure 3), which further motivates the foray toward experimental confirmation of these predictions by the community.

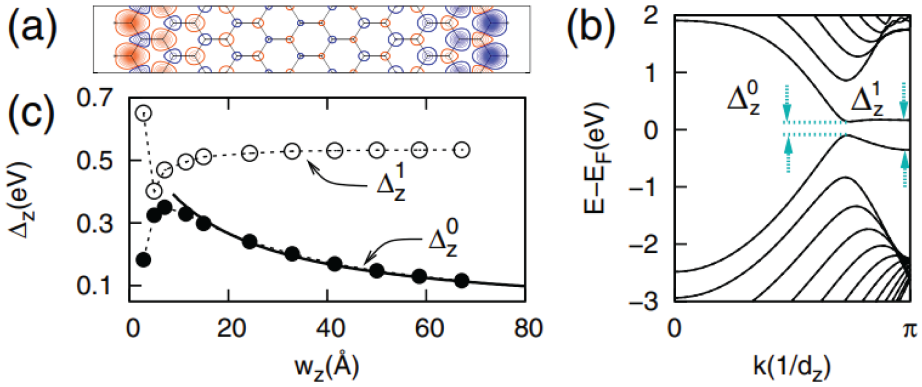

Figure 24: (a) Contour graph for a 12-ZGNR showing ground state spatial spin distribution on opposite sides of the ribbon. (b) The band structure of a 12-ZGNR. (c) The variation of the direct band gap and the energy splitting at $k(1/d_z) = \pi$ as function of the width of ZGNRs. Figure reproduced from reference [34].

The electronic properties of ZGNR come at the price of kinetic instability. Prior to resurgence of the GNR field, extended acenes (in principle, an extended linear acene can be considered as a 2-ZGNRs) were a focus of many synthetic chemists due to their spin-related properties such as singlet-to-triplet transition and partial (or full) radical character. A classical study on acenes by Biermann and Schmidt showed that the elongation of the ring system leads to increased reactivity toward a Diels-Alder reaction with maleimide.[102] More recent studies on pentacene,[103] teranthene,[104] quateranthene,[105] and hexacene[106] have noted the instability of acenes toward ambient conditions (light, oxygen). Therefore there is an expectation that authentic ZGNRs are expected to exhibit a high degree of reactivity toward of atmospheric oxygen and moisture. Our group reported in 2015 that *peri*-pentacene,[107] a small molecule fragment of 4-ZGNR, can be reliably sythesized and characterized on Au(111).[107] Thus bottom-up metal surface-mediated synthesis in UHV conditions thus

has been singled out as the most promising route to an authentic sample of a pristine ZGNR.

The synthetic access to the first example of ZGNR revitalized the community's perspective on the ZGNRs in terms of their accessibility. In 2016, Ruffieux *et al*. has reported a 14-step total synthesis of the monomeric U-shaped precursor **80** (Scheme 26) toward the 6-ZGNR.[50] The experimental results of the ribbon growth were extremely encouraging, as the surface reaction has readily furnished the desired 6-ZGNR (Figure 25a-c). Spectroscopic characterization of the 6-ZGNR on a NaCl island has confirmed the existence of edge-localized states with large energy splittings. It was determined that the electronic structure of the zigzag edge is extremely sensitive to the interaction with the supporting substrate, as no evidence of the zigzag edge states was observed on bare Au(111) substrate.

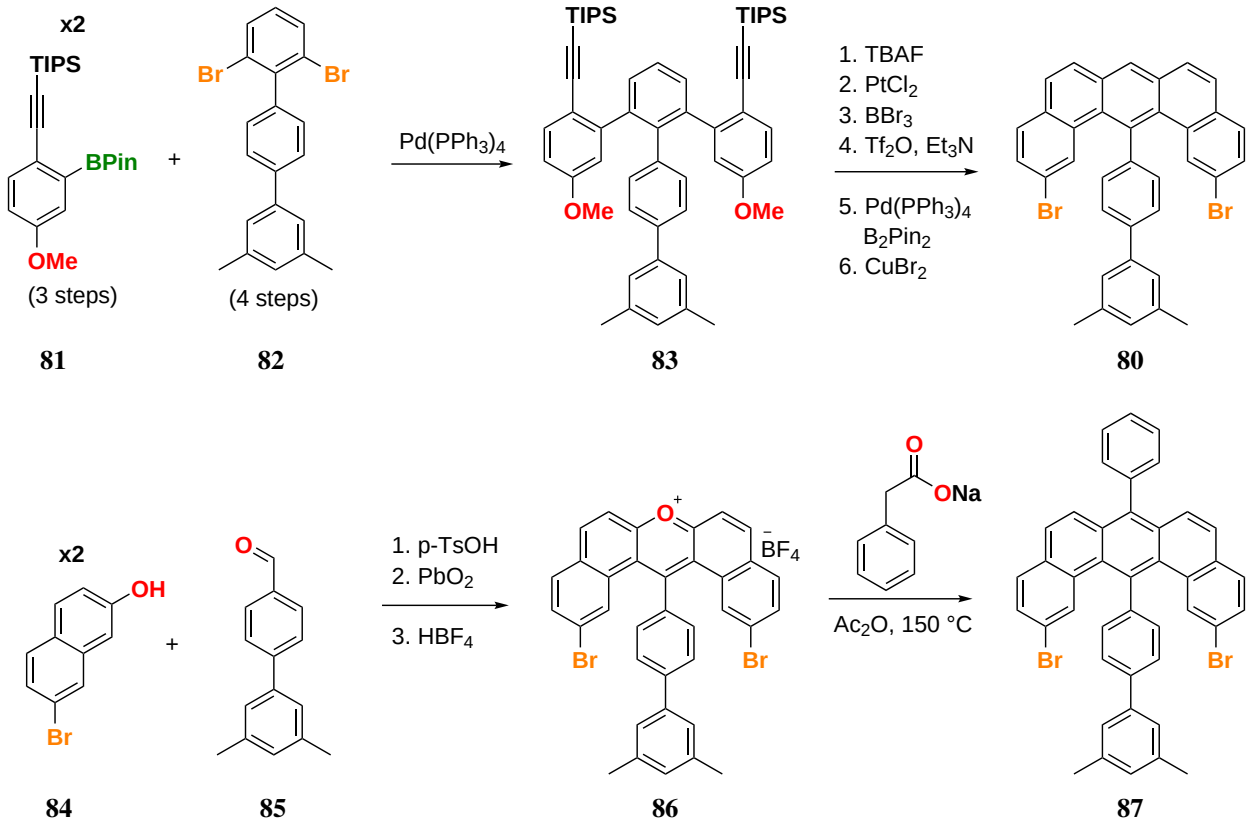

Scheme 26: Summary and contrast of synthetic approach toward pristine 6-ZGNR and phenyl-functionalized 6-ZGNR monomeric precursors.

The ZGNR precursor synthesis itself was a formidable achievement that is certainly worth mentioning – an abbreviated version of the original synthesis is described in Scheme 26. The key transformation that allows the assembly of such complex structure is the double Suzuki coupling to assemble the core of the molecule from **81** and **82** to obtain **83**. From **83**, the 6-ZGNR precursor can be obtained in 6 linear steps–TIPS deprotection followed by $PtCl_2$-mediated cyclization furnishes final carbon skeleton with two methoxy groups as placeholders for the halogenation site, and last four synthetic steps transform the methoxy groups into the desired halogen functionality.

In addition to the pristine 6-ZGNR synthesis, the synthesis of a phenyl-substituted 6-ZGNR is also reported (Scheme 26) in the same work. The concise strategy toward phenylated monomer **87**

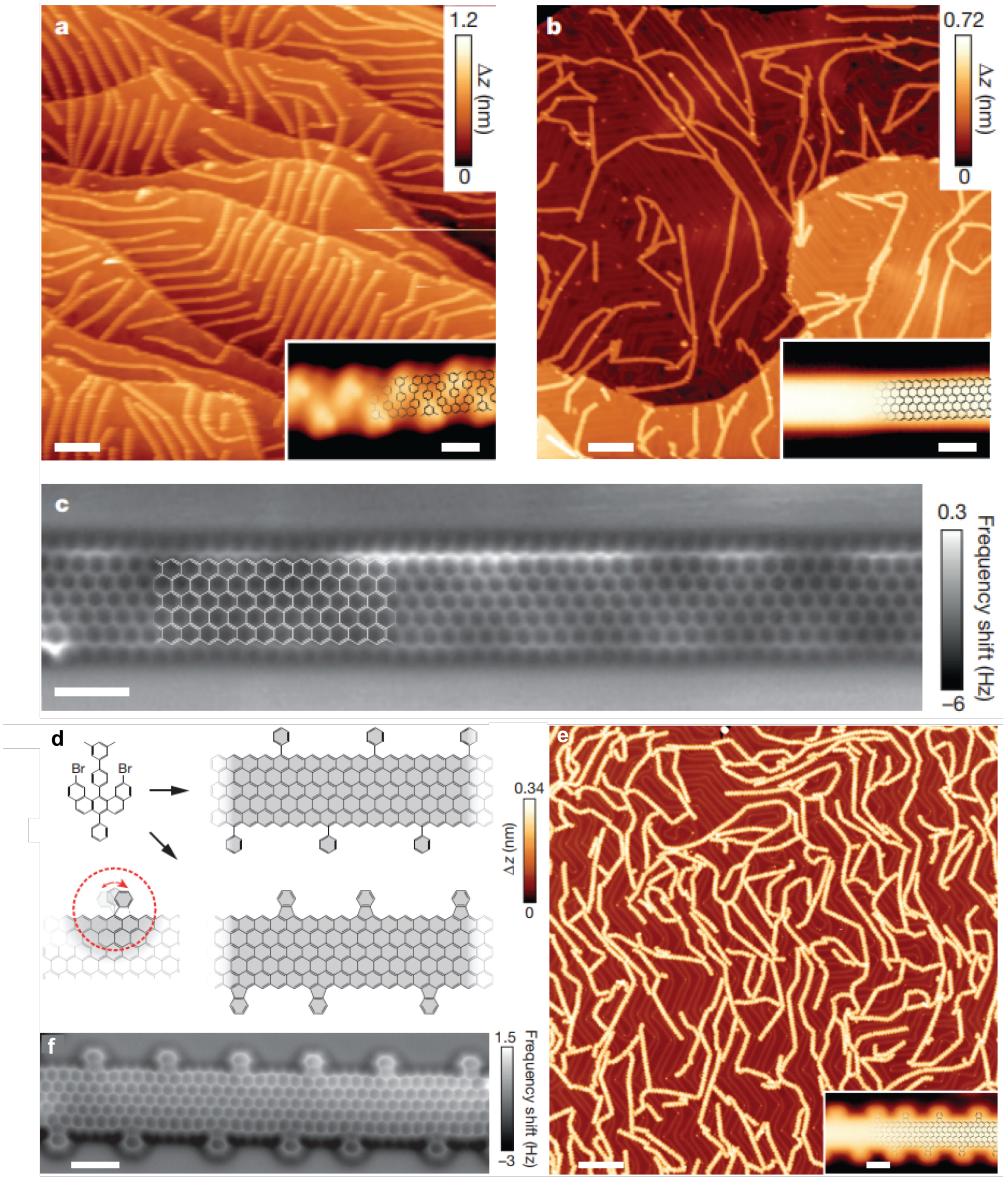

Figure 25: Summary of the on-surface synthesis results for pristine 6-ZGNR and phenylated 6-ZGNR, adapted from reference [50]. (a) 6-ZGNR precursor polymer and (b) Low coverage of 6-ZGNR on Au(111) surface (scale bar = 20 nm, inset scale bar = 1 nm). (c) nc-AFM image of the defect-free 6-ZGNR, overlaid with a ChemDraw structure, which substantiates that the cyclodehydrogenation step yields a fully planar ribbon (scale bar = 1 nm). (d) A scheme of phenyl-substituted 6-ZGNR monomer-to-GNR transformation which emphasizes the non-regioregular fluoranthene defect. (e) Overview of the phenylated 6-ZGNR with a zoom-in on a representative ribbon (scale bar = 20 nm, inset scale bar = 1 nm). (f) AFM image of defect-free phenylated 6-ZGNR, which proves the fluorathene formation (scale bar = 1 nm).

is in stark contrast to the long linear synthesis of pristine monomer **80**–this approach relies on the pyrilium salt chemistry, which drastically shortens the synthesis (5 total steps for **87** vs. 14 total steps for **80**). In this case, a substituted xanthene condensation method is employed to assemble the monomer core from a simple bromonaphthol **84** and the *m*-xylyl-functionalized benzaldehyde **85**, which is further oxidized with PbO_2 and dehydrated with HBF_4 to achieve the dinaphthopyrillium salt **86**. The pyrillium salt can then be subjected to a condensation with sodium phenylacetate[108,109] to obtain the final phenyl-substituted monomer **87**.

The original rationale behind including the phenyl substitution on the edge was to laterally separate the ribbons without any additional reactivity, and potentially decouple them from the surface by steric hindrance. However, it was found that the phenyl ring can undergo a ring closure (Figure 25d) to form non-regioregular flouranthene units along the edge. Breaking up the continuity of the zigzag edge with these defects was beneficial in observing the increased intensity along the zigzag edges in the STS on bare Au(111), but the lack of regioregularity of this closure might be an issue going toward atomically precise structures with fully reproducible properties.

3.2 Introducing nitrogen substitution in 6-ZGNR scaffold

Working along my interest in introducing heteroatoms in the GNR, the zizgag scaffold is a high-value target as the Fasel report stands as the sole report of a bottom-up synthesized pristine ZGNR. We have considered edge substitution of some of the carbon atoms with nitrogen atoms in hopes of improving physical and electronic properties in the resulting GNR: (1) breaking up the spin chains on the reactive zigzag edges, (2) introducing the electronegative atom effect to lower the overall energy of the VB/CB bands (similar to previous work in chevron GNRs[77]), and (3) enabling a simpler synthetic route.

Replacement of every sixth C–H group along the zigzag edge of a 6-ZGNR (a zigzag GNR featuring 6 lines of carbon atoms across the width of the ribbon) by a nitrogen atom leads to the structure of the N-6-ZGNR depicted in Figure 26. In this thought experiment, the superlattice of N-atoms confines the extended zigzag edge state to shorter segments reminiscent of the zigzag edge of pentacene — one of the largest chemically persistent unsubstituted acenes. The key to retaining the most exciting magnetic phenomena emerging from the spatially separated spin-ordered edge states however, is the isoelectronic structure of the trigonal planar N-atom dopants. Each N-atom contributes the same number of electrons (a single electron in a half-filled p_z-orbital) to the extended π-system of the N-6-ZGNR as the trigonal planar C–H groups they replace. We can therefore confidently expect that the magnetic edge states will be largely retained while the subtle localization of frontier orbitals imposed by a superlattice of electronegative dopant atoms should lead to a passivation of the reactive zigzag edge. Similarly, a 2N-6-ZGNR can be envisioned, where every third carbon atom is replaced with nitrogen.

The computational analysis of pristine 6-ZGNR, N-6-ZGNR, and 2N-6-ZGNR has been performed by Dr. Yea-Lee Lee and Fangzhou Zhao (S. Louie group, Dept. of Physics, UC Berkeley) and is shown in Figure 26. The previously postulated correlation of lowering the overall Fermi energy level of the ribbon as edge nitrogen content is increased is confirmed by DFT-LDA calculations.

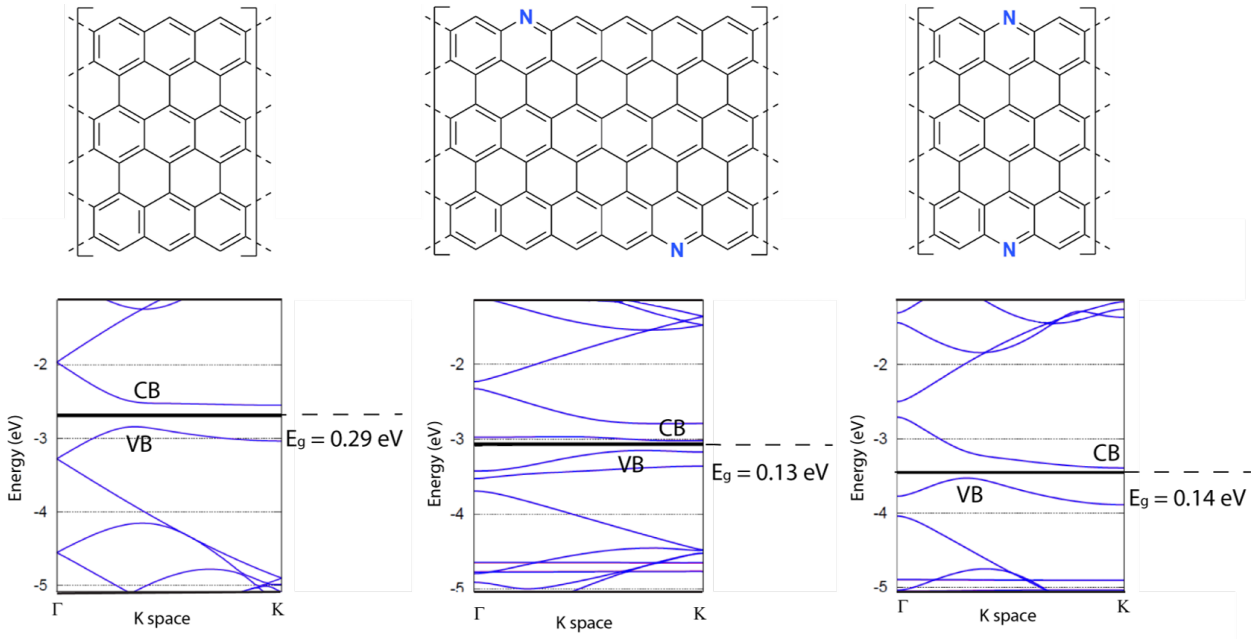

Figure 26: Comparison of energy levels of the N–ZGNRs and the pristine ZGNR by DFT-level calculations. The energy diagrams are aligned at the vacuum level, and the solid black line denotes the Fermi level in the system. It is evident that increased electronegative nitrogen doping systematically lowers the Fermi level energy of the GNRs, which should correspond to a decrease in their reactivity toward oxidative degradation.

Hypothesis Introduction of nitrogen along the edge of the ZGNR would provide multiple benefits–(1) local disruption of bipartite lattice that will lead to a possibility of spin center generation and increased edge state intensity, (2) passivation of the edge which might make the ribbon less reactive to ambient conditions (oxygen, moisture, etc), and (3) simplfied and easily diversifiable synthesis.

3.2.1 Precursor synthesis and surface-induced growth toward N-6-ZGNR

The synthetic route to the N-6-ZGNR is outlined in Scheme 27. An aldehyde wing **85** is assembled via Suzuki cross-coupling of a 4-formylphenylboronic acid and 1-bromo-3,5-dimethylbenzene. Then two other condensation partners are procured–**84** can either be purchased or prepared on large scale from 2,7-dihydroxynaphthalene, and **88** is prepared from **84** via Bucherer reaction with benzyl amine in excellent yield. Three synthons **84**, **88**, **85** are combined in refluxing glacial acetic acid, and condensation product **89** can be isolated in 25% overall yield on ∼1g scale of starting materials. With **89** in hand, conditions that selectively deprotect the benzylamine group without disturbing the aryl halide functionality were investigated, with a transition metal-free condition of KOtBu/O_2/DMSO combination affording the best isolated yield of **90** of 50%.

Precursor **90** was deposited from a Knudsen cell evaporator under UHV onto a Au(111) surface held at 24 °C, which resulted in clean deposition. The formation of self-assembled monomer chains is observed (Figure 27b). Further annealing at 650 K induces a thermal cyclodehydrogenation

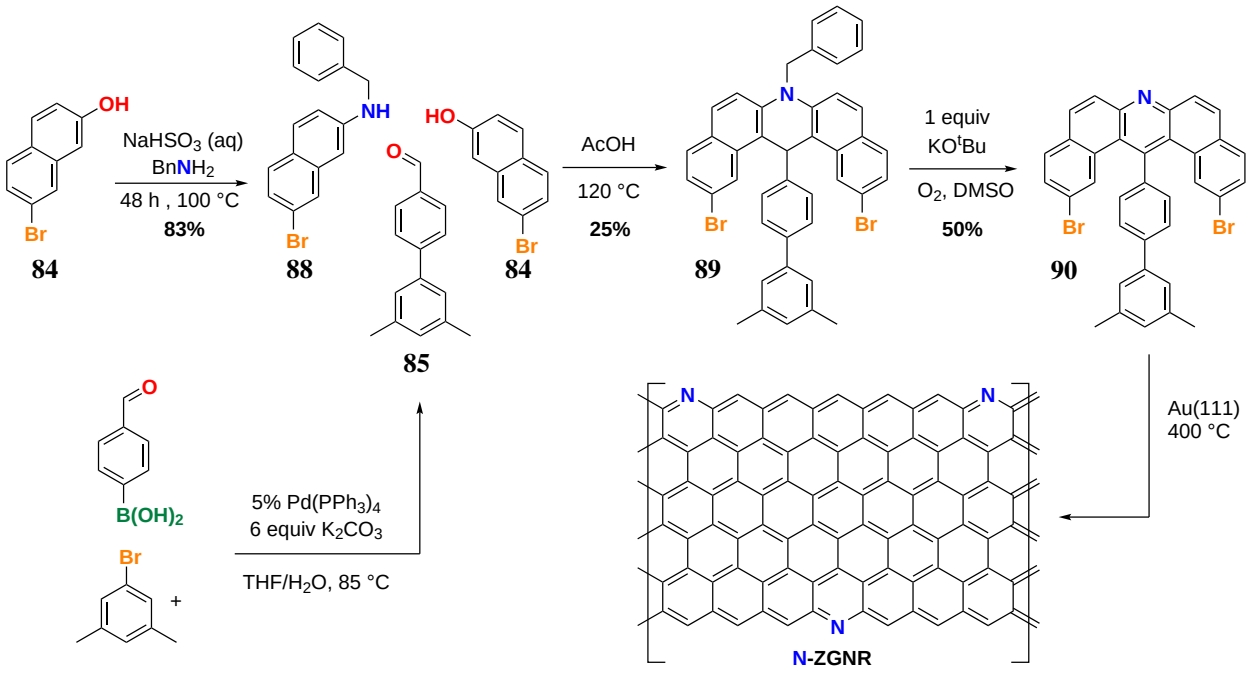

Scheme 27: Precursor synthesis of N-6-ZGNR brominated monomer **90**

that leads to the fully fused N-6-ZGNRs, depicted in Figure 27c. STM topographic images reveal extended GNRs featuring atomically smooth zigzag edges with an apparent height and width of 0.23 nm $\pm$ 0.03 nm and 1.95 nm $\pm$ 0.05 nm, respectively, consistent with the formation of the fully conjugated N-6-ZGNR backbone. Large-area SPM scans show the average length of N-6-ZGNRs ranges between 15–25 nm. High-resolution metal tip STM images (Figure 27d) of N-6-ZGNRs do not reveal characteristic topographic features that could hint at the position of nitrogen atoms along the edges of the ribbon. We attribute this observation to the strong electronic coupling between the edge state and the underlying Au(111) substate. A characteristic mousebite edge-defect, previously observed for all-carbon 6-ZGNRs, is used to infer the exact position of nitrogen atoms along the edges on N-6-ZGNRs. The excision defect emerges from the homolytic cleavage of a biphenyl C–C bond during the thermal cyclodehydrogenation step and results in a unique concave indentation along the zigzag edge of the GNR associated with the loss of a m-xylene group (see inset Figure 27d). Based on the chemical structure of the molecular building block **90** we can infer the position of a nitrogen dopant atom to be precisely at the opposing zigzag edge perpendicular across the ribbon from the defect site.

3.2.2 Topographic imaging of N-ZGNR: decoupling protocol leads to BRSTM

Topographic and bond-resolved scanning tunneling microscopy (BRSTM) images utilizing CO-functionalized STM tips were recorded on a fully cyclized segment of N-6-ZGNR featuring the same m-xylene deletion defect (BRSTM images were acquired by recording the out-of-phase component of constant-height dI/dV maps at zero tip-sample bias). While the topographic STM image (Figure 28a) resolves the zigzag edge structure of N-6-ZGNRs and hints at a superlattice associated with the position of substitutional nitrogen dopants, the BRSTM image (Figure 28b) clearly shows a unique alternating pattern of five bright lobes protruding from the edge of the N-6-ZGNRs.

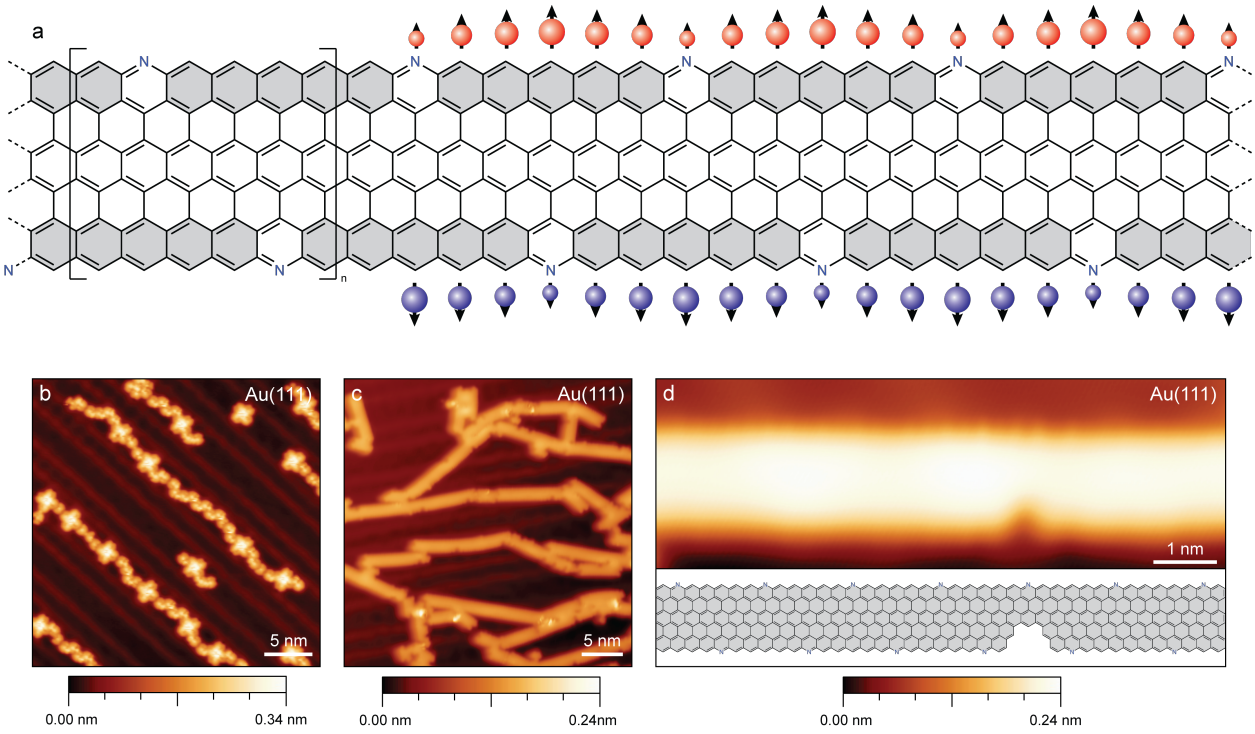

Figure 27: (a) Schematic representation of spin-ordered edge states in N-6-ZGNRs. The substitutional doping pattern along the edges of N-6-ZGNRs replaces every sixth C–H group with a nitrogen atom confining the spin-ordered edge stats to shorter localized segments reminiscent of pentacene units. (b) Deposition of **90** on Au(111) surface held at 24 °C. (c) A representative image of the surface after annealing to 350 °C. Multiple long ribbons can be observed. (d) A STM topographic image on a single ribbon with a metal STM tip. A small mousebite defect is observed, likely due to the cleavage of the *m*-xylene fragment.

These lobes are flanked on either side by apparent indentations of darker contrast. Most notably the pattern on one zigzag edge of the nanoribbon is offset by half of a period from the opposite edge and is superimposable with the position of nitrogen atoms derived from the analysis of m-xylene deletion edge defects. The backbone of the ribbon remains featureless and BRSTM imaging does not resolve any of the C–C bonds that constitute the central core of N-6-ZGNRs. The enhanced signal in zero-bias dI/dV imaging suggests a strong hybridization of the up-shifted Au(111) surface state with the low-lying magnetic edge state of the ribbon. dI/dV point spectra recorded along the edges of N-6-ZGNRs show only a broad featureless local density of states (LDOS) that cannot be assigned to discrete valence band (VB) and conduction band (CB) edge states (Figure 29a, as grown).

As we have pursued the dI/dV mapping of the N-6-ZGNR, we have serendipitously discovered a decoupling event that irreversibly disrupts the strong hybridization of the N-6-ZGNR from the underlying Au(111) surface. When placing an STM tip above the center of the GNR (position marked with a red cross in Figure 28a), shutting off the feedback loop and ramping up the bias voltage from V_s = 0.00 V to V_s = +2.50 V, a discontinuous drop (ΔI_t^+ = 0.16 nA) in the tunneling current can be observed at a bias of V_s = +2.23 $\pm$ 0.05 V (Figure 28e). The abrupt shift in the tunneling current is suggestive of an electronic decoupling of the GNR from the Au(111) substrate. Subsequent bias sweeps ranging from V_s = –2.50 V to +2.50 V near the position of the red cross yield no further change in the tunneling current, and the decoupling event therefore is assumed to be irreversible. STM imaging of the same N-6-ZGNR segment following SPM tip-induced decoupling reveals a local change in the constant-height dI/dV map (Figure 28c).

The immediate area of the ribbon surrounding the position of the STM tip during the decoupling step (1–2 nm surrounding the position of the red cross) is clearly resolved and shows the distinctive structure of the N-6-ZGNR backbone as well as the characteristic pattern of N-atoms along both zigzag edges (see arrows in Figure 28c; nitrogen atoms appear with a darker contrast when compared to the C–H groups). The same irreversible decoupling event can be observed by applying a negative bias. Moving the STM tip to the position marked with a blue cross in Figure 2a, shutting off the feedback loop and ramping the bias voltage from V_s = 0.00 V to V_s = –2.50 V, reveals a comparable drop in the tunneling current at V_s^- = –2.16 $\pm$ 0.05 V (ΔI_t^- = 0.15 nA). The resulting BRSTM images (Figure 28d) show the bond resolved structure of the N-6-ZGNR backbone along the entire length of the ribbon.

3.2.3 Electronic structure of N-ZGNR: experimental results

The local electronic structure of surface-decoupled N-6-ZGNRs was characterized using dI/dV point spectroscopy as shown in Figure 29a. All spectra were collected after calibrating a CO-functionalized STM tip to the Au(111) Shockley surface state. dI/dV spectra recorded along the edge of a N-6-ZGNRs (post-decopuling) show two reproducible electronic states, a sharp peak centered at V_s = –0.30 $\pm$ 0.03 V and a broader feature centered at V_s = +0.50 $\pm$ 0.03 V, relative to the Fermi energy (V_s = 0.0 V). The peak at –0.30 V is identified as the N-6-ZGNR valence band (VB) edge, while the peak at +0.50 V corresponds to the conduction band (CB) edge. The resulting bandgap for a nitrogen edge-doped N-6-ZGNRs is ΔE_{exp} = 0.80 $\pm$ 0.05 eV, smaller than the experimental bandgap of the parent all-carbon 6-ZGNRs (ΔE = 1.5 eV). The introduction of N-atom edge-dopants in to 6-ZGNRs leads to a shift of the CB edge to lower energy resulting in an overall reduction of the bandgap by $\sim$0.7 eV compared to that of the pristine 6-ZGNR.

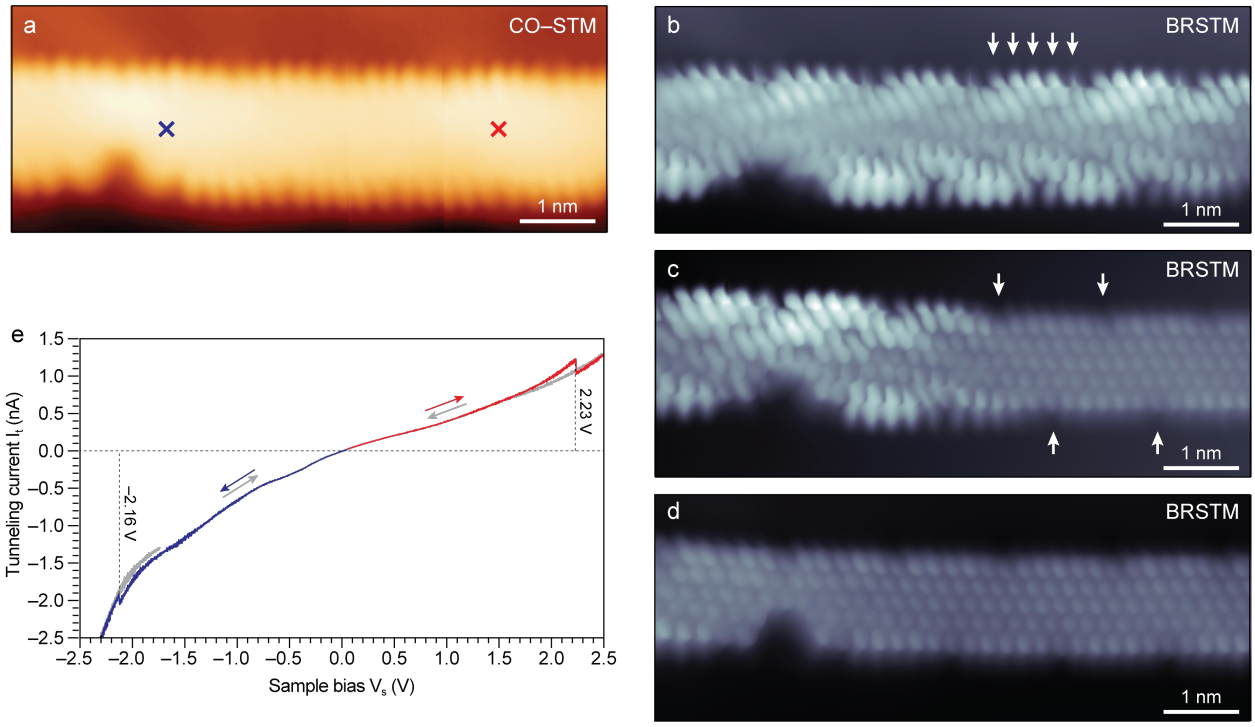

Figure 28: Tip induced decoupling of magnetic edge states in N-6-ZGNRs. (a) Topographic image of a fully cyclized N-6-ZGNR segment recorded with CO-functionalized STM tip. Red and blue crosses mark the position of the STM tip during the tip induced decoupling procedure. (b) Constant-height BRSTM image of the same N-6-ZGNR segment as in (a). Arrows mark the position of the five lobes associated with the C–H groups along the edges of the N-6-ZGNR. The pattern is offset by 0.5 period from one edge to the other (V_s = 0 mV, V_{ac} = 11 mV, f = 455 Hz). (c) Constant-height BRSTM image of the same N-6-ZGNR segment as in (a) following tip induced decoupling using a positive voltage sweep from V_s = 0.0 V to V_s = 2.5 V at the position marked by the red cross (V_s = 0 mV, V_{ac} = 11 mV, f = 455 Hz). (d) BRSTM image of the same N-6-ZGNR segment as in (a) following tip induced decoupling using a negative voltage sweep from V_s = 0.0 V to V_s = –2.5 V at the position marked by the blue cross (V_s = 0 mV, V_{ac} = 11 mV, f = 455 Hz). Arrows mark the position of selected N-atom along the edge of the N-6-ZGNR. (e) I_t vs. V_s plot showing the positive (red) and negative (blue) voltage sweeps used during the decoupling procedure. The respective return sweeps are depicted in gray and show the shift in the tunneling current I_t to be irreversible. All STM data obtained at T = 4 K.

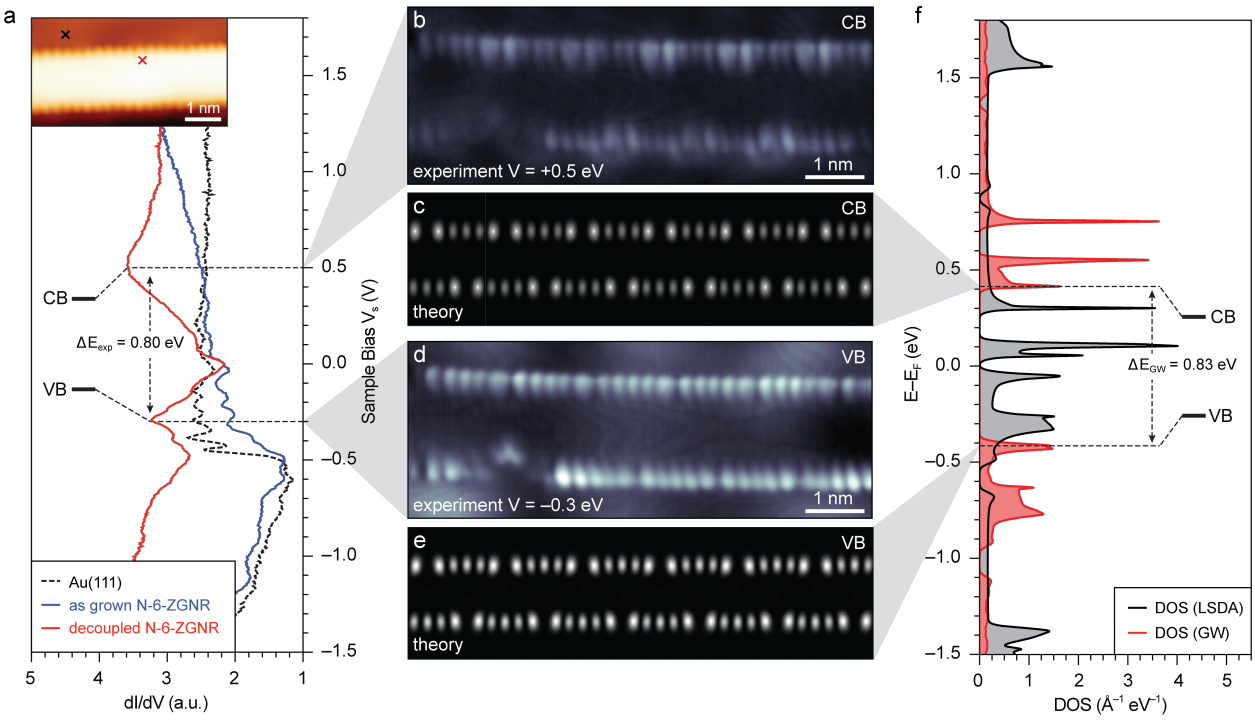

Figure 29: (a) STS results on the N-6-ZGNR sample. Lowest trace: bare Au surface, middle trace: STS point spectra at the cross location over the ribbon prior to surface decoupling, top trace: STS point spectra at the cross location over the ribbon after surface decoupling. (b)-(e) dI/dV mapping of states dected in STS. (f) GW-level calculation of the band structure of N-6-ZGNR.

The spatial distribution of the N-6-ZGNR local density of states (LDOS) at energies close to the CB and VB edges was experimentally determined by recording constant-current dI/dV maps at V_s = +0.50 V and V_s = –0.30 V, respectively (Figure 29b,d). At an imaging bias of +0.50 V, the LDOS associated with the CB edge shows the largest contrast along the zigzag edge C–H groups immediately flanking the position of N-atom dopants while the intensity decreases toward the N-6-ZGNR backbone. dI/dV maps recorded at an imaging bias of –0.30 V reveal the LDOS associated with the VB state evenly distributed over the C–H groups lining the zigzag edges. Both dI/dV maps of the CB and VB edges show a weaker contrast at the position of the N-atom dopants suggestive of a segmentation of the magnetic edge state into a superlattice of pentacene-like fragments. This lateral confinement of VB and CB states along the zigzag edge of N-6-ZGNRs is further corroborated by the independent interaction of isolated zigzag edges with the Au(111) surface state observed as part of the highly localized tip induced decoupling.

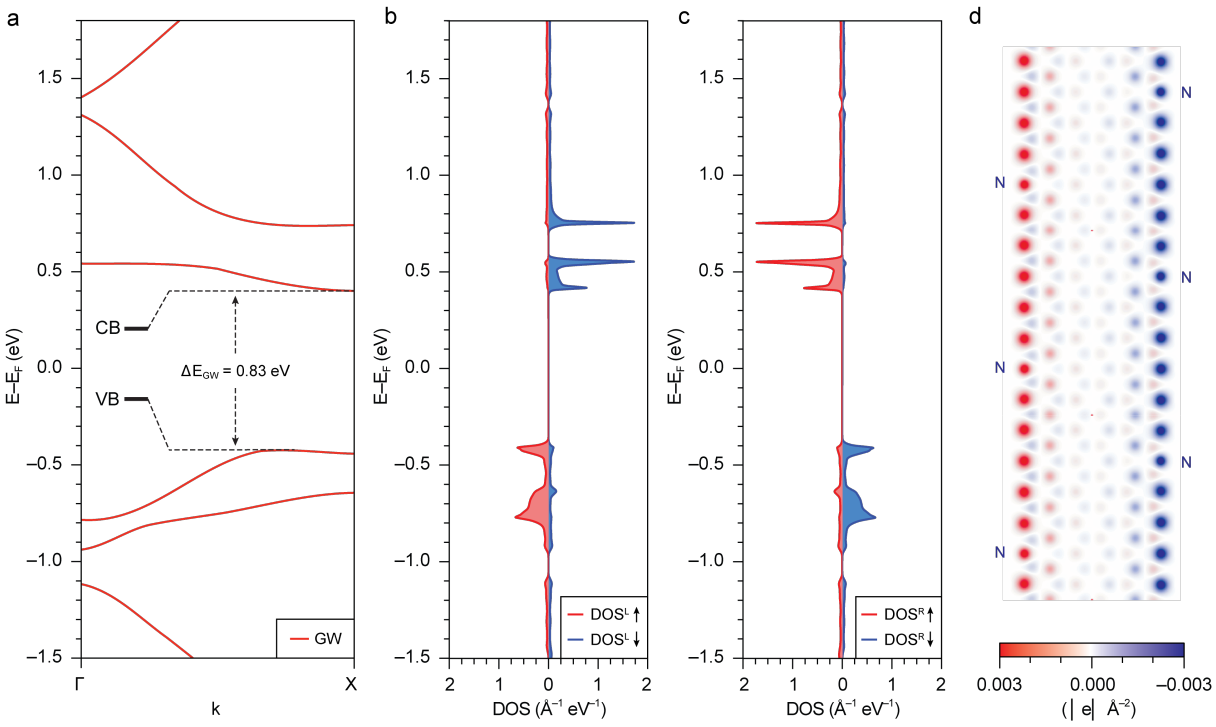

Figure 30: Band structure and spatial distribution of spin-ordered edge states in N-6-ZGNRs. (a) The GW band structure of a freestanding N-6-ZGNR. (b) The LDOS of up (red line) and down (blue line) spin on the left half of a N-6-ZGNR at GW level. (c) The LDOS of up (red line) and down (blue line) spin on the right half of a N-6-ZGNR. (d) The spatial distribution of the charge difference between up spin and down spin for the ground state. The density is integrated in the direction out of the GNR plane.

3.2.4 Electronic structure of N-ZGNR: GW-level theory

Our experimental results are in excellent agreement with theoretical simulations based on ab initio pseudopotential density functional theory (DFT) within the local spin density approximation (LSDA),[110] and the GW calculation[93] which includes quasiparticle self-energy corrections to the LSDA Kohn-Sham energy eigenvalues. This provides further evidence that the SPM tip-induced decoupling has resulted in a full recovery of the intrinsic magnetic edge states of N-6-ZGNRs. Figure 29c and Figure 29e show the theoretical LDOS map at a distance of 4 Å above the plane of the N-6-ZGNR at energies corresponding to CB and VB edges. The characteristic pattern and relative contrast of protrusions lining the zigzag edges of N-6-ZGNRs seen in the experimental dI/dV maps of CB and VB states (Figure 29b,d) are faithfully reproduced in the corresponding LDOS maps (Figure 29c,e). This agreement between theory and experiment further corroborates the assignment of the peaks at V_s = +0.50 V and V_s = –0.30 V to the magnetic CB and VB edge states. The DFT band gap of the freestanding N-6-ZGNR is $\delta = E_{DFT}$ = 0.23 eV, while the quasiparticle band gap calculated by GW approximation is increased to $\delta = E_{GW}$ = 0.83 eV, showing large self-energy corrections. The GW quasiparticle band structure and the corresponding density of states (DOS) are shown in Figure 30a and Figure 29f, respectively. The qualitative agreement between experimental dI/dV maps and projections of the theoretically predicted LDOS, in conjunction with the quantitative match between the experimental and the quasiparticle GW bandgap, confirms that the tip-induced electronic decoupling of N-6-ZGNRs greatly reduces the effective screening from the underlying metallic Au(111) substrate. While this represents an interesting and potentially useful strategy to stabilize and manipulate the exotic magnetic edge states in ZGNRs, the question remains whether the isoelectronic substitution of 1/6 of the C–H groups along the zigzag edge with N-atoms itself has had an undesired effect on the spin polarization.

Similar to the pristine ZGNRs, the N-6-ZGNR also exhibit edge states that are ferromagnetically ordered along one each edge but antiferromagnetically coupled between the two edges. That is, the total spin is zero. Because the isoelectronic substitution of the C–H groups along the zigzag edge with N-atoms does not change the occupation of the pz orbitals, the electronic structure within the π electron manifold remains similar, thus N-6-ZGNR exhibit similar behavior to the pristine 6-ZGNR. According to the DFT calculations, the top VB and bottom CB are all edge states that extended along the GNR long axis and decay exponentially toward the center of the ribbon. The band structure of N-6-ZGNR is similar to the folded band structure of pristine 6-ZGNR. The small dispersion of the top VB and bottom CB result from the flat bands of ZGNR near the Fermi energy, existing in about one-third of the Brillouin zone away from the zone center.[24,100] Our calculation shows that the configuration with equal density of different spin species on each edge has higher energy than the configuration with opposite spin (antiferromagnetic) between each ferromagnetically ordered edge. The total energy difference between the two configurations is 16 meV per edge atom, which shows quite large magnetic interaction energies. The antiferromagnetic spin configuration ground state is consistent with Lieb's theorem for electrons on a bipartite lattice.[111] To show the spatial distribution of different spin species, we plot the GW level LDOS of up and down spin integrated at the left and right half of the N-6-ZGNR, respectively. The bottom CB and top VB and a large portion of second CB and VB counting from the Fermi energy has uneven distribution of both spin species across the left and right edge. This suggests the possibility of accessing half-metallicity properties[112] by applying a transverse electric field in the GNR plane. The spatial distribution of the ground state magnetization is shown in Figure 30d. The magnetization on one N-atom amounts

to roughly 80% of the magnetization on a C-atom along the edge. We therefore conclude that the isoelectronic substitution of 1/6 of C–H groups with N-atoms, while leading to a chemical passivation of the zigzag edges, does not disrupt the intrinsic edge magnetization of the ZGNR.

3.3 2N-ZGNR: precursor synthesis and surface growth optimization

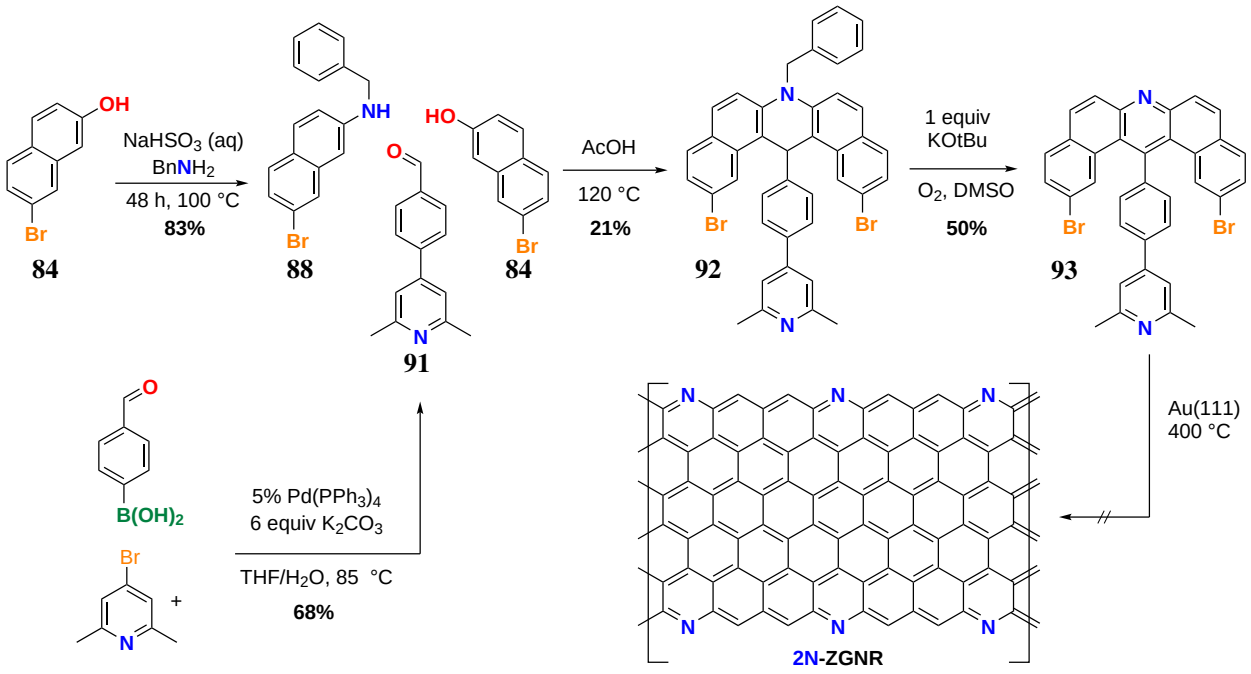

Scheme 28: Precursor synthesis of 2N-6-ZGNR brominated monomer **93**

An exciting attribute of the acridine synthetic route is that the central aldehyde wing can be exchanged for any substitution that is desired with high modularity. As a next logical step, we attempted to double the number of nitrogen atoms in the ZGNR by swapping out the xylylene wing for a lutidine wing, therefore introducing a nitrogen directly opposite the original acridinic nitrogen. The synthesis of the brominated monomer **93** for such a 2N-6-ZGNR is outlined in Scheme 28 – it is essentially identical to the synthesis of **90** with the difference in that the aldehyde synthon **91** in the three-component condensation now has a 2,6-lutidine wing rather than *m*-xylyl wing. Final precursor **93** can be obtained on a 100 mg scale with ease.

However, the growth of 2N-6-ZGNR did not proceed as smooth as that of the N-6-ZGNR from the brominated precursor. After multiple unsuccessful attempts to grow ribbons the brominated monomer **93** (Figure 31a,b show the most promising data), we have considered what limitations we are facing as compared to the N-6-ZGNR monomer that is described previously. The structure-reactivity difference will likely come from the newly incorporated lutidine wing, where we have to consider the possible bond breaking reactions at elevated temperatures. The bond dissociation energy (BDE) of Ar–Br bond is similar to the BDE of the C–H bond at the 2-methylpyrdine position (80 kcal/mol vs. 88 kcal/mol).[113] It is also likely that the lutidine lone pair will interact with the gold surface, and will be brought into closer proximity with the gold surface compared to that of the *m*-xylyl wing. This interaction can lower the energy barrier for the C–H cleavage. At this

junction, a preparation of the iodinated monomer **94** is a reasonable approach toward improving the on-surface polymerization, since the esimated BDE for a generic Ar–I bond is ~65 kcal/mol, which offers a somewhat larger temperature operation window for the polymerization *vs* deleterious processes hypothetically caused by methylpyridinic C–H bond cleavage.

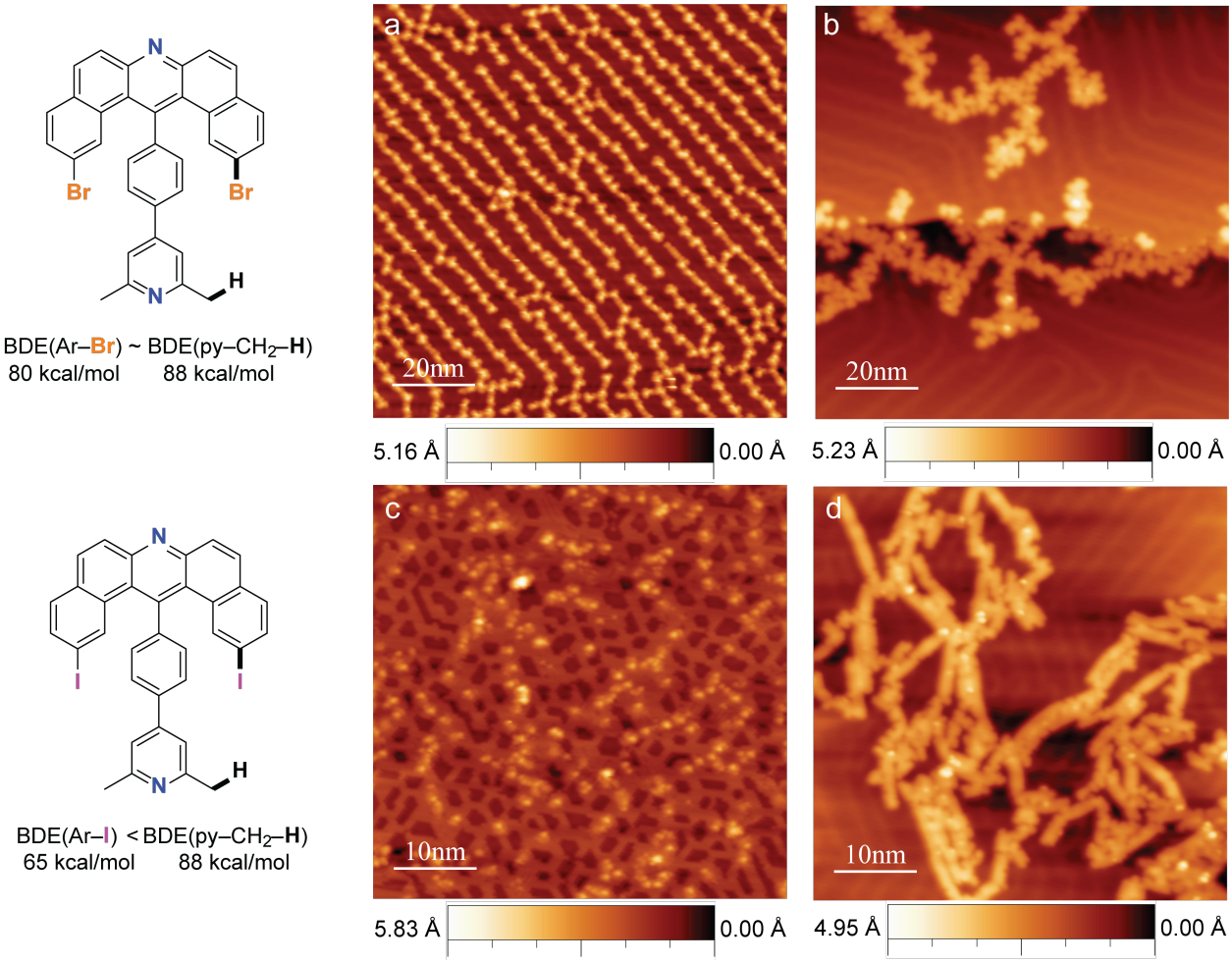

Figure 31: Attempts to grow 2N-6-ZGNR via brominated monomer **93** and iodinated monomer **94**. (a) Brominated monomer **93** as deposited. (b) Representative image of monomer **93** after annealing to 300 °C. Across multiple attempts the monomer does not appear to grow GNRs–only random dendritic structures are observed. (c) Iodinated monomer **94** as deposited – bright spots are the monomer which is sitting on top of some molecular iodine islands. (d) Representative image of monomer **94** after anneal to 300 °C. It is apparent that this monomer is capable of producing GNR growth, which still requires further optimization.

The halogenation functionality in this scaffold must be pre-installed at the outset of the synthesis (outlined in Scheme 29), which in this case relies on efficient scale-up of the 7-iodonaphth-2-ol **95**. Starting from 7-bromonaphth-2-ol **84**, the hydroxy group is protected by methylation with iodomethane to obtain **96**, and the halogen exchange is accomplished with lithium-halogen exchange / iodine quench. The methoxy group of **97** is then deprotected with BBr_3 in excellent yield (90% over 3 steps). The other synthons for the three-component condensation were also prepared

with ease: Bucherer reaction of **95** with benzyl amine affords **98**, and a general Suzuki coupling coditions were utilized to obtain the lutidine-functionalized benzaldehyde **91**. The condensation of **95**, **98**, and **91** in glacial acetic acid proceeded to give 35% yield of **99**, which was further oxidized to obtain the final monomer **94** in 25% yield.

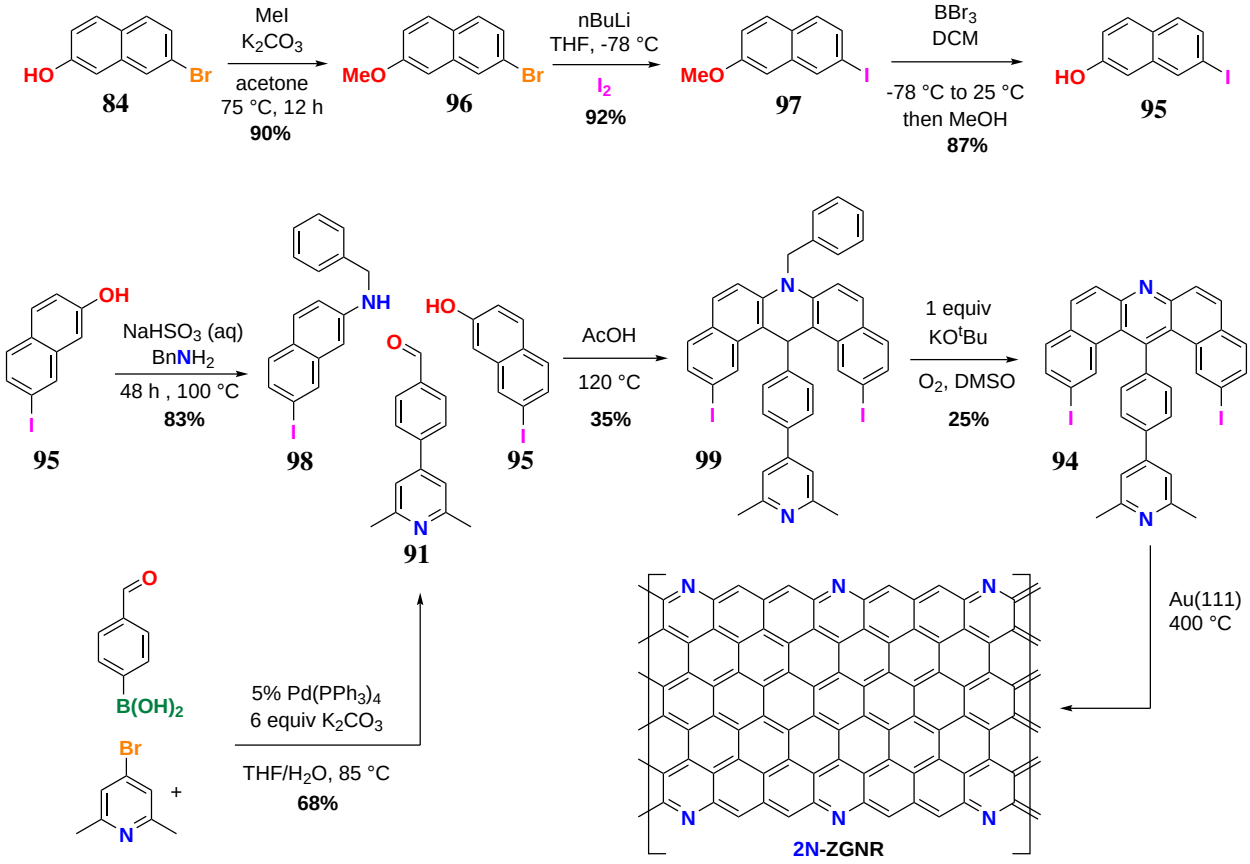

Scheme 29: Precursor synthesis of 2N-6-ZGNR iodinated monomer **94**

The preliminary results of the Au(111) surface reactivity studies of **93** and **94** are summarized in Figure 31. It is apparent that the brominated monomer **93** does not produce the desired GNRs, whereas iodinated monomer **94** does - one can observe a great deal of improvement in generating linear structures, as Figure 31b and Figure 31d show. The BDE-directed monomer design has proven fruitful in this case, which further improved our understanding of the limits of the surface-induced polymerization technique for GNR growth. Optimization of growth conditions (temperature ramp optimization, coverage variation) is underway in order to obtain better quality 2N-6-ZGNR for spectroscopic analysis and bond-resolved imaging.

3.4 Carrying the modular synthesis into solution - cove/zigzag hybrid GNRs

3.4.1 Solution-synthesized GNRs - advantages and drawbacks

The exceptional ease of diversification of the dihydroacridine synthesis invites the opportunity to apply it toward the solution-synthesized nanoribbons. The acridine moeity has multiple values in this scaffold: in addition to streamlining the synthetic access, the nitrogen atom can serve as a potential post-graphitization handle for the GNR modification. Scheme 30 summarizes the value of the dihydroacridine condensation as it is leveraged toward both surface-induced GNR growth and the solution sythesized GNRs.

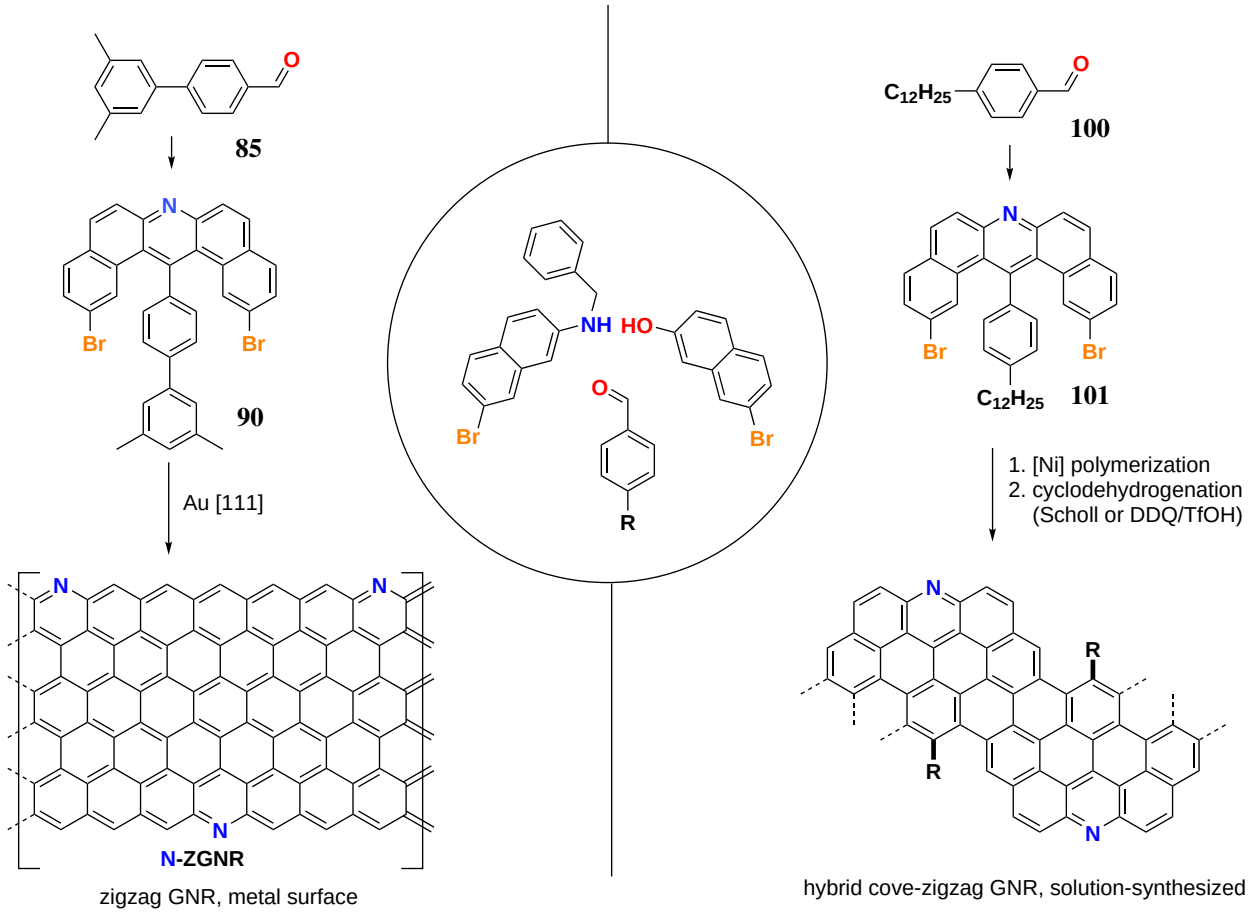

Scheme 30: The potential of the dihydroacridine three-component condensation toward access to both surface-synthesized and solution-synthesized GNRs.

Hypothesis The removal of the dimethylarene (as compared to the 6-ZGNR/N-ZGNR) will afford a new cove/zigzag hybrid N-GNR scaffold that can be prepared in solution and fully characterized via available solution methods. Both polar and non-polar solubilizing groups can be easily installed and carried through the synthesis. Post-graphitization modification of the scaffold is possible via acridinic nitrogen.

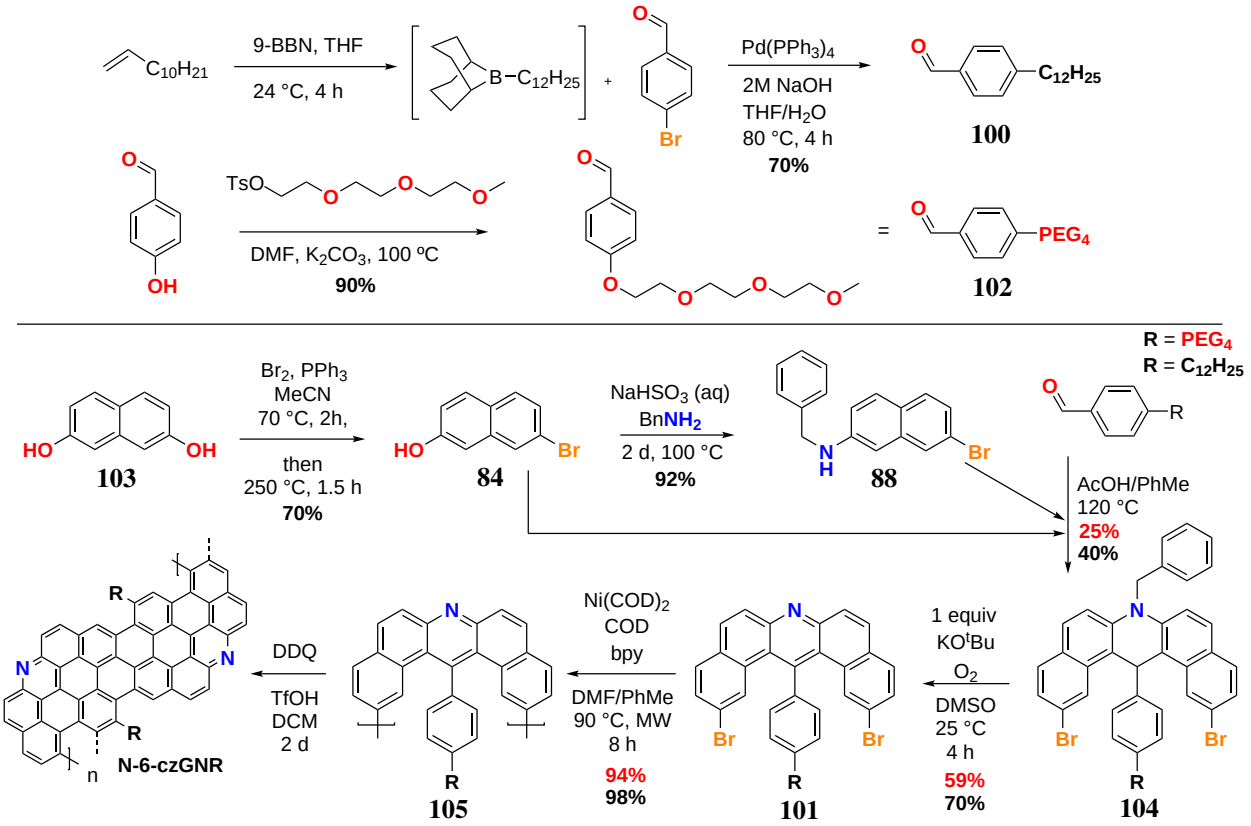

Scheme 31: Synthesis of hybrid cove-zigzag GNRs with varied solubilizing groups - alkyl and oligo-ethylene glycol side chains

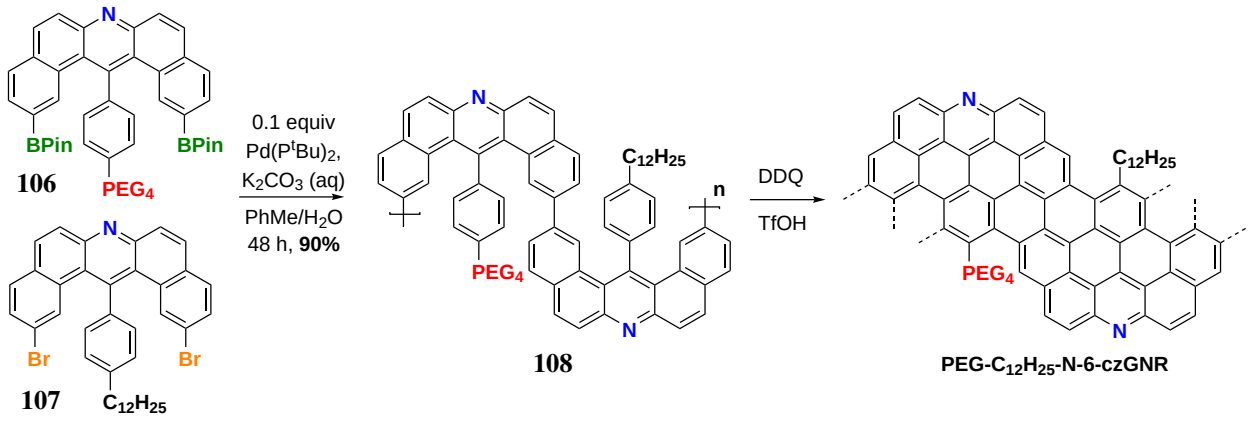

Scheme 32: Exercising control over the solubilizing group edge specificity via Suzuki polymerization - PEG-$C_{12}H_{25}$-N-6-czGNR

The full synthesis of the novel nitrogen-substituted cove/zigzag hybrid GNR is outlined in Scheme 31. Firstly, two benzaldehydes with solubilizing groups are chosen to prepare the hydrophobic and hydrophilic variants. I chose dodecyl ($C_{12}H_{25}$) and oligoethylene glycol as target structures - both of these groups have been used to enable the dispersion of solution-synthesized GNRs. Dodec-1-ene is treated with 9-BBN to create a 9-BBN-dodecane which is immediately used in a Suzuki cross-copuling to obtain **100** in 70% yield. The installation of the oligoethylene glycol solubilizing chain is accomplished via simple S_N2 reaction between 4-hydroxy-benzaldehyde and a tosylated oligo(ethylene glycol) derivative to obtain **102**.

At this stage, the synthetic pathway yet again relies on the three-component dihydroacridine synthesis as discussed previously in N-ZGNR section. A note of improvement here is the addition of toluene as a co-solvent to the acetic acid for the condensation as compared to the original surface monomer synthesis–this boosts the yields significantly (40% for R=$C_{12}H_{25}$, 25% for R=PEG), acetic acid only: 16% for R=$C_{12}H_{25}$, 5% for R=PEG). The KOtBu/O_2/DMSO conditions are applied again successfully for the oxidation to dibenzoacridine scaffold **101**.

Yamamoto condensation is the polymerization process of choice for many successful syntheses of polyphenylene-derived polymers[114–116] that are present in literature, starting with the original report by Yamamoto *et al*.[117] These conditions have also been recently reported as a polymerization of choice to prepare bulk quantity of solution-synthesized chevron GNRs.[59]

The polymerization condition optimization results for R=PEG are displayed in Table 5. The microwave application of heat has yielded longer polymer chains as assayed by MALDI-TOF. Polymer lengths up to 13 kDa can be reliably observed which corresponds to roughly a 26-mer. The MALDI spectra that compare both MW and non-MW experiments is shown in Figure 32. It is important to emphasize that MALDI peak intensity data should not be interpreted as relative amounts of the oligomers due to differences in ionization, but it should be merely used to assess the presence of the molecular species in the mixture. In conclusion, both MW and non-MW heating of the polymerization yield acceptable polymer formation, with MW method yielding longer polymers in shorter time. The set of conditions from Table 5, row 2, was also used for the growth of the R=$C_{12}H_{25}$ polymer, with a 12-mer as a maximum unit observed. Unfortunately neither alkyl nor PEG functionalized polymer mixture is soluble enough to assess the actual molecular weight distribution by our gel permeation chromatography setup, which relies on the solubility of the polymer in chloroform.

Table 5: Optimization of the polymerization conditions of **105-PEG**

no.	$Ni(COD)_2$	bipyridine	COD	T	t	longest oligomer
1	3.8 equiv	3.8 equiv	2.5 equiv	80 °C	48 h	6-mer
2	2.5 equiv	2.5 equiv	2.0 equiv	90 °C, **MW**	8 h	26-mer
3	2.5 equiv	2.5 equiv	2.0 equiv	90 °C	16 h	20-mer

Polymers were then used as is for the cyclodehydrogenation step. A summary of attempted conditions is summarized in Table 6. Firstly, a classic $FeCl_3$-DCM-$MeNO_2$ heterogeneous Scholl condition has been investigated, followed by $AlCl_3$-$Cu(OTf)_2$-CS_2, and followed by harsher DDQ-TfOH conditions. At this point the characterization of the material becomes limited, as the resulting GNRs were not expected to be soluble in any solvent for NMR analysis–therefore, Raman and IR spectroscopy were used to qualitatively understand the extent of cyclodehydrogenation (Figure 33).

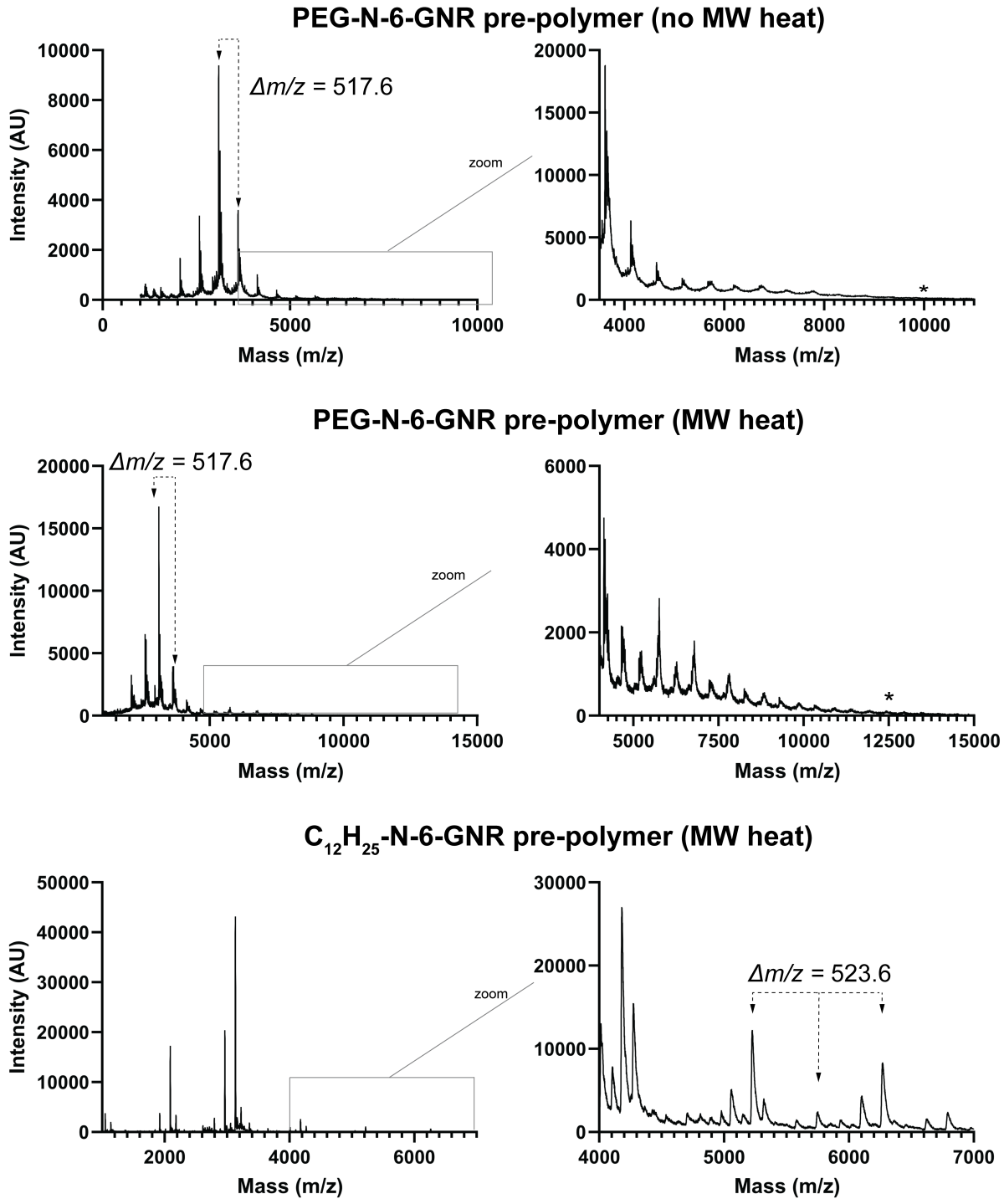

Figure 32: MALDI mass spectrometry of N-6-czGNR polymer precursors. * signifies largest MW polymer that can be observed.

Table 6: Optimization of the cyclodehydrogenation conditions on the czGNR precursors

side chain	conditions	T	t	mass yield	Raman
PEG	$AlCl_3$, $Cu(OTf)_2$, $CS_2/MeNO_2$	24 °C	48 h	95%	N.R.
PEG	$FeCl_3$ (8 equiv) DCM/$MeNO_2$	24 °C	48 h	57%	non-uniform
PEG	DDQ (4 equiv) TfOH	24 °C	24 h	110-118% (mass excess)	Figure 33 top
$C_{12}H_{25}$	DDQ (4 equiv) TfOH	24 °C	24 h	96%	Figure 33 middle

The results from representative homopolymeric ribbon samples are shown in Figure 33. Both D and G peaks are present, and the 2G, D+G and 2D overtones can be observed, which is agreement with other graphene nanoribbons that have been synthesized in solution.[71] D and G peaks correspond to in-plane vibrations in sp^2-bonded-materials–D peak is a signature of the π-confinement in the narrow ribbons,[118] while G peak signifies the uniform graphitic structure.[18] IR spectroscopy was used to ascertain whether the solubilizing chains were still present after the graphitization. In both cases, it is clear that both PEG and alkyl solubilizing chains remain intact by observing signature peaks for C–O and alkyl C–H bond stretching (Figure 33). Combined inference from Raman and IR data confirm that the desired structure of the ribbon is obtained.

As the homopolymers of PEG and alkyl chain were sythesized and characterized, a route toward heteropolymer of PEG and alkyl chains was also explored (Scheme 32). The idea here is to create a defined GNR where the solubilizing chains are different on each side of the ribbon. This strategy has potential in enforcing GNR self-assembly based on hydrophilic/hydrophobic interchain interactions. Suzuki heterocoupling polymerization were selected for the realization of this concept – due to the S-shape of the resulting ribbon, such dicoupling polymerization ensures that the solubilizing groups are positioned on the opposite sides of the ribbon. Scheme 32 summarizes the forward synthetic route toward PEG-$C_{12}H_{25}$-N-6-czGNR. Diboronic ester **106** was prepared from the corresponding dibromo species **101**, and the polymerization was achieved using $Pd(P^tBu_3)_2$ as a pre-catalyst in 90% mass yield. The ^{1}H NMR of polymer **109** clearly shows the presence of both ethylene glycol and alkyl peaks, and DDQ/TfOH conditions were used to yield PEG-$C_{12}H_{25}$-N-6-czGNR, which structure is also confirmed by Raman and IR spectroscopy (Figure 33 bottom).

The acridinic nitrogen reactivity investigation was another goal for this project. In a context of a small molecule, an acridine can be alkylated with an electrophilic carbon source such as 1,3-propanesultone.[119] An initial experiment where the N-6-czGNR are subjected to neat 1,3-propanesultone for 48 h at 120 °C has been performed on small samples of the PEG and alkyl-GNR (Scheme 33), with the goal of evaluating the mass increase, and using Raman and IR spectroscopy to ascertain any spectroscopic differences. Approximately 10% mass increase is observed in the case of each ribbon (theo. mass increase is $\sim$20%, depending on the solubilizing group). Raman spectra are consistent with expected ribbon structure (i.e. graphitic structure is not degraded) and the IR spectra yield a new medium intensity stretching mode at approx. 1340 cm^{-1} that can be attributed to the partial incorporation of the sulfonate (Figure 34).

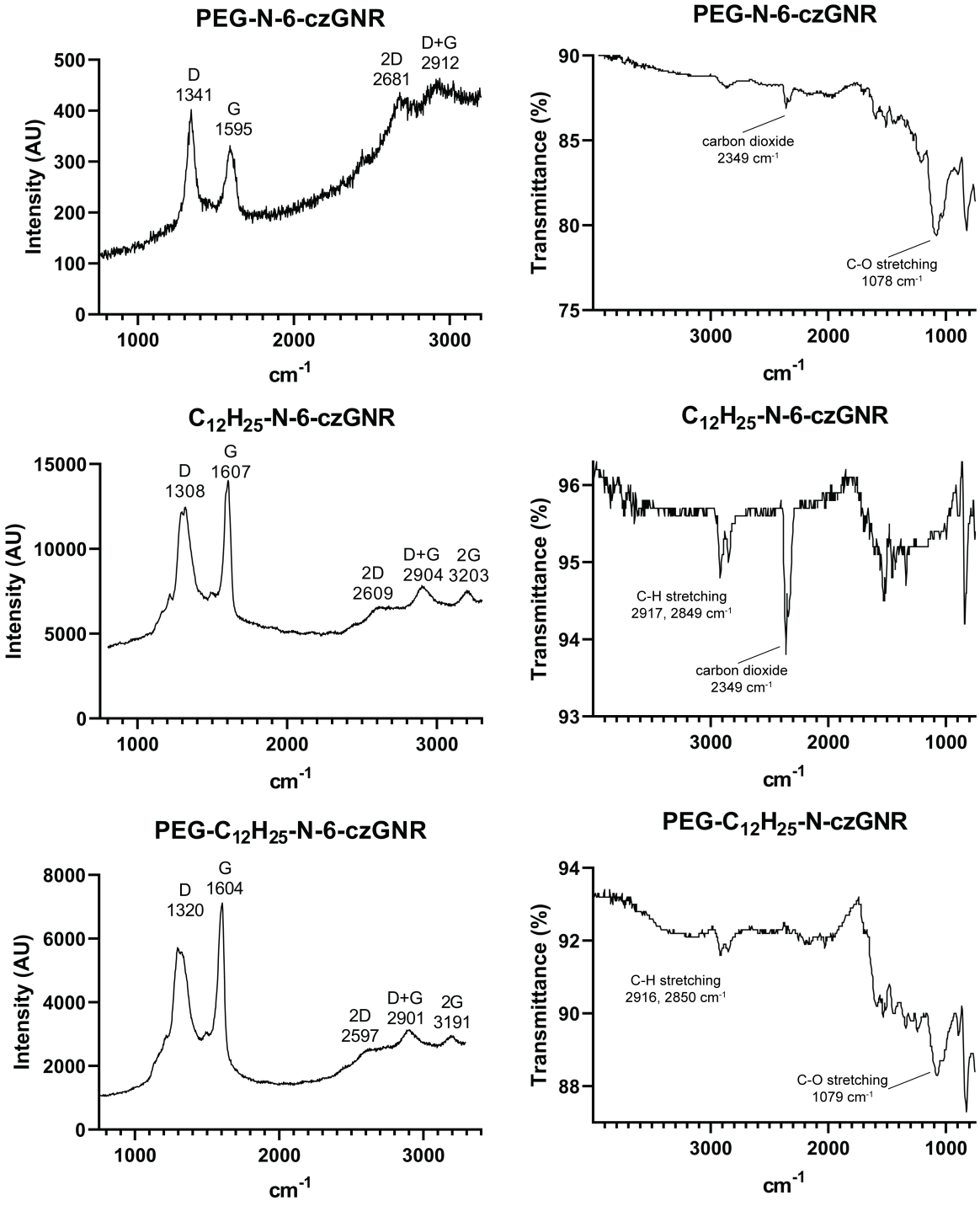

Figure 33: Characterization of the czGNR samples via Raman and IR spectroscopy.

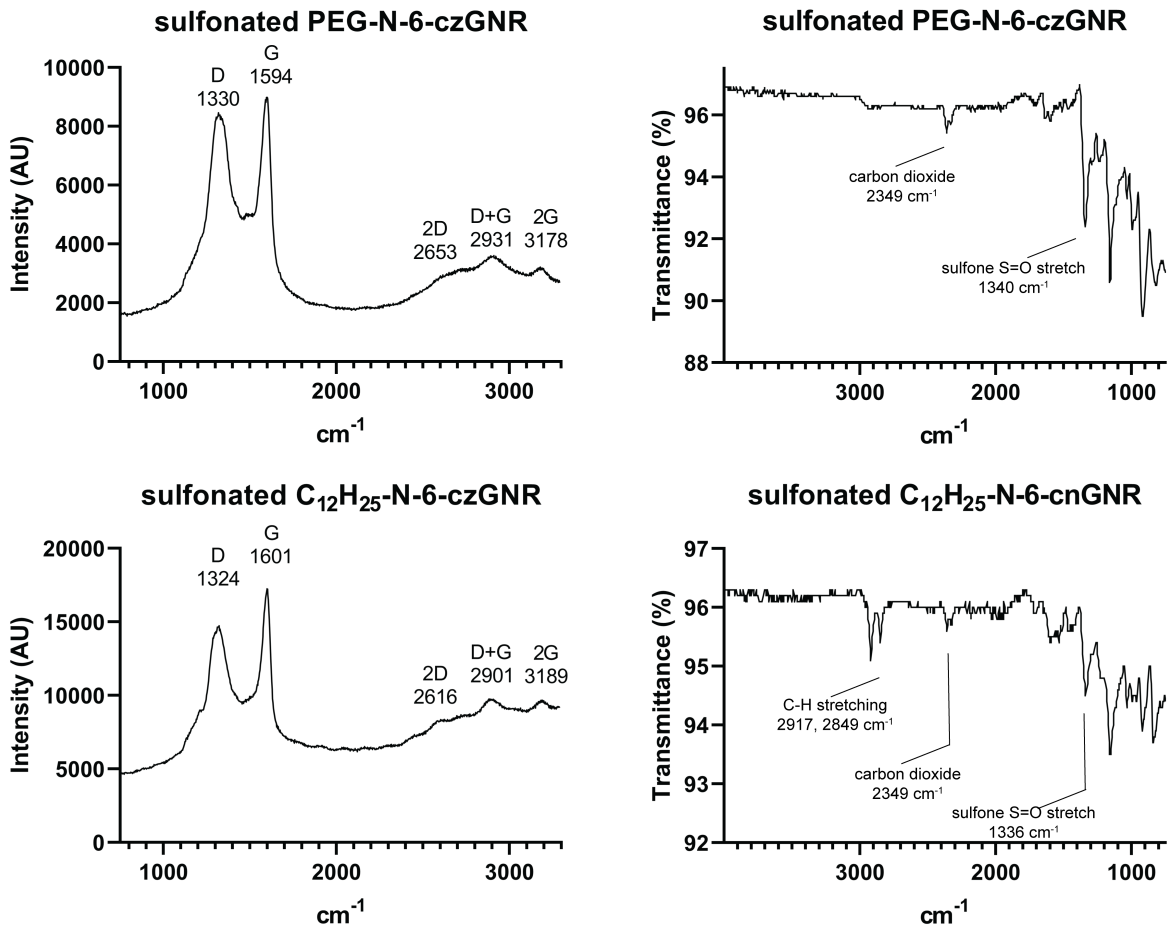

Figure 34: Raman and IR spectra of sulfornated czNGRs in Scheme 33

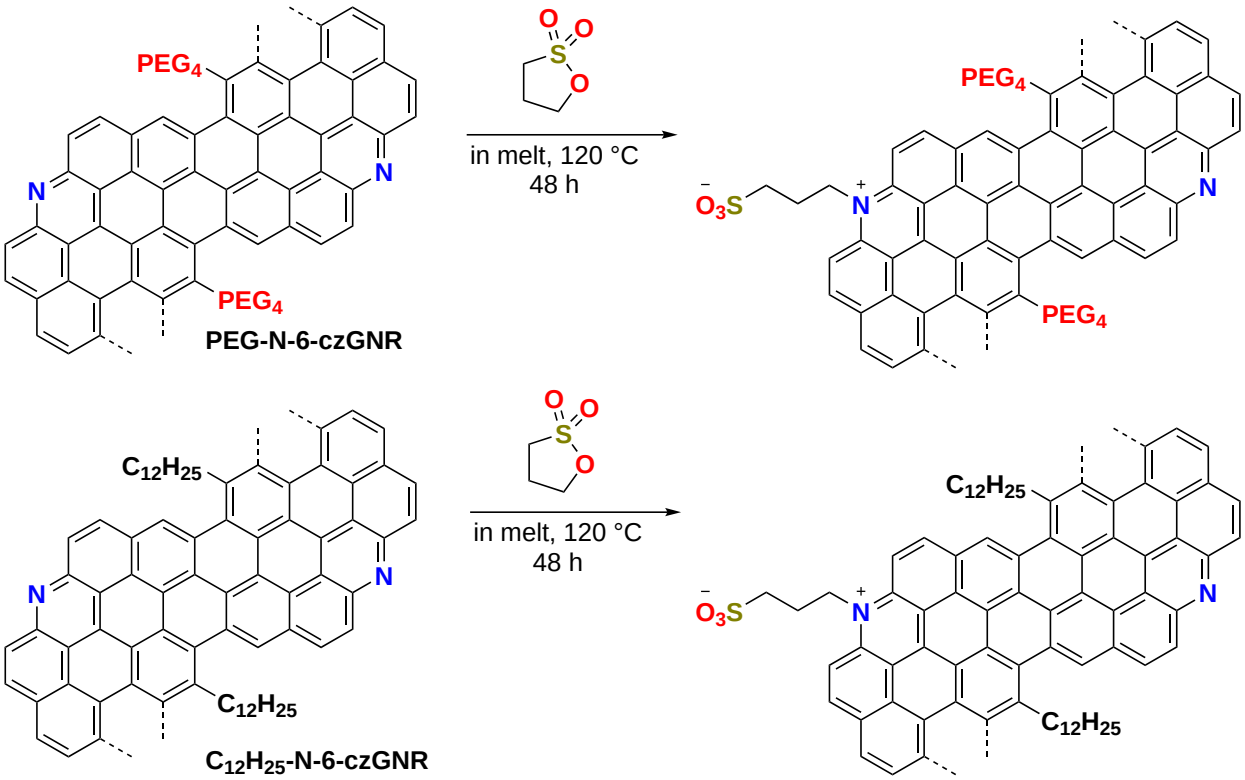

Scheme 33: Acridinic nitrogen functionalization in N-6-czGNR scaffold with 1,3-propanesultone

3.4.2 Overall summary and future directions in the N-ZGNR project

The application of the substituted acridine synthesis has allowed rapid access to a heteroatom modified zigzag GNR families. The N-6-ZGNR has been synthesized, investigated via STM topographic imaging, STS, and dI/dV mapping, and GW-level calculations to assess the intriguing electronic structure. Furthermore, significant progress toward 2N-6-ZGNR has been made via halogen modification of the precursor monomer, and the careful optimization of surface growth is slated to yield pristine samples that can be further analyzed.

The hybrid cove-zigzag GNRs bearing an acridine moeity have also been prepared fully via solution synthesis, and characterized via Raman and IR spectroscopy. The synthesis is amenable to rapid introduction of solubilizing groups to improve the dispersibility of the GNRs. In regard to post-graphitization modification of the czGNRs, there is an opportunity to continue to investigate various reagents that can lead to solubility improvement and/or lead to new class of 2D materials. For example, an incorporation of a ditopic linker with dynamic crosslinking behaviour can potentially lead to a crosslinked network of GNRs which might be beneficial for GNR alignment and thin film formation.

4 Topological band engineering in graphene nanoribbons

The research of topologically induced states in carbon-based materials has been on the rise in the recent years, directly stemming from the resurgence of the concept in 2016, when the Nobel Prize in Physics was awarded to D. J. Thouless, F. Duncan. M. Haldane, and J. M. Kosterlitz for theoretical discoveries of topological phase transitions and topological phases of matter. Continuing with the theme of establishing useful heterojunctions in GNRs, topological state theory has made a pronounced impact, and has added another creative approach in modulating the electronic properties of a GNR.

This chapter focuses on extension of the topological band engineering concept in GNRs which was experimentally pioneered in our research group with 7/9-AGNR superlattice of topological junction states, and refocused the field's direction onto studying width, legth, and edge dependence of the GNR superlattice electronic properties. Two original projects are described – theory-driven pursuit of asymmetric cove GNR scaffold which an has unusually small bandgap due to unit cell symmetry effects, and a 5/7-AGNR superlattice segment length study which expands the surface synthetic toolkit toward well-defined nanoribbons.

4.1 Topological states in materials

Topological insulators—materials that have a bulk electronic band gap like an ordinary insulator but have protected conducting states on their edge or surface—have been at the forefront of research efforts toward spintronics[120] and quantum computing.[121,122] When topological insulators of two different topological classes are joined, the boundary states appear in the bandgap, leading to exotic electronic properties in the material.[123]

Electron spin is a promising candidate that can be used for a solid-state qubit,[124] and new technologies in computation, communications, security, and sensing rely on the quantum manipulation of spin.[125] In carbon nanomaterials, long coherence times of spin in open-shell structures is expected due to low spin-orbit coupling in carbon.[126] The rational design of topological states in conjugated sp^2 lattice of graphenoid structures therefore has enormous potential in providing robustness against decoherence and possibility of spintronic manupulation.[16] The efforts toward exploring Majorana fermions in 1D semiconducting wire (such as a GNR) / superconductor heterojunctions are also rooted in topological state theory, which is also an extremely promising venue for quantum computing.[127–129]

4.1.1 Discovery and first experimental proof of topological states in GNRs

The field of graphene nanoribbons was introduced to the potential of topological state theory in 2017, when the Louie group at UC Berkeley published the mathematically cogent description of topological invariants in armchair edge graphene nanoribbons. This work provides a stand-alone entry for the understanding of topological effects in GNRs.[130] In the manuscript, authors produce a derivation of the topological invariants based on the width or the ribbon and the unit cell termination. Starting from the Zak phase—a quantity that dictates the bulk-boundary correspondence which states that localized states will emerge at the boundary between two topologically distinct regions—the $\mathbb{Z}_2$ invariant is derived, and values of the $\mathbb{Z}_2$ invariants of two interfacing GNR segments determine whether there is an odd or even number of states at the junction. The topological invariants for AGNR cases are defined in the fourth row of the Figure 35, where N is the width of the GNR. These formulae have been derived and have been validated through explicit density functional theory (DFT) supercell calculations[131] on AGNRs with $3 \leq \mathrm{N} \leq 10$.

Termination type	Zigzag (N = Odd)	Zigzag' (N = Odd)	Zigzag (N = Even)	Bearded (N = Even)
Unit cell shape	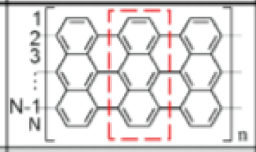	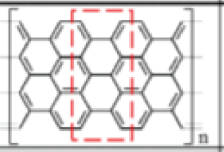	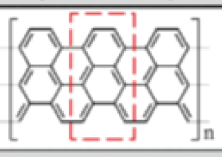	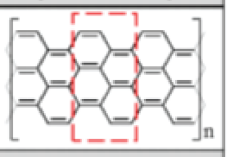
Bulk Symmetry	Inversion/mirror	Inversion/mirror	Mirror	Inversion
Z_2	$\frac{1+(-1)^{\left\lfloor\frac{N}{3}\right\rfloor+\left\lfloor\frac{N+1}{2}\right\rfloor}}{2}$	$\frac{1-(-1)^{\left\lfloor\frac{N}{3}\right\rfloor+\left\lfloor\frac{N+1}{2}\right\rfloor}}{2}$		$\frac{1-(-1)^{\left\lfloor\frac{N}{3}\right\rfloor}}{2}$

Figure 35: Categorization of electronic topology via $\mathbb{Z}_2$ invariant in AGNRs. $\lfloor x \rfloor$ is a floor function that takes the largest integer less than or equal to a real number x.

Rizzo *et al*. have provided the first experimental proof of the existence of topoloigcally induced bands in a 7/9-AGNR superlattice.[132] The monomer precursor that resulted in the 7/9-AGNR superlattice (Figure 36b) has been rationally desgined with two sterically different sites for the superlattice formation, i.e. th anthracenyl site will only reacting with another anthracenyl site, and the same applies to the phenylene site. The superlattice of regioregular 7/9 segments has been indeed observed upon deposition of the monomer on Au(111) surface and annealing to 300 °C.

Zooming in on a single junction (Figure 36a) in comparison to pristine 7-AGNR and 9-AGNR, the 7-AGNR segment has a $\mathbb{Z}_2$ invariant of 0, and the 9-AGNR segment has a $\mathbb{Z}_2$ invariant of 1, which signifies that there should be a topological interface state at this junction. Since this junction is periodically embedded in the ribbon, these topologically induced states were predicted, and experimentally found via STS and dI/dV mapping, to result in distinct bands, labeled UTB (unoccupied topological band) and OTB (occupied topological band) respectively (Figure 36b, inset). It is interesting to point out that the resulting bandgap of the 7/9-AGNR is smaller than that of either 7-AGNR or 9-AGNR - therefore, topological states are shown to be an effective tool to dial in desired electronic properties into a GNR scaffold.

Another example of robust topological states in 7-AGNR scaffold was co-published in the same journal issue by Groning *et al*.,[133] where an approach toward controlled and regioregular extension of 7-AGNR was achieved from the bis(anthryl)dimethyltetracene scaffold (Figure 36c), and the resulting topological states are also due to the regioregular arrangement and unit cell terminations of 7/9-AGNR junctions. An interesting feature of this monomer scaffold is the steric compatibility with DBBA, which was co-deposited with the tetracene monomer, and special cases of extended and short segments of various topologies were found and investigated to confirm the predicted robust topological states.

The origin of the band gap stems from the coupling of these states with each other. Since 7-AGNR and 9-AGNR segments differ in length, these states' interaction can be expressed as hopping amplitudes t_1 (hopping across a 9-AGNR segment) and t_2 (hopping across a 7-AGNR segment). The standard two-band tight binding form can be used to derive the band dispersion magnitude, and to predict the tunable energy gap that is formed by these new topologically induced states. If $t_1 \neq t_2$, then the topologically induced bandgap is defined as $E_g = 2||t_1| - |t_2||$. A special case of this general formula where the hopping amplitudes are identical can lead to a metallic GNR, and the proof-of-concept of a case where $t_1 = t_2$ was explored and recently published by Rizzo, Veber, Jiang *et al*.[134]

Overall, the use of topological states is an effective tool in modulating the electronics of GNR has very recently been established and discussed. In the following sections, I present my take on the synthetic access toward two new heterojunctions that possesss intriguing electronic properties that are attributed to topological state phenomenon - a theory-drived *asymmetric-even* cove GNR, and synthesis-driven design of the 5/7-AGNR superlattice.

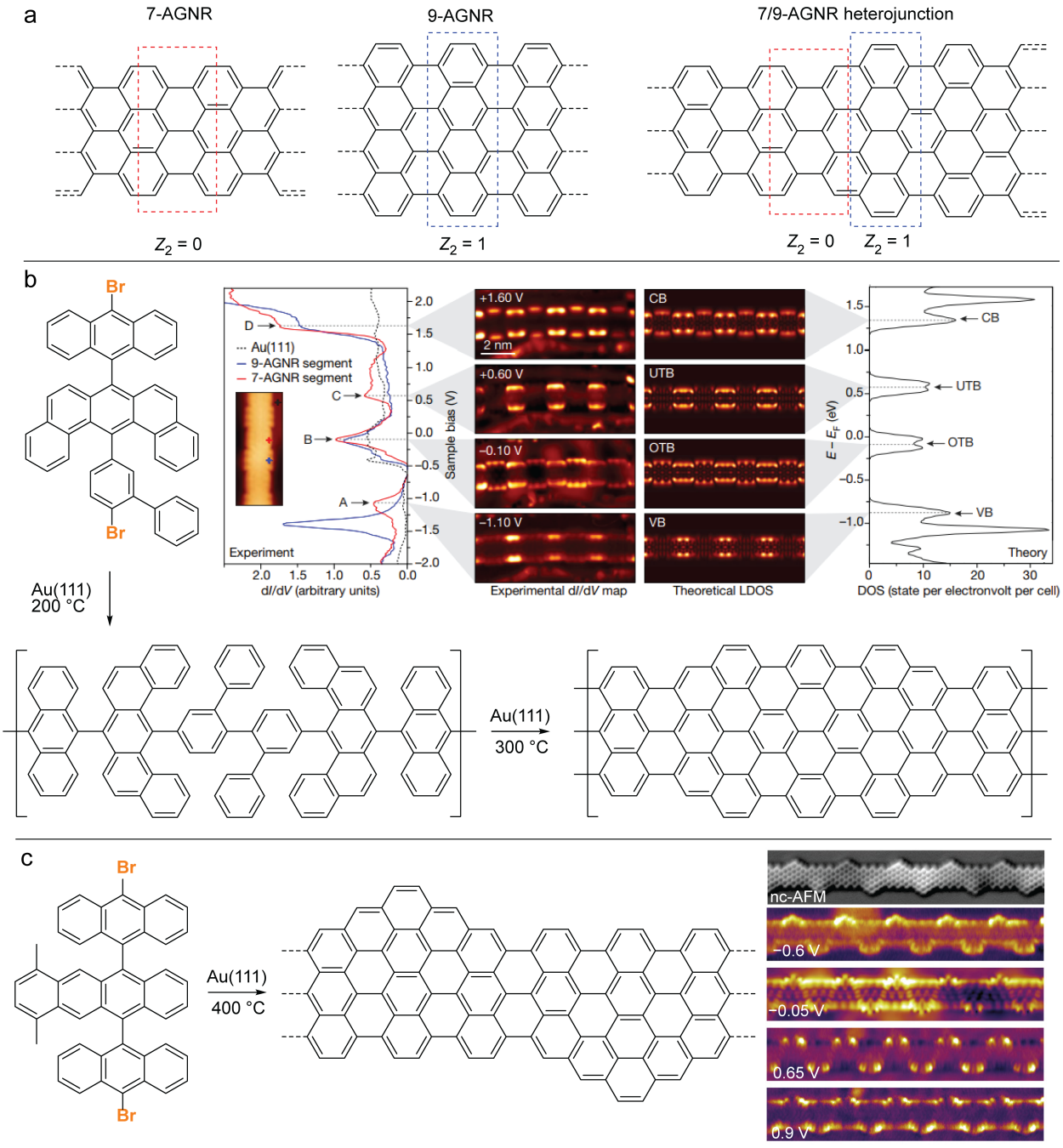

Figure 36: (a) Unit cell comparison, and the construction of a 7/9-AGNR heterojunction with topologically induced states. (b) 7/9-AGNR superlattice synthesis on Au(111), and its electronic characterization. Note the new states, labeled OTB and UTB (occupied and unoccupied topological band, respectively).[132] (c) Synthesis of an extended 7-AGNR with robust topological phases.[133]

4.2 Asymmetric cove scaffold - novel monomer design, theory and synthesis

4.2.1 Background: topological states in cove-type GNRs and target ribbon selection

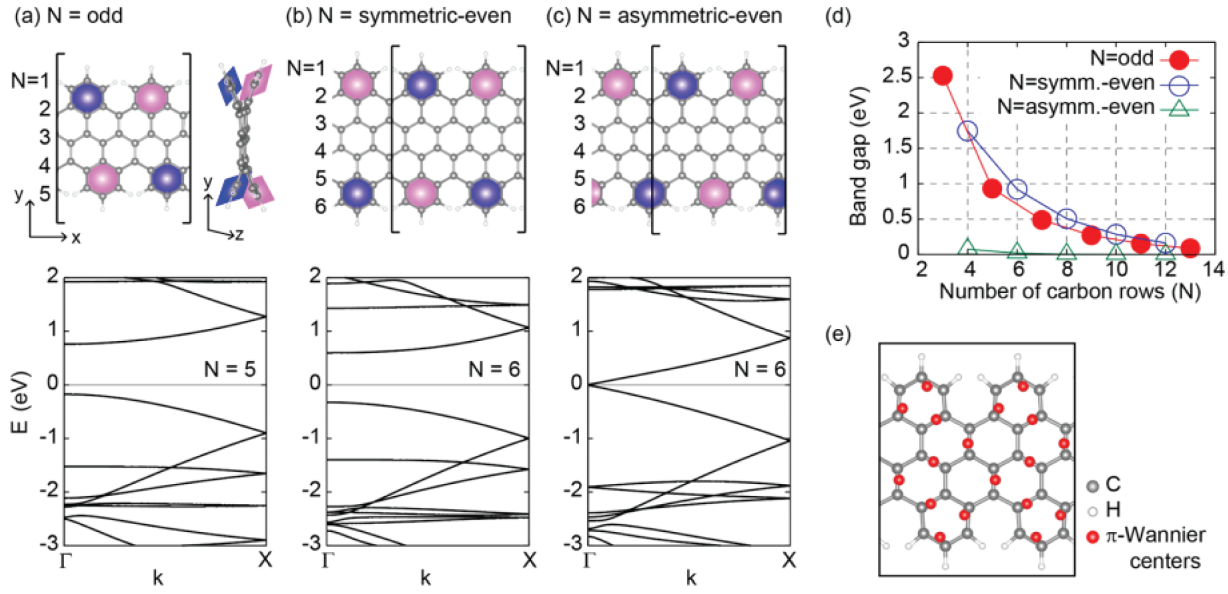

Figure 37: Band structures of various cove GNRs using DFT-LSDA. Figure reproduced from reference [135]

Topological phases in cove-type GNRs In 2018, Lee *et al*. have reported an in-depth theoretical study of cove-edged and chevron GNRs.[135] The derivation and values of topological invariatins for a number of cove and chevron ribbons is presented, and junction states between two topologically distinct segments are discussed in detail. Figure 37 shows a select figure from the manuscript where the band structures of cove-edged ribbons are shown. In panel (d), three families of cove-edged GNRs are compared - whereas the *odd* and *symmetric-even* families show pronounced effects of lowering the band over increasing the width of the ribbon, the *asymmetric-even* family appears to have a near-zero band gap even at small width. *Odd* 5-cove-GNR was previously sythesized by Liu *et al*.[49] on Au(111) surface, but other ribbons have not been previously explored.

The *asymmetric-even* family of ribbons is of particular interest to our group, as we have searched for metallic GNR scaffolds toward the lateral TFET device, and this family of ribbons is one of the few cases in the literature that are predicted to be near-zero gap (think the original report of zigzag GNR and how that motivated the field toward its synthesis). The linear band dispersion near the Fermi energy that originates from the Dirac-like band dispersion at the K point of graphene folds to the zone center of the 1D Brillouin zone. This feature of the band structure for *asymmetric-even* family survives in LSDA and fully relativistic calculations including spin–orbit interaction, which is a promising factor for being able to analyze the ribbon's electronic structure via on-surface methods. Therefore, I have decided to pursue a design of the molecular precursor towards the *asymmetric-even* N=6 ribbon.

4.2.2 Precursor synthesis and surface deposition results

Monomer design Retrosynthetic analysis of the target cove ribbon is shown in Scheme 34. Building back from the symmetry of the ribbon, **110** has been postulated as the surface polymerization precursor in order to achieve an authentic sample of the target cove ribbon. Dibromide **110** can be derived from dimethoxy scaffold **111**. In order to assemble **111**, Negishi-type cross-coupling was determined to be a key step in this synthesis, as both **112** and **113** can be easily prepared.

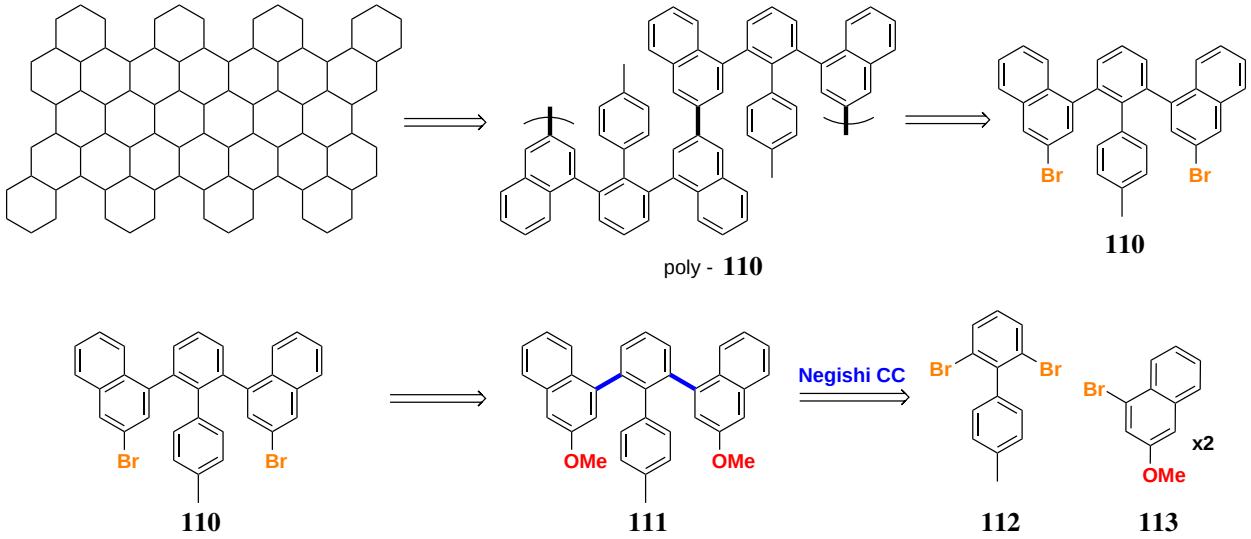

Scheme 34: Retrosynthetic design of the precursor toward asymmetric-even cove GNR

The complete forward synthesis of **110** is shown in Scheme 35. Elecrophilic bromination of **114**, yields **115** which can be easily converted into a 1,2,3-naphthooxadiazole **116** (a zwitterionic structure is shown for clarity). Then the diazonium salt is reduced with sodium borohydride, and the 4-bromonaphth-2-ol **117** is isolated. Methylation with MeI yields 4-bromo-2-methoxynaphthalene **118**, which is first coupling partner precursor for the key Negishi cross-coupling step. On the other hand, the biphenyl core **112** was assembled in one step via a LDA deprotonation of **119** followed by transmetallation with zinc (II) chloride, and Negishi cross-coupling with 4-iodotolane **120**.

With **112** and **118** in hand, a Negishi cross-coupling was used successfully to assemble the carbon core of the target monomer: **111** was obtained in 44% yield. Conversion of the **111** to ditriflate **121** was accomplished by treatment with BBr_3, hydrolysis, and Tf_2O/collidine. The ditriflate could then be converted to the final target **110** via either two-step borylation/halogenation protocol, or in one step with $(RuCp^*Cl)_2$/LiBr in DMPU, although $(RuCp^*Cl)_2$ is not commerically available and needs to be prepared from $RuCl_3$ hydrate (Scheme 36, top). In any case, both borylation/halogenation and Ru-catalyzed routes yield the target **110** in 76-80% yield.

It is prudent to point out the temperature and reaction time control importance for the Cu-catalyzed borylation of **122**. The procedure that results in the best yield for **110** is **122** treated with excess $CuBr_2$ stirred in a THF/MeOH/H_2O mixture at 90 °C. The reaction must be monitored and worked up as soon as the starting material's disappearance has been confirmed by thin layer chromatography. If the reaction temperature and time is not controlled (a.k.a. left overnight at a slightly higher temp), one can still isolate **110** but higher oligomers can be observed in mass spectrometry (Scheme 36, bottom).

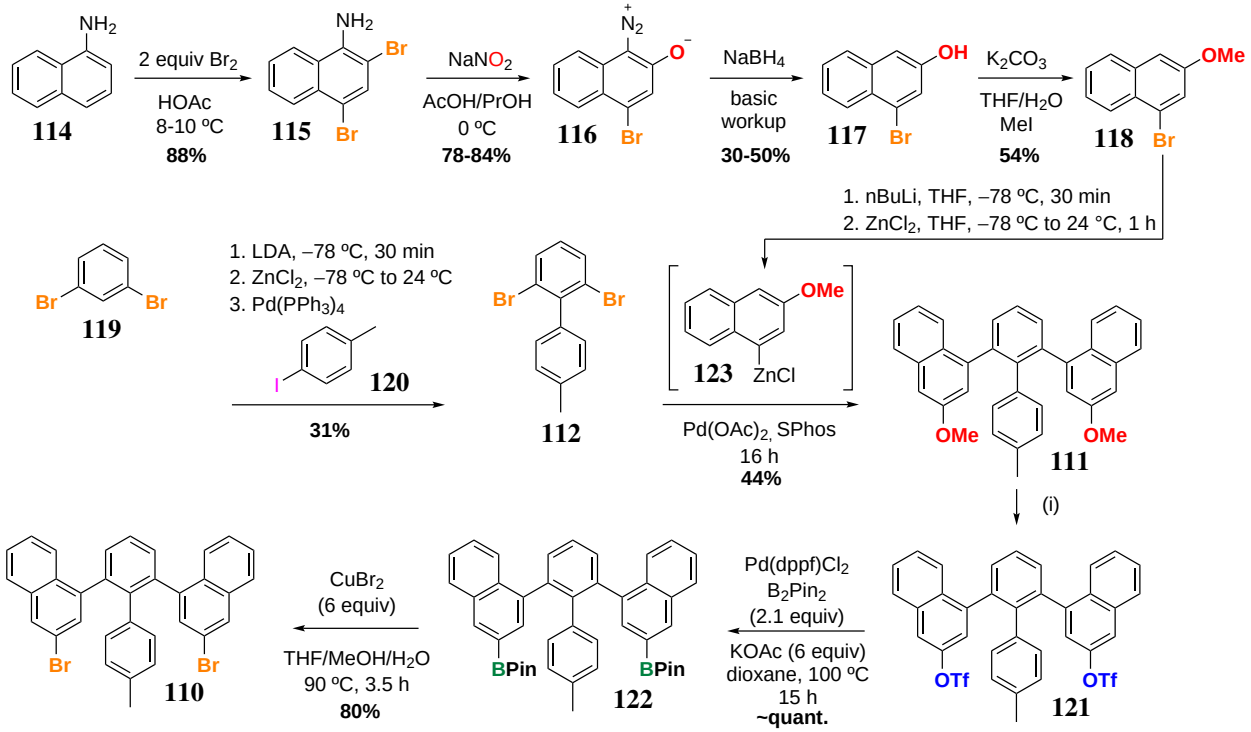

(i) 1. BBr_3, DCM, 0 °C, 1 h, then warm to 24 °C, 1 h. **96%**. 2. 2,4,6-collidine, Tf_2O, DCM, 0 °C to 24 °C, 16 h, **76%**

Scheme 35: Forward synthesis of the precursor **110** toward asymmetric-even cove GNR

With monomer **110** in hand, an deposition onto Au(111) was performed. The monomer is observed to adsorb to the surface with high fidelity as shown in Figure 38. The anneal to higher temperatures has unfortunately never yielded the desired polymer/GNR on the surface. Fast anneal (24 °C to 350 °C, 3K/min, image) and slow anneal (24 °C to 200 °C, 1K/min, image) both yielded a clean surface after the imaging stage. Therefore we conclude that the monomer desorbs from the surface at elevated tempreature without being able to diffuse across the surface and form the polymer.

The computational studies of this monomer adsorption geometry were not continued due to the disappointing surface results. In hindsight, the architecture of the monomer does provide an intuitive reason for the reason as to why the polymerization is disfavored when compared with the 6-ZGNR monomer **80**, for example. Scheme 37 showcases hypothetical adsorption geometries of **80** and **110** . The freedom of rotation of the naphthalene wings on **110** can allow for the adsorption where both bromide sites can directly point downward to the surface, thus allowing for both radical sites to be activated in close proximity to the surface. Such "bidentate" anchoring likely limits the diffusion of the molecule around the surface, as there is nothing that prevents this molecule from adopting this conformation. In comparison to 6–ZGNR precursor **80**, the fully fused backbone likely prevents strong monomer-surface interaction, and **80** will not adsorb as strongly which allows for the efficient diffusion and polymerization of the molecule.

In conclusion, the experimental confirmation of the existence of topological states in the cove-GNR scaffold was not successful due to lack of surface-induced polymerization of **110**. The syn-

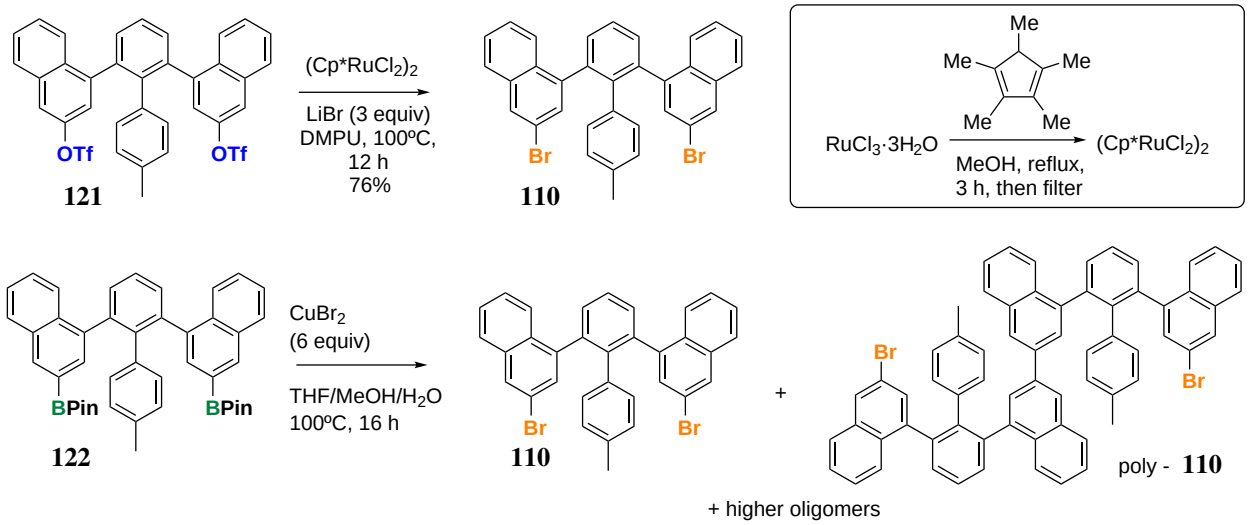

Scheme 36: Additional experiments toward **110** - Ru-catalyzed route and higher oligomer formation

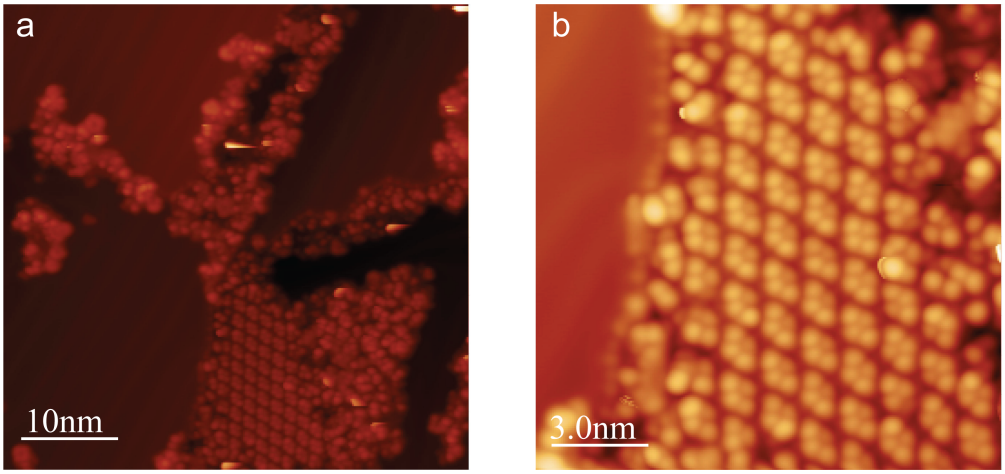

Figure 38: Surface deposition results of **110** - only monomer deposition is observed (no GNR formation)

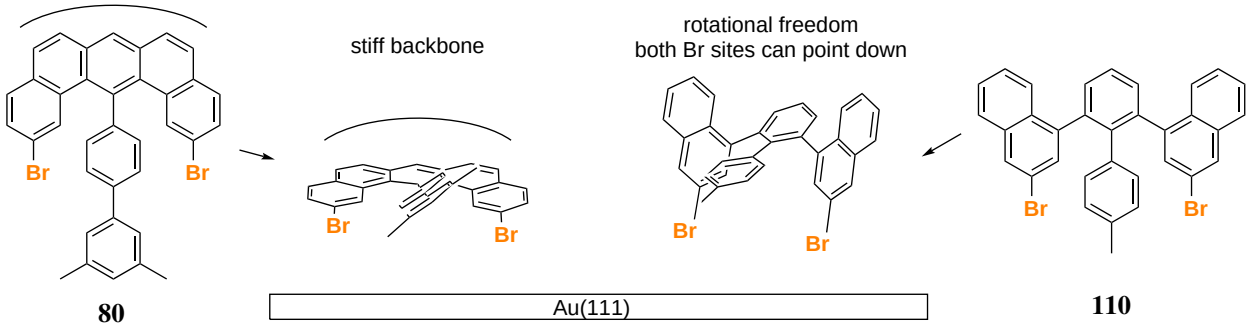

Scheme 37: Exploration of similarities and differnces between zigzag monomer **80** and asymmetric cove monomer **110**.

thetic access to the monomer scaffold however, is certainly a valuable research effort which uses the convergent strategy that culminates in the double Negishi cross coupling to assemble the monomer skeleton. The final conversion sequence from methoxyaryl to aryl bromide is also re-iterated as a robust, good-yielding route to guide further monomer design. The solution polymerization of **110** is assessed as a lower-value target that was not explored any further after the discovery due to the lack of the immediate testing availability for the direct contact transfer setup. Making these nanoribbons in solution from the precursor polymer does not seem practical due to the lack of literature precedent for the oxidative cyclodehydrogenation conditions that involve methyl groups.

4.3 5/7-AGNR: segment length variation

Non-Kekulean structures–polycyclic aromatic hydrocarbons that exhibit unpaired electrons in the ground state–have captivated the interest of synthetic minds over the last century. These compounds' unique proposed properties are of enormous theoretical and practical interest, as it would drive the new generation of carbon electronics forward enabling new magnetism, absorption/emission, and electronic transport properties. In particular, Erich Clar was interested in structures such as triangulene–also known as Clar's hydrocarbon–and many others.[136] The totality of his work, including the ubiquitous Clar π-sextet rule, serves as inspiration to many synthetic chemists in the PAH field, and his creativity coming up with molecular structures to study for generations of scientists to come is astonishing.[137,138] The advent of scanning tunneling microscopy and atomic force microscopy in tandem with metal surface-catalyzed reactions has made the exploration of previously unknown reactivity of molecular precursors possible. Properties of individual molecules can now be resolved atomically with regard to their charge distribution,[139] bond order,[140] and adsorption geometry.[141] Elusive graphene fragments with radical character like triangulenes of various size,[142,143] *peri*-pentacene,[107] rhombene[144] and others have been sythesized and characterized (both on surface and in solution).[22]

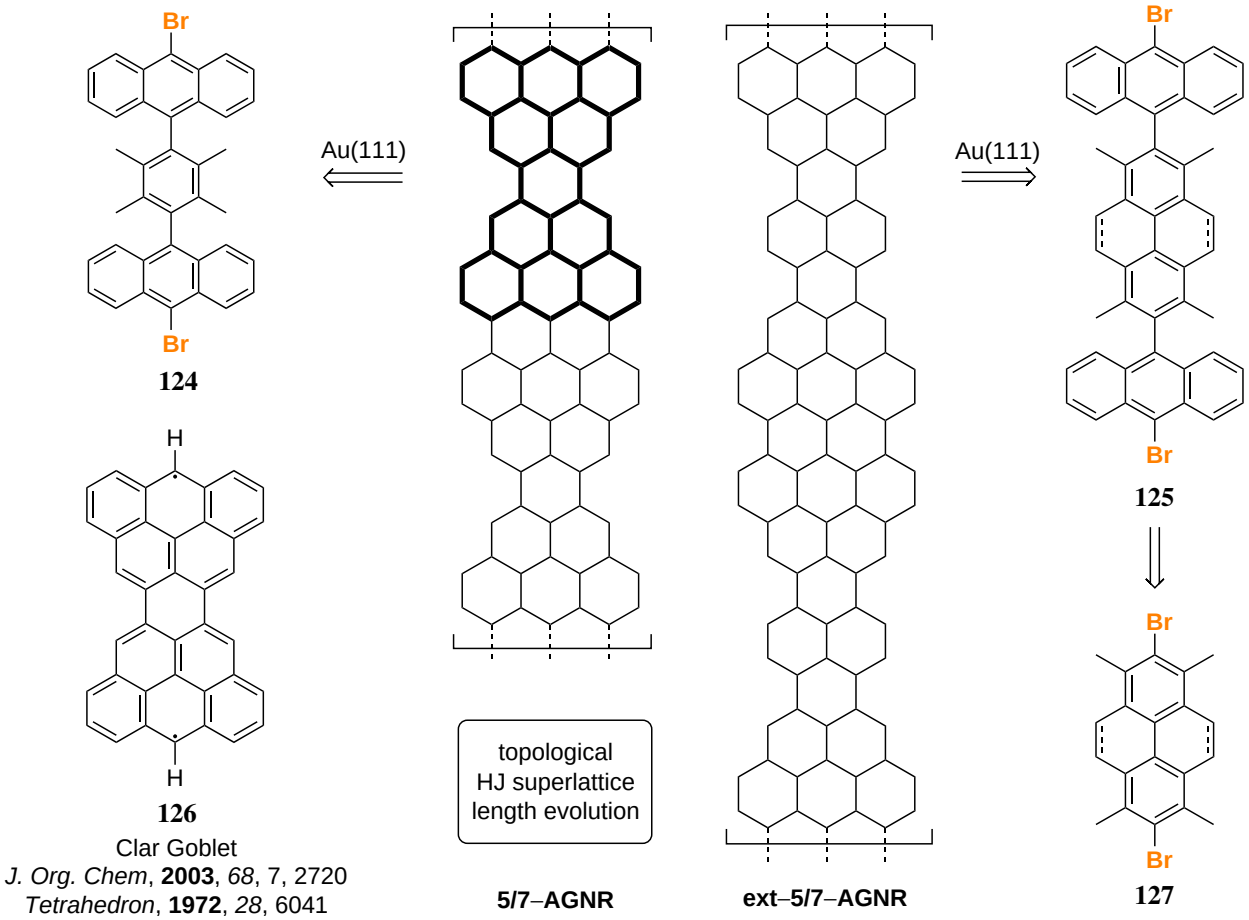

Scheme 38: 5/7-AGNR project overview - segment length variation in topologically induced heterojunction superlattice.

The Clar goblet molecule has been postulated by Clar in 1972, where he predicted that the structure **126** should be realistic to prepare and isolate.[136] A later theoretical study from 2003 by Pogodin and Agranat explored the Clar goblet and related non-Kekule strucutres by *ab initio* simulations,[145] with a verdict that the thermodynamic stability of the Clar goblet might be sufficient for its isolation. However, they also warrant against underestimating the kinetic instability.

The retrosynthetic breakdown for the molecule is informed by the Au(111) surface reactivity, where there is precedent for the cyclodehydrogenation reactions that invovle benzyl groups. Herefore, I have proposed a structure **128** as the baseline for the Clar goblet. The extension of this monomer for polymer/GNR synthesis is straightforward via halogenation of the anthracene in 10-position, which results in **124**, or **129** if the iodinated precursor is required. In a similar vein, the combination of my interest in Clar goblet and topologically induced states led me to propose the following experiment: creating a graphene nanoribbon that is comprised of anthracene-fused Clar goblets. This would lead, in GNR topology terms, to a nontrivial 5/7-AGNR superlattice (Scheme 38).

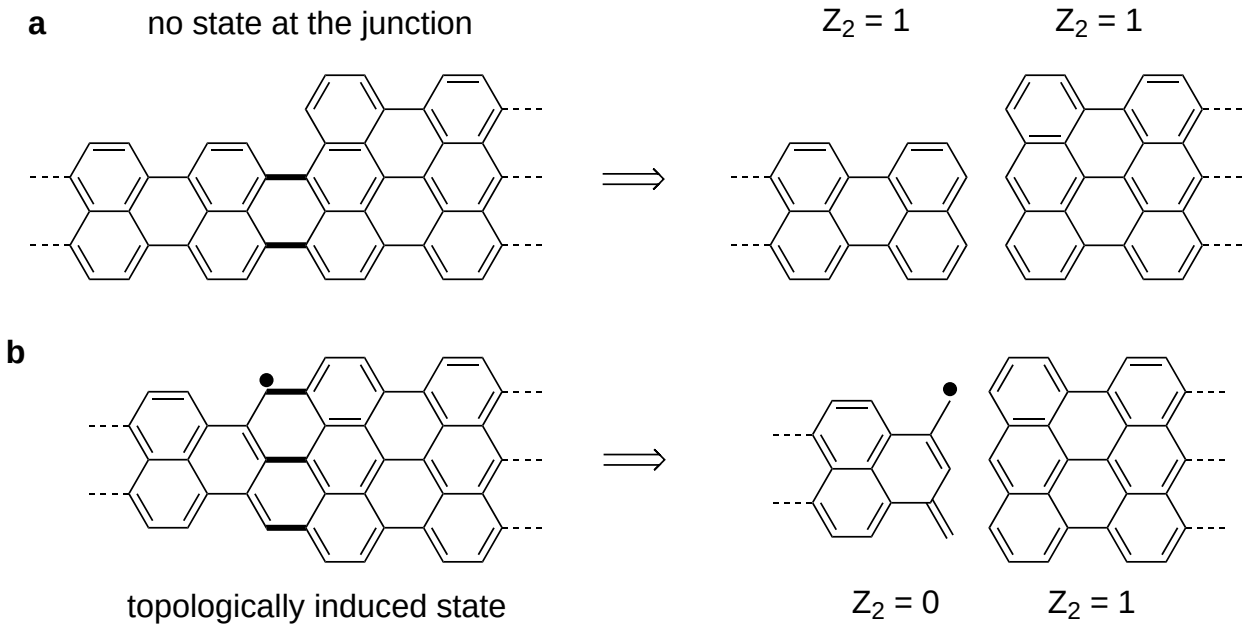

Scheme 39: Two different 5/7-AGNR juctions: (a) trivial and (b) non-trivial, accompanied by calculated $\mathbb{Z}_2$ invariants based on the width and edge termination. Unpaired electron is emphasized in (b) - this is helpful to brainstorm simple junctions and perform "back of the envelope" check.

As rigorous as topological invariants are, a quick rule of thumb/unpaired electron count can yield similar results with simple systems, such as the 5/7-AGNR, as shown in Scheme 39. Here, two different heterojunctions of 5-AGNR and 7-AGNR are shown alongside the calculated $\mathbb{Z}_2$ invariants. In the case of Scheme 39a, two unit cells that are joined together do not have any unpaired electrons after the Clar sextets have been drawn in, thus we do not expect to see any topologically induced junction states (as confirmed by $\mathbb{Z}_2$ invariants). In the second (Scheme 39b) heterojunction one can note an unpaired electron in the 5-AGNR termination after the aromatic sextets are filled in, thus we would expect it to show up in the heterojunction which is indeed the case after consulatition with topological invariants. This method fueled many fruitful discussions in the joint meetings

with collaborators, as this was a useful conceptual tool that can easily unify solid state physicists, chemists, and electrical engineers in understanding the properties of the junction.

The brainstorming toward the suitable monomeric precursor was relatively quick, as once can simply envision a 2,3,5,6-tetramethylbenzene flanked by two anthracene units in 1,4-positions which can be easily modified at the 10- position of anthracene via electrophilic substitution, resulting in **124**. The polymerization of such monomer is expected to be straightforward, as the geometry of the monomer does not have any heteroatoms in the middle segment (see chapter 2), and is structurally similar to previously reported scaffolds. Furthermore, there is enough precedent to deem C-C bond formation reactions that are needed for the GNR formation–C(sp^2)-C(sp^2) and C(sp^2)-C(sp^3) to be plausible, methyl groups in benzylic positions have been shown to react accordingly to for desired 6-membered rings in select systems (i.e ZGNR precursors, chapter 3).

Aside from the original work by Cao *et al*., it is prudent to note that this idea of repeating intra-ribbon states based purely on edge structure has been around since 2008, when Sevincli *et al*.[146] proposed what they noted as superlattice structures in graphene-based armchair ribbons. Their approach was to have periodically spaced out quantum well structures in AGNR. A summary of the length of the 5–AGNR segment variation has been explored, and the resulting trend of decreasing the gap as the 5–AGNR segment is lengthened is observed.

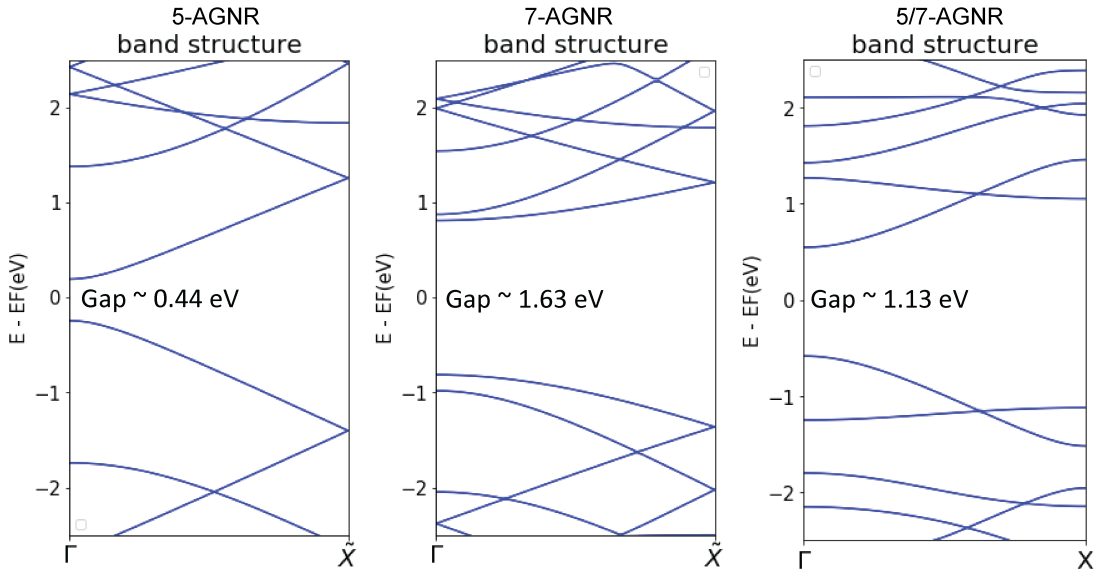

Figure 39: DFT-LDA calculation of the band structure of 5-AGNR, 7-AGNR, and 5/7-AGNR.

The independently performed calculation by DFT-LDA method of the Clar-Goblet derived 5/7-AGNR superlattice system was performed by F. Zhao (S. Louie group, UC Berkeley), and the results are summarized in figure Figure 39. Cosine-like bands that form the bandgap are expected to be topologically induced states. The decrease in the bandgap of 5/7-AGNR as compared to 7-AGNR is an interesting feature of combination of the 3p+1 and 3p+2 GNR families into the superlattice (previously, 7/9-AGNR was an example of 3p and 3p+1 combination).

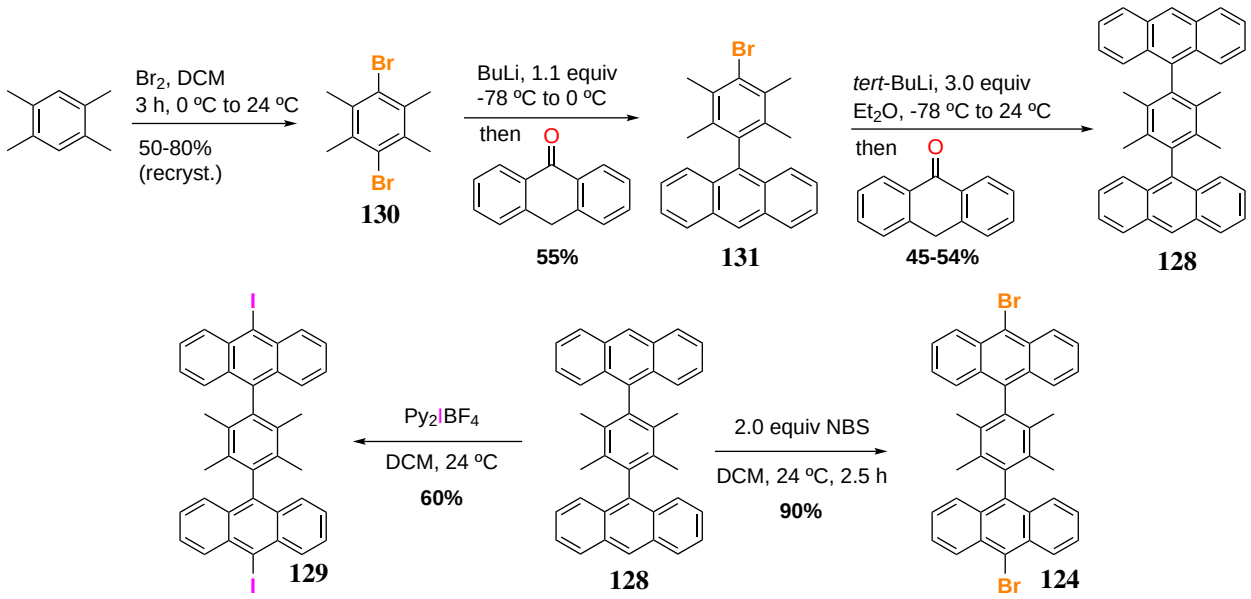

Scheme 40: Synthetic route toward 5/7-AGNR precursors

The synthesis of the Clar-Goblet inspired junction monomer **124** is described in Scheme 40. First, durene is brominated with elemental bromine to yield in 1,4-dibromo-2,3,5,6-tetramethylbenzene **130**. Stepwise lithium-halogen exchange followed by quench with anthrone and acidic workup was used for sequential installation of anthracene units in the position of bromines, with an isolation of intermediate **131**, which resulted in the unhalogenated Clar goblet precursor **128**. Direct bromination of **128** with NBS, or a direct iodination with Barluenga's reagent is used to achieve **124** and **129**, respectively, in good yield.

4.3.1 Deposition, polymerization and cyclodehydrogenation of the 5/7-AGNR precursors on Au(111)

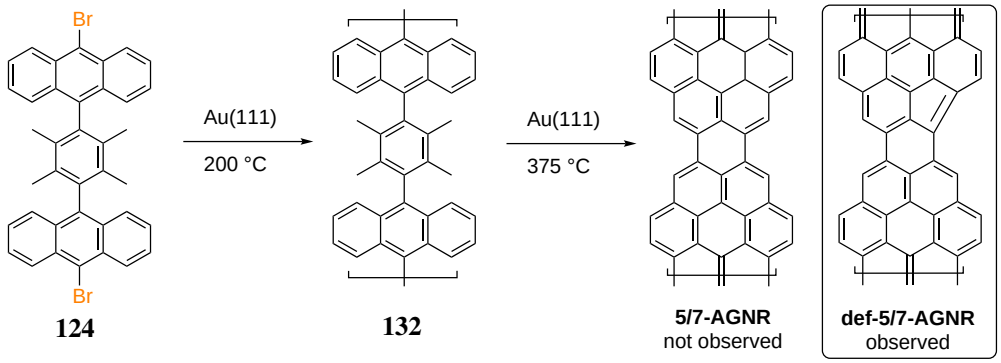

Scheme 41: Schematic representation of the 5/7-AGNR ribbon synthesis - first experimental results

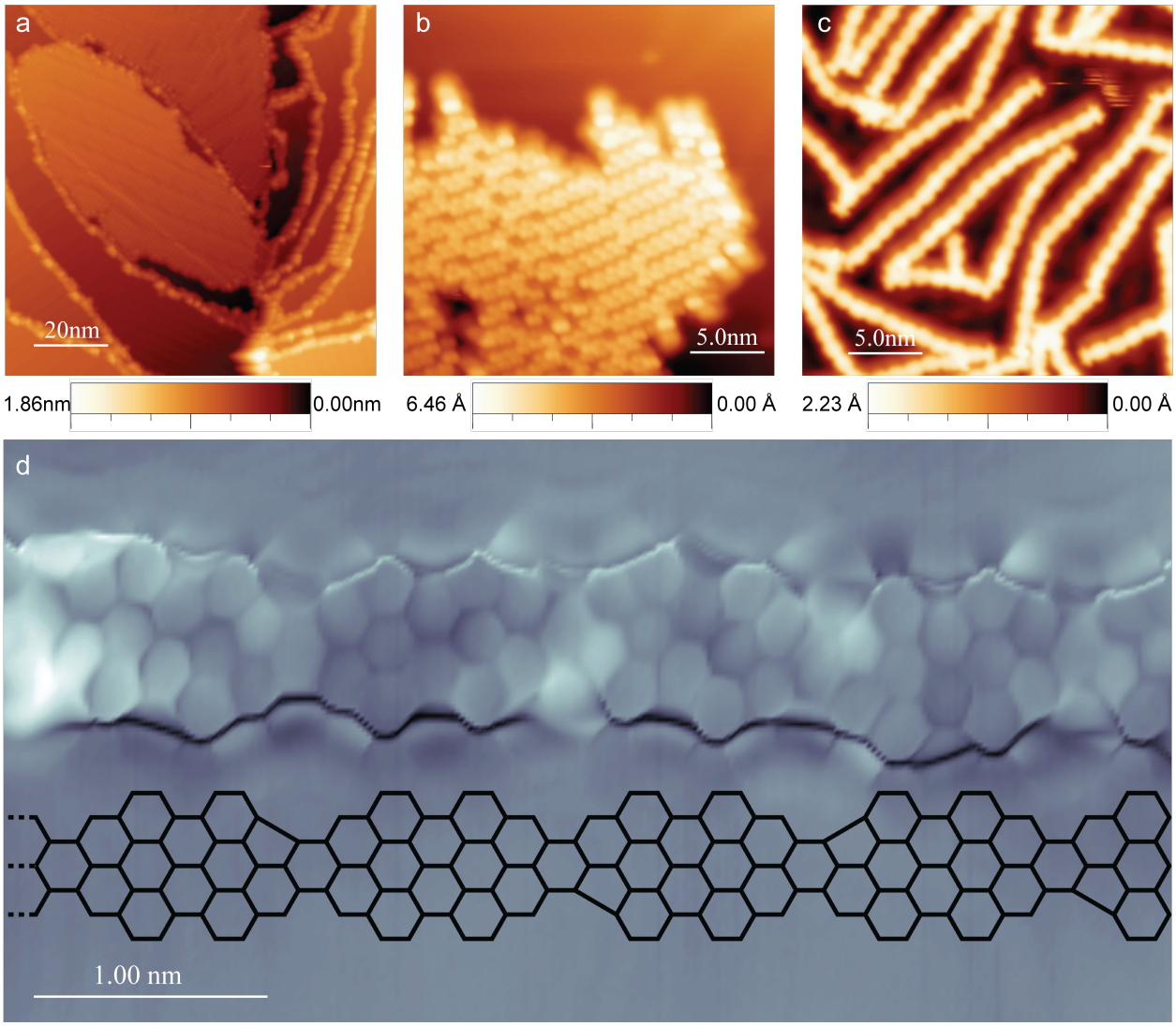

Figure 40: (a) **124** as deposited on Au(111) surface held at 24 °C. (b) Representative surface image after anneal to 200 °C - polymeric species are observed. (c) Representative surface image after anneal to 400 °C. GNRs appear on the surface, and are longer than 10 nm in length (d) BRSTM image of a representative ribbon, and the carbon skeleton outline that corresponds to the observed structure. It is evident that each monomer unit is missing a carbon in a non-regioregular fashion.

In a first experiment, **124** was deposited from a Knudsen cell evaporator in ultrahigh vacuum onto a Au(111) surface held at 24 °C. Figure 40a, shows a surface image after deposition but before annealing, and one can clearly observe the molecule adsorb to the surface edges and form extended self-assembled islands. Upon annealing to 200 °C (ramp rate = 1K/min), some polymeric strutures are observed (Figure 40b), which was encougarging enough to press onward with the synthesis. After anneal to 400 °C (ramp rate = 1K/min), we were elated to observe highly regular, fully planarized long GNRs (Figure 40c). The apparent edge state corresponds well with previous report of edge state of 7-AGNR,[85] which confirms that the majority of GNRs are terninatated appropriately.

However, a cause for concern in the fidelity of the proposed reaction was brought forward after a closer inspection - any given long ribbon appears somewhat kinked, with seemingly random bends left/right relative to the polymerization axis. BRSTM imaging was employed to fully ascertain the atomic structure of the ribbon. It appears that every monomer unit has a poignant yet persistent defect of missing one carbon atom per unit. Judging from multiple BRSTM samples, it appears the left/right side (relative to polymerization axis) of the defect alternates regularly, but the up/down side (relative to the polymerization axis of symmetry of the monomer unit) appears to be random. Figure 40, panel (d), demonstrates this in a BRSTM image / side-by-side carbon skeleton outline structure of the apparent ribbon. We have not been able to observe a desired Clar goblet units as a part of any GNR that we have analyzed with BRSTM (n=10).

Additional experiments with the iodinated precursor **129** and a non-halogenated **128** are shown in Figure 41. In the case of iodianted precursor **129** was akin to the case of the brominated precursor, where the formation of GNRs is observed, but the methyl group excision defect can be observed in each monomer subunit as illustrated in a sample BRSTM image (Figure 41b). The non-halogenated precursor has yielded a medley of isolated small molecules on the surface, with some of them being dimer units (Figure 41e) which was surprising. Chronologically, this experiment was performed after the halogenated precursor experiments, with the rationale to confirm that no robust polymerization happens without the halogen functionalization. The reactivity of the monomer outside of the polymer scaffold was therefore briefly assessed, but no additional samples were prepared beyond what is shown in Figure 41c-e, as our focus was on accessing the 5/7-AGNR superlattice.

At this junction, Fasel group reported their studies toward the Clar goblet, which focuses on the single molecule reactivity of **128** on Au(111)[147] and the magnetic properties of this unique nanographene segment. The pristine Clar goblet is observed on the surface, along with a few oligomeric structures, and the electronic structure of Clar goblet is reported along with unique magnetism properties. This surface-induced reactivity of **128** certainly differs from what is observed in our attempts to cyclodehydrogenate the 5/7–AGNR precursor polymers that are discussed in Figure 40b. With this information in hand, we have rationalized that the 5-membered ring formation is induced by the polymer superstructure (possibly due to the restriction of certain surface adsorption in our polymer due to the interlocked anthracene subunits). The investigation of the electronic structure was not performed due to the inability to procure an atomically precise 5/7–AGNR superlattice.

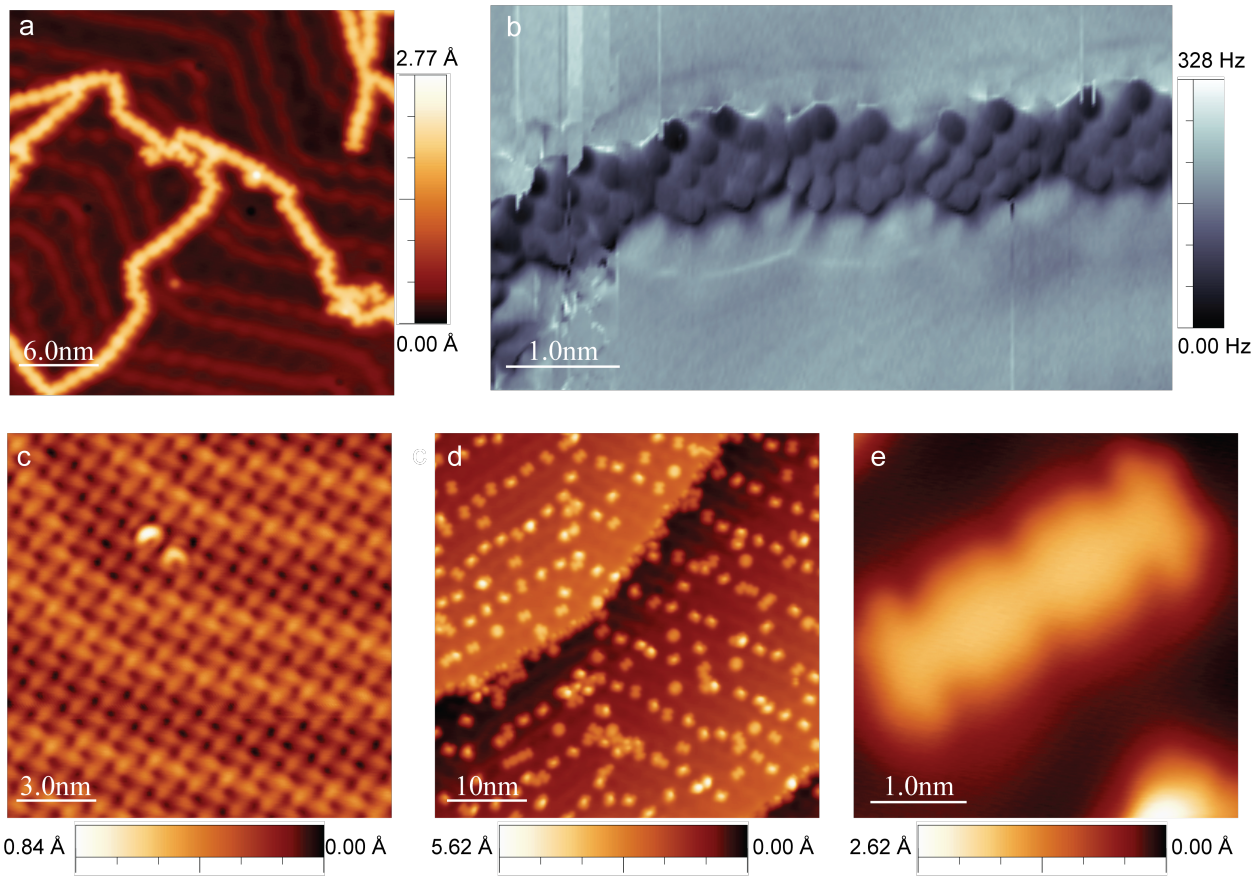

Figure 41: Additional experiments with the "Clar goblet" precursor series. (a) Iodinated monomer **129** as annealed on Au(111) surface to 350 °C. (b) Bond-resolved STM image of a representative ribbon in the sample from (a) – 5-membered ring defects are observed in *each* monomer unit. (c) **128** as deposited onto a Au(111) surface helt at 24 °C. (d) An image of the surface after the anneal of sample from (c) to 300 °C, which shows a variety of planar isolated molecules. (e) An observed dimer unit of the Clar goblet unit, which is in correspondence with the report from Fasel group.[147]

4.3.2 ext-5/7-AGNR junction - extending the 5- segment

At the outset of the study, the extension of the 5/7-AGNR segment is intended to improve our understanding of the superlattice heterojunction lengths as it relates to the hopping parameter *t*. With data for both 5/7-AGNR and ext-5/7-AGNR, it would be possible to directly correlate the change in length of the 5-segments with the change in *t*, which would be a good step forward in correlating the theoretical predictions of the hopping parameters from the tight-binding calculations with experimental results. To date, the experimental segment length change in a topological heterojunction in a GNR has not been investigated. Unfortunately, the atomically precise 5/7-AGNR was not successful, as described in previous section. In any case, I was interested in investigaing the tetramethylpyrene-based monomer architecture toward ext-5/7-AGNR for the purpose of obtaining more information about the unexpected 5-membered ring formation in the 5/7-AGNR.

I have hypothezied that changing the length of the 5-segment will be easier synthetically than changing the length of 7-segment for fine-tuning the electronics of the junction, if successful. Retrosynthetically, a tetramethyldibromopyrene **127** should serve as a precursor to **125** using the same lithium-halogen exchange/anthrone quench strategy as I have used with the original monomer **124** (Scheme 38, right side). Toward **125**, I have tested two approaches: (1) stepwise buildup of the pyrene unit via dithiacyclophane strategy (Scheme 42), and (2) direct functionalization of pyrene core (Scheme 43).

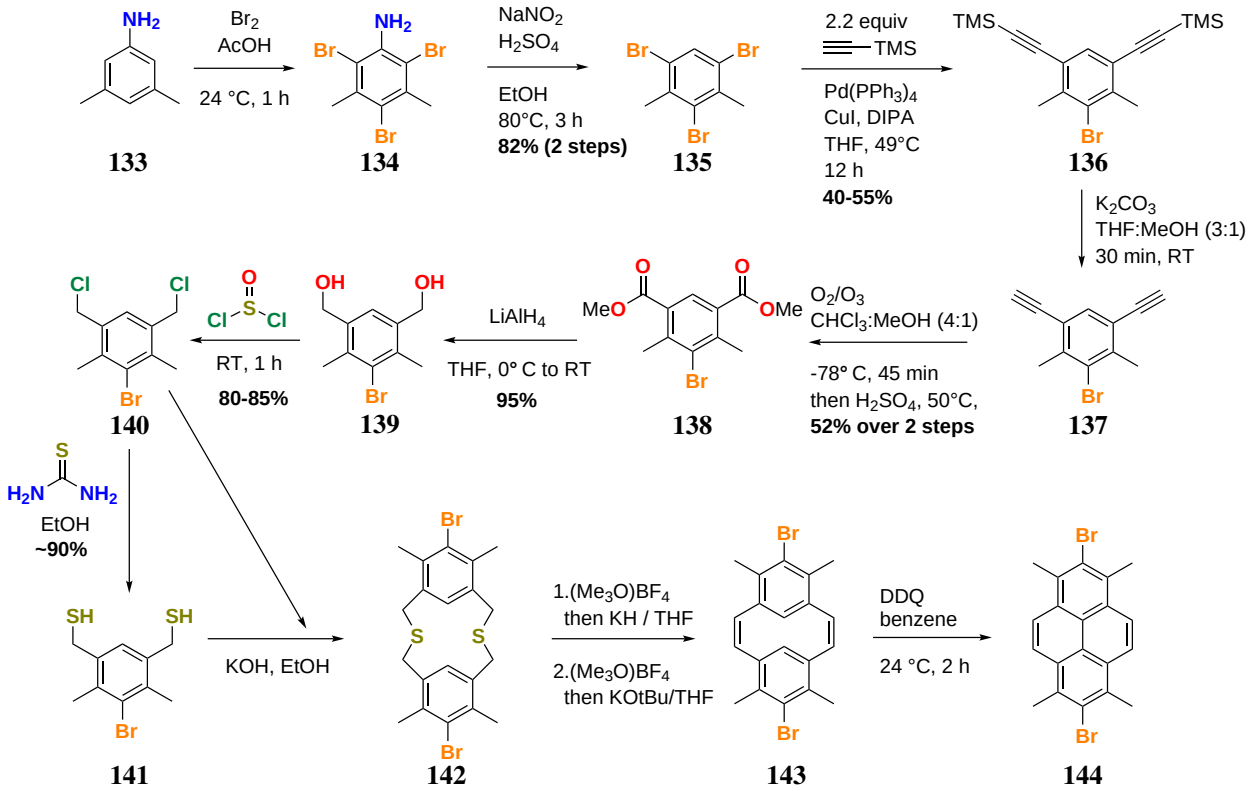

Scheme 42: Synthetic route towards ext-5/7-AGNR via the dithiacyclophane

The first approach via the dithiacyclophane was inspired by the work of Mitchell and Carruthers,[148] where a strategy of the assembling a substituted pyrene from two symmetrical blocks

is reported. In the original report, an aromatic dihalide is reacted with an aromatic dithiol at low dilution conditions in order to obtain a dithiametacyclophane that defines the desired pyrene substitution, and then a sequence of Stevens rearrangement followed by Hoffmann elimination was utilized to remove the sulfur linkages and to the metacyclophane of choice. At the last step mild DDQ oxidation conditions are used to oxidize the metacyclophane to the target pyrene. After the initial report, this method has been reported for the assembly of multiple substituted pyrenes.[149]

Scheme 42 outlines the forward synthesis via the cyclophane route. The synthesis of ext-5/7-AGNR precursor began with 3,5-dimethylaniline, and it's electrophilic bromination to exhaustively functionalize every available position on the ring to obtain **134**. The diazonium salt is then generated and reduced by treatment of **134** with $NaNO_2$/H_2SO_4/EtOH conditions, which results in a 1,3,5-tribromo-2,4-dimethylbenzene **135**. At this stage, I decided to employ an ozonolysis strategy to install a benzylic alcohol moeties as in **139**. A sterically-directed Sonogashira cross-coupling with (trimethylsilyl)acetylene has resulted in **136**. This particular set of conditions requires very careful temperature control – running this reaction at 45 °C does not result in satisfactory conversion, whereas increasing the reaction temperature to above 50 °C results in a inseparable mixture of di- and tri-alkynylated dimethylbenzene – the regioselectivity of the cross-coupling is negated. It was found that 49 °C is an ideal temperature to obtain approximately 45-55% yield in 12 hours and minimize the amount of trialkynyl species generated. TMS-protected diethynyldimethylbenzene **136** is purified by column chromatography, and TMS groups are deprotected with generic mild basic conditions to yield **137**, which was moved forward to the ozonolysis procedure without further purification.

The primary product of alkyne ozonolysis after aqueous workup is a carboxylic acid–it is with that expectation that the reactant mixture is ozonolyzed in presence of MeOH, is quenched with excess MeOH, and is heated with cat. H_2SO_4 after ozonolysis is complete in order to assure that the product is isolated as a methoxy ester, which is easily purifiable by chromatography. From this point, the forward synthesis of the dimerization reactants is straightforward – the $LiAlH_4$ ester reduction of **138** is followed by treatment with thionyl chloride to obtain **140** in excellent yield. The batch is separated in two equal amounts, and half of the material is converted to a dithiol **141** with assistance of thiourea followed by an acidic workup.

With **141** and **140**, the stage has been set for the marcocyclization toward dithiametacyclophane. A slow reverse addition of both starting materials to excess of KOH in boiling EtOH is employed in order to maximize the formation of the cyclic dimer rather than a linear polymer, which is a realistic side product in this reaction. Yields of up to 60% were achieved. However, the Stevens rearrangement / Hoffmann elimination condition were not successful in procuring a scalable amount of the dibromopyrene **144**. Miligram quantities of the dibromopyrene **144** were isolated by column chromatography, but it was certainly not enough to move forward. With several bottlenecks along the way, the synthetic approach toward the extended 5/7-AGNR junction precursor must be reassessed. Firstly, the sterically-controlled Sonogashira coupling must be performed on multigram scale, which levies injustifiable cost of Pd(0) precatalyst. Secondly, the conversion of metadithiacyclophane **142** to metacyclophane **143** is limited by the solubility of the product, and it does not furnish reasonable throughput of the material on scale. Lastly, the neccessity of the column chromatography at the tetramethylpyrene juncture cannot be avoided, and the lack of solubility of **144** greatly complicates the purification and throughput of the material. It is with this rationale that this synthetic route was abandoned, but it was nevertheless a great training experience in ozonolysis chemistry, reduction / oxidation transformations, and simple substitution chemistry.

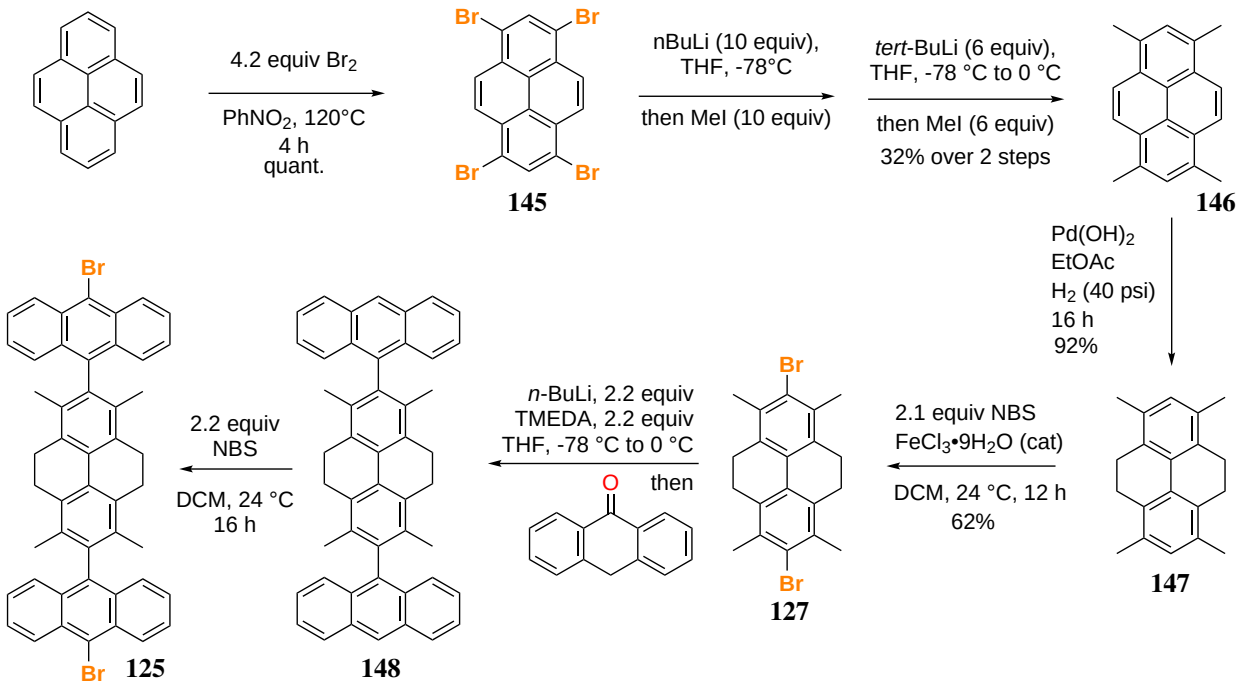

Scheme 43: Synthetic route towards ext-5/7-AGNR via **125**

The second approach was based on the direct functionalization of pyrene core. Starting directly from pyrene, an exhaustive elecrophilic bromination of pyrene was performed to yield the tertabromopyrene **145** quantitatively. Even though characterization of the material is impossible by solution state NMR, the transformation is omnipresent in literature, and the regioselectivity has been clarified via later functionalization in a multitude of organic materials.[149] Toward the desired product, the two-stage lithium-halogen exchange / iodomethane quench protocol was employed, which was followed directly from a previous report by Li *et al.*[150] to obtain 1,3,6,8-tetramethylpyrene **146** in 32% yield.

In order to effect the electrophilic substitution reactivity at 2- and 7- positions of the resulting tetramethylpyrene **146**, the palladium-catalyzed reduction of the pyrene was performed with $Pd(OH)_2$/C and 35 psi of H_2 in pressurized Parr bomb, which results in **147** in excellent yield. The bromination is accomplished via treatment of **147** with NBS with catalytic $FeCl_3$. The dibromotetrahydropyrene **127** is brought up to scale (the hydrogenation was limited by the size and availability of the Parr bomb, and could only be performed at ∼200 mg scale efficiently and with high purity) and the optimization of the conditions to install the anthracene units was performed.

Table 7: Conditions screen for lithium-halogen exchange / anthrone quench toward **148**

no.	reagent	Li equiv	solvent, T, of Li-X exchange	T after anthrone add-n	**148** yield	additive
1	BuLi	2.0	Et_2O, − 78 °C to 0 °C	0 °C to 24 °C	N.R	n/a
2	BuLi	1.0	THF, −78 °C	−78 °C to 24 °C	detected	n/a
3	tBuLi	4.4	THF, −78 °C to 0 °C	0 °C to 24 °C	∼ 1%	n/a
4	BuLi	2.0	THF, −78 °C to 0 °C	0 °C to 24 °C	5.5%	TMEDA

Dibromotetrahydropyrene **127** was subjected to an array of lithium-halogen exchange / anthrone quench conditions which is outlined in Table 7. After treating the dibromopyrene **127** with 1.0 equiv of BuLi, the double Li-X exchange product was nevertheless detected by MALDI. Therefore I have decided to push the material forward with a double Li-X exchange, as the purification of the mono-anthracenylpyrene proved challenging via column chromatography / recrystallization. This is in stark comparison with synthesis of Clar goblet precursor **128**, where the stepwise anthracene installation is essential. The final carbon skeleton **148** was obtained in 5.5% yield (no further optimization besides the results tabulated in Table 7), and the final double bromination with NBS has been accomplished in 15% isolated yield after accounting for multiple recrystallizations needed to achieve desired purity for the surface deposition. The monomer **125** is awaiting surface studies, but the COVID–19-related setbacks have pushed the instrument schedule behind so the analysis of the reactivity of this monomer will be reported in a separate work.

In summary, two types of monomer for 5/7-AGNR superlattice junction were prepared. The first family (**128**, **124**, **129**) was a Clar goblet-inspired venture, which resulted in a the GNR formation with a poignant yet persistent defect of missing one carbon atom per unit cell. The carbon loss position is found to alternate along the width of the ribbon, but is completely random along the axis of polymerization. The defect is deduced to be a feature of the polymer, as no temperature conditions resulted in a formation of the proposed GNR, and the monomer **128** was reported by Fasel group and independently confirmed by our results to yield the Clar goblet as a single molecule. The second type of monomer, **125**, possesses an extended tetramethylpyrene core rather than a tetramethylbenzene core and is expected to result in ext-5/7-AGNR. The synthetic access to the monomer **125** has been explored, and the pyrene route has proven more scalable than that of dithiacyclophane. Monomer **125** is awaiting surface reactivity investigation, and its reactivity will become a deteriming factor in investigating the electronic structure the 5/7–AGNR superlattice.

5 Supporting Information

5.0.1 Materials and General Methods

Unless otherwise stated, all manipulations of air and/or moisture sensitive compounds were carried out in oven-dried glassware, under an atmosphere of nitrogen. All solvents and reagents were purchased from Alfa Aesar, Spectrum Chemicals, Acros Organics, TCI America, and Sigma-Aldrich and were used as received unless otherwise noted. Organic solvents were dried by passing through a column of alumina and were degassed by vigorous bubbling of N_2 through the solvent for 20 min. Flash column chromatography was performed on SiliCycle silica gel (particle size 40–63 μm) unless specified otherwise. Thin layer chromatography was carried out using SiliCycle silica gel 60 Å F-254 precoated plates (0.25 mm thick) and visualized by UV absorption. All ^{1}H and ^{13}C NMR spectra were recorded on Bruker AV-700, AV-600, NEO-500, and AV-500, AVB-400, and AV-300 MHz spectrometers, and are referenced to residual solvent peaks ($CDCl_3$ ^{1}H NMR = 7.26 ppm, ^{13}C NMR = 77.16 ppm; CD_2Cl_2 ^{1}H NMR = 5.32 ppm, ^{13}C NMR = 53.84 ppm; C_6D_6 ^{1}H NMR = 7.16 ppm, ^{13}C NMR = 128.06 ppm; TCE-d_2 ^{1}H NMR = 6.00 ppm, ^{13}C NMR = 73.78 ppm). All ^{13}C spectra are proton-decoupled unless otherwise noted. UC Berkeley NMR Facility is supported in part by NIH grants 1S10RR016634-01, SRR023679A, and S10OD024998.

GC/MS was performed on Agilent Technologies 7890A GC system in tandem with 5975C VL mass spec detector. ESI mass spectrometry was performed on a Finnigan LTQFT (Thermo) spectrometer in positive ionization mode. MALDI mass spectrometry was performed on a Voyager-DE PRO (Allied Biosystems Voyager System 6322) in positive mode using a matrix of dithranol or 2,5-dihydroxybenzoic acid. Raman characterization of the GNRs were made with a Horiba Jobin Yvon LabRAM ARAMIS Raman microscope using 532 nm diode laser with $<$10 mW power each and a 100x objective lens, resulting in a laser spot size $<$1 μm. No thermal effects were observed under these measurement conditions, and at least three spectra from different points was collected for each sample. IR spectroscopy was performed with Thermo Scientific Nicolet 6700 FTIR.

STM imaging and STS were conducted in UHV ($p <$ 5-11 Torr) using an Omicron LT STM held at T = 4.5 K. STM images and dI/dV maps were recorded in constant current mode with a CO-functionalized W tip. STS point spectra were acquired at constant height (open feedback loop, tip set points indicated in figure captions) using the lock-in technique with f = 455 Hz and V_{mod} = 10 mV. The W tip was prepared by repeated indentation into the Au(111) substrate prior to each measurement, and bare Au background spectra were recorded before and after measuring each GNR.

5.0.2 Synthetic procedures.

Chapter 2.

Bis(2,4-dibromophenyl)amine (**20**): A 300 mL Erlenmeyer flask was charged with NBS (8.4 g, 47 mmol) in acetone (150 mL) and cooled to 0 °C. Diphenylamine (2.0 g, 0.012 mol) was slowly added to the reaction mixture over 15 min. The reaction mixture was stirred for 15 min and quenched with cold H_2O (100 mL). The solid precipitate was isolated by filtration, washed with saturated aqueous $Na_2S_2O_3$ (30 mL), and H_2O (150 mL). Recrystallization from toluene yielded **20** (4.5 g, 0.0086 mmol, 78%) as colorless needles. ^{1}H NMR (400 MHz, $CDCl_3$, 22 °C) δ = 7.72 (d, J = 2.3 Hz, 2H), 7.33 (dd, J = 8.8, 2.2 Hz, 2H), 7.10 (d, J = 8.7 Hz, 2H), 6.32 (s, 1H) ppm; ^{13}C NMR (151 MHz, $CDCl_3$, 22 °C) δ = 139.1, 135.6, 131.3, 119.2, 115.1, 114.1 ppm; HRMS (EI) m/z: $[C_{12}H_7NBr_4]^+$ calcd. 484.7271 found 484.7271.

2,4-dibromo-N-(2,4-dibromophenyl)-N-(ethoxymethyl)aniline (**21**): A flame dried 200 mL Schlenk flask was charged under N_2 with 2 (2.00 g, 4.12 mmol) in THF (120 mL) and cooled to –78 °C. LDA (2.0 M in THF, 2.40 mL, 4.80 mmol) was added dropwise and the reaction mixture stirred for 1 h at –78 °C. Chloromethyl ethyl ether (0.76 mL, 8.2 mmol) was added, the reaction mixture allowed to warm to 24 °C and stirred for 4 h. The reaction mixture was quenched with saturated aqueous $NaHCO_3$. The combined organic phases were washed with H_2O, dried over $MgSO_4$ and concentrated on a rotary evaporator. Column chromatography (SiO_2; hexane) yielded **21** (1.46 g, 2.67 mmol, 65%) as a colorless solid. ^{1}H NMR (400 MHz, $CDCl_3$, 22 °C) δ = 7.69 (d, J = 2.3 Hz, 2H), 7.36 (dd, J = 8.6, 2.3 Hz, 2H), 7.20 (d, J = 8.6 Hz, 2H), 4.99 (s, 2H), 3.39 (q, J = 7.0 Hz, 2H), 1.54 (s, 1H), 1.10 (t, J = 7.0 Hz, 3H) ppm; ^{13}C NMR (150 MHz, $CDCl_3$, 22 °C) δ = 145.1, 136.5, 131.3, 128.0, 120.8, 117.9, 83.2, 65.0, 15.4 ppm; HRMS (EI) m/z: $[C_{15}H_{13}NOBr_4]^+$ calcd. 542.7690 found 542.7703.

10-(anthracen-9-yl)-2,8-dibromo-5-(ethoxymethyl)-5,10-dihydrodibenzo[b,e][1,4]azaborinine (**23**): A 100 mL Schlenk flask was charged with 9-bromoanthracene (500 mg, 1.94 mmol) in Et_2O (40 mL) and cooled to –78 °C. n-Butyllithium (2.0 M in THF, 0.80 mL, 1.6 mmol) was added and the reaction mixture was stirred for 30 min at –78 °C. Trimethyl borate (221 mg, 2.14 mmol) is added and the reaction mixture is warmed to 24 °C. The reaction mixture is concentrated under vacuum. A second 100 mL round bottom flask was charged with 3 (706 mg, 1.30 mmol) in Et_2O and cooled to –78 °C. n-Butyllithium (2.0 M in THF, 1.04 mL, 2.60 mmol) was added and the reaction mixture stirred for 30 min at –78 °C. The reaction mixture is cannulated into the Schlenk flask containing the boronic ester and stirred for 15 min at 24 °C. The reaction mixture was quenched with saturated aqueous NaCl (25 mL) and extracted with CH_2Cl_2 twice (20 mL each extraction). The combined organic layers were dried over $MgSO_4$ and concentrated on a rotary evaporator. Column chromatography (SiO_2, 3:1 hexanes/$CHCl_3$) yielded **23** (350 mg, 0.61 mmol, 42%) as a yellow crystalline solid. ^{1}H NMR (600 MHz, $CDCl_3$, 22 °C) δ = 8.57 (s, 1H), 8.12 (d, J = 8.6 Hz, 2H), 7.82 (dd, J = 9.2, 2.4 Hz, 2H), 7.74 (d, J = 9.3 Hz, 2H), 7.59 (d, J = 2.5 Hz, 2H), 7.44 (dd, J = 8.5, 6.5 Hz, 2H), 7.34 (d, J = 8.6 Hz, 2H), 7.26 (s, 1H), 7.18 (dd, J = 8.6, 6.5 Hz, 2H), 5.88 (s, 2H), 3.93 (q, J = 7.0 Hz, 2H), 1.46 (t, J = 7.0 Hz, 3H) ppm; ^{13}C NMR (150 MHz, $CDCl_3$, 22 °C) δ = 145.0, 139.7, 137.3, 134.5, 131.4, 130.1, 128.9, 127.0, 125.1, 124.7, 117.8, 114.7, 79.1, 64.0, 15.4 ppm; HRMS (EI): m/z: $[C_{29}H_{22}BNOBr_2]^+$ calcd. 571.0141 found: 571.0143.

10-(anthracen-9-yl)-5-(ethoxymethyl)-5,10-dihydrodibenzo[b,e][1,4]azaborinine (**24**): A 50 mL Schlenk flask was charged with **23** (65 mg, 0.114 mmol) in THF (20 mL) and cooled to –78 °C. Butyllithium (2.0 M in THF, 0.10 mL, 0.25 mmol) was added and the reaction mixture stirred for 30 min at –78 °C. The reaction mixture is quenched with aqueous HCl (1 M, 1 mL) and extracted with CH_2Cl_2 (10 mL). The combined organic phases were dried over $MgSO_4$ and concentrated on a rotary evaporator. Column chromatography (SiO_2, 80:20 hexanes/AcOEt) yielded **24** (46 mg, 0.11 mmol, 98%) as a yellow solid. ^{1}H NMR (500 MHz, $CDCl_3$, 22 °C) δ = 8.54 (d, J = 7.2 Hz, 1H), 8.09 (d, J = 8.6 Hz, 2H), 7.86 (d, J = 8.7 Hz, 2H), 7.76 (ddd, J = 8.6, 6.6, 1.8 Hz, 2H), 7.59–7.54 (m, 2H), 7.47 (d, J = 8.6 Hz, 2H), 7.41 (dd, J = 8.6, 6.3 Hz, 2H), 7.16–7.10 (m, 2H), 7.02 (t, J = 7.1 Hz, 2H), 5.97 (d, J = 5.5 Hz, 2H), 3.97 (q, J = 7.1 Hz, 2H), 1.48 (t, J = 7.0 Hz, 3H) ppm; ^{13}C NMR (126 MHz, $CDCl_3$, 22 °C) δ = 146.5, 138.2, 134.5, 134.2, 131.4, 130.7, 128.7, 126.2, 125.0, 124.2, 120.8, 115.4, 79.0, 63.7, 15.5 ppm; HRMS (EI) *m*/*z*: $[C_{29}H_{24}BNO]^+$ calcd. 413.1951 found 413.1957.

10-(anthracen-9-yl)-5,10-dihydrodibenzo[b,e][1,4]azaborinine (**17**): A 20 mL scintillation vial was charged with **24** (46 mg, 0.11 mmol) in AcOEt (10 mL). Aqueous HCl (12 M, 0.5 mL) was added and the reaction mixture stirred for 30 min at 24 °C. The reaction mixture was neutralized with a saturated aqueous Na_2CO_3 and extracted with CH_2Cl_2 (10 mL). The combined organic phases were dried over $MgSO_4$ and concentrated on a rotary evaporator to yield **17** (39 mg, 0.11 mmol, 99%) as a yellow solid. ^{1}H NMR (500 MHz, $CDCl_3$, 22 °C) δ = 8.69 (s, 1H), 8.54 (s, 1H), 8.09 (d, J = 8.5 Hz, 2H), 7.69 (ddd, J = 8.5, 6.9, 1.7 Hz, 2H), 7.59–7.49 (m, 6H), 7.41 (dd, J = 8.5, 6.5 Hz, 2H), 7.17–7.11 (m, 2H), 6.98 (t, J = 7.3 Hz, 2H) ppm; ^{13}C NMR (126 MHz, $CDCl_3$, 22 °C) δ = 143.6, 137.7, 134.5, 133.5, 131.4, 130.7, 128.7, 126.2, 124.9, 124.1, 120.3, 116.3 ppm; HRMS (EI) *m*/*z*: $[C_{26}H_{18}BN]^+$ calcd. 355.1532 found 355.1536.

10-(10-bromoanthracen-9-yl)-5-(ethoxymethyl)-5,10-dihydrodibenzo[b,e][1,4]azaborinine (**25**): A 20 mL scintillation vial was charged with **24** (74 mg, 0.18 mmol) in CH_2Cl_2 (10 mL). NBS (31.9 mg, 0.180 mmol) was added, and reaction was stirred for 1 h at 24 °C. The reaction mixture was quenched with H_2O (5 mL) and extracted with CH_2Cl_2 twice (5 mL each extraction). The combined organic phases were dried over $MgSO_4$ and concentrated on a rotary evaporator. Column chromatography (SiO_2, 3:2 hexanes/$CHCl_3$) yielded **25** (58 mg, 0.12 mmol, 66%) as a yellow solid. ^{1}H NMR NMR (500 MHz, $CDCl_3$, 22 °C) δ = 8.63 (d, J = 8.9 Hz, 2H), 7.87 (d, J = 8.8 Hz, 2H), 7.77 (ddd, J = 8.8, 6.9, 1.8 Hz, 2H), 7.57–7.50 (m, 4H), 7.47 (d, J = 8.6 Hz, 2H), 7.19–7.13 (m, 2H), 7.03 (t, J = 7.3 Hz, 2H), 5.96 (s, 2H), 3.97 (q, J = 7.0 Hz, 2H), 1.48 (t, J = 7.0 Hz, 3H) ppm.

10-(10-bromoanthracen-9-yl)-5,10-dihydrodibenzo[b,e][1,4]azaborinine (**26**): A 20 mL scintillation vial was charged with **25** (46 mg, 0.11 mmol) in AcOEt (10 mL). Aqueous HCl (12 M, 0.5 mL) was added and the reaction mixture stirred for 30 min at 24 °C. The reaction mixture was neutralized with a saturated aqueous Na_2CO_3 and extracted with CH_2Cl_2 (10 mL). The combined organic phases were dried over $MgSO_4$ and concentrated on a rotary evaporator to yield **26** (39 mg, 0.11 mmol, 99%) as a yellow solid. ^{1}H NMR (500 MHz, $CDCl_3$, 22 °C) δ = 8.77 (s, 1H), 8.67–8.62 (m, 2H), 7.70 (m, 2H), 1.32–1.20 (m, 9H), 7.60–7.50 (m, 8H), 2.07–2.03 (m, 5H), 7.21–7.13 (m, 2H), 7.02–6.96 (m, 2H) ppm; HRMS (MALDI-TOF) *m*/*z*: $[C_{26}H_{17}BNBr]^+$ calcd. 434.0666 found: 434.0479.

bis(2-bromophenyl)amine (**34**): A 200 mL Schlenk flask is charged with 2-bromo-1-iodobenzene (4.0 g, 0.014 mol), 2-bromoaniline (2.4 g, 0.014 mol), $Pd(OAc)_2$ (79 mg, 0.35 mmol), and DPEPhos (380 mg, 0.71 mmol). The atmosphere is evacuated for 5 min and refilled with N_2 (three cycles), then 100 mL of dry, degassed toluene is added. The reaction mixture is preheated to 90 °C, NaO^tBu (1.6 g, 0.017 mol) is added, then the reaction mixture is stirred for 12 h. The reaction mixture is cooled, diluted with AcOEt, filtered through Celite, and the filtrate is washed with saturated aqueous NaCl solution. Column chromatography (SiO_2, 2:98 AcOEt:hexanes) yielded **34** (4.06 g, 88% yield). ^{1}H NMR NMR (400 MHz, $CDCl_3$) δ = 7.65 (dd, J = 8.0, 1.5 Hz, 2H), 7.37 (dd, J = 8.2, 1.6 Hz, 2H), 7.33 – 7.24 (m, 2H), 6.91 (m, 2H), 6.54 (s, 1H) ppm; GC/MS: m/z $[C_{12}H_9Br_2N]^+$ calcd. 326.9 found 326.9

bis(2-methoxyphenyl)amine (**35**): A 100 mL Schlenk flask is charged with o-anisidine (2.5 g, 0.0203 mol, 1.0 equiv), 2-iodoanisole (4.75 g, 0.0203 mol), $Pd(OAc)_2$ (15 mg), DPEPhos (30 mg), and dry, degassed toluene (50 mL). Sodium *tert*-butoxide (2.15 g, 0.022 mol) is added under N_2 blanket flow, and the reaction mixture is heated at 85 °C for 4 h. The reaction mixture is cooled, diluted with EtOAc, and the organic phase is washed with saturated aqueous NaCl solution (30 mL) twice. Column chromatography (3:97 EtOAc:hexanes) yielded **35** (4.57 g, 98% yield) as an oil. ^{1}H NMR (600 MHz, $CDCl_3$) δ = 7.38 (m, 2H), 6.90 (m, 6H), 3.90 (s, 6H) ppm; ^{13}C NMR (151 MHz, $CDCl_3$) δ = 149.2, 132.6, 120.9, 120.3, 115.7, 110.7, 55.8 ppm; GC/MS: m/z $[C_{14}H_{15}NO_2]^+$ calcd. 229.1 found 229.1. ^{1}H NMR, ^{13}C NMR and mass spectra are in accordance with previous literature report.[151]

N,N-bis(2-methoxyphenyl)anthracen-9-amine (**36**: A 200 mL Schlenk flask is charged with **35** (4.57 g, 0.02 mol), **37** (5.14 g, 0.02 mol), $Pd(OAc)_2$ (25 mg), and dry toluene (100 mL). Sodium *tert*-butoxide is added as a solid under N_2 blanket flow, and a solution of $P(^tBu)_3$ in PhMe (25 mg of ligand) is added via syringe. The reaction is heated at 100 °C for 24 h, then more $Pd(OAc)_2$/$P(^tBu)_3$ is added (25 mg each), and the reaction is heated at 100 for another 24 h. The reaction mixture is cooled down, diluted with EtOAc, and the organic layer is washed with saturated aqueous NaCl solution (150 mL) twice and DI H_2O (100 mL) twice. Column chromatography (5:95 EtOAc/hexanes) followed by a recrystallization from hexanes/CH_2Cl_2 yielded **36** (4.76 g, 58% yield) as an orange solid. ^{1}H NMR (600 MHz, $CDCl_3$) δ = 8.40 (s, 1H), 8.23 (d, J = 8.8, 2H), 8.01 (d, J = 8.4 Hz, 2H), 7.43 – 7.37 (m, 2H), 7.37 – 7.31 (m, 2H), 6.93 – 6.86 (m, 4H), 6.71 – 6.63 (m, 4H), 3.51 (d, J = 0.9 Hz, 6H) ppm; ^{13}C NMR (151 MHz, $CDCl_3$) δ = 152.4, 140.6, 138.9, 132.7, 130.7, 128.7, 126.2, 125.6, 125.3, 124.9, 123.2, 122.4, 121.1, 112.5, 55.9 ppm; GC/MS: m/z $[C_{28}H_{23}NO_2]^+$ calcd. 405.2 found 405.2.

(anthracen-9-ylazanediyl)bis(2,1-phenylene) bis(trifluoromethanesulfonate) (**31**): A dry 50 mL round bottom flask is charged with **36** (1.0 g, 2.47 mmol) and dry, degassed CH_2Cl_2 (25 mL). The reaction mixture is cooled to 0 °C, and BBr_3 (neat, 1.0 mL, 2.64 g, 9.86 mmol, 4.4 equiv) is added dropwise. The reaction is kept at 0 °C for additional h after BBr_3 addition is complete, and then warmed to room temperature over 3 h. Plug column chromatography (silica, 2:98 EtOAc hexanes (100 mL), then 15 EtOAc % / hexanes (300 mL), last 300 mL of eluent is collected) yielded the dihydroxy intermediate (571 mg, 1.51 mmol, 51% yield).

The 100 mL Schlenk flask is charged with the crude dihydroxy intermediate (571 mg, 1.51 mmol)

and dry CH_2Cl_2 (50 mL), and reaction mixture is cooled to 0 °C. 2,6-lutidine (0.44 mL, 403 mg, 3.33 mmol, 2.2 equiv) is added, followed by dropwise addition of Tf_2O (0.56 mL, 942 mg, 3.33 mmol, 2.2 equiv) . The reaction mixture is warmed to 24 °C over 5 h and quenched with saturated ammonium chloride solution (50 mL). Aqueous layer is extracted with CH_2Cl_2, and the combined organic phase is dried over $MgSO_4$. Column chromatography (3:97 EtOAc/hexanes) yielded **31** (467 mg, 0.72 mmol, 48% yield) as a yellow solid. ^{1}H NMR (600 MHz, $CDCl_3$) δ = 8.56 (s, 1H), 8.12 (d, J = 8.5 Hz, 2H), 8.08 (d , J = 8.5 Hz, 2H), 7.51 – 7.39 (m, 6H), 7.03 (m, 4H), 6.79 (dd, J = 7.5, 2.4 Hz, 2H) ppm; ^{13}C NMR (151 MHz, $CDCl_3$) δ = 141.4, 139.0, 136.6, 132.7, 130.1, 129.2, 128.6, 128.3, 127.6, 125.8, 125.6, 123.9, 123.3, 121.4, 118.2 (q, CF_3 group, J = 320 Hz) ppm; ^{19}F NMR (565 MHz, $CDCl_3$) δ = −74.5 ppm; MALDI-TOF: m/z $[C_{28}H_{17}F_6NO_6S_2]^+$ calcd. 641.0401 found 641.0683.

bis(2-chlorophenyl)amine (**33**): A 100 mL Schlenk flask is charged with 2-chloroaniline (1.0 g, 7.84 mmol, 1.0 equiv), 1-bromo-2-chlorobenene (1.5 g, 7.84 mmol), $Pd(OAc)_2$ (15 mg), DPEPhos (30 mg), and dry, degassed toluene (50 mL). NaO^tBu (750 mg, 8.5 mmol) is added under N_2 blanket flow, and the reaction mixture is heated at 85 °C for 4 h. The reaction mixture is cooled and filtered through Celite. Column chromatography (hexanes) yielded **33** (1.81 g, 97% yield) as a clear oil. ^{1}H NMR (600 MHz, $CDCl_3$) δ = 7.42 (d, J = 8.1 Hz, 2H), 7.33 (d, J = 7.8 Hz, 2H), 7.19 (dt, J = 7.8, 1.5 Hz, 2H), 6.92 (dt, J = 8.1, 1.5 Hz, 2H), 6.44 (s, 1H) ppm; ^{13}C NMR (151 MHz, $CDCl_3$) δ = 138.9, 130.1, 127.5, 123.8, 122.2, 117.9 ppm; GC/MS: m/z $[C_{12}H_9NCl_2]^+$ calcd. 238.1 found 238.1.

N,N-bis(2-chlorophenyl)anthracen-9-amine (**29**): A 200 mL Schlenk flask was charged under N_2 with diphenyl amine (1.0 g, 5.90 mmol), 9-bromoanthracene (1.38 g, 5.35 mmol), $Pd(OAc)_2$ (60 mg, 0.25mmol), $P(^tBu)_3$ (105 mg, 0.50 mmol), and NaO^tBu (720 mg, 7.50 mmol) in toluene (85 mL). The reaction mixture was stirred for 3 h at 110 °C. The reaction mixture was cooled to 24 °C, diluted with AcOEt (40 mL) and filtered through a plug of Celite. The organic phase was washed with H_2O, dried over $MgSO_4$ and concentrated on a rotary evaporator. Column chromatography (SiO_2, 39/1 hexanes/AcOEt) yielded **29**. (1.57g, 4.5 mmol, 85%) as a yellow solid. ^{1}H NMR (600 MHz, $CDCl_3$) δ = 8.47 (s, 1H), 8.21 (d, J = 8.5 Hz, 2H), 8.03 (d, J = 8.5, 2H), 7.45-7.39 (m, 4H), 7.37 – 7.30 (m, 2H), 7.01 – 6.87 (m, 4H), 6.83 (d, J = 7.9 Hz, 2H) ppm; ^{13}C NMR (151 MHz, $CDCl_3$) δ = 145.3, 138.9, 132.6, 131.2, 130.7, 129.0, 127.7, 127.1, 127.0, 125.5, 124.3, 124.0 ppm; GC/MS: m/z $[C_{26}H_{17}NCl_2]^+$ calcd. 414.1 found 414.2.

2-ethynylpyrimidine (**46**): A 50 mL round bottom flask is charged with 2-bromopyrimidine (600 mg, 3.77 mmol, 1 equiv), $Pd(PPh_3)_2Cl_2$ (26.4 mg, .037 mmol, 0.01 equiv), copper (I) iodide (14.5 mg, 0.075 mmol, 0.02 equiv), and triethylamine (25 mL) as a reaction solvent. The solution is then sparged with N_2 gas for 15 min. Then trimethylsilylacetylene (389 mg, 3.96 mmol, 1.05 equiv) is added to the reaction mixture as a neat oil, immediately followed by freshly prepared solution of tri-*tert*-butylphosphine (15.2 mg, 0.075 mmol, 0.02 equiv) in THF (2 mL). The resulting reaction mixture is stirred at 45 °C for 7 h. Reaction is then diluted with EtOAc and transfeed to separatory funnel. Organic phase is washed with saturated ammonium chloride solution and with saturated aqueous NaCl solution twice, and is then dried over Na_2SO_4. Solvent is removed by rotary evaporation, and the resulting oil is passed through a silica gel plug with EtOAc as eluent. 2-((Trimethylsilyl)ethynyl)pyrimidine (470 mg, 71% yield) is isolated as a clear oil. ^{1}H NMR (500 MHz, $CDCl_3$): δ = 0.28 (s, 9H), 7.23 (t, J = 5.2 Hz, 1H), 8.72 (d, J = 5.2 Hz, 2H) ppm; ^{1}H NMR

spectrum is consistent with literature values.[152]

A 50 mL round bottom flask is charged with ((trimethylsilyl)ethynyl)pyrimidine (470 mg, 2.66 mmol), potassium carbonate (740 mg, 5.33 mmol), and 3:1 mixture of THF:MeOH (20 mL total volume) under ambient atmosphere. The reaction mixture is stirred at 24 °C as the reaction is analyzed by thin layer chromatography every 30 min. Full conversion of starting material is evident after 2 h. The reaction mixture is diluted with EtOAc, and the organic phase is washed with saturated aqueous NaCl solution twice, and then dried over Na_2SO_4. Rotary evaporation of the solvent yielded title compound (270 mg, 99% yield) as a colorless oil. ^{1}H NMR (400 MHz, $CDCl_3$) δ = 3.15 (s, 1H), 7.29 (t, J = 5.0 Hz, 1H), 8.74 (d, J = 5.0 Hz, 2H) ppm; ^{1}H NMR spectrum is consistent with literature values.[153]

1,2-di(pyrimidin-2-yl)ethyne (**47**): A 50 mL 2-neck round bottom flask is charged with 2-bromopyrimidine (413 mg, 2.66 mmol, 1 equiv), $Pd(PPh_3)_2Cl_2$ (36.5 mg, 0.052 mmol, 0.02 equiv), copper (I) iodide (19.8 mg, 0.1 mmol, 0.04 equiv), and triethylamine (25 mL) as a reaction solvent. The solution is then sparged with N_2 gas for 15 min. A second flask is charged with **46** (270 mg, 2.6 mmol, 1 equiv) in triethylamine (10 mL), and this solution is also sparged with N_2 for 15 min. Then, the solution of **46** in triethylamine is added to the 2-neck main reaction flask, immediately followed by freshly prepared solution of tri-*tert*-butylphosphine (21 mg, 0.1 mmol, 0.04 equiv) in THF (2 mL). The reaction mixture is stirred at 65 °C for 16 h. Reaction is then diluted with EtOAc and transferred to separatory funnel. Organic phase is washed with saturated ammonium chloride solution twice, with saturated aqueous NaCl solution twice, and is dried over Na_2SO_4. Rotary evaporation of solvent and column chromatography (basic alumina, 90:10 EtOAc:hexanes, R_f = 0.4) yielded **47** (133 mg, 0.73 mmol, 28% yield) as a colorless solid. ^{1}H NMR (500 MHz, CD_2Cl_2) δ = 8.79 (d, J = 4.9 Hz, 2H), 7.34 (t, J = 4.9 Hz, 1H) ppm; ^{13}C NMR (126 MHz, CD_2Cl_2) δ = 157.47, 152.20, 120.85, 84.03 ppm; GC-MS: m/z $[C_{10}H_6N_4]^+$, calcd. 182.1 found 182.1.

2,2'-(6,11-dibromo-1,4-diphenyltriphenylene-2,3-diyl)dipyrimidine (**44**): A 5 mL Schlenk tube with a Kontes stopper is charged with 1,2-di(pyrimidin-2-yl)ethyne **47** (30 mg, 0.165 mmol, 1.0 equiv) and 5,10-dibromo-1,3-diphenyl-2H-cyclopenta[l]phenanthren-2-one **48** (87 mg, 0.161 mmol, 0.98 equiv). The headspace of the tube is evacuated for 15 min and refilled with N_2 (repeated for 3 cycles). Then, 1.5 mL of nitrobenzene (99%, reagent grade) is added to the tube under N_2 blanket flow. The tube is sealed, and the reaction mixture is heated at 210 °C in a sand bath for 24 h. Upon completion the tube is cooled to 24 °C, and brown crude solid is obtained after trituration of the nitrobenzene solution with MeOH. Column chromatography (basic alumina, 50:50 EtOAc:hexanes, R_f = 0.7) yielded title compound (30 mg, 0.043 mmol, 26% yield) as a colorless solid. ^{1}H NMR (700 MHz, $CDCl_3$) δ = 8.33 (d, J = 4.9 Hz, 4H), 8.21 (d, J = 8.7 Hz, 2H), 7.65 (d, J = 2.0 Hz, 2H), 7.50 (dd, J = 8.7, 2.0 Hz, 2H), 7.23 – 7.15 (m, 6H), 7.15 – 7.09 (m, 4H), 6.83 (t, J = 4.9 Hz, 2H) ppm; MALDI-TOF: m/z $[C_{38}H_{22}N_4Br_2]^+$, calcd. 694.0191 found 696.5869. Increase in mass is likely due to a single reduction on a pyrimidine ring during ionization.

Pyrazino[2,3-g]quinoxaline (**59**): A 200 mL round bottom flask was charged with 2,5-dihydroxy-1,4-benzoquinone (4.5 g, 32.2 mmol) in H_2O (100 mL) and fitted with a reflux condenser. The reaction mixture is heated to 95 °C and stirred for 5 min before ethylenediamine (10 mL) is added to the reaction mixture. The reaction mixture is stirred at 95 °C for 1 h, cooled rapidly in a 0 °C

ice bath, and the precipitate is filtered to yield a crude brown solid. A 100 mL round bottom flask with reflux condenser is charged with the crude brown solid (1 g), 10% palladium on carbon (1.5 g), and nitrobenzene (30 mL). The reaction mixture is heated at 213 °C for 21 h. The solution is cooled to 25 °C, filtered over a medium-fritted glass funnel, and concentrated on a rotary evaporator. Column chromatography (SiO_2, EtOAc, R_f = 0.4) yielded pyrazino[2,3-g]quinoxaline **59** (175 mg, 0.96 mmol, 10%) as a colorless solid. ^{1}H NMR (500 MHz, $CDCl_3$) δ = 9.02 (s, 4H), 9.01 (s, 2H) ppm; ^{13}C NMR (125 MHz, $CDCl_3$) δ = 147.2, 141.6, 130.3 ppm;

5,10-dibromopyrazino[2,3-g]quinoxaline (**60**) A 20 mL glass vial was charged with pyrazino[2,3-g]quinoxaline **59** (175 mg, 0.96 mmol) and NBS (400 mg, 2.24 mmol) under an atmosphere of N_2. Degassed DMF (10 mL) is added, and the reaction mixture is stirred at 60 °C for 16 h. Upon cooling H_2O (10 mL) is added, and the reaction mixture is filtered and the precipitate washed with of H_2O (100 mL), and cold CH_2Cl_2 (100 mL) to yield **60** (218 mg, 0.64 mmol, 67%) as a yellow solid. ^{1}H NMR (600 MHz, $CDCl_3$) δ = 9.17 (s, 4H) ppm; The solubility of **60** in common deuterated solvents is insufficient to acquire a ^{13}C NMR spectrum.

5,10-di(anthracen-9-yl)pyrazino[2,3-g]quinoxaline (**61**): A 20 mL glass vial was charged with **60** (50 mg, 0.147 mmol), 2-(anthracen-9-yl)-4,4,5,5-tetramethyl-1,3,2-dioxaborolane (89.5 mg, 0.295 mmol), $Pd(PPh_3)_4$ (20 mg, 0.0147 mmol), Cs_2CO_3 (280 mg, 0.870 mmol), and toluene (8 mL) under an atmosphere of N_2. The vial is sealed and heated to 120 °C for 48 h. Upon cooling to 25 °C, the reaction mixture is concentrated on a rotary evaporator. The solid residue is suspended in CH_2Cl_2 and filtered. The filter cake is resuspended in H_2O (15 mL), sonicated, filtered and washed with H_2O (200 mL). The solid is resuspended in CH_2Cl_2, sonicated, filtered and washed with CH_2Cl_2 and EtOAc until the eluent is colorless. Collection of filter cake yielded **61** (40 mg, 0.076 mmol, 52%) as a red solid. FTMS (MALDI-TOF): *m/z*: $[C_{38}H_{21}N_4]^+$, calcd. 534.1844; found 534.1730. The solubility of **61** in common deuterated solvents is insufficient to acquire ^{1}H or ^{13}C NMR spectra.

5,10-bis(10-bromoanthracen-9-yl)pyrazino[2,3-g]quinoxaline (**55**): A 4 mL glass vial was charged with 5,10-di(anthracen-9-yl)pyrazino[2,3-g]quinoxaline **61** (20 mg, 0.037 mmol), and NBS (10.8 mg, 0.077 mmol). Trifluoroacetic acid (1 mL) is added, and the reaction mixture is stirred for 90 min. The reaction mixture is poured into cold aqueous 1M NaOH (15 mL), and the precipitate is isolated by filtration. Column chromatography (SiO_2, CH_2Cl_2, R_f = 0.85) yielded **55** (15 mg, 0.021 mmol, 57%) as an orange solid. ^{1}H NMR (600 MHz, CD_2Cl_2) δ = 8.75 (d, J = 8.8 Hz, 4H), 8.69 (s, 4H), 7.66 (dd, J = 8.8, 6.5 Hz, 4H), 7.35 (dd, J = 8.7, 6.5 Hz, 4H), 7.26 (d, J = 8.7 Hz, 4H) ppm; ^{13}C NMR (151 MHz, CD_2Cl_2) = 147.7, 141.4, 139.0, 132.6, 132.4, 130.7, 128.7, 127.55, 127.4, 126.6, 124.3 ppm; FTMS (ESI-TOF): *m/z* $[C_{38}H_{21}N_4Br_2]^+$, calcd. $C_{38}H_{21}N_4Br_2$ 692.0040 found 692.0034.

5,10-bis(10-iodoanthracen-9-yl)pyrazino[2,3-g]quinoxaline (**63**): A 20 mL glass vial was charged with **55** (30.0 mg, 0.043 mmol), bis(neopentylglycolato)diboron (59 mg, 0.260 mmol), $Pd(OAc)_2$ (2.0 mg, 0.009 mmol), potassium acetate (51 mg, 0.52 mmol), and DMF (4 mL) under an atmosphere of N_2. The vial is sealed and heated to 80 °C for 16 h. The crude mixture was diluted with CH_2Cl_2 (40 mL) and washed with a saturated aqueous NaCl solution. Column chromatography (1:1 to 0:1 hexanes/CH_2Cl_2) yields a crude mixture of mono- and diborylated intermediates that were subjected to the iodination without further purification. A 4 mL glass vial was charged with the crude mixture of mono- and diborylated intermediates (20 mg), CuI (20 mg) and KI (40

mg), in a mixture of THF (1 mL), MeOH (0.2 mL), and H_2O (0.1 mL). The vial is sealed, and the reaction mixture is heated to 80 °C for 16 h. The crude reaction mixture is concentrated onto Celite on a rotary evaporator. Column chromatography (SiO_2, CH_2Cl_2, R_f = 0.85) yielded **63** (2.2 mg, 7% yield over 2 steps) as an orange solid. ^{1}H NMR (600 MHz, $CDCl_3$) δ = 8.76–8.71 (m, 8H), 7.66–7.60 (m, 4H), 7.38–7.32 (m, 4H), 7.19 (d, J = 8.6 Hz, 4H) ppm; ^{13}C NMR (151 MHz, $CDCl_3$) δ = 147.4, 141.1, 139.1, 134.6, 133.7, 132.9, 132.2, 127.6, 127.1, 126.4, 108.3 ppm; FTMS (ESI-TOF): m/z $[C_{38}H_{21}N_4I_2]^+$, calcd. $C_{38}H_{21}N_4I_2$ 786.9862; found 786.9850.

5,14-dihydroquinoxalino[2,3-b]phenazine (**71**): A medium-sized mortar is charged with phenylene-1,2-diamine (1.62 g, 15 mmol) and 1,4-benzoquinone (0.42 g, 3 mmol), and both solids are ground with pestle for 10 min to achieve a fine powder. The resulting powder is transferred to a 20 mL scintillation vial, the headspace of the vial is sparged with N_2, and the reaction mixture is heated to 160 °C for 4 h (no solvent or stirbar necessary). The vial is cooled to 24 °C. Sonication in acetone and filtration of resulting solid yielded **71** as a solid. (815 mg, 2.87 mmol. 96% yield). ^{1}H NMR (300 MHz, DMSO-d_6) δ = 9.71 (s, 2H), 7.66 (dd, J = 6.4, 3.5 Hz, 2H), 7.42 (dd, J = 6.4, 3.4 Hz, 2H), 6.60 (dd, J = 5.7, 3.4 Hz, 2H), 6.49 (dd, J = 5.7, 3.4 Hz, 2H) ppm; ^{1}H NMR is in accordance with previous literature report.[154]

Quinoxalino[2,3-b]phenazine-6,13-dione (**70**):A 200 mL round bottom flask is charged with **71** (815 mg, 2.87 mmol, 1.0 equiv), H_2O (100 mL) and 12M H_2SO_4 (25 mL), and the mixture is warmed to 70 °C with stirring. Potassium dichromate (4.1 g, 13.7 mmol, 4.8 equiv) is added in small portions over 5 min, and then reaction mixture is heated to 110 °C for 1 h. The resulting mixture is poured onto ice (200 mL). Filtration of the aqueous suspension yielded **70** (641 mg, 71.5% yield) as a brown solid.

6,13-bis(10-bromoanthracen-9-yl)-5,14-dihydroquinoxalino[2,3-b]phenazine (**72**): A flame dried Schlenk flask is charged with 9,10-dibromoanthracene (537.6 mg, 1.60 mmol) and dry, degassed THF (50 mL). The mixture is cooled to −78 °C, and BuLi (1.68 mmol, 0.67 mL of 2.5 M solution in hexanes) is added dropwise, and solution is stirred at − 78 °C for 1 h. **70** (250 mg, 0.80 mmol) is added as a solid under N_2 blanket flow, and the reaction mixture is warmed to 24 °C over 16 h. The mixture is diluted with Et_2O (20 mL) and 2 drops of 1M HCl, and the solvent is removed by rotary evaporation, which results in black residue. The residue is suspended in 25% EtOAc/hexanes and loaded on a 2 in silica plug. The loaded band is eluted with EtOAc (750 mL), and solvent is removed by rotary evaporation. Red solid is isolated in the flask, and brown solid remains on top of silica (unreacted **70**). A 50 mL round bottom flask is charged with crude red solid (50 mg), AcOH (20 mL), KI (1.0 g) and sodium hypophosphite (0.53 g), and trifluoroacetic acid (1 mL). The reaction mixture is heated to 120 °C for 1 h. The reaction mixture is cooled, quenched with triethylamine (2.0 mL) and the aqueous layer is extracted with CH_2Cl_2 (30 mL) twice. Column chromatography (50:50 hexanes/CH_2Cl_2, R_f = 0.3) yielded **72** (8.2 mg, 1.4% yield) as a red powder. HRMS (MALDI-TOF) m/z $[C_{46}H_{26}Br_2N_4][H]^+$ calcd. 795.0582 found 794.9302.

6,13-bis(10-bromoanthracen-9-yl)quinoxalino[2,3-b]phenazine (**66**): A 20 mL scintillation vial is charged with **72** (13 mg), manganese dioxide (60.0 mg), and CH_2Cl_2 (10 mL). The reaction mixture is stirred for 12 h at 24 °C. The mixture is directly loaded onto Celite and then loaded onto a silica plug column. Column chromatography (50:50 EtOAc/hexanes) yielded **66** as a brown solid

(10.4 mg, 80% yield). ^{1}H NMR (500 MHz, CD_2Cl_2) δ = 8.73 (m, 4H), 7.61 – 7.55 (m, 4H), 7.55 – 7.50 (m, 4H), 7.47 (m, 4H), 7.23 – 7.12 (m, 8H) ppm; FTMS (ESI+): *m/z* $[C_{46}H_{24}N_4Br_2]^+$, calcd. $C_{46}H_{24}N_4Br_2$ 790.0373; found 790.0364

5,10-bis(10'-bromo-[9,9'-bianthracen]-10-yl)pyrazino[2,3-g]quinoxaline (**73**): A 20 mL scintillation vial is charged with **60** (50 mg, 0.142 mmol, 1 equiv), **76** (400 mg, 0.68 mmol, 4.8 equiv), $Pd(PPh_3)_4$ (10 mg), cesium carbonate (275 mg, 0.85 mmol, 6 equiv) and dry toulene (12 mL) under N_2 atmosphere. The reaction mixture is heated to 110 °C for 72 h. The reaction mixture is concentrated by rotary evaporation. The crude solid is suspended in CH_2Cl_2 (15 mL), sonicated in water bath sonicator and filtered (repeated twice). The remaining crude solid is suspended in H_2O (15 mL), sonicated in water bath sonicator and fitered (also repeated twice). Brown/yellow powder containing **60** and **73** is isolated (40 mg) and suspended in TFA (10 mL), sonicated in water bath sonicator and filtered (**60** is soluble in TFA while **73** isn't). Isolation of remaining solid yielded **73** as a brown solid (2.5 mg). The solubility of **73** in all common deuterated solvents is insufficient for acquiring ^{1}H and ^{13}C NMR spectra. MALDI-TOF: *m/z* $[C_{66}H_{36}Br_2N_4]^+$ calcd. 1044.13 found 1044.95.

Polymerization procedure for the preparation of (**69**): A 20 mL scintillation vial is charged with **60** (50 mg, 0.142 mmol, 1 equiv), **77** (65 mg, 0.15 mmol, 1.02 equiv), $Pd(PPh_3)_4$ (8.5 mg, 0.05 equiv), cesium carbonate (288 mg, 0.88 mmol, 6.1 equiv) and dry toulene (12 mL) under a N_2 atmosphere. The reaction mixture is heated to 110 °C for 96 h. The reaction mixture is concentrated by rotary evaporation. The crude solid is suspended in MeOH (15 mL), sonicated in a water bath sonicatior and filtered (repeated twice). Then the crude solid is suspended in CH_2Cl_2 (15 mL), sonicated in a water bath sonicator and filtered (repeated twice). Concentration of the CH_2Cl_2 eluent fractions yielded the oligomeric mixture **69** as assayed by MALDI mass spectrometry (Figure 42, Scheme 44).

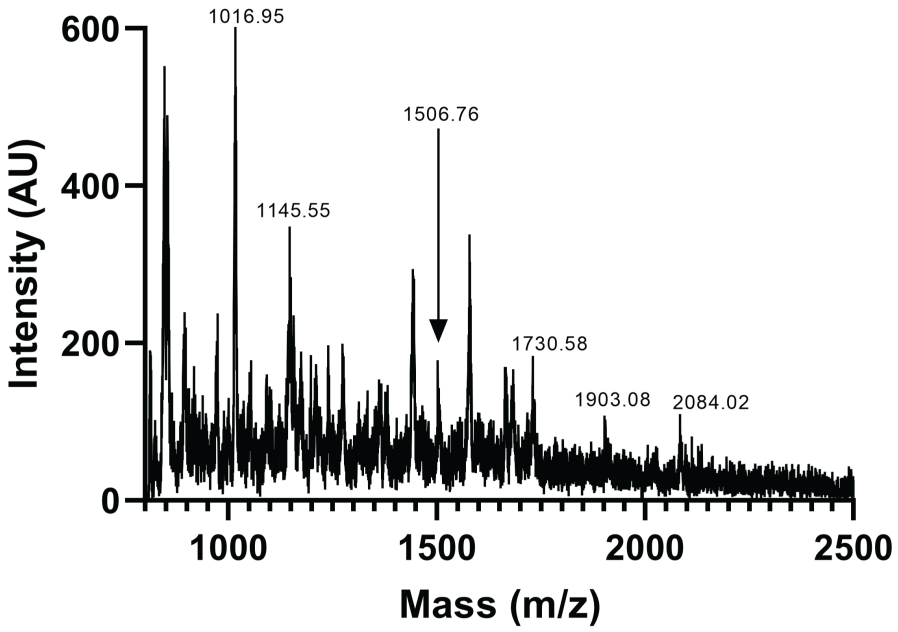

Figure 42: MALDI spectra of the oligomer **69** after work-up.

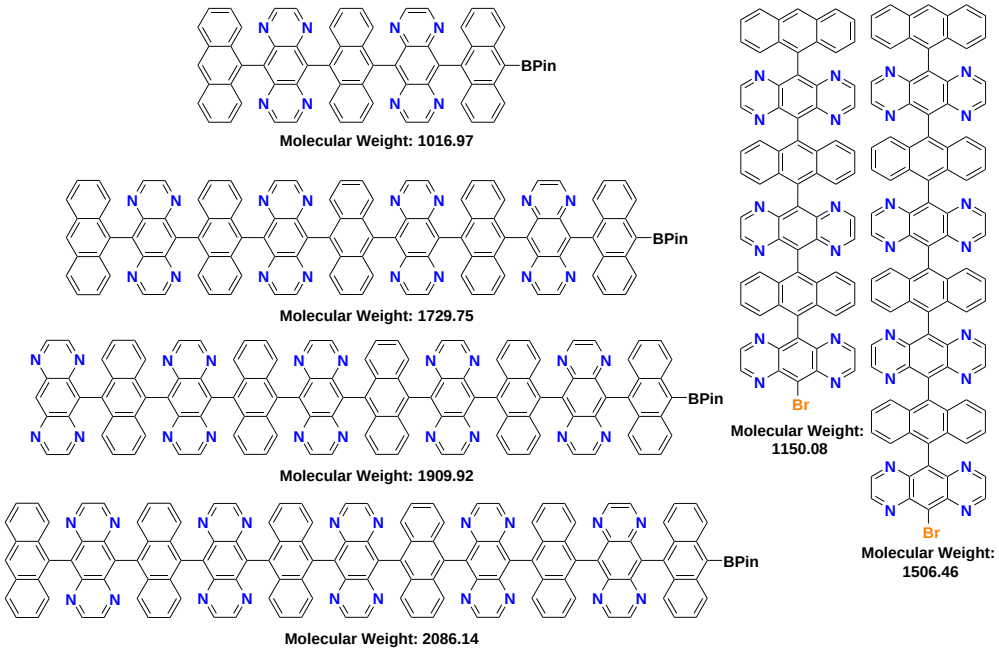

Scheme 44: Oligomer molecular weight prediction of observed peaks in MALDI spectra of **69**

Chapter 3.

N-benzyl-7-bromonaphthalen-2-amine (**88**): A 20 mL pressure tube is charged with, in this particular order, a stirbar, 7-bromonaphth-2-ol **84**, (2.0 g, 8.9 mmol), $NaHSO_3$ (4.63g, 44.5 mmol), benzylamine (4.85 mL, 44.5 mmol), and DI H_2O (8 mL). Without disturbing the formed layers, the pressure tube is submerged in a pre-heated oil bath and heated to 100 °C for 48 h with stirring. After cooling, the reaction mixture is diluted with EtOAc and DI H_2O, and organic phase is washed with saturated aqueous NaCl solution twice, and dried over $MgSO_4$. Rotary evaporation yielded crude product as a semi-solid, which was resuspended in Et_2O, and 1.0 mL of conc HCl is added to precipitate the amine salt. Filtration and consequent diethyl ether wash yielded pure amine hydrochloride salt, which was suspended in a separatory funnel containing EtOAc and 1M KOH and shaken until all solid is dissolved and both phases are homogeneous. The organic layer is isolated and dried over $MgSO_4$. Rotary evaporation yielded **88** as light brown solid (2.31 g, 7.4 mmol, 83% yield). ^{1}H NMR (400 MHz, $(CD_3)_2SO$, 24 °C) δ = 7.72 (d, J = 2.0 Hz, 1H), 7.59 (dd, J = 11.9, 8.7 Hz, 2H), 7.44–7.38 (m, 2H), 7.33 (dd, J = 8.5, 6.8 Hz, 2H), 7.27–7.21 (m, 1H), 7.17 (dd, J = 8.6, 2.0 Hz, 1H), 7.07 (dd, J = 8.9, 2.3 Hz, 1H), 6.75 (t, J = 6.0 Hz, 1H), 6.68 (d, J = 2.2 Hz, 1H), 4.36 (d, J = 5.8 Hz, 2H) ppm; ^{13}C NMR (126 MHz, $(CD_3)_2SO$, 24 °C) δ = 147.4, 139.6, 136.5, 129.6, 128.5, 128.35, 127.4, 126.9, 126.8, 124.8, 123.7, 119.5, 118.8, 101.7, 46.3 ppm; FTMS (ESI-TOF) m/z: $[M]^+$ calcd $[C_{17}H_{15}NBr]$ 312.0382; found 312.0381.

3',5'-Dimethyl-[1,1'-biphenyl]-4-carbaldehyde (**85**): A 250 mL Schlenk flask is charged with 1-bromo-3,5-dimethylbenzene (5.0 g, 27 mmol), 4-formylphenylboronic acid (5.25 g, 35 mmol), potassium carbonate (11.2 g, 81 mmol), 10 mL H_2O, and 60 mL THF under an atmosphere of N_2. The reaction mixture was degassed for 15 min with N_2 flow, then $Pd(PPh_3)_4$ (1.56 g, 1.35 mmol) was added. The reaction mixture was heated for 18 h at 80 °C. After cooling to 24 °C, the reaction mixture was diluted with EtOAc and washed with saturated aqueous NaCl solution once. The organic phase was dried over $MgSO_4$, filtered, and concentrated on a rotary evaporator. Column chromatography (silica; 1:3 EtOAc/hexane) yielded **85** as a colorless oil (4.78 g, 22.7 mmol, 85% yield). ^{1}H NMR (400 MHz, $CDCl_3$, 24 °C) δ = 10.05 (s, 1H), 7.94 (dd, J = 8.4, 4.6 Hz, 2H), 7.74 (dd, J = 8.5, 5.0 Hz, 2H), 7.25 (s, 2H), 7.07 (s, 1H), 2.40 (s, 6H) ppm; spectroscopic data are consistent with previous literature report.[50]

7-Benzyl-2,12-dibromo-14-(3',5'-dimethyl-[1,1'-biphenyl]-4-yl)-7,14-dihydrodibenzo[a,j]acridine (**89**): A 25 mL round bottom flask is charged with **84** (0.714 g, 3.2 mmol), **88** (1.0 g, 3.2 mmol), **85**, (0.674 g, 3.2 mmol) and glacial acetic acid (7 mL). The mixture was heated to 120 °C for 48 h. The reaction mixture is slowly cooled to 24 °C over 4 h, and the yellow precipitate is collected by filtration and washed with acetone (20 mL). Recrystallization from acetone yielded **92** as a colorless crystalline solid (600 mg, 0.8 mmol, 25%). ^{1}H NMR (500 MHz, CD_2Cl_2, 24 °C) δ = 8.66 (d, J = 1.9 Hz, 2H), 7.68 (dd, J = 8.8, 2.5 Hz, 4H), 7.46 (dd, J = 8.5, 1.8 Hz, 2H), 7.37–7.27 (m, 9H), 7.24–7.19 (m, 2H), 7.05 (s, 2H), 6.92 (s, 1H), 6.68 (s, 1H), 5.49 (s, 2H), 2.28 (s, 6H) ppm; ^{13}C NMR (126 MHz, $CDCl_3$) δ = 143.9, 140.9, 140.3, 139.7, 138.7, 137.5, 133.5, 130.8, 129.5, 129.3, 128.8, 128.7, 128.2, 127.9, 127.8, 127.3, 126.7, 125.3, 124.9, 122.2, 117.3, 117.0, 54.0, 38.3, 21.6 ppm; HRMS (EI+) m/z: $[M]^+$ calcd $[C_{42}H_{31}NBr_2]$ 709.0803; found 709.0805.

2,12-Dibromo-14-(3',5'-dimethyl-[1,1'-biphenyl]-4-yl)dibenzo[a,j]acridine (**90**): A 10 mL flask is

charged with **92**, (50 mg, 0.07 mmol), anhydrous DMSO (1 mL) and anhydrous THF (1 mL). KO^{t}Bu (0.7 mmol) was added under ambient atmosphere, and the reaction mixture is sparged with oxygen gas for 4 h. The reaction mixture is triturated with DI H_2O, and the precipitate collected by filtration. Reprecipitation from acetone followed by recrystallization from $CHCl_3$ yielded **90** (10 mg, 0.016 mmol, 23%) as a colorless solid. ^{1}H NMR (500 MHz, $CDCl_3$, 24 °C) δ = 8.06 (d, J = 9.0 Hz, 2H), 7.96 (dd, J = 12.1, 8.5 Hz, 4H), 7.72 (d, J = 8.3 Hz, 2H), 7.58 (dd, J = 8.3, 1.9 Hz, 2H), 7.52–7.47 (m, 4H), 7.45 (s, 2H), 7.11 (s, 1H), 2.47 (s, 6H) ppm; ^{13}C NMR (126 MHz, $CDCl_3$) δ = 148.8, 147.1, 143.6, 141.0, 140.5, 138.5, 132.3, 132.2, 131.9, 131.9, 130.3, 130.0, 129.7, 129.5, 129.4, 128.7, 125.6, 121.7, 120.4, 21.6 ppm; HRMS (EI) *m/z*: $[M]^+$ calcd $[C_{35}H_{23}NBr_2]$ 617.0177; found 617.0180.

4-(2,6-dimethylpyridin-4-yl)benzaldehyde (**91**): A 50 mL round bottom 20neck round bottom flask is charged with 4-formylphenylboronic acid (524 mg, 3.5 mmol), 4-bromo-2,6-dimethylpyridine (500 mg, 2.6 mmol), potassium carbonate (1.1 g, 7.8 mmol), toluene (20 mL), and H_2O (15 mL). The solution is sparged with N_2 for 15 min with vigorous stirring, then $Pd(PPh_3)_4$ is added under N_2 blanket flow, and the reaction mixture is degassed with N_2 for 15 more min with vigorous stirring. The reaction is then heated to 85 °C for 16 h. The reaction is cooled to 24 °C and diluted with EtOAc (50 mL) and DI H_2O (20 mL). The organic layer is washed with 1M NaOH (20 mL) twice and dried over $MgSO_4$. Column chromatography yielded **91** (372 mg, 1.77 mmol, 68% yield). as a light brown oil. ^{1}H NMR (400 MHz, $CDCl_3$) δ = 10.08 (s, 1H), 7.98 (d, J = 8.3, 2H), 7.77 (d, J = 8.2, 2H), 7.22 (s, 2H), 2.62 (s, 6H) ppm; ^{13}C NMR (151 MHz, $CDCl_3$) δ = 191.8, 158.7, 147.8, 144.8, 136.5, 130.5, 127.9, 118.6, 24.7 ppm;^{1}H NMR and ^{13}C NMR is in accordance with previous literature report.[155]

7-benzyl-2,12-dibromo-14-(4-(2,6-dimethylpyridin-4-yl)phenyl)-7,14-dihydrodibenzo[a,j]acridine (**92**): A 25 mL round bottom flask is charged with **84** (593 mg, 2.66 mmol, 1 equiv), **88** (831 mg, 2.66 mmol, 1 eqiiv), **91** (561 mg, 2.66 mmol, 1 equiv) and acetic acid (5 mL). The reaction mixture is heated to 120 °C for 72 h. The reaction mixture is cooled to 24 °C, and the excess acetic acid is removed via rotary evaporation. The resulting crude oil is triturated with acetone (10 mL), and the reaction mixture is allowed to stand for 3 h. Filtration of the precipitate (washed with cold acetone until eluent is clear) yielded **92** as a colorless solid (397 mg, 0.56 mmol, 21% yield). ^{1}H NMR (500 MHZ, CD_2Cl_2) δ = 8.67 (s, 2H), 7-67-7.65 (m, 4H), 7.47-7.38 (m, 6H), 7.34-7.20 (m, 7H), 7.01 (s, 2H), 6.72 (s, 1H), 5.47 (s, 2H), 2.45 (s, 6H) ppm; ^{13}C NMR (125 MHZ, CD_2Cl_2) δ = 130.9, 129.5, 128.8, 128.7, 128.5, 127.9, 127.7, 127.3, 126.7, 124.8, 122.2, 118.4, 117.0, 116.9, 52.1, 38.4, 24.7 ppm; HRMS (ESI+) *m/z* $[C_{41}H_{31}N_2Br_2]^+$ calcd. 709.0848, found 709.0858.

2,12-dibromo-14-(4-(2,6-dimethylpyridin-4-yl)phenyl)dibenzo[a,j]acridine (**93**): A 20 mL scinitllation vial is charged with **92** (50 mg, 0.07 mmol), DMSO (4 mL) and potassium *tert*-butoxide (7.8 mg, 0.07 mmol). Note: reaction mixture turns dark purple upon addition of base. An oxygen gas balloon is attached, and the reaction is sparged with oxygen for 4 h. DMSO is removed via rotary evaporation, and the crude solid is sonicated in MeOH (10 mL). Filtration and subsequent MeOH wash until eluent is clear yielded **93** as a colorless crystalline solid (22 mg, 0.035 mmol, 50% yield). ^{1}H NMR (500 MHz, CD_2Cl_2) δ = 8.07 (d, J = 5 Hz, 2H), 8.02 (d, J = 6 Hz, 2H), 7.96 (d, J = 6 Hz, 2H), 7.74 (d, J = 5 Hz, 2H), 7.60-7.57 (m, 4 H), 7.43 (d, J = 5 Hz, 2H), 7.42 (s, 2H) ppm; ^{13}C NMR (125 MHz, CD_2Cl_2) δ = 158.8, 149.2, 149.1, 146.7, 142.6, 141.2, 132.6, 132.4,

132.3, 132.0, 130.5, 130.4, 130.2, 130.1, 129.1, 121.8, 120.6, 119.2, 25.1 ppm; HRMS (ESI+) *m/z* $[C_{34}H_{23}N_2Br_2]^+$ calcd. 617.0222, found 617.0230.

2-bromo-7-methoxynaphthalene (**96**): A 200 mL round bottom flask is charged with 7-bromonaphthalen-2-ol **84** (4.76 g, 0.0213 mol), potassium carbonate (8.84 g, 0.064 mol) and acetone (100 mL) under ambient conditions. Iodomethane (15.15 g, 6.64 mL, 0.1 mol) was added in one portion. Reflux condenser is attached and the reaction mixture is heated to 60 °C for 16 h. Reaction is cooled to 0 °C and resulting crude solid is isolated by filtration. Column chromatography (silica, 5% EtOAc:hexanes) yielded **96** (4.4 g, 0.0143 mol, 87% yield) as a colorless solid. ^{1}H NMR (300 MHz, $CDCl_3$) δ = 7.90 (d, *J* = 1.9 Hz, 1H), 7.70 (d, *J* = 9.0 Hz, 1H), 7.63 (d, *J* = 8.7 Hz, 1H), 7.40 (dd, *J* = 8.6, 1.9 Hz, 1H), 7.14 (dd, *J* = 9.0, 2.5 Hz, 1H), 7.03 (d, *J* = 2.5 Hz, 1H), 3.92 (s, 3H) ppm.

2-iodo-7-methoxynaphthalene (**97**): A 200 mL Schlenk flask is charged with 2-bromo-7-methoxynaphthalene **96** (0.99 g, 4.18 mmol, 1 equiv) and dry, degassed THF (100 mL). The solution is cooled to −78 °C, and n-butyllithium (4.4 mmol, 1.75 mL of 2.5 M solution in hexanes, 1.05 equiv) is added dropwise. Reaction is stirred for 45 min at −78 °C, and iodine (1.59 g, 6.26 mmol, 1.5 equiv) is added as a solid under N_2 blanket flow. Reaction is warmed up to 24 °C over 16 h. Reaction is quenched with saturated $N_2S_2O_3$ soluton, diluted with CH_2Cl_2, and shaken until brown discoloration has disappeared. Organic layer is washed twice with saturated aqueous NaCl solution and dried over $MgSO_4$. Rotary evaporation yielded the **97** (1.09 g, 92% yield) as a colorless solid. ^{1}H NMR (600 MHz, $CDCl_3$) δ = 8.15 – 8.12 (d, *J* = 1.7 Hz, 1H), 7.68 (d, *J* = 8.9 Hz, 1H), 7.57 (dd, *J* = 8.5, 1.7 Hz, 1H), 7.48 (d, *J* = 8.5 Hz, 1H), 7.14 (dd, *J* = 8.9, 2.5 Hz, 1H), 7.00 (d, *J* = 2.5 Hz, 1H), 3.91 (s, 3H) ppm; ^{13}C NMR (151 MHz, $CDCl_3$) δ = 158.1, 136.2, 135.3, 132.1, 129.3, 129.1, 127.6, 119.4, 104.6, 92.3, 55.3 ppm; GC/MS: *m/z* $[C_{11}H_9IO]^+$ calcd. 284.0 found 284.0.

7-iodonaphthalen-2-ol (**95**): A 50 mL Schlenk flask is charged with 2-iodo-7-methoxynaphthalene **97** (1.09 g, 3.83 mmol, 1 equiv) and dry, degassed CH_2Cl_2 (20 mL). The solution is cooled to −78 °C, and BBr_3 (7.6 mmol, 7.6 M of 1M solution in CH_2Cl_2, 2 equiv) is added, and the reaction mixture is warmed to 24 °C over 16 h. The reaction is quenched with addition of MeOH (20 mL). Rotary evaporation yielded title compound (893 mg, 3.30 mmol, 87% yield) as a colorless solid. ^{1}H NMR (300 MHz, $CDCl_3$) δ = 8.07 (d, *J* = 1.7 Hz, 1H), 7.70 (d, *J* = 8.8 Hz, 1H), 7.57 (dd, *J* = 8.6, 1.7 Hz, 1H), 7.48 (d, *J* = 8.6 Hz, 1H), 7.10 (dd, *J* = 8.8, 2.5 Hz, 1H), 7.02 (d, *J* = 2.5 Hz, 1H), 5.06 (s, broad, 1H) ppm; ^{13}C NMR (151 MHz, $CDCl_3$) δ = 154.0, 136.4, 135.1, 132.4, 130.1, 129.4, 127.8, 118.55, 108.6, 92.8 ppm; GC/MS: *m/z* $[C_{10}H_7IO]^+$ calcd. 270.0 found 270.0.

N-benzyl-7-iodonaphthalen-2-amine (**98**): A 20 mL pressure tube is charged with, in this particular order, a stirbar, 7-iodonaphthalen-2-ol **95** (893 mg, 3.3 mmol, 1 equiv), sodium bisulfite (1.71 g, 16.5 mmol, 5 equiv), benzylamine (1.76 g, 16.5 mmol, 5 equiv), and DI H_2O (5 mL). Without disturbing the formed layers, the pressure tube is submerged in a pre-heated oil bath and heated to 100 °C for 48 h with stirring. After cooling, the reaction mixture is diluted with EtOAc and DI H_2O, organic phase is washed with saturated aqueous NaCl solution twice and dried over $MgSO_4$. Rotary evaporation yielded crude product as a semi-solid, which was resuspended in Et_2O, and 0.5 mL of conc. HCl is added to precipitate the amine salt. Filtration and consequent diethyl ether wash yielded pure amine hydrochloride salt, which was suspended in a separatory funnel contain-

ing EtOAc and 1M KOH and shaken until both phases are homogeneous. Organic layer is isolated and dried over $MgSO_4$. Rotary evaporation yielded **98** (800 mg, 67% yield) as a brown oil, which turns into a colorless solid after standing for 24 h. ^{1}H NMR (600 MHz, $CDCl_3$) δ = 7.97 (d, J = 1.7 Hz, 1H), 7.57 (d, J = 8.8 Hz, 1H), 7.45 – 7.34 (m, 6H), 7.33 – 7.28 (m, 1H), 6.91 (dd, J = 8.8, 2.4 Hz, 1H), 6.67 (d, J = 2.4 Hz, 1H), 4.42 (s, 2H) ppm; ^{13}C NMR (151 MHz, $CDCl_3$) δ = 146.4, 138.9, 137.0, 134.7, 130.6, 129.3, 129.1, 128.9, 127.7, 127.6, 126.3, 118.5, 103.4, 92.6, 48.3 ppm.

*7-benzyl-14-(4-(2,6-dimethylpyridin-4-yl)phenyl)-2,12-diiodo-7,14-dihydrodibenzo[a,j]*acridine (**99**): A 10 mL round bottom flask is charged with 7-iodonaphthalen-2-ol **95**. (475 mg, 1.76 mmol, 1 equiv), 4-(2,6-dimethylpyridin-4-yl)benzaldehyde **91** (372 mg, 1.76 mmol, 1 equiv), N-benzyl-7-iodonaphthalen-2-amine **98** (633 mg, 1.76 mmol, 1 equiv), and acetic acid (2.5 mL). Reflux condenser is attached, and the reaction is heated to 120 °C for 48 h. Reaction mixture is cooled, and excess acetic acid is removed by rotary evaporation. The crude solid is suspended in acetone (7 mL) and is kept still for 3 h. Filtration yielded 90 mg of colorless solid. The acetone eluent is diluted with 3 mL of H_2O, whereupon more colorless solid precipitates out. Filtration yielded 400 mg more of pure desired product. Combination of both batches yielded **99** (490 mg, 21% yield) as a colorless powder. ^{1}H NMR (600 MHz, CD_2Cl_2) δ 8.88 – 8.84 (m, 2H), 7.67 – 7.63 (m, 4H), 7.54 – 7.51 (m, 2H), 7.44 – 7.39 (m, 2H), 7.36 – 7.26 (m, 7H), 7.23 – 7.18 (m, 2H), 7.04 (s, 2H), 6.69 (s, 1H), 5.47 (s, 2H), 2.46 (s, 6H) ppm; HRMS (ESI) *m/z*: $[M]^+$ calcd $[C_{41}H_{31}N_2I_2]$ 805.0571; found 805.0558.

14-(4-(2,6-dimethylpyridin-4-yl)phenyl)-2,12-diiododibenzo[a,j]acridine (**94**): A dry 20 mL scintillation vial with septum cap is charged with potassium *tert*-butoxide (10.3 mg, 9.2 mmol, 1 equiv) and a magnetic stirbar under N_2 atmosphere. A solution of **99** in dry DMSO (6 mL) and the reaction is sparged with a balloon of O_2, resulting in a red clear solution after 5 min of stirring. Reaction is stirred for additional 2 h, during which the color of the reaction mixture changes from red to green, and a white solid precipitates out. DMSO is removed by rotary evaporation, and the resulting crude solid is triturated with MeOH with sonication (15 mL, three times). Isolation of solid yielded **94** (16.4 mg, 25% yield). ^{1}H NMR (600 MHz, $CDCl_3$) δ 8.10 (d, J = 9.0 Hz, 2H), 8.07 (d, J = 7.9 Hz, 2H), 7.97 (d, J = 9.0 Hz, 2H), 7.79 (dd, J = 8.2, 1.6 Hz, 2H), 7.67 (s, 2H), 7.62 (d, J = 8.1 Hz, 4H), 7.57 (s, broad, 2H), 2.81 (s, 6H) ppm;. HRMS (ESI) *m/z*: $[M]^+$ calcd $[C_{34}H_{23}N_2I_2]$ 712.9945; found 712.9930.

4-dodecylbenzaldehyde (**100**): A 100 mL dry 3-neck round bottom flask is charged with dodec-1-ene (3.0 g, 0.0178 mol, 3.96 mL, 1 equiv) under N_2 atmosphere. 9-BBN (0.0178 mol, 35.6 mL of 0.5 M solution in THF, 1 equiv) is added, and the mixture is stirred at 24 °C for 3 h. Aqueous NaOH (15 mL of 3 M solution, 0.045 mol, 3.0 equiv) is sparged with N_2 for 15 min and added to reaction mixture. Then, 4-bromobenzaldehyde (2.2 g, 0.012 mol, 0.66 equiv) and $Pd(PPh_3)_4$ (200 mg, 0.01 equiv) are added, a reflux condenser is attached, and the reaction is heated to 70 °C for 16 h. The reaction mixture is cooled and diluted with hexanes (100 mL) and DI H_2O (100 mL), and the resulting organic layer is washed with DI H_2O twice. Column chromatography (silica, 3% EtOAc:hexanes) yielded the title compound (1.58 g, 32% yield) as a clear oil. ^{1}H NMR (500 MHz, $CDCl_3$) δ = 9.95 (s, 1H), 7.79 – 7.74 (m, 2H), 7.35 – 7.28 (m, 2H), 2.70 – 2.63 (t, J = 7.7 Hz, 2H), 1.62 (m,2H), 1.33 – 1.19 (m, 18H), 0.86 (t, J = 7.0 Hz, 3H) ppm; ^{13}C NMR (126 MHz, $CDCl_3$) δ = 192.2, 150.7, 134.5, 130.0, 129.2, 36.4, 32.1, 31.2, 29.8, 29.8, 29.7, 29.6, 29.5, 29.4, 22.8, 14.3

ppm; GC/MS: *m/z* [$C_{19}H_{30}O$ calcd. 274.2 found 274.3.

4-(2-(2-(2-methoxyethoxy)ethoxy)ethoxy)benzaldehyde (**102**): A 100 mL round bottom flask is charged with 4-hydroxybenzaldehyde (767 mg, 6.3 mmol, 1 equiv), potassium carbonate (2.6 g, 18.8 mmol, 3 equiv), tri(ethylene glycol) monomethyl ether tosylate (6.0 g, 18.8 mmol, 3 equiv) and DMF (50 mL) under ambient conditions. The reaction mixture is heated at 100 °C for 6 h. The reaction mixture is cooled, diluted with EtOAc (100 mL) and DI H_2O (100 mL) and transferred to separatory funnel. The aqueous phase was extracted with EtOAc three times, and combined organic phase is dried over Na_2SO_2. Column chromatography (SiO2, 98% EtOAc:hexane) yielded title compound (1.37 g, 81% yield) as a clear yellow oil. ^{1}H NMR (500 MHz, $CDCl_3$) δ = 9.86 (s, 1H), 7.81 (d, *J* = 8.8 Hz, 2H), 7.00 (d, *J* = 8.7 Hz, 2H), 4.22 – 4.17 (m, 2H), 3.90 – 3.84 (m, 2H), 3.75 – 3.70 (m, 2H), 3.69 – 3.61 (m, 2H), 3.56 – 3.50 (m, 2H), 3.36 (s, 3H) ppm; ^{13}C NMR (126 MHz, $CDCl_3$) δ = 190.9, 163.9, 132.0, 130.1, 115.0, 72.0, 71.0, 70.7, 70.6, 69.6, 67.8, 59.1 ppm; GC/MS: *m/z* $[C_{14}H_{20}O_5]^+$ calcd. 268.1 found 268.1.

7-benzyl-2,12-dibromo-14-(4-dodecylphenyl)-7,14-dihydrodibenzo[a,j]acridine (**$C_{12}H_{25}$-104**): A 25 mL round bottom flask is charged with **84** (1.10 g, 4.9 mmol), **88** (1.54 g, 4.9 mmol), **100** (1.35 g, 4.9 mmol), acetic acid (5 mL) and toluene (5 mL). The mixture was heated to 120 °C for 48 h. The reaction mixture is cooled to 24 °C and excess solvent is removed by rotary evaporation. Column chromatography (SiO_2, 2% EtOAc/hexanes, R_f = 0.6) and trituration of resulting solid with MeOH yielded **$C_{12}H_{25}$-104** (1.60 g mg, 0.7 mmol, 25% yield) as a tan solid. ^{1}H NMR (500 MHz, $CDCl_3$) δ = 8.62 (d, *J* = 1.8 Hz, 2H), 7.63 (t, *J* = 8.8 Hz, 4H), 7.46 (dd, *J* = 8.6, 1.9 Hz, 2H), 7.37 – 7.30 (m, 4H), 7.26 – 7.18 (m, 5H), 7.11 (d, *J* = 8.0 Hz, 2H), 6.95 (d, *J* = 7.9 Hz, 2H), 6.61 (s, 1H), 5.45 (s, 2H), 2.49 – 2.40 (m, 2H), 1.49 (t, *J* = 7.7 Hz, 2H), 1.32 – 1.21 (m, 18H), 0.90 (t, *J* = 6.9 Hz, 3H) ppm; ^{13}C NMR (126 MHz, $CDCl_3$) δ = 141.3, 141.1, 139.2, 137.0, 133.2, 130.1, 129.0, 128.5, 128.2, 128.0, 127.4, 127.2, 126.7, 126.1, 124.5, 121.6, 117.2, 116.3, 51.7, 37.4, 35.5, 31.9, 31.3, 29.7, 29.6, 29.6, 29.5, 29.4, 29.3, 22.7, 14.1 ppm; HRMS (ESI-TOF) *m/z*: $[M]^+$ calcd $[C_{46}H_{47}NBr_2]$ 773.6970; found 773.2045.

2,12-dibromo-14-(4-dodecylphenyl)dibenzo[a,j]acridine (**$C_{12}H_{25}$-101**): A 20 mL scintillation vial is charged with potassium *tert*-butoxide (19.6 mg, 0.17 mmol, 1.5 equiv) and **$C_{12}H_{25}$-104** (90 mg, 0.12 mmol, 1 equiv) under N_2 atmosphere. DMSO (5 mL) is added, and the reaction mixture is sparged with oxygen gas for 4 h. DMSO is removed by rotary evaporation, and the remaining crude solid is triturated with MeOH (50 mL). Column chromatography (silica, 10% EtOAc:hexanes) yielded title compound (55 mg, 0.08 mmol, 70% yield) as colorless solid. ^{1}H NMR (400 MHz, $CDCl_3$) δ = 8.64 (d, *J* = 1.9 Hz, 2H), 7.66 (t, *J* = 8.4 Hz, 4H), 7.48 (dd, *J* = 8.6, 1.9 Hz, 2H), 7.34 (m, 3H), 7.28 – 7.18 (m, 4H), 7.13 (d, *J* = 8.2 Hz, H), 6.97 (d, *J* = 8.2 Hz, 2H), 6.63 (s, 1H), 5.47 (s, 2H), 2.54 – 2.38 (m, 2H), 1.50 (mz, 2H), 1.39 – 1.16 (m, 18H), 0.91 (t, *J* = 6.9 Hz, 3H) ppm; ^{13}C NMR (126 MHz, $CDCl_3$) δ = 141.3, 141.1, 139.2, 137.0, 133.15, 130.2, 130.1, 129.0, 128.6, 128.5, 128.2, 128.0, 127.4, 127.35, 127.2, 126.8, 126.7, 126.2, 126.1, 124.5, 124.4, 121.6, 117.2, 116.3, 51.7, 37.4, 35.5, 31.9, 31.3, 29.7, 29.6, 29.6, 29.5, 29.4, 29.3, 22.7, 14.1 ppm; HRMS [ESI-TOF] $[C_{39}H_{39}Br_2N]_+$. calcd. 682.1462 found 682.1510.

7-benzyl-2,12-dibromo-14-(4-(2-(2-(2-methoxyethoxy)ethoxy)ethoxy)phenyl)-7,14-dihydrodibenzo [a,j]acridine (**PEG-104**): A 25 mL round bottom flask is charged with **84** (632 mg, 2.83 mmol),

88 (884 mg, 2.83 mmol), **102** (760 mg, 2.83 mmol), acetic acid (5 mL), and toluene (5 mL). The mixture was heated to 120 °C for 48 h. Excess solvent is removed by rotary evaporation. Column chromatography (silica, 30% to 50% gradient of EtOAc/hexanes, R_f = 0.4) and trituration of resulting solid with cold MeOH yielded title compound (401 mg, 0.7 mmol, 25% yield) as a tan solid. ^{1}H NMR (500 MHz, $CDCl_3$) δ 8.57 (d, J = 1.8 Hz, 2H), 7.63 – 7.58 (m, 4H), 7.43 (dd, J = 8.5, 1.8 Hz, 2H), 7.35 – 7.28 (m, 4H), 7.19 (m, 4H), 7.12 – 7.07 (m, 2H), 6.69 – 6.64 (m, 2H), 6.56 (s, 1H), 5.42 (s, 2H), 3.97 (m, 2H), 3.76 – 3.72 (m, 2H), 3.68 – 3.62 (m, 2H), 3.62 – 3.55 (m, 4H), 3.51 – 3.46 (m, 2H), 3.32 (s, 3H) ppm; ^{13}C NMR (126 MHz, $CDCl_3$) δ = 157.4, 139.1, 137.0, 136.7, 133.2, 130.3, 129.1, 128.5, 128.3, 128.1, 127.5, 126.8, 126.2, 124.5, 121.8, 117.3, 116.4, 114.7, 72.0, 70.9, 70.7, 70.6, 69.7, 67.4, 59.1, 51.8, 37.2 ppm.

2,12-dibromo-14-(4-(2-(2-(2-methoxyethoxy)ethoxy)ethoxy)phenyl)dibenzo[a,j]acridine (**PEG-101**): A 20 mL scintillation vial is charged with potassium tert-butoxide (146 mg, 1.3 mmol, 2 equiv) and **PEG-104** (500 mg, 0.65 mmol, 1 equiv) under N_2 atmosphere. DMSO (7 mL) is added, and the reaction mixture is sparged with oxygen gas for 4 h. DMSO is removed by rotary evaporation. Trituration of crude tan solid with MeOH (15 mL) yielded title compound (261 mg, 0.38 mmol, 59% yield) as colorless solid. ^{1}H NMR (500 MHz, C_6D_6) δ = 8.22 (d, J = 9.0 Hz, 1H), 7.57 (d, J = 1.8 Hz, 2H), 7.44 (d, J = 9.0 Hz, 2H), 7.32 (dd, J = 8.3, 1.9 Hz, 2H), 7.14 (d, J = 8.3 Hz, 2H), 7.10 – 7.05 (m, 2H), 6.87 – 6.82 (m, 2H), 4.08 (t, J = 5.0 Hz, 2H), 3.70 (dd, J = 5.7, 4.3 Hz, 2H), 3.58 (dd, J = 4.8, 1.9 Hz, 2H), 3.56 – 3.49 (m, 2H), 3.39 (dd, J = 5.8, 4.1 Hz, 2H), 3.15 (s, 3H) ppm; ^{13}C NMR (126 MHz, C_6D_6) δ = 161.2, 149.8, 147.6, 134.5, 133.0, 132.9, 132.7, 132.4, 130.9, 130.6, 130.1, 130.0, 120.8, 118.4, 72.8, 71.6, 71.5, 71.3, 70.1, 68.8, 59.1 ppm; HRMS (ESI-TOF) m/z $[C_{34}H_{29}Br_2NO_4]^+$ calcd. 675.0443 found 675.0507.

14-(4-(2-(2-(2-methoxyethoxy)ethoxy)ethoxy)phenyl)-2,12-bis(4,4,5,5-tetramethyl-1,3,2 dioxaborol an-2-yl)dibenzo[a,j]acridine (**PEG-106**): A 20 mL scintillation vial is charged with **PEG-101** (100 mg, 0.148 mmol), Pd(dppf)Cl_2 (10 mg, 0.015 mmol), $B_2(pin)_2$ (94 mg, 0.37 mmol), potassium acetate (87 mg, 0.89 mmol). The vial is sealed with a septum cap, and DMF (degassed by N_2 sparging for 20 minutes, 10 mL) is added, and the reaction mixture is heated to 80 °C for 16 hours. The reaction mixture is cooled, and diluted with DCM (50 ml) and H_2O (25 mL). Organic layer is washed with saturated ammonium chloride solution (30 mL) twice and dried over $MgSO_4$. Column chromatography (50:50 EtOAc/hexanes, R_f = 0.3) yielded **PEG-106** (35 mg, 31% yield) as a colorless solid. ^{1}H NMR (500 MHz, Acetone-d_6) δ = 8.10 – 8.05 (m, 2H), 8.03 – 8.01 (m, 2H), 7.96 – 7.92 (m, 2H), 7.82 – 7.77 (m, 2H), 7.33 – 7.24 (m, 4H), 4.37 – 4.29 (m, 2H), 4.02 – 3.96 (m, 2H), 3.78 – 3.72 (m, 2H), 3.71 – 3.66 (m, 2H), 3.66 – 3.60 (m, 2H), 3.57 – 3.48 (m, 2H), 3.35 – 3.28 (s, 3H), 1.31 (s, 24H) ppm; HRMS (MALDI-TOF) m/z $[C_{46}H_{53}B_2NO_8][H]^+$ calcd. 770.4036 found 770.2736.

Yamamoto polymerization general procedure (applied to both PEG and alkyl functionalized precursors **PEG-101** and **$C_{12}H_{25}$-101**): A 10 mL microwave sealable tube is charged with Ni(COD)$_2$, 2,2'-bipyridyl, 1,5-cyclooctadiene, and DMF (3 mL) under argon atmosphere. The mixture is stirred at 60 °C for 1 h. A separate scintillation vial is charged with the monomer and dry, degassed toluene (2 mL), and the monomer solution is transferred into microwave tube under inert atmosphere. The reaction is heated to 90 °C with microwave irradiation for 16 h. The reaction mixture is quenched with MeOH (25 mL) and filtered.

Iron(III) chloride cyclodehydrogenation general procedure: A 50 mL dry Schlenk flask is charged with the polymer and dry, degassed CH_2Cl_2 (30 mL) under N_2 atmosphere. $FeCl_3$ (8 equiv per H, solution in dry nitromethane, 2 mL total volume) is added in one portion. The reaction is stirred at 24 °C with sparging of CH_2Cl_2 pre-saturated N_2 gas directly through the reaction mixture for 48 h (a secondary Schlenk vessel is charged with 200 mL of CH_2Cl_2, and house N_2 is passed through the dry, degassed CH_2Cl_2 prior to the connection with the reaction vessel; the solvent is refilled as necessary). The reaction is quenched with MeOH (25 mL), and filtered. The solid is resuspended in CH_2Cl_2, sonicated in bath sonicator for 5 min and filtered. The suspension/filtration procedure is repeated with $CHCl_3$, hexanes, EtOAc, and 2M NaOH(aq). The isolation of black powder yielded the GNR sample.

DDQ/TfOH cyclodehydrogenation general procedure: A 25 mL dry Schlenk flask is charged with the polymer (1 equiv), DDQ, and dry, degassed CH_2Cl_2 (15 mL) under N_2 atmosphere. The reaction mixture is cooled to 0 °C, and TfOH is added dropwise. The reaction mixture is then stirred at 24 °C for 24 h. The reaction mixture is quenched with MeOH, the crude solid is filtered. The solid was re-suspended in CH_2Cl_2, sonicated in bath sonicator for 5 min and filtered. The suspension/-filtration procedure is repeated with $CHCl_3$, hexanes, EtOAc, and 2M NaOH(aq). The isolation of black powder yielded the GNR sample.

Chapter 4.

2,4-dibromonaphthalen-1-amine (**115**): A 250 mL round bottom flask is charged with 1-aminonaphthalene **114** (28.0 g, 0.195 mol) inside of the fumehood with extreme precaution, then 100 mL of AcOH was added with gentle stirring. A separate 500 mL round bottom flask is charged with bromine liquid (68.4 g, 22 mL, 0.43 mol) and 200 mL of AcOH. 500 mL round bottom flask was cooled in 12 °C ice bath (caution was exercised to stay just above the freezing point of acetic acid, but below room temperature), and the solution of 1-aminonaphthalene was slowly poured in with heavy stirring. An extra aliquot of AcOH was used to rinse the 250 mL round bottom flask to ensure complete transfer of 1-aminonaphthalene. The resulting mixture was briefly heated at 60 °C for 10 min, then cooled to 24 °C. The resulting salt is filtered off, washed with excess acetic acid, and suspended in 450 mL of 0.05M NaOH(aq) with stirring. Isolated purple solid was then suspended in 300 mL of saturated $NaHCO_3$ solution and the suspension was stirred for 1 h. Filtration of the suspension afforded **115** (52.1 g, 89% yield) as purple solid. ^{1}H NMR (300 MHz, $CDCl_3$) δ = 8.17 (dd, J = 8.2, 1.7 Hz, 1H), 7.85 – 7.70 (m, 2H), 7.66 – 7.47 (m, 2H) ppm; GC/MS: m/z $[C_{10}H_7Br_2N]^+$ calcd. 300.9 found 300.9.

5-bromonaphtho[1,2-d][1,2,3]oxadiazole (**116**): A 250 mL round bottom flask is charged with 2,4-dibromonaphthalen-1-amine **115**. (10.88 g, 0.036 mol, 1 equiv), AcOH (150 mL), and PrOH (propionic acid, 30 mL). The suspension is cooled to 4 °C with an ice bath, and $NaNO_2$ (2.88 g, 0.0397 mol, 1.1 equiv) was added in small portions over 2 min. Over 10 min, the purple suspension turns to yellow-brown homogeneous solution. The reaction mixture is then poured into ice water (T = 4 °C, 250 mL) and filtered immediately, which resulted in aroximately 500 mL of yellow-brown filtrate. Two 2 L Erlenmeyer flasks are charged with 1.5 L of DI H_2O in each flask, then the filtrate is split in equal portions and poured into water. Upon pouring the filtrate into the 2 L Erlenmeyer

flask, precipitation of an off-while solid is immediately observed. Erlenmeyer flasks are allowed to stand for 1 h, while more solid precipitated out. Two batches are filtered through the same filtration setup while the resulting solid is collected on the filter paper. Rotary evaporation (required to remove remaining water from the solid) yielded title compound **116** (7.61 g, 0.03 mol, 84% yield) as a yellow solid. ^{1}H NMR (400 MHz, Acetone-d_6) δ = 8.13 – 7.99 (m, 1H), 7.72 – 7.64 (m, 1H), 7.62 (m, 1H), 7.43 (m, 1H), 7.11 (s, 1H) ppm.

4-bromonaphthalen-2-ol (**117**): A 250 mL round bottom flask is charged with **116** (7.61 g, 0.03 mol, 1 equiv) and 150 mL of 100% EtOH. The reaction mixture is cooled to 0 °C, and granular $NaBH_4$ (1.7 g, 0.046 mol, 1.5 equiv) is added slowly over 5 min, and the reaction mixture is stirred for 3 h. The resulting solution is poured into 500 mL of 1% v:v conc. H_2SO_4 (aq). Then the solution is brought to pH = 1 and extracted with CH_2Cl_2 three times. Rotary evaporation of the organic phase yielded the title compound (3.35 g, 50% yield). ^{1}H NMR (300 MHz, $CDCl_3$) δ = 8.23 – 8.12 (m, 1H), 7.76 – 7.65 (m, 1H), 7.59 – 7.40 (m, 3H), 7.19 (d, J = 2.4 Hz, 1H). 4.86 (s, br, 1H) ppm; GC/MS: m/z $[C_{10}H_7BrO]^+$ calcd. 222.0 found 222.0.

1-bromo-3-methoxynaphthalene (**118**): A 100 mL round bottom flask is charged with **117** (3.35 g, 0.015 mol) and THF (50 mL) under ambient atmosphere. 20 mL of 2M NaOH solution is added, followed by iodomethane (2.3 g, 1.0 mL, 2 equiv). The reaction is stirred at 24 °C and monitored by TLC. After 3 h, the starting material spot has disappeared. The reaction mixture is transferred to separatory funnel, washed with saturated aqueous NaCl solution twice, and the organic phase is dried over Na_2SO_4. Column chromatography (silica, hexanes, R_f = 0.8) yielded the title compound (1.92 g, 54% yield) as a red oil. ^{1}H NMR (700 MHz, $CDCl_3$) δ = 8.31 – 7.95 (m, 1H), 7.78 – 7.72 (m, 1H), 7.53 (d, J = 2.4 Hz, 1H), 7.51 (ddd, J = 8.1, 6.8, 1.3 Hz, 1H), 7.47 (ddd, J = 8.2, 6.8, 1.3 Hz, 1H), 7.15 (d, J = 2.4 Hz, 1H), 3.95 (s, 3H) ppm; GC/MS: m/z $[C_{10}H_9BrO]^+$ calcd. 236.0 found 236.0.

2,6-dibromo-4'-methyl-1,1'-biphenyl (**112**): A 100 mL dry Schlenk Flask is charged with 1,3-dibromobenzene (2.5 g, 0.01 mol, 1.0 equiv) and dry, degassed THF (50 mL) under N_2 atmosphere. The solution is cooled to −78 °C and lithium diisopropylamide solution (0.011 mol, 5.5 mL of 2.0 M solution in THF, 1.1 equiv) is added dropwise. Anhydrous $ZnCl_2$ (1.4 g, 0.011 mol, 1.1 equiv) is then added under a N_2 blanket flow, and the solution is warmed to 24 °C over 3 h. A separate 20 mL scintillation vial with septum cap is charged with $Pd(PPh_3)_4$ (150 mg, 0.015 equiv) and 4-iodotoluene (2.3 g, 0.011 mmol, 1.1 equiv) and dry, degassed THF (8 mL) under N_2 atmosphere. $Pd(PPh_3)_4$ / 4-iodotoluene solution is added to main reaction mixture, and the complete reaction mixture is stirred for 3 h to 24 °C. Reaction is poured into separatory funnel with EtOAc/DI H_2O, shaken, and the organic phase is washed with saturated aqueous NaCl twice and dried over Na_2SO_4. Column chromatography (silica, hexanes, R_f = 0.5) yielded the title compound (1.01 g, 31% yield) as a clear oil/semisolid. ^{1}H NMR (500 MHz, $CDCl_3$) δ = 7.62 (d, J = 8.0 Hz, 2H), 7.28 (d, J = 7.8 Hz, 2H), 7.11 (d, J = 8.1 Hz, 2H), 7.05 (t, J = 8.0 Hz, 1H), 2.43 (s, 3H) ppm; ^{13}C NMR (126 MHz, $CDCl_3$) δ = 143.2, 138.4, 138.0, 131.9, 129.8, 129.2, 129.1, 124.9, 21.6 ppm; GCMS: m/z $[C_{13}H_{10}Br_2]^+$calcd. 325.9 found 326.0.

4,4'-(4'-methyl-[1,1'-biphenyl]-2,6-diyl)bis(2-methoxynaphthalene) (**111**): A 100 mL dry Schlenk flask is charged with 1-bromo-3-methoxynaphthalene **118** (780 mg, 3.29 mmol, 3.1 equiv)

and dry, degassed THF (50 mL). The solution is cooled to −78 °C, and n-butyllithium (3.29 mmol, 1.6 mL of 2.5M solution in THF, 3.1 equiv) is added dropwise. The solution changes color to dark orange/brown over 30 min. Anhydrous $ZnCl_2$ (444 mg, 3.35 mmol, 3.2 equiv) is added under a N_2 blanket flow, and the solution is warmed to 30 °C until all solid has dissolved. Palladium (II) acetate (40 mg) and SPhos (80 mg) are added as solid under N_2 blanket flow, and then the solution of **112** (345 mg, 1.06 mmol, 1.0 equiv) in 5 mL dry THF is added in one portion. The reaction mixture is heated to 30 °C for 3 h. The reaction mixture is diluted with EtOAc, and washed with saturated aqueous NaCl solution twice. The organic phase is dried over Na_2SO_4. Column chromatography (silica, 2% EtOAc:hexanes to 15% EtOAc:hexanes gradient elution, R_f = 0.45) yielded title compound **111** (250 mg, 49% yield) as a colorless solid. ^{1}H NMR (600 MHz, $CDCl_3$) δ = 7.72 – 7.62 (m, 4H), 7.54 – 7.44 (m, 4H), 7.37 (m, 3H), 7.28 – 7.20 (m, 3H), 7.00 (t, J = 2.9 Hz, 2H), 6.91 (dd, J = 49.4, 2.6 Hz, 2H), 6.63 – 6.56 (m, 2H), 6.44 – 6.37 (m, 2H), 3.81 (d, 6H), 1.88 (d, 3H) ppm; ^{13}C NMR (151 MHz, $CDCl_3$) δ = 156.6, 156.5, 141.6, 141.5, 140.1, 139.9, 136.3, 135.1, 134.7, 134.6, 130.75, 130.7, 129.6, 128.5, 128.4, 127.5, 127.4, 127.0, 126.9, 126.7, 126.6, 126.4, 126.2, 126.1, 126.0, 123.5, 123.4, 120.7, 120.5, 105.7, 105.6, 55.4, 21.0, 20.9 ppm; FTMS (EI+): m/z $[C_{35}H_{28}O_2]^+$, calcd. $C_{35}H_{28}O_2$ 480.2089; found 480.2097.

(4'-methyl-[1,1'-biphenyl]-2,6-diyl)bis(naphthalene-4,2-diyl) bis(trifluoromethanesulfonate) (**121**): A 20 mL scintillation vial with septum cap is charged **111** (125 mg, 0.26 mmol) and dry, degassed CH_2Cl_2 (10 mL). Reaction mixture is cooled to 0 °C, and BBr_3 (290 mg, 0.11 mL, neat) is added dropwise. As addition is finished, the ice bath is removed and the reaction mixture is warmed up to 24 °C over 2 h. The reaction mixture is poured into 50 mL 1:1 CH_2Cl_2/H_2O mixture, 15 mL of MeOH is added and the flask is shaken for 1 min. Organic phase is separated and dried over minimal amount of $MgSO_4$ needed to achieve clear solution. Rotary evaporation yielded the 4,4'-(4'-methyl-[1,1'-biphenyl]-2,6-diyl)bis(naphthalen-2-ol) (113 mg, 96% yield) as an off-white solid. FTMS (EI+): m/z $[C_{33}H_{24}O_2]^+$, calcd. $C_{33}H_{24}O_2$ 453.1810; found 453.1817. A 20 mL scintillation vial with septum cap is charged with 4,4'-(4'-methyl-[1,1'-biphenyl]-2,6-diyl)bis(naphthalen-2-ol) (113.5 mg) and dry, degassed CH_2Cl_2 (10 mL). Reaction mixture is cooled to 0 °C, collidine (0.2 mL, 6 equiv) and trifluoromethanesulfonic anhydride (0.2 mL, 4.8 equiv) are added in quick succession. The reaction is warmed up to 24 °C over 16 h, quenched with saturated $NaHCO_3$, and the aqueous phase is extracted with CH_2Cl_2 twice. The resulting organic phase is isolated and dried over $MgSO_4$. Column chromatography (silica, 5% EtOAc:hexanes, R_f = 0.8) yielded the title compound (141 mg, 76% yield over 2 steps) as a colorless solid. ^{1}H NMR (700 MHz, $CDCl_3$) δ = 7.88 – 7.74 (m, 4H), 7.64 – 7.48 (m, 9H), 7.15 (dd, J = 62.8, 2.5 Hz, 2H), 6.51 (d, J = 8.1 Hz, 2H), 6.43 (d, J = 8.0 Hz, 2H), 1.91 (m, 3H) ppm; ^{13}C NMR (176 MHz, $CDCl_3$) δ = 146.3, 146.2, 142.9, 142.8, 142.1, 142.0, 138.9, 138.8, 136.2, 136.1, 134.9, 134.8, 133.5, 133.4, 131.8, 131.5, 131.2, 131.1, 129.4, 128.5, 127.9, 127.7, 127.4, 127.3, 127.2, 127.1, 126.9, 126.8, 126.7, 126.6, 121.6, 121.5, 118.4, 118.2, 20.8 ppm; FTMS (EI+): m/z $[C_{35}H_{22}O_2F_6S_2]^+$, calcd. 716.0762; found 716.0770.

2,2'-((4'-methyl-[1,1'-biphenyl]-2,6-diyl)bis(naphthalene-4,2-diyl))bis(4,4,5,5-tetramethyl-1,3, 2-dioxaborolane) (**122**): A 20 mL scintillation vial with a septum cap in charged with bis(pinacolato) diboron (71.1 mg, 0.28 mmol, 2 equiv), $PdCl_2$(dppf) (6 mg, 0.1 equiv) and potassium acetate (82 mg, 0.84 mmol, 6 equiv) under N_2 atmosphere. A second 20 mL vial with a septum cap is charged with **121** (100 mg, 0.14 mmol, 1 equiv) and dry dioxane (8 mL). The dioxane solution is transferred to the first vial under N_2 atmosphere, and the resulting mixture is heated to 100 °C for 16 h. The

resulting solution is cooled, diluted with CH_2Cl_2 and washed with saturated aqueous NaCl. The organic phase is dried over Na_2SO_4. Column chromatography (silica, 20% EtOAc/hexanes) yielded the title compound **122** (94 mg, 99% yield) as a colorless solid, which is used in the next step with no further purification. FTMS (EI+): *m/z* $[C_{45}H_{46}B_2O_4]^+$, calcd. $C_{45}H_{46}B_2O_4$ 672.3582; found 672.3600.

4,4'-(4'-methyl-[1,1'-biphenyl]-2,6-diyl)bis(2-bromonaphthalene) (**110**): A 20 mL scintillation vial is charged with **122** (33.5 mg, 0.05 mmol, 1 equiv), THF (2.5 mL) and MeOH (2.5 mL). Copper (II) bromide (66.7 mg, 0.3 mmol, 6 equiv) is added as an aqueous solution (light blue coloration). The reaction mixture is heated to 90 °C for 4 h, over which the originally heterogeneous mixture gradually becomes homogeneous. Then, the reaction mixture is cooled and diluted with EtOAc and saturated aqueous NaCl solution. Organic layer is isolated and dried over $MgSO_4$. Column chromatography (silica, 2% EtOAc: hexanes) yielded the title compound **110** (9.3 mg, 0.016 mmol, 32% yield) as a colorless solid. ^{1}H NMR (500 MHz, $CDCl_3$) δ = 7.88 (m, J = 2.4 Hz, 2H), 7.73 (m, 4H), 7.55 – 7.50 (m, 1H), 7.50 – 7.45 (m, 2H), 7.50 – 7.40 (m, 4H), 7.38 (dd, J = 9.2, 2.0 Hz, 2H), 6.60 (d, J = 7.7 Hz, 2H), 6.46 (d, J = 7.7 Hz, 2H), 1.95 (d, J = 6.5 Hz, 3H) ppm; ^{13}C NMR (151 MHz, $CDCl_3$) δ = 142.0, 141.7, 139.2, 139.1, 135.7, 135.6, 134.5, 134.4, 131.3, 131.2, 131.1, 131.0, 130.9, 129.6, 129.2, 129.1, 127.6, 127.5, 127.3, 127.2, 126.8, 126.7, 126.7, 126.6, 126.5, 126.2, 126.1, 118.9, 118.8, 20.9 ppm; FTMS (EI+): *m/z* $[C_{33}H_{22}Br_2]^+$, calcd. $C_{33}H_{22}Br_2$ 578.0068; found 578.0071.

1,4-dibromo-2,3,5,6-tetramethylbenzene (**130**): A 100 mL round bottom flask is charged with durene (2.03 g, 0.015 mol) and CH_2Cl_2 (30 mL) under ambient conditions. The reaction flask is cooled to 0 °C, and bromine liquid (4.78 g, 1.55 mL, 0.03 mol) is added dropwise. The reaction is stirred at 0 °C for 30 min, then warmed to 24 °C over 3 h. The stirbar is removed, and reaction mixture is then cooled to −30 °C for 3 h. Filtration of cold solution and cold CH_2Cl_2 rinse (50 mL, cooled to −30 °C) yielded the title compound (3.5 g, 0.012 mol, 80% yield) as colorless crystalline solid. ^{1}H NMR (400 MHz, $CDCl_3$) δ = 2.48 ppm; ^{13}C NMR (126 MHz, $CDCl_3$) δ = 135.2, 128.3, 22.4 ppm; GC-MS *m/z*: $[C_{10}H_{12}Br_2]^+$ calcd. 291.9; found 291.9.

9-(4-bromo-2,3,5,6-tetramethylphenyl)anthracene (**131**): A 100 mL dry Schlenk flask is charged with **130**(500 mg, 1.71 mmol) and dry, degassed THF (50 mL). The solution is cooled to −78 °C, and n-butyllithium (1.79 mmol, 1.12 mL of 1.6M solution in hexanes, 1.1 equiv) is added dropwise. The solution is warmed up to 0 °C and stirred for 1 h. Anthrone (364 mg, 1.88 mmol, 1.2 equiv) is added as a solid under N_2 blanket flow. Solution is warmed up to 24 °C over 12 h. The reaction mixture is diluted with EtOAc and 1M HCl and shaken until the coloration in organic phase disappears. Organic phase is washed with saturated aqueous NaCl solution twice and is dried over Na_2SO_4. Recrystallization from EtOAc / MeOH (layered diffusion in 0 °C fridge over 12 h) yielded **131** as an colorless solid (366 mg, 0.94 mmol, 55% yield). ^{1}H NMR (600 MHz, $CDCl_3$) δ = 8.49 (s, 1H), 8.07-8.05 (m, 2H), 7.47 – 7.45 (m, 2H), 7.42 – 7.40 (m, 2H) 7.34 – 7.32 (m, 2H), 2.53 (s, 6H), 1.68 (s, 6H) ppm; ^{13}C NMR (151 MHz, $CDCl_3$) δ = 136.8, 136.6, 135.2, 134.2, 131.7, 129.9, 129.1, 128.8, 126.3, 126.2, 125.8, 125.4, 21.4, 18.5 ppm; GC-MS *m/z*: $[C_{24}H_{21}Br]^+$ calcd. 388.1 found 388.1.

9,9'-(2,3,5,6-tetramethyl-1,4-phenylene)dianthracene (**128**): A 100 mL dry Schlenk flask is charged

with 9-(4-bromo-2,3,5,6-tetramethylphenyl)anthracene (100 mg, 0.26 mmol) and dry, degassed diethyl ether (50 mL). The solution is cooled to −78 °C, and *tert*-butyllithium (0.57 mmol, 0.33 mL of 1.7 M solution in pentane, 2.2 equiv) is added dropwise. Soltuion is stirred at −78 °C for 1 h, and anthrone (50 mg, 0.26 mmol) is added as a solid under N_2 blanket flow. Solution is warmed up to 24 °C over 12 h. The reaction mixture is diluted with EtOAc and 1M HCl and shaken until the coloration in organic phase disappears. Organic phase is washed with saturated aqueous NaCl solution once and dried over Na_2SO_4. Removal of solvent by rotary evaporation yields a crude desired product, which is triturated with cold $CHCl_3$ (2 mL) to remove soluble impurities. Filtration of cold $CHCl_3$ suspension yielded **128** (68 mg, .014 mmol, 54% yield) as a colorless solid. The solubility of the material is insufficient in common NMR solvents to obtain a ^{13}C NMR.

10,10'-(2,3,5,6-tetramethyl-1,4-phenylene)bis(9-bromoanthracene) (**124**): A 20 mL scintillation vial is charged with **128** (54.0 mg, 0.11 mmol), NBS (39.6 mg, 0.22 mmol) and anhydrous CH_2Cl_2 (8 mL) under N_2 atmosphere. The reaction mixture is stirred at 24 °C for 2 h. Reaction is poured into a separatory funnel containing CH_2Cl_2 (20 mL) and saturated aqueous NaCl solution (20 mL), and organic phase is washed with saturated aqueous NaCl twice and dried over $MgSO_4$. Recrystallization from $CHCl_3$ / hexanes yielded **124** (65 mg, 90%) as a yellow powder. ^1H NMR (600 MHz, CD_2Cl_2) δ = 8.67 (d, J = 8.8 Hz, 4H), 7.75 (d, J = 8.6 Hz, 4H), 7.72 – 7.66 (m, 4H), 7.56 – 7.50 (m, 4H), 1.71 (s, 12H) ppm; ^{13}C NMR (151 MHz, CD_2Cl_2) δ = 138.7, 137.4, 134.1, 131.3, 131.0, 128.4, 127.7, 127.3, 126.5, 122.4, 17.5 ppm; HRMS (EI) *m/z*: $[C_{38}H_{28}Br_2]^+$ calcd. 642.0558; found 642.0561.

10,10'-(2,3,5,6-tetramethyl-1,4-phenylene)bis(9-iodoanthracene) **129**. A 20 mL scintillation vial with a septum cap is charged with 9,9'-(2,3,5,6-tetramethyl-1,4-phenylene)dianthracene (9.0 mg, 0.0185 mmol), dry CH_2Cl_2 (10 mL) and TFA (0.3 mL) under N_2 atmosphere. A separate 20 mL scintillation vial with a septum cap is charged with Barluenga's reagent (Py_2IBF_4, 29 mg, 0.08 mmol, 4.2 equiv) and dry CH_2Cl_2 (3 mL). Solution of Barluenga's reagent is transferred into the main reaction vial dropwise, and the reaction is stirred for 3 h. Reaction mixture is quenched with saturated $Na_2S_2O_3$ solution, diluted with CH_2Cl_2, and the resulting organic phase is washed with saturated aqueous NaCl solution twice. Column chromatography (SiO_2, 5% EtOAc:hexanes) and recrystallization from EtOAc/hexanes yielded the **129** (8.2 mg, 0.011 mmol, 60% yield) as a colorless solid. ^1H NMR (500 MHz, CD_2Cl_2) δ = 8.63 (d, J = 8.8 Hz, 4H), 7.71 (d, J = 8.6 Hz, 4H), 7.69 – 7.63 (m, 4H), 7.52 (m, 4H), 1.70 (s, 12H) ppm; ^{13}C NMR (151 MHz, $CDCl_3$) δ = 139.6, 137.3, 134.2, 134.0, 133.8, 131.0, 127.9, 127.1, 126.2, 105.2, 17.6 ppm; HRMS (EI) *m/z*: $[C_{38}H_{28}I_2]^+$ calcd. 738.0281; found 738.0286.

2,4,6-tribromo-3,5-dimethylaniline (**134**): A 100 mL flask is charged with 3,5-dimethylaniline **133** (3.05 g, 25.2 mmol) and acetic acid (50 mL). The reaction vessel is immersed in an ice bath to cool the mixture to ∼10 °C, and bromine (12.47 g, 75.6 mmol, 4.0 mL) is added in 4 separate aliquots. Ice bath is removed, and the reaction is stirred for 30 min. Then, the reaction mixture is poured into DI H_2O (200 mL). Filtration yielded 2,4,6-tribromo-3,5-dimethylaniline **134** (8.80 g, 24.6 mmol, 98%) as a colorless solid. The material is used as is for the next step.

1,3,5-tribromo-2,4-dimethylbenzene (**134**): A 250 mL flask is charged with 2,4,6-tribromo-3,5-dimethylaniline **134** (8.80 g, 24.6 mmol) and ethanol (150 mL). The reaction mixture is heated to

90 °C for 30 min of continuous reflux. The hot oil bath is removed, and 6.0 mL of 12M hydrochloric acid is added dropwise with stirring. The reaction is stirred for 10 min, and then sodium nitrite (3.76 g, 38.4 mmol) is added in one portion. The reaction mixture is stirred for 15 min, and then the oil bath is reinstalled and the reaction mixture is heated to reflux at 90 °C for 3 h. The reaction mixture is removed from heat, allowed to stand for 2 h, then poured into H_2O (200 mL) and cooled to 0 °C. Filtration yielded **135** (7.0 g, 20.4 mmol) as a colorless solid. ^{1}H NMR (300 MHz, $CDCl_3$) δ = 7.75 (s, 1H), 2.57 (s, 6H). GC/MS: *m/z* $[C_8H_7Br_2]^+$ calcd. 342.8 found 342.8.

((5-bromo-4,6-dimethyl-1,3-phenylene)bis(ethyne-2,1-diyl))bis(trimethylsilane) (**136**): A 100 mL flask is charged with **135** (200 mg, 0.62 mmol), diisopropylamine (0.2 mL, 135 mg, 1.35 mmol, 2.2 equiv), copper (I) iodide (6.0 mg, 0.03 mmol, 0.05 equiv), THF (50 mL). The reaction mixture is sparged with N_2 gas for 30 min with vigorous stirring. Then, $Pd(PPh_3)_4$ (35 mg, 0.03 mmol, 0.05 equiv) is added, followed by trimethylsilylacetylene (0.18 mL, 126 mg, 1.29 mmol, 2.1 equiv). The reaction is stirred at 49 °C for 12 h. The reaction is then transferred to a separatory funnel, diluted with H_2O (50 mL) and EtOAc (50 mL), and the organic phase is washed with saturated NH_4Cl(aq) and saturated aqueous NaCl solution. The organic phase is dried over $MgSO_4$ and is loaded onto Celite via rotary evaporation. Column chromatography (hexanes) yielded title product (1.21 g, 3.2 mmol, 55% yield) as a colorless solid. ^{1}H NMR (600 MHz, $CDCl_3$) δ = 7.52 (s, 1H), 2.56 (s, 6H), 0.25 (s, 18H) ppm; ^{13}C NMR (151 MHz, $CDCl_3$) δ = 141.1, 134.8, 128.2, 121.8, 103.0, 98.7, 22.7, 0.1 ppm; GCMS: *m/z* $[C_{18}H_{25}BrSi_2]^+$ calcd. 377.1 found 377.1.

Dimethyl-5-bromo-4,6-dimethylisophthalate (**138**): A 100 mL flask is charged with **136** (2.0 g, 5.3 mmol), potassium carbonate (1.5 g), THF (40 mL), and MeOH (10 mL). The reaction mixture is stirred for 45 min, and full conversion of SM is observed by TLC (silica, hexanes). The mixture is diluted with EtOAc (50 mL) and H_2O (20 mL). Rotary evaporation of organic phase in a 100 mL flask yielded **137**, which is used in the ozonolysis reaction without further purification.

The 100 mL flask with **137** is charged with $CHCl_3$ (50 mL) and MeOH (10 mL). The reaction mixture is cooled to −78 °C and sparged with oxygen gas for 10 min while connected to an ozone generator. After 10 min, the ozone generator is turned on, and the reaction is sparged with O_2/O_3 gas flow for 30 min – at this time, the solution attains a light blue color. The ozone generator is turned off, and the reaction is sparged with oxygen until the solution becomes clear. The reaction mixture is warmed back up to 24 °C, and 12 M sulfuric acid (1.0 mL) is added. The reaction mixture is heated to 50 °C for 1 h to ensure the esterification of any remaining carboxylic acid. The reaction is quenched with sodium bicarbonate and diluted with dichloromethane. The organic phase is washed with saturated aqueous NaCl solution and dried over $MgSO_4$. Column chromatography (SiO_2, 5% EtOAc/hexanes) yielded **138** (830 mg, 2.76 mmol, 52% yield over 2 steps) as a colorless solid. ^{1}H NMR (400 MHz, $CDCl_3$) δ = 8.20 (s, 1H), 3.91 (s, 6H), 2.72 (s, 6H) ppm; ^{13}C NMR (151 MHz, $CDCl_3$) δ = 167.2, 143.0, 132.1, 130.4, 129.5, 52.4, 22.1 ppm; GCMS: *m/z* $[C_{12}H_{13}BrO_4]^+$ calcd. 301.0 found 301.0.

(5-bromo-4,6-dimethyl-1,3-phenylene)dimethanol (**139**): A 100 mL flask is charged with **138** (1.1 g, 3.65 mmol) and THF (50 mL). The reaction mixture is cooled to 0 °C, and LAH (305 mg, 8 mmol) is added. The reaction mixture is heated to 50 °C for 30 min. The reaction mixture is cooled to 0 °C, and H_2O is added dropwise with stirring. The reaction mixture is filtered over a fritted

funnel, and the remaining solid is sonicated in EtOAc and filtered again. Rotary evaporation of the filtrate yielded **139** (835 mg, 3.4 mmol, 93% yield) as a colorless solid. ^{1}H NMR (300 MHz, $CDCl_3$) δ = 7.37 (s, 1H), 4.77 (s, 4H), 2.51 (s, 6H) ppm; GC/MS: *m*/*z* $[C_{10}H_{13}BrO_2]^+$ calcd. 245.0 found 245.0.

3-bromo-1,5-bis(chloromethyl)-2,4-dimethylbenzene (**140**): A 20 mL scintillation vial is charged with **139** (835 mg, 3.4 mmol, 1 equiv) and anhydrous CH_2Cl_2 (15 mL) under N_2 atmosphere. The reaction mixture is cooled to 0 °C, then pyridine (594 mg, 7.5 mmol, 0.61 mL, 2.2 equiv) is added, followed by a dropwise addition of thionyl chloride (892 mg, 7.5 mmol, 0.55 mL, 2.2 equiv). The reaction is warmed up to 24 °C over 16 h. The reaction mixture is diluted with CH_2Cl_2 (40 mL) and 1M HCl (40 mL), and the organic phase is washed with saturated aqueous NaCl solution twice. The organic phase is dried over $MgSO_4$. Rotary evaporation yielded **140** (761 mg, 2.60 mmol, 80% yield) as an off-yellow solid. ^{1}H NMR (300 MHz, $CDCl_3$) δ 7.05 (s, 1H), 4.58 (s, 4H), 2.39 (s, 6H) ppm; GC/MS: *m*/*z* $[C_{10}H_{11}BrCl_4]^+$ calcd. 281.9 found 282.0.

(5-bromo-4,6-dimethyl-1,3-phenylene)dimethanethiol (**141**): A 100 mL flask is charged with thiourea (227 mg, 3.64 mmol, 2.5 equiv) and ethanol (50 mL). The mixture is warmed to 60 °C, then **140** (410 mg, 1.45 mmol, 1.0 equiv) is added, and the reaction is heated to 90 °C for 2 h. The reaction is then cooled, and excess ethanol is removed by rotary evaporation. The crude solid is suspended in aqueous conc. ammonia solution (20 mL), and heated to 120 °C until the solution becomes homogeneous (1 h). The reaction mixture is then cooled to 0 °C, and the pH is adjusted to 0 with dilute hydrochloric acid. The aqueous phase is extracted with EtOAc three times, and the organic phase is dried over $MgSO_4$. Rotary evaporation yielded **141** (340 mg, 1.24 mmol, 85% yield) as a clear oil which solidifies upon standing. ^{1}H NMR (300 MHz, $CDCl_3$) δ 7.07 (s, 1H), 3.78 – 3.71 (m, 4H), 2.50 – 2.43 (m, 8H) ppm; GC/MS: *m*/*z* $[C_{10}H_{13}BrS_4]^+$ calcd. 277.1 found 277.1.

1,3,6,8-tetrabromopyrene (**145**): A 100 mL flask is charged with pyrene (1.00 g, 4.95 mmol, 1 equiv) and nitrobenzene (45 mL) under ambient atmosphere and outfitted with a gas trap filled with 2M NaOH (300 mL). The mixture is heated to 40 °C with stirring, and bromine liquid (3.47 g, 1.12 mL, 21.7 mmol, 4.4 equiv) is added dropwise as the solution is warmed up to 120 °C. 15 mL of nitrobenzene is added to aid in stirring as a large amount of precipitation appears within 5 min of addition of bromine. In 4 h, the generation of HBr has stopped, and the reaction is quenched with MeOH. The heterogeneous mixture is filtered, and the solid is washed with MeOH (50 mL) and acetone (50 mL). Isolation of filtered solid yielded **145** (2.52 g, 98% yield) as an off-green solid. ^{1}H and ^{13}C NMR could not be obtained due to low solubility in all common organic solvents. MALDI-TOF: *m*/*z*: $[M]^+$ calcd. $[C_{16}H_6Br_4]$ 517.72; found 517.69.

1,3,6,8-tetramethylpyrene (**146**): A 100 mL dried Schlenk flask is charged with **145** (1.00 g, 1.93 mmol, 1 equiv) and dry, degassed THF (50 mL). The solution is cooled to −78 °C, and n-butyllithium (15.5 mmol, 6.2 mL of 2.5M solution in THF, 8 equiv) is added dropwise. The solution is stirred for 15 min at −78 °C, then the cold bath is replaced with 0 °C bath, in which the reaction mixture is stirred for 15 min. Then iodomethane (2.2 g, 0.96 mL, 15.5 mmol, 8 equiv) is added in one portion. The solution is warmed up to 24 °C over 2 h with stirring. The reaction is diluted with 1M HCl (25 mL) and stirred for 10 min. Filtration and DI water rinse yielded a crude yellow powder, which consists or a mixture of dimethyl, trimethyl, and tetramethylpyrene as assayed by

GC/MS. The crude yellow solid is resubjected to *tert*-butyllitium (3.0 mL of 1.6M solution, 4.5 mmol) followed by iodomethane quench using the same procedure as above. Filtration yielded title compound (225 mg) as fine colorless solid. ^{1}H NMR (500 MHz, $CDCl_3$) δ = 8.22 (s, 4H), 7.77 (s, 2H), 3.00 (s, 12H) ppm; GC-MS: *m/z*: $[M]^+$ calcd. $[C_{20}H_{18}]$ 258.1; found 258.1.

*Note: any hint of yellow color in the compound is deleterious in the next step, even it may appear pure by NMR and GC-MS – it is essential to ensure that the solid is completely devoid of yellow color before moving on to the next step by rinsing with excess MeOH and H_2O as necessary.

1,3,6,8-tetramethyl-4,5,9,10-tetrahydropyrene (**147**): A 20 mL Parr pressure bomb is charged with **146** (225 mg), palladium hydroxide on carbon (250 mg, 10% Pd by weight) and EtOAc (15 mL). The resulting suspension is sonicated in a water sonicator bath for 5 min. The bomb is pressurized with hydrogen gas (35–40 psi), and the reaction is stirred for 16 h. The bomb is depressurized, and the resulting heterogeneous mixture is filtered over a fritted funnel. The filter cake is resuspended in EtOAc, sonicated in water sonicator bath, and filtered again (repeated twice). Rotary evaporation of combined EtOAc eluent yielded **147** (220 mg, 92 % yield) as a crystalline colorless solid. ^{1}H NMR (400 MHz, $CDCl_3$) δ = 6.94 (s, 2H), 2.79 (s, 8H), 2.32 (s, 12H) ppm; ^{13}C NMR (101 MHz, $CDCl_3$) δ = 132.1, 131.9, 131.2, 130.9, 24.3, 19.5 ppm; GCMS: *m/z* $[M]^+$ calcd. $[C_{20}H_{22}]$ 262.2 found 262.1.

2,7-dibromo-1,3,6,8-tetramethyl-4,5,9,10-tetrahydropyrene (**127**): A 20 mL scintillation vial is charged with **147** (220 mg, 0.84 mmol, 1 equiv), NBS (310 mg, 1.75 mmol, 2.1 equiv), $FeCl_3 \cdot 9\ H_2O$ (5 mg), and CH_2Cl_2 (10 mL) under ambient conditions. The reaction mixture is stirred for 6 h while yellow precipitate slowly appears in the solution. The reaction mixture is poured into separatory funnel, and diluted with CH_2Cl_2 and saturated aqueous NaCl solution (40 mL each). Organic phase is washed with saturated aqueous NaCl solution twice, dried over $MgSO_4$ and concentrated down to approximately 10 mL. Recrystallization (layering MeOH (60 mL) / CH_2Cl_2 (10 mL)) at -30 °C yielded **127** (218 mg, 62% yield) as a yellow solid. ^{1}H NMR (500 MHz, $CDCl_3$) δ = 2.84 (s, 8H), 2.48 (s, 12H) ppm; ^{13}C NMR (126 MHz, $CDCl_3$) δ = 133.3, 132.6, 129.9, 128.9, 26.1, 20.5 ppm; HRMS (EI) *m/z*: $[M]^+$ calcd. $[C_{20}H_{10}Br_2]$ 419.9911; found 419.9910.

2,7-di(anthracen-9-yl)-1,3,6,8-tetramethyl-4,5,9,10-tetrahydropyrene (**148**): A 50 mL Schlenk flask is charged with **127** (170 mg, 0.404 mmol, 1.0 equiv) and THF (25 mL) under N_2 atmosphere. The reaction mixture is cooled to -78 °C, n-butyllithium (0.85 mmol, 0.34 mL of 2.5 M solution in THF, 2.2 equiv) is added dropwise, and TMEDA (0.85 mL) is added in one portion. The reaction mixture is stirred for 45 min at -78 °C, then warmed up to 0 °C over 15 min. Anthrone (167 mg, 0.85 mmol, 2.2 equiv) is added as a solid in one portion under N_2 blanket flow, and the reaction mixture is warmed up to 24 °C over 16 h. The reaction mixture is quenched with 1M HCl (20 mL), transferred to separatory funnel and diluted with EtOAc (50 mL). The organic phase is washed with saturated aqueous NaCl solution (40 mL) three times and dried over $MgSO_4$. Column chromatography ($CHCl_3$/hexanes gradient: 0%, 25%, 50%, 75%, 100%) yielded **148** as a yellow powder (12 mg, 0.02 mmol, 5% yield, mixed with the monocoupled product). All fractions that contain the desired spot are collected and moved forward to the bromination (next step).

2,7-bis(10-bromoanthracen-9-yl)-1,3,6,8-tetramethyl-4,5,9,10-tetrahydropyrene (**125**): A 20 mL

scintillation vial is charged with the mixed fraction of **148** (32 mg, 0.052 mmol, 1.0 equiv) and NBS (26 mg, 0.145 mmol, 2.8 equiv) and CH_2Cl_2 (10 mL) under ambient conditions. The reaction mixture is stirred for 16 h. The reaction is quenched with saturated aqueous NaCl solution, and the organic phase is washed with DI H_2O and dried over $MgSO_4$. Column chromatography ($CHCl_3$/hexanes gradient: 10% to 25% to 50%, R_f = 0.8, third spot) followed by a recrystallization from CH_2Cl_2/hexanes yielded the title compound (6.2 mg, 8.0 μmol, 15% yield) as a colorless solid. ^{1}H NMR (600 MHz, TCE-d_2) δ = 8.69 – 8.57 (m, 8H), 7.68-7.64 (m, 8H), 7.48 – 7.39 (m, 4H), 3.02 (s, 8H), 1.73 (s, 12H) ppm; ^{13}C NMR (151 MHz, TCE-d_2) δ = 138.3, 136.4, 131.8, 131.7, 130.7, 130.6, 130.2, 127.8, 127.1, 126.9, 125.7, 121.7, 24.8, 16.5 ppm; HRMS (EI) *m*/*z*: $[M]^+$ calcd. [$C_{48}H_{36}Br_2$] 772.1163; found 772.1156.

References

(1) Dresselhaus, M. S.; Dresslhaus, G. *Annu. Rev. Mater. Sci* **1995**, *25*, 487–523.

(2) Moore, G. *Proc. IEEE* **1998**, *86*, 82–85.

(3) Ionescu, A. M.; Riel, H. *Nature* **2011**, *479*, 329–337.

(4) Bimo, C. S. P.; Noor, F. A.; Abdullah, M.; Khairurrijal *AMR* **2014**, *896*, 371–374.

(5) Vadlamani, S. K.; Agarwal, S.; Limmer, D. T.; Louie, S. G.; Fischer, F. R.; Yablonovitch, E. *Proc. IEEE* **2020**, *108*, 1235–1244.

(6) Lv, Y.; Qin, W.; Wang, C.; Liao, L.; Liu, X. *Adv. Electron. Mater.* **2019**, *5*, 1800569.

(7) Su, W. P.; Schrieffer, J. R.; Heeger, A. J. *Phys. Rev. B* **1980**, *22*, 2099–2111.

(8) Kroto, H.; Heath, J.; O'Brien, C.; Curl, R.; Smalley, R. *Nature* **1985**, *318*, 162–163.

(9) Iijima, S.; Ichihashi, T. *Nature* **1993**, *363*, 603–605.

(10) Jiao, L.; Zhang, L.; Wang, X.; Diankov, G.; Dai, H. *Nature* **2009**, *458*, 877–880.

(11) Rao, R. et al. *ACS Nano* **2018**, *12*, 11756–11784.

(12) Novoselov, K. S. *Science* **2004**, *306*, 666–669.

(13) Kamran, U.; Heo, Y.-J.; Lee, J. W.; Park, S.-J. *Micromachines* **2019**, *10*, 234.

(14) Khair, N.; Islam, R.; Shahariar, H. *J Mater Sci* **2019**, *54*, 10079–10101.

(15) Childres, I.; Jauregui, L. A.; Park, W.; Cao, H.; Chen, Y. P. *New Developments in Photon and Materials Research* **2013**, 403–418.

(16) Han, W.; Kawakami, R. K.; Gmitra, M.; Fabian, J. *Nature Nanotech* **2014**, *9*, 794–807.

(17) Kane, C. L.; Mele, E. J. *Phys. Rev. Lett.* **2005**, *95*, 226801.

(18) Malard, L.; Pimenta, M.; Dresselhaus, G.; Dresselhaus, M. *Physics Reports* **2009**, *473*, 51–87.

(19) Manocha, P.; Kandpal, K.; Goswami, R. *Silicon* **2020**, DOI: 10.1007/s12633-020-00452-y.

(20) Qiu, C.; Liu, F.; Xu, L.; Deng, B.; Xiao, M.; Si, J.; Lin, L.; Zhang, Z.; Wang, J.; Guo, H.; Peng, H.; Peng, L.-M. *Science* **2018**, *361*, 387–392.

(21) Schultz, B. J.; Dennis, R. V.; Lee, V.; Banerjee, S. *Nanoscale* **2014**, 3444–3466.

(22) Zeng, W.; Wu, J. *Chem* **2020**, 1–29.

(23) Lee, H. C.; Liu, W.-W.; Chai, S.-P.; Mohamed, A. R.; Aziz, A.; Khe, C.-S.; Hidayah, N. M. S.; Hashim, U. *RSC Adv.* **2017**, *7*, 15644–15693.

(24) Fujita, M.; Wakabayashi, K.; Nakada, K.; Kusakabe, K. *J. Phys. Soc. Jpn.* **1996**, *65*, 1920–1923.

(25) Zhang, Q.; Fang, T.; Xing, H.; Seabaugh, A.; Jena, D. *IEEE Electron Device Lett.* **2008**, *29*, 1344–1346.

(26) Seabaugh, A. C.; Zhang, Q. *Proc. IEEE* **2010**, *98*, 2095–2110.

(27) Jena, D.; Fang, T.; Zhang, Q.; Xing, H. *Appl. Phys. Lett.* **2008**, *93*, 112106.

(28) Baughman, R. H. *Science* **2002**, *297*, 787–792.

(29) Javey, A.; Guo, J.; Wang, Q.; Lundstrom, M.; Dai, H. *Nature* **2003**, *424*, 654–657.

(30) Javey, A.; Guo, J.; Farmer, D. B.; Wang, Q.; Yenilmez, E.; Gordon, R. G.; Lundstrom, M.; Dai, H. *Nano Lett.* **2004**, *4*, 1319–1322.

(31) Luisier, M.; Lundstrom, M.; Antoniadis, D. A.; Bokor, J. In *2011 International Electron Devices Meeting*, IEEE: Washington, DC, USA, 2011, pp 11.2.1–11.2.4.

(32) Franklin, A. D.; Luisier, M.; Han, S.-J.; Tulevski, G.; Breslin, C. M.; Gignac, L.; Lundstrom, M. S.; Haensch, W. *Nano Lett.* **2012**, *12*, 758–762.

(33) Franklin, A. *Nature* **2013**, *498*, 443–444.

(34) Son, Y.-W.; Cohen, M. L.; Louie, S. G. *Phys. Rev. Lett.* **2006**, *97*, 216803.

(35) Han, M. Y.; Özyilmaz, B.; Zhang, Y.; Kim, P. *Phys. Rev. Lett.* **2007**, *98*, 206805.

(36) Bai, J.; Duan, X.; Huang, Y. *Nano Lett.* **2009**, *9*, 2083–2087.

(37) Tapasztó, L.; Dobrik, G.; Lambin, P.; Biró, L. P. *Nature Nanotech* **2008**, *3*, 397–401.

(38) Abbas, A. N.; Liu, G.; Liu, B.; Zhang, L.; Liu, H.; Ohlberg, D.; Wu, W.; Zhou, C. *ACS Nano* **2014**, *8*, 1538–1546.

(39) Kosynkin, D. V.; Higginbotham, A. L.; Sinitskii, A.; Lomeda, J. R.; Dimiev, A.; Price, B. K.; Tour, J. M. *Nature* **2009**, *458*, 872–876.

(40) Jiao, L.; Wang, X.; Diankov, G.; Wang, H.; Dai, H. *Nature Nanotech* **2010**, *5*, 321–325.

(41) Cai, J.; Ruffieux, P.; Jaafar, R.; Bieri, M.; Braun, T.; Blankenburg, S.; Muoth, M.; Seitsonen, A. P.; Saleh, M.; Feng, X.; Müllen, K.; Fasel, R. *Nature* **2010**, *466*, 470–473.

(42) Zandvliet, H. J.; van Houselt, A. *Annual Rev. Anal. Chem.* **2009**, *2*, 37–55.

(43) Swart, I.; Liljeroth, P.; Vanmaekelbergh, D. *Chem. Rev.* **2016**, *116*, 11181–11219.

(44) Merino-Díez, N.; Garcia-Lekue, A.; Carbonell-Sanromà, E.; Li, J.; Corso, M.; Colazzo, L.; Sedona, F.; Sánchez-Portal, D.; Pascual, J. I.; de Oteyza, D. G. *ACS Nano* **2017**, *11*, 11661–11668.

(45) Talirz, L.; Ruffieux, P.; Fasel, R. *Adv. Mater.* **2016**, *28*, 6222–6231.

(46) Zhang, H.; Lin, H.; Sun, K.; Chen, L.; Zagranyarski, Y.; Aghdassi, N.; Duhm, S.; Li, Q.; Zhong, D.; Li, Y.; Müllen, K.; Fuchs, H.; Chi, L. *J. Am. Chem. Soc.* **2015**, *137*, 4022–4025.

(47) Talirz, L. et al. *ACS Nano* **2017**, *11*, 1380–1388.

(48) Chen, Y.-C.; de Oteyza, D. G.; Pedramrazi, Z.; Chen, C.; Fischer, F. R.; Crommie, M. F. *ACS Nano* **2013**, *7*, 6123–6128.

(49) Liu, J.; Li, B.-W.; Tan, Y.-Z.; Giannakopoulos, A.; Sanchez-Sanchez, C.; Beljonne, D.; Ruffieux, P.; Fasel, R.; Feng, X.; Müllen, K. *J. Am. Chem. Soc.* **2015**, *137*, 6097–6103.

(50) Ruffieux, P.; Wang, S.; Yang, B.; Sánchez-Sánchez, C.; Liu, J.; Dienel, T.; Talirz, L.; Shinde, P.; Pignedoli, C. A.; Passerone, D.; Dumslaff, T.; Feng, X.; Müllen, K.; Fasel, R. *Nature* **2016**, *531*, 489–492.

(51) Chen, Y.-C.; Cao, T.; Chen, C.; Pedramrazi, Z.; Haberer, D.; de Oteyza, D. G.; Fischer, F. R.; Louie, S. G.; Crommie, M. F. *Nature Nanotech* **2015**, *10*, 156–160.

(52) Bronner, C.; Durr, R. A.; Rizzo, D. J.; Lee, Y.-L.; Marangoni, T.; Kalayjian, A. M.; Rodriguez, H.; Zhao, W.; Louie, S. G.; Fischer, F. R.; Crommie, M. F. *ACS Nano* **2018**, *12*, 2193–2200.

(53) Marangoni, T.; Haberer, D.; Rizzo, D. J.; Cloke, R. R.; Fischer, F. R. *Chem. Eur. J.* **2016**, *22*, 13037–13040.

(54) Nguyen, G. D. et al. *Nature Nanotech* **2017**, *12*, 1077–1082.

(55) Simonov, K. A.; Generalov, A. V.; Vinogradov, A. S.; Svirskiy, G. I.; Cafolla, A. A.; McGuinness, C.; Taketsugu, T.; Lyalin, A.; Mårtensson, N.; Preobrajenski, A. B. *Sci Rep* **2018**, *8*, 3506.

(56) Sánchez-Sánchez, C.; Dienel, T.; Deniz, O.; Ruffieux, P.; Berger, R.; Feng, X.; Müllen, K.; Fasel, R. *ACS Nano* **2016**, *10*, 8006–8011.

(57) Narita, A.; Wang, X.-Y.; Feng, X.; Müllen, K. *Chem. Soc. Rev.* **2015**, *44*, 6616–6643.

(58) Grzybowski, M.; Skonieczny, K.; Butenschön, H.; Gryko, D. T. *Angew. Chem. Int. Ed.* **2013**, *52*, 9900–9930.

(59) Vo, T. H.; Shekhirev, M.; Kunkel, D. A.; Morton, M. D.; Berglund, E.; Kong, L.; Wilson, P. M.; Dowben, P. A.; Enders, A.; Sinitskii, A. *Nat Commun* **2014**, *5*, 3189.

(60) Vo, T. H.; Shekhirev, M.; Lipatov, A.; Korlacki, R. A.; Sinitskii, A. *Faraday Discuss.* **2014**, 10.1039.C4FD00131A.

(61) Saleh, M.; Baumgarten, M.; Mavrinskiy, A.; Schäfer, T.; Müllen, K. *Macromolecules* **2010**, *43*, 137–143.

(62) Liu, X.; Li, G.; Lipatov, A.; Sun, T.; Mehdi Pour, M.; Aluru, N. R.; Lyding, J. W.; Sinitskii, A. *Nano Res.* **2020**, *13*, 1713–1722.

(63) Li, G.; Yoon, K.-Y.; Zhong, X.; Zhu, X.; Dong, G. *Chem. Eur. J.* **2016**, *22*, 9116–9120.

(64) Shifrina, Z. B.; Averina, M. S.; Rusanov, A. L.; Wagner, M.; Müllen, K. *Macromolecules* **2000**, *33*, 3525–3529.

(65) Kumar, U.; Neenan, T. X. *Macromolecules* **1995**, *28*, 124–130.

(66) Narita, A. et al. *Nature Chem* **2014**, *6*, 126–132.

(67) Narita, A.; Verzhbitskiy, I. A.; Frederickx, W.; Mali, K. S.; Jensen, S. A.; Hansen, M. R.; Bonn, M.; De Feyter, S.; Casiraghi, C.; Feng, X.; Müllen, K. *ACS Nano* **2014**, *8*, 11622–11630.

(68) Hu, Y. et al. *J. Am. Chem. Soc.* **2018**, *140*, 7803–7809.

(69) Joshi, D.; Hauser, M.; Veber, G.; Berl, A.; Xu, K.; Fischer, F. R. *J. Am. Chem. Soc.* **2018**, *140*, 9574–9580.

(70) von Kugelgen, S.; Piskun, I.; Griffin, J. H.; Eckdahl, C. T.; Jarenwattananon, N. N.; Fischer, F. R. *J. Am. Chem. Soc.* **2019**, *141*, 11050–11058.

(71) Verzhbitskiy, I. A.; Corato, M. D.; Ruini, A.; Molinari, E.; Narita, A.; Hu, Y.; Schwab, M. G.; Bruna, M.; Yoon, D.; Milana, S.; Feng, X.; Müllen, K.; Ferrari, A. C.; Casiraghi, C.; Prezzi, D. *Nano Lett.* **2016**, *16*, 3442–3447.

(72) Luo, G.; Li, H.; Wang, L.; Lai, L.; Zhou, J.; Qin, R.; Lu, J.; Mei, W.-N.; Gao, Z. *J. Phys. Chem. C* **2010**, *114*, 6959–6965.

(73) Yamada, Y.; Masaki, S.; Sato, S. *J Mater Sci* **2020**, *55*, 10522–10542.

(74) Bennett, P. B.; Pedramrazi, Z.; Madani, A.; Chen, Y.-C.; de Oteyza, D. G.; Chen, C.; Fischer, F. R.; Crommie, M. F.; Bokor, J. *Appl. Phys. Lett.* **2013**, *103*, 253114.

(75) Llinas, J. P. et al. *Nat Commun* **2017**, *8*, 633.

(76) Linden, S.; Zhong, D.; Timmer, A.; Aghdassi, N.; Franke, J. H.; Zhang, H.; Feng, X.; Müllen, K.; Fuchs, H.; Chi, L.; Zacharias, H. *Phys. Rev. Lett.* **2012**, *108*, 216801.

(77) Bronner, C.; Stremlau, S.; Gille, M.; Braße, F.; Haase, A.; Hecht, S.; Tegeder, P. *Angew. Chem. Int. Ed.* **2013**, *52*, 4422–4425.

(78) Cloke, R. R.; Marangoni, T.; Nguyen, G. D.; Joshi, T.; Rizzo, D. J.; Bronner, C.; Cao, T.; Louie, S. G.; Crommie, M. F.; Fischer, F. R. *J. Am. Chem. Soc.* **2015**, *137*, 8872–8875.

(79) Kawai, S.; Saito, S.; Osumi, S.; Yamaguchi, S.; Foster, A. S.; Spijker, P.; Meyer, E. *Nat Commun* **2015**, *6*, 8098.

(80) Baranac-Stojanović, M. *Chem. Eur. J.* **2014**, *20*, 16558–16565.

(81) Agou, T.; Kojima, T.; Kobayashi, J.; Kawashima, T. *Organic Letters* **2009**, *11*, 3534–3537.

(82) Rieke, R. D.; Bales, S. E.; Hundall, P.; Burns, T. P.; Poindexter, G. S. *Org. Synth.* **1979**, *59*, 85.

(83) Igarashi, T.; Tobisu, M.; Chatani, N. *Angew. Chem. Int. Ed.* **2017**, *56*, 2069–2073.

(84) Guerrand, H.; Vaultier, M.; Pinet, S.; Pucheault, M. *Adv. Synth. Catal.* **2015**, 8.

(85) Talirz, L.; Söde, H.; Cai, J.; Ruffieux, P.; Blankenburg, S.; Jafaar, R.; Berger, R.; Feng, X.; Müllen, K.; Passerone, D.; Fasel, R.; Pignedoli, C. A. *J. Am. Chem. Soc.* **2013**, *135*, 2060–2063.

(86) Durr, R. A.; Haberer, D.; Lee, Y.-L.; Blackwell, R.; Kalayjian, A. M.; Marangoni, T.; Ihm, J.; Louie, S. G.; Fischer, F. R. *J. Am. Chem. Soc.* **2018**, *140*, 807–813.

(87) Rizzo, D. J. et al. *Nano Lett.* **2019**, *19*, 3221–3228.

(88) Cao, Y.; Qi, J.; Zhang, Y.-F.; Huang, L.; Zheng, Q.; Lin, X.; Cheng, Z.; Zhang, Y.-Y.; Feng, X.; Du, S.; Pantelides, S. T.; Gao, H.-J. *Nano Res.* **2018**, *11*, 6190–6196.

(89) Zhang, Y.-F.; Zhang, Y.; Li, G.; Lu, J.; Que, Y.; Chen, H.; Berger, R.; Feng, X.; Müllen, K.; Lin, X.; Zhang, Y.-Y.; Du, S.; Pantelides, S. T.; Gao, H.-J. *Nano Res.* **2017**, *10*, 3377–3384.

(90) Perkins, W. S. Synthesis and Applications of Graphene Nanoribbons and Heterostructures from Molecular Precursors, en, Ph.D. Thesis.

(91) Cloke, R. R. Synthesis of Doped Graphene Nanoribbons from Molecular and Polymeric Precursors, en, Ph.D. Thesis.

(92) Giannozzi, P. et al. *J. Phys.: Condens. Matter* **2009**, *21*, 395502.

(93) Hybertsen, M. S.; Louie, S. G. *Phys. Rev. B* **1986**, *34*, 5390–5413.

(94) Deslippe, J.; Samsonidze, G.; Strubbe, D. A.; Jain, M.; Cohen, M. L.; Louie, S. G. *Computer Physics Communications* **2012**, *183*, 1269–1289.

(95) Blum, V.; Gehrke, R.; Hanke, F.; Havu, P.; Havu, V.; Ren, X.; Reuter, K.; Scheffler, M. *Computer Physics Communications* **2009**, *180*, 2175–2196.

(96) Lelaidier, T.; Leoni, T.; Arumugam, P.; Ranguis, A.; Becker, C.; Siri, O. *Langmuir* **2014**, *30*, 5700–5704.

(97) Hayashi, H.; Yamaguchi, J.; Jippo, H.; Hayashi, R.; Aratani, N.; Ohfuchi, M.; Sato, S.; Yamada, H. *ACS Nano* **2017**, *11*, 6204–6210.

(98) Radocea, A.; Sun, T.; Vo, T. H.; Sinitskii, A.; Aluru, N. R.; Lyding, J. W. *Nano Lett.* **2017**, *17*, 170–178.

(99) Li, G.; Yoon, K.-Y.; Zhong, X.; Wang, J.; Zhang, R.; Guest, J. R.; Wen, J.; Zhu, X.-Y.; Dong, G. *Nat Commun* **2018**, *9*, 1687.

(100) Nakada, K.; Fujita, M.; Dresselhaus, G.; Dresselhaus, M. S. *Phys. Rev. B* **1996**, *54*, 17954–17961.

(101) Wolf, S. A. *Science* **2001**, *294*, 1488–1495.

(102) Biermann, D.; Schmidt, W. *J. Am. Chem. Soc.* **1980**, *102*, 3163–3173.

(103) Maliakal, A.; Raghavachari, K.; Katz, H.; Chandross, E.; Siegrist, T. *Chem. Mater.* **2004**, *16*, 4980–4986.

(104) Konishi, A.; Hirao, Y.; Nakano, M.; Shimizu, A.; Botek, E.; Champagne, B.; Shiomi, D.; Sato, K.; Takui, T.; Matsumoto, K.; Kurata, H.; Kubo, T. *J. Am. Chem. Soc.* **2010**, *132*, 11021–11023.

(105) Konishi, A.; Hirao, Y.; Matsumoto, K.; Kurata, H.; Kishi, R.; Shigeta, Y.; Nakano, M.; Tokunaga, K.; Kamada, K.; Kubo, T. *J. Am. Chem. Soc.* **2013**, *135*, 1430–1437.

(106) Watanabe, M.; Chang, Y. J.; Liu, S.-W.; Chao, T.-H.; Goto, K.; Islam, M. M.; Yuan, C.-H.; Tao, Y.-T.; Shinmyozu, T.; Chow, T. J. *Nature Chem* **2012**, *4*, 574–578.

(107) Rogers, C.; Chen, C.; Pedramrazi, Z.; Omrani, A. A.; Tsai, H.-Z.; Jung, H. S.; Lin, S.; Crommie, M. F.; Fischer, F. R. *Angew. Chem. Int. Ed.* **2015**, *54*, 15143–15146.

(108) Zimmermann, T.; Fischer, G. W. *J. Prakt. Chem.* **1987**, *329*, 975–984.

(109) Mahler, C.; Müller, U.; Müller, W. M.; Enkelmann, V.; Moon, C.; Brunklaus, G.; Zimmermann, H.; Höger, S. *Chem. Commun.* **2008**, 4816.

(110) Perdew, J. P.; Zunger, A. *Phys. Rev. B* **1981**, *23*, 5048–5079.

(111) Lieb, E. H. *Phys. Rev. Lett.* **1989**, *62*, 1201–1204.

(112) Son, Y.-W.; Cohen, M. L.; Louie, S. G. *Nature* **2006**, *444*, 347–349.

(113) Hayes, C. J.; Hadad, C. M. *J. Phys. Chem. A* **2009**, *113*, 12370–12379.

(114) Chmil, K.; Scherf, U. *Makromol. Chem., Rapid Commun.* **1993**, *14*, 217–222.

(115) Scherf, U.; List, E. J. W. *Adv. Mater.* **2002**, 11.

(116) Schmidt, J.; Werner, M.; Thomas, A. *Macromolecules* **2009**, *42*, 4426–4429.

(117) Yamamoto, T.; Morita, A.; Miyazaki, Y.; Maruyama, T.; Wakayama, H.; Zhou, Z.-h.; Nakamura, Y.; Kanbara, T.; Sasaki, S. **1992**, *25*, 10.

(118) Castiglioni, C.; Mapelli, C.; Negri, F.; Zerbi, G. *J. Chem. Phys.* **2001**, *114*, 963.

(119) Natrajan, A.; Wen, D. **2011**, 9.

(120) Garate, I.; Franz, M. *Phys. Rev. Lett.* **2010**, *104*, 146802.

(121) Hasan, M. Z.; Kane, C. L. *Rev. Mod. Phys.* **2010**, *82*, 3045–3067.

(122) Moore, J. E. *Nature* **2010**, *464*, 194–198.

(123) Qi, X.-L.; Zhang, S.-C. *Rev. Mod. Phys.* **2011**, *83*, 1057–1110.

(124) Loss, D.; DiVincenzo, D. P. *Phys. Rev. A* **1998**, *57*, 120–126.

(125) Trauzettel, B. R.; Bulaev, D. V.; Loss, D.; Burkard, G. **2007**, *3*, 5.

(126) Lombardi, F.; Lodi, A.; Ma, J.; Liu, J.; Slota, M.; Narita, A.; Myers, W. K.; Müllen, K.; Feng, X.; Bogani, L. *Science* **2019**, *366*, 1107–1110.

(127) Alicea, J.; Oreg, Y.; Refael, G.; von Oppen, F.; Fisher, M. P. A. *Nature Phys* **2011**, *7*, 412–417.

(128) Lutchyn, R. M.; Sau, J. D.; Das Sarma, S. *Phys. Rev. Lett.* **2010**, *105*, 077001.

(129) Oreg, Y.; Refael, G.; von Oppen, F. *Phys. Rev. Lett.* **2010**, *105*, 177002.

(130) Cao, T.; Zhao, F.; Louie, S. G. *Phys. Rev. Lett.* **2017**, *119*, 076401.

(131) Cohen, M. L.; Schlüter, M.; Chelikowsky, J. R.; Louie, S. G. *Phys. Rev. B* **1975**, *12*, 5575–5579.

(132) Rizzo, D. J.; Veber, G.; Cao, T.; Bronner, C.; Chen, T.; Zhao, F.; Rodriguez, H.; Louie, S. G.; Crommie, M. F.; Fischer, F. R. *Nature* **2018**, *560*, 204–208.

(133) Gröning, O.; Wang, S.; Yao, X.; Pignedoli, C. A.; Borin Barin, G.; Daniels, C.; Cupo, A.; Meunier, V.; Feng, X.; Narita, A.; Müllen, K.; Ruffieux, P.; Fasel, R. *Nature* **2018**, *560*, 209–213.

(134) Rizzo, D. J.; Veber, G.; Jiang, J.; McCurdy, R.; Cao, T.; Bronner, C.; Chen, T.; Louie, S. G.; Fischer, F. R.; Crommie, M. F. **2020**, 8.

(135) Lee, Y.-L.; Zhao, F.; Cao, T.; Ihm, J.; Louie, S. G. *Nano Lett.* **2018**, *18*, 7247–7253.

(136) Clar, E.; Mackay, C. C. *Tetrahedron* **1972**, *28*, 6041–6047.

(137) Clar, E., *Polycyclic Hydrocarbons*; Springer Berlin Heidelberg: Berlin, Heidelberg, 1964.

(138) Solà, M. *Front. Chem.* **2013**, *1*, DOI: 10.3389/fchem.2013.00022.

(139) Mohn, F.; Gross, L.; Moll, N.; Meyer, G. *Nature Nanotech* **2012**, *7*, 227–231.

(140) Gross, L.; Mohn, F.; Moll, N.; Schuler, B.; Criado, A.; Guitian, E.; Pena, D.; Gourdon, A.; Meyer, G. *Science* **2012**, *337*, 1326–1329.

(141) Schuler, B.; Liu, W.; Tkatchenko, A.; Moll, N.; Meyer, G.; Mistry, A.; Fox, D.; Gross, L. *Phys. Rev. Lett.* **2013**, *111*, 106103.

(142) Pavliček, N.; Mistry, A.; Majzik, Z.; Moll, N.; Meyer, G.; Fox, D. J.; Gross, L. *Nature Nanotech* **2017**, *12*, 308–311.

(143) Mishra, S.; Beyer, D.; Eimre, K.; Liu, J.; Berger, R.; Gröning, O.; Pignedoli, C. A.; Müllen, K.; Fasel, R.; Feng, X.; Ruffieux, P. *J. Am. Chem. Soc.* **2019**, *141*, 10621–10625.

(144) Mishra, S.; Yao, X.; Chen, Q.; Eimre, K.; Gröning, O.; Ortiz, R.; Giovannantonio, M. D.; Sancho-García, J. C.; Fernández-Rossier, J.; Pignedoli, C. A.; Müllen, K.; Ruffieux, P.; Narita, A.; Fasel, R., 34.

(145) Pogodin, S.; Agranat, I. *J. Org. Chem.* **2003**, *68*, 2720–2727.

(146) Sevinçli, H.; Topsakal, M.; Ciraci, S. *Phys. Rev. B* **2008**, *78*, 245402.

(147) Mishra, S.; Beyer, D.; Eimre, K.; Kezilebieke, S.; Berger, R.; Gröning, O.; Pignedoli, C. A.; Müllen, K.; Liljeroth, P.; Ruffieux, P.; Feng, X.; Fasel, R. *Nat. Nanotechnol.* **2020**, *15*, 22–28.

(148) Mitchell, R. H.; Carruthers, R. J. *Can. J. Chem.* **1974**, *52*, 3054–3056.

(149) Figueira-Duarte, T. M.; Müllen, K. *Chem. Rev.* **2011**, *111*, 7260–7314.

(150) Li, J.; Takaishi, S.; Fujinuma, N.; Endo, K.; Yamashita, M.; Matsuzaki, H.; Okamoto, H.; Sawabe, K.; Takenobu, T.; Iwasa, Y. **2011**, 5.

(151) Lan, X.-B.; Li, Y.; Li, Y.-F.; Shen, D.-S.; Ke, Z.; Liu, F.-S. *J. Org. Chem.* **2017**, *82*, 2914–2925.

(152) Li, T.; Guo, L.; Zhang, Y.; Wang, J.; Li, Z.; Lin, L.; Zhang, Z.; Li, L.; Lin, J.; Zhao, W.; Li, J.; Wang, P. G. *Carbohydrate Research* **2011**, *346*, 1083–1092.

(153) Lottermoser, U.; Rademacher, P.; Mazik, M.; Kowski, K. *Eur. J. Org. Chem.* **2005**, *2005*, 522–531.

(154) Tang, Q.; Liu, J.; Chan, H. S.; Miao, Q. *Chem. Eur. J.* **2009**, *15*, 3965–3969.

(155) Schwarzenböck, C.; Schaffer, A.; Pahl, P.; Nelson, P. J.; Huss, R.; Rieger, B. *Polym. Chem.* **2018**, *9*, 284–290.